

POLITECNICO DI TORINO

Corso di Laurea Magistrale in Ingegneria Elettrica

Tesi di Laurea Magistrale

**Sensorless algorithm for  
synchronous machines using  
current oversampling and PWM  
harmonics**



Relatori:

Dr. Luca Peretti, Principal Scientist

Prof. Michele Angelo Pastorelli

Candidato:

Giorgio GULLONE



## **Ringraziamenti**

Il candidato ringrazia ABB Corporate Research Sweden, Västerås, dove ha avuto l'occasione e l'onore di poter svolgere il presente lavoro.

Un ringraziamento particolare è rivolto al Dr. Luca Peretti, Principal scientist, nella sua veste di supervisor, per gli insegnamenti offerti durante i sei mesi spesi nel centro di ricerca ABB.





Sensorless algorithm for synchronous machines  
using current oversampling and PWM harmonics

Giorgio GULLONE

March 2018



## TABLE OF CONTENTS

<b>1</b>	<b>INTRODUCTION</b>	<b>7</b>
1.1	Purpose . . . . .	7
1.2	Scope . . . . .	7
1.3	Definitions . . . . .	8
1.4	Structure . . . . .	13
<b>2</b>	<b>PROBLEM DESCRIPTION</b>	<b>15</b>
2.1	Sensorless control methods . . . . .	15
<b>3</b>	<b>INTRINSIC INJECTION SENSORLESS CONTROL</b>	<b>19</b>
3.1	Analytical operation of the intrinsic injection sensorless control . . . . .	19
3.1.1	Searched voltage harmonic content calculation . . . . .	20
3.1.2	Searched current harmonic content calculation . . . . .	24
3.1.3	Demodulation . . . . .	25
3.2	Considerations on the intrinsic injection sensorless estimator . . . . .	27
3.2.1	Motor speed and load influence . . . . .	27
3.2.2	Saliency influence . . . . .	30
3.2.3	Filtering actions . . . . .	32
3.2.4	Position error considerations . . . . .	35
3.2.5	Searched harmonic content . . . . .	36
3.2.6	Overmodulation . . . . .	38
3.2.7	Intrinsic injection sensorless summary . . . . .	38
<b>4</b>	<b>MODELLING OF THE SUBSYSTEMS</b>	<b>41</b>
4.1	Motor model . . . . .	41
4.1.1	SynRM equations . . . . .	42
4.1.2	SynRM model . . . . .	46
4.2	PWM converter model . . . . .	48
4.2.1	PWM converter model . . . . .	48
4.2.2	Modulator model using carrier-reference comparison . . . . .	50

---

4.2.3	Modulator model using UVMT . . . . .	52
4.2.4	Modulation schemes implementation for regularly sampled carrier . . . . .	56
4.3	Control model . . . . .	62
4.3.1	Drive model without speed estimator . . . . .	62
4.3.2	Current regulator . . . . .	63
4.3.3	Speed regulator . . . . .	68
4.4	Intrinsic injection sensorless control model . . . . .	70
4.4.1	Estimator alternative 1 . . . . .	71
4.4.2	Current PLL and ripple calculator . . . . .	76
4.4.3	Estimator alternative 2 . . . . .	79
4.4.4	Estimator alternative 3 . . . . .	80
4.5	Parameter values . . . . .	84
<b>5</b>	<b>SIMULATIONS</b>	<b>87</b>
5.1	Introduction . . . . .	87
5.2	Harmonic analysis . . . . .	87
5.2.1	UVMT modulation validation . . . . .	88
5.2.2	Comparison of the simulation spectra with the theory . . . . .	93
5.2.3	Torque and speed influence . . . . .	99
5.3	Current PLL and ripple calculator simulations . . . . .	111
5.4	Open-loop simulations . . . . .	112
5.4.1	Estimator 1 in open-loop . . . . .	114
5.4.2	Estimator 1 in open-loop, other modulations . . . . .	118
5.4.3	Estimator 2 in open-loop . . . . .	121
5.4.4	Estimator 2 in open-loop, other modulations . . . . .	124
5.4.5	Estimator 3 in open-loop . . . . .	127
5.4.6	Estimator 3 in open-loop, other modulations . . . . .	130
5.4.7	Open-Loop torque and inductances . . . . .	133
5.5	Closed-loop simulations . . . . .	134
5.5.1	Estimator 1 in closed-loop . . . . .	136
5.5.2	Estimator 1 in closed-loop, other modulations . . . . .	138
5.5.3	Estimator 2 in closed-loop . . . . .	141
5.5.4	Estimator 2 in closed-loop, other modulations . . . . .	143
5.6	Sampling and oversampling . . . . .	146
5.6.1	Estimator 1 . . . . .	147
5.6.2	Estimator 2 . . . . .	151
5.6.3	Estimator 3 . . . . .	155
5.7	Fan or pump application . . . . .	159
5.7.1	Estimator 1 and 2 . . . . .	159
5.8	DC link voltage amplitude influence . . . . .	165

---

<b>6</b>	<b>CONCLUSIONS</b>	<b>171</b>
<b>7</b>	<b>FUTURE WORK</b>	<b>175</b>
<b>A</b>	<b>APPENDIX</b>	<b>177</b>
A.1	Theoretical complex Fourier coefficients . . . . .	177
A.2	UVMT offset time calculation blocks . . . . .	179
	<b>REFERENCES</b>	<b>183</b>



# Chapter 1

## INTRODUCTION

### 1.1 Purpose

The purpose of this report is the description of the intrinsic injection sensorless algorithm and its implementation in a MATLAB/Simulink environment. The targeted reader for this report is a professional working in the electrical machines and drives area, with particular focus on the control and on the PWM modulation techniques.

### 1.2 Scope

In this work, the theoretical foundation of the intrinsic injection sensorless control is deeply analysed, together with the phenomena and the operating conditions that might affect its performance. The drive model is described and three different alternatives for the estimator have been proposed. Simulations have been firstly run in order to check that the implemented drive is able to work with different PWM modulation strategies and in order to verify the sampling frequency influence on the estimator performance. Therefore, simulations have been run firstly with the estimator operating in open-loop, afterwards with the estimator working in closed-loop, and the influences of the motor speed, of the load torque, of the implemented modulation strategy and of the DC-link voltage amplitude have been analysed. Lastly, the drive has been simulated with regard to a fan or pump application.

## 1.3 Definitions

The following terms have been used throughout the report:

### PWM theoretical harmonic content and speed estimator parameters

$f_c$	Carrier frequency
$\omega_c$	Carrier angular frequency
$T_c$	Carrier period
$\theta_c$	Phase offset angle of the carrier waveform
$f_o$	Fundamental frequency
$\omega_o$	Fundamental angular frequency
$T_o$	Fundamental period
$\theta_o$	Phase offset angle of the fundamental component
$M$	Modulation index
$p$	Pulse number
$m$	Carrier index variable
$n$	Sideband index variable
$C_{mn}$	Complex Fourier coefficient
$J_k(x)$	Bessel function of order $k$ and argument $x$
$u_{an}, u_{bn}, u_{cn}$	Phase to negative terminal voltages
$u_{az}, u_{bz}, u_{cz}$	Phase to DC link midpoint voltages
$u_{an_c}, u_{bn_c}, u_{cn_c}$	Phase to converter negative terminal voltages relative to $m = 1, n = \pm 1$ harmonic content
$u_{az_c}, u_{bz_c}, u_{cz_c}$	Phase to DC link midpoint voltages relative to $m = 1, n = \pm 1$ harmonic content
$u_{\alpha_c}, u_{\beta_c}$	$\alpha\beta$ coordinates voltages relative to $m = 1, n = \pm 1$ harmonic content
$i_{\alpha_c}, i_{\beta_c}$	$\alpha\beta$ coordinates currents relative to $m = 1, n = \pm 1$ harmonic content
$A^c, A^+, A^-$	Voltage harmonic coefficients relative to $m = 1, n = \pm 1$
$I_0^+, I_0^-, I_1^+, I_1^-$	Current harmonic coefficients relative to $m = 1, n = \pm 1$
$\theta_u^r$	Voltage vector angle in the $dq$ reference frame

$\theta_{u,0}^r$	Voltage vector angle in the $dq$ reference frame at the initial instant
$\hat{\omega}_{me}$	Estimated motor electrical speed
$\hat{\omega}_m$	Estimated motor mechanical speed
$\hat{\theta}_{me}$	Estimated motor electrical angle
$\hat{\theta}'_{me}$	Estimated motor electrical angle added by $\theta_{u,0}^r$
$\hat{\theta}_m$	Estimated motor mechanical angle
$\Delta\theta'_{me}$	Position error between $\hat{\theta}'_{me}$ and $\theta_{me}$
$\Delta\theta_{me}$	Position error between $\hat{\theta}_{me}$ and $\theta_{me}$
$\epsilon$	Error signal containing the position information
$\epsilon_{LP}$	Low Pass Filtered $\epsilon$
$i_{\alpha_1}, i_{\beta_1}$	Simplified $\alpha\beta$ coordinates currents including $m = 1$ , $n = \pm 1$ harmonic content
$i_{\alpha_3}, i_{\beta_3}$	Simplified $\alpha\beta$ coordinates currents including $m = 1$ , $n = \pm 1, \pm 2 \pm 3$ harmonic content
$I_1, I_2, I_3$	Simplified current harmonic coefficients relative to $m = 1$ and respectively $n = \pm 1, \pm 2 \pm 3$
$\epsilon_1, \epsilon_3$	Simplified error signals
$\epsilon_{1LP}, \epsilon_{3LP}$	Low Pass Filtered $\epsilon_1$ and $\epsilon_3$

### Synchronous reluctance machine parameters

SynRM	Synchronous Reluctance Machine
MTPA	Maximum Torque Per Ampère
LUT	Look-Up Table
EMF	ElectroMotive Force
$V_n$	Motor nominal voltage
$I_n$	Motor nominal current
$\tau$	Motor electromechanical torque
$\tau_n$	Motor electromechanical nominal torque
$\tau_l$	Load torque torque
$\omega_m$	Motor mechanical speed in $rad/s$

$\omega_{mn}$	Motor mechanical nominal speed in <i>rad/s</i>
$\omega_{me}$	Motor electromechanical speed in <i>rad/s</i>
$n_{mn}$	Motor mechanical nominal speed in <i>rpm</i>
$\theta_m$	Motor mechanical angle
$\theta_{me}$	Motor electromechanical angle
$p$	Motor pole pairs
$J$	Motor inertia
$J_{btb}$	Motor inertia with a complete back-to-back connection
$B$	Viscous damping
$u_{abc}$	Stator phase voltages
$u_{\alpha\beta}$	Stator phase voltages in the $\alpha\beta$ fixed reference frame
$u_{dq}$	Stator phase voltages in the $dq$ synchronous reference frame
$i_{abc}$	Stator phase currents
$i_{\alpha\beta}$	Stator phase currents in the $\alpha\beta$ fixed reference frame
$i_{dq}$	Stator phase currents in the $dq$ synchronous reference frame
$\lambda_{\alpha\beta}$	Flux linkages in the $\alpha\beta$ fixed reference frame
$\lambda_{dq}$	Flux linkages in the $dq$ synchronous reference frame
$R_s$	Stator resistance
$L_m$	Magnetizing inductance in the $\alpha\beta$ fixed reference frame
$L_d$	Magnetizing inductance on the $d$ axis
$L_q$	Magnetizing inductance on the $q$ axis

**Converter parameters**

PWM	Pulse Width Modulation
DPWM	Discontinuous Pulse Width Modulation
SVM	Space Vector Modulation
n.s.	Naturally sampled
r.s.	Regularly sampled
s.r.s.	Symmetrical regularly sampled
a.r.s.	Asymmetrical regularly sampled
p.a.s.	Phase advanced sampled

comp.	Carrier-reference ”comparison”, relative to the modulation strategies #10 and #11
$U_{dc}$	DC-link voltage
$f_c$	Carrier frequency
$\omega_c$	Carrier angular frequency
$T_c$	Carrier period
$S_{abc}$	Upper legs IGBTs gate commands
UVMT	Unified Voltage Modulation Technique
DTC	Direct Torque Control
$T_{eff}$	Effective time
$T_0$	Zero space vector time
$T_h$	Half of the carrier period
$T_{sa}, T_{sb}, T_{sc}$	Imaginary switching times
$T_{min}$	Smallest of the three imaginary switching times
$T_{max}$	Largest of the three imaginary switching times
$T_{ga}, T_{gb}, T_{gc}$	Gating times for each inverter arm
$T_{offset}$	Offset time of the $T_{eff}$ interval
$T_{offset,min}$	Minimum value allowed for $T_{offset}$
$T_{offset,max}$	Maximum value allowed for $T_{offset}$
$T_{min,x}$	$T_{min}$ for the 30°delayed references
$T_{max,x}$	$T_{max}$ for the 30°delayed references

**Control parameters**

PI	Proportional-Integral regulator
$T_s$	Sampling time
$f_s$	Sampling frequency
$T_{ramp}$	Nominal speed reference ramp rise time
$T_{ri}$	Current rise time
$\alpha_c$	Current regulator bandwidth
$\alpha_s$	Speed regulator bandwidth
$k_{pd}$	Proportional $d$ axis gain of the current regulator

$k_{id}$	Integral $d$ axis gain of the current regulator
$k_{pq}$	Proportional $q$ axis gain of the current regulator
$k_{iq}$	Integral $q$ axis gain of the current regulator
$k_{kxy}$	Corrective factor for the $x$ (proportional or integral) $y$ ( $d$ or $q$ ) axis gain of the current regulator
$k_{ps}$	Proportional gain of the speed regulator
$k_{is}$	Integral gain of the speed regulator

### Estimator parameters

$T_s$	Measurements sampling period
$f_s$	Measurements sampling frequency
$T_{FPGA}$	FPGA period
$f_{FPGA}$	FPGA frequency
LPF	Low Pass Filter
BPF	Band Pass Filter
$H_{LPF}(s)$	Analog LPF transfer function
$H_{LPF}(z)$	Discrete LPF transfer function
$H_{BPF}(s)$	Analog BPF transfer function
$H_{BPF}(z)$	Discrete BPF transfer function
$c$	Frequency warping coefficient
$n_0, n_1, n_2$	Nominator discrete filters coefficients
$d_0, d_1, d_2$	denominator discrete filters coefficients
$\omega_{lc}$	LPF cut-off frequency
$\omega_{lce}$	Cut-off frequency for the LPF operating on $\epsilon$
$\omega_{lcw}$	Cut-off frequency for the LPF operating on $\hat{\omega}_{me}$
$\omega_{cc}$	BPF centre frequency
DF	BPF Depth Factor
QF	BPF Quality Factor
$k_{pe}$	Proportional gain of the estimator regulator
$k_{ie}$	Integral gain of the estimator regulator
$\hat{\omega}_{me}^{PLL}$	PLL estimated motor electrical speed

$\hat{f}_{me}^{PLL}$	PLL estimated motor electrical frequency
$\hat{\theta}_{me}^{PLL}$	PLL estimated motor electrical position
$\Delta i_{\alpha\beta}$	PLL calculated $\alpha\beta$ current ripple
$k_p^{PLL}$	Proportional gain of the current PLL
$k_i^{PLL}$	Integral gain of the current PLL

## 1.4 Structure

This report has the following structure.

Chapter 1 INTRODUCTION describes the purpose and scope for this report as well as terms, abbreviations and acronyms used.

Chapter 2 PROBLEM DESCRIPTION illustrates the state of art of the currently available sensorless control methods.

Chapter 3 INTRINSIC INJECTION SENSORLESS CONTROL introduces the intrinsic injection sensorless control.

Chapter 4 MODELLING OF THE SUBSYSTEMS describes the model of the drive making use of the signal injection sensorless control in a Matlab/Simulink environment.

Chapter 5 SIMULATIONS analyses the simulations run making use of the intrinsic injection sensorless control.

Chapter 6 CONCLUSIONS reports some conclusive remarks on the work.

Chapter 7 FUTURE WORK indicates how the results of this report will be used in future activities.

REFERENCES specifies some material for further reading.



# Chapter 2

## PROBLEM DESCRIPTION

In this Chapter, the state of art of the currently available sensorless control methods is illustrated. The two main topologies, the model-based and the injection-based sensorless controls, are described together with their strong and weak points. Afterwards, the intrinsic injection sensorless algorithm object of this work, defined for the first time in [1] and [2], is presented together with its advantages.

### 2.1 Sensorless control methods

The implementation of sensorless drives for synchronous machine has received more and more attention during the recent past. The reason for this interest is the great number of benefits that a sensorless drive involves, all interwoven with the absence of the device in charge of the position and speed measurements [3]. In fact, this reduces the complexity, the cost and the size of the drive, resulting in benefits in terms of reliability and maintenance requirements. Furthermore, the elimination of the sensor cable involves the enhancement of the noise immunity. On the other hand, the main drawback of sensorless drives remains the poor dynamics performance, which, relatively to the algorithms of the very last years, can be comparable at most with drives provided with low-resolution encoders [4]. The other drawbacks depend, instead, on the particular sensorless control method.

As illustrated in [4], [5] and [6], there are two main topologies of sensorless control for synchronous machines.

The first typology, which is also the first one implemented chronologically, is

based on the mathematical model of the machine. It has been developed from the already existing sensorless methods for induction machines and it is valid both for isotropic and salient machines. These algorithms, basing the rotor flux estimation on the integration of the back-EMF (ElectroMotive Force) of the machine, fail at low-speeds, where the EMF voltage is relatively small compared to the resistive voltage drop and the signal to noise ratio is small [7]. Furthermore, identification of the parameters, in particular the stator resistance and the synchronous inductance, plays a key role. Even making use of other estimation techniques, such as the analysis of slot harmonics, of winding asymmetries and of stator and rotor eccentricities, ends not to be working at zero speed. To face these inconvenients, flux observers [8] and Kalman filters [9] can be adopted, bringing to solutions that can result too complex and expensive to be used in practical systems though.

At low and zero speed, instead, the other sensorless control topology is more effective. It makes use of voltage signal injections and requires that machine is designed with some magnetic reluctance. These high-frequency signals are superimposed on the fundamental voltages that feed the machine and can be characterized by different waveforms:

- rotating signal injection relies on an high frequency voltage vector rotating in the stationary frame  $\alpha\beta$ ;
- pulsating signal injection relies on a pulsating signal injected along the  $d$ -axis either the  $q$ - axis direction of the estimated rotor reference frame. This solution is more stable with different geometries of the rotor, generates less torque ripple and requires a lower amplitude voltage signal;
- square-wave signal injection relies on a square-wave pulsating voltage signal in the estimated rotor reference frame  $d$ -axis. This solution allows to reach speed bandwidths up to 40  $Hz$  [10];
- ellipse-shaped voltage injection, whose minor axis is speed dependent, can operate from zero to the rated speed [11];
- alternative injection methods such as the INFORM (Indirect Flux detection by On-line Reactance Measurement) method [12] and the Zero voltage injection [13].

With the exception of the INFORM and Zero-voltage injection methods, all the injection methods rely on the measurement of the motor currents and the creation of an error signal through a demodulation process consisting in the multiplication of the current components with an appropriate sinusoidal

signal. The extraction of the speed and position information can be therefore extracted through a mechanism consisting of a low-pass filter (LPF) and a proportional-integral (PI) regulator. From another perspective, this mechanism can be seen also as a Phase-Locked Loop (PLL) [11].

Injection sensorless control presents as well different drawbacks. First of all, the request of the superimposed voltage signal reduces the voltage margin for the machine, considering a limited DC link voltage. This involves on one side the not practicability of the operation at high speed, on the other side a performance impoverishment. In fact, if the increase of the signal frequency would be beneficial for the dynamics of the control, on the other hand it would imply the increase of the machine reactance and, as consequence, it would require an higher signal amplitude in order to improve the signal-to-noise ratio [7]. A second drawback is an important increase of the iron losses, being the frequency of the injected voltage as high as possible [4]. The last drawback is the raise of the torque ripple and, consequently, of the acoustic noise. Studies have been carried out in order to adjust the signal frequency in order to reduce this further noise, but the most suitable solutions seem nowadays the injection of square-waves signals and/or the reduction of the signal magnitudes, at the cost, as mentioned before, of a worse signal-to-noise ratio [6].

Even though both the model-based and the signal injected sensorless methods have strong limitations, these limitation are somehow complementary and these two methods can be successfully matched in an hybrid seamless operation, allowing a drive to work completely sensorless [6]. The sensorless control makes use of the injection method for the starting and at low speed (around 10÷20%) and it switches seamless to the model-based method for higher and highest speeds.

An alternative solution to the problems faced by the traditional injection methods, which is defined in [1] and [2] as "intrinsic injection method", is the object of this work. The reason for which it is an "injection" method is that the concept is the same of the traditional method, making use of a current demodulation providing a signal containing the speed and the position information. The reason for which this injection is defined "intrinsic" is that the high frequency signals, which the speed and the position are estimated from, come from the voltage harmonics generated by the PWM. This harmonic content represents usually an undesired product which it is not possible to get rid of and merely increases the power losses. Hence, with this method there is no need to inject a further high frequency voltage signal and it is possible to avoid the drawback of the conventional signal injection methods such as the reduced voltage margin for the machine and the increase in the iron losses, in the torque ripple and in the acoustic noise.

In addition, since the current sampling frequency plays a key role in the intrinsic injection methods, this method meets the future drives requirements from the point of view of the drive self-diagnosis capability [14]. Making the drive itself the primary diagnostic sensor, without the need for the installation of further external devices in charge of that duty, represents a key technology that would doubtless increase the system reliability. In an horizon where power density requirements are higher and higher and the drive components are exploited up to their limits, the research carried out in [15] shows how faults occurrence can be successfully avoided through the insulation ageing diagnosis. This diagnosis requires, as well as the intrinsic injection sensorless control, an extremely high current sampling frequency, in order to catch in a satisfactory manner oscillatory phenomena with frequencies that, for the insulation ageing diagnosis, can go up to  $5\text{ MHz}$ . Therefore, the implementation of a drive making use of the intrinsic injection sensorless control, whose specifications would allow it to perform a self-diagnosis of the insulation status, has the potential to prove exceptional reliability, efficiency and low cost standards.

# Chapter 3

## INTRINSIC INJECTION SENSORLESS CONTROL

In this Chapter, the intrinsic injection sensorless control is introduced. In Section 3.1, the analytical voltage and current harmonic contents required by the sensorless algorithm are illustrated and the demodulation process is described. Therefore, in Section 3.2, the limits on the drive operation imposed by the motor load, speed and saturation conditions are treated and considerations are drawn relatively to the filtering needs, the demodulation process and the choice of the particular harmonic content to focus on.

### **3.1 Analytical operation of the intrinsic injection sensorless control**

In this Section, the theoretical foundation of the intrinsic injection sensorless control is illustrated. The expression of the harmonic content of interest deriving from the PWM modulation is firstly analysed in Subsection 3.1.1. Leaning on the superposition principle and making use of the machine mathematical model, the current harmonic content of interest is then calculated in 3.1.2. Lastly, the demodulation operation is described in 3.1.3.

### 3.1.1 Seeked voltage harmonic content calculation

Differently from the conventional injection sensorless algorithms, the one considered in this work relies on harmonics characterized by a variable frequency. These harmonics are an unavoidable consequence of the PWM modulation, the reason why this control has been defined "intrinsic" injection. Since the PWM modulation strategies are many and each of them presents a different harmonic content, it is therefore crucial to choose the strategy from which it is possible to extract the required signals in the most efficient way. As it will be clarified in Subsection 3.2.5, the PWM Single-Edge modulation is one of these desirable modulations and one of the simplest to implement, since it can be easily achieved through the comparison of the reference voltages and a sawtooth carrier. Furthermore, as it will be discussed in Subsection 4.2.2, a symmetrical regularly sampled modulation is more desirable than a naturally sampled modulation in a digital control system. The time-domain expression of phase leg voltage for this modulation strategy is analytically calculated in [16] and can be expressed as:

$$u_{an} = \underbrace{\frac{U_{dc}}{2}}_{\text{DC offset}} \quad (3.1)$$

$$+ \underbrace{\sum_{n=1}^{+\infty} \frac{U_{dc}}{\pi \frac{n}{p}} J_n \left( \frac{n}{p} \pi M \right) \left[ \sin \left( n \frac{\pi}{2} \right) \cos(n[\omega_o t + \theta_o]) - \cos \left( n \frac{\pi}{2} \right) \sin(n[\omega_o t + \theta_o]) \right]}_{\text{Fundamental and Baseband harmonics}} \quad (3.2)$$

$$+ \underbrace{\sum_{m=1}^{+\infty} \frac{U_{dc}}{m\pi} [J_0(m\pi M) - \cos(m\pi)] \sin(m[\omega_c t + \theta_c])}_{\text{Carrier harmonics}} \quad (3.3)$$

$$+ \underbrace{\sum_{m=1}^{+\infty} \sum_{\substack{n=-\infty \\ (n \neq 0)}}^{+\infty} \frac{U_{dc}}{\pi} \frac{J_n \left( \left[ m + \frac{n}{p} \right] \pi M \right)}{m + \frac{n}{p}} \begin{bmatrix} \sin \left( n \frac{\pi}{2} \right) \cos(m[\omega_c t + \theta_c] + n[\omega_o t + \theta_o]) \\ -\cos \left( n \frac{\pi}{2} \right) \sin(m[\omega_c t + \theta_c] + n[\omega_o t + \theta_o]) \end{bmatrix}}_{\text{Sideband harmonics}} \quad (3.4)$$

where  $U_{dc}$  is the DC-link voltage,  $M$  is the modulation index,  $m$  is the carrier index variable,  $n$  is the baseband index variable,  $J_k(x)$  is the Bessel function of order  $k$  and argument  $x$ ,  $\omega_o$  is the fundamental angular frequency,  $\theta_o$  is the

phase offset angle of the fundamental component,  $\omega_c$  is the carrier angular frequency,  $\theta_c$  is the phase offset angle of the carrier waveform and  $p = \omega_c/\omega_o$  is the pulse number. The DC offset (3.1) is present because the phase voltage  $v_{an}$  is defined with respect to the negative bus terminal. The analytical expression of the phase voltage with respect to the DC-link midpoint  $v_{az}$  would be the exactly same of the one for  $v_{an}$ , but with no DC offset. That can be easily realised looking at the converter schematic of Figure 3.1. Regarding the fundamental and the baseband harmonics expression (3.2), the carrier index variable  $m$  is set to zero, while the baseband index variable  $n$  varies from 1 to  $+\infty$ . On the other way around, in the carrier harmonics expression (3.3),  $n$  is set to zero and  $m$  varies from 1 to  $+\infty$ . Lastly, in the sideband harmonics expression (3.4), both the indexes have to vary:  $m$  from 1 to  $+\infty$  in order to take care of all the carrier multiples, and  $n$  from  $-\infty$  to  $+\infty$  in order to take care both of the left and the right sideband harmonics with respect to the carrier multiples, which are excluded by excluding the index  $n = 0$ . In Figure 3.2 the theoretical spectrum is plotted for  $M = 0.8$  and  $f_o = 100 \text{ Hz}$  and the aforementioned harmonics groups are pointed out. The modulation strategy used is the PWM Single-Edge r.s. (regularly sampled) and it will be discussed with further details in Subsection 4.2.2.

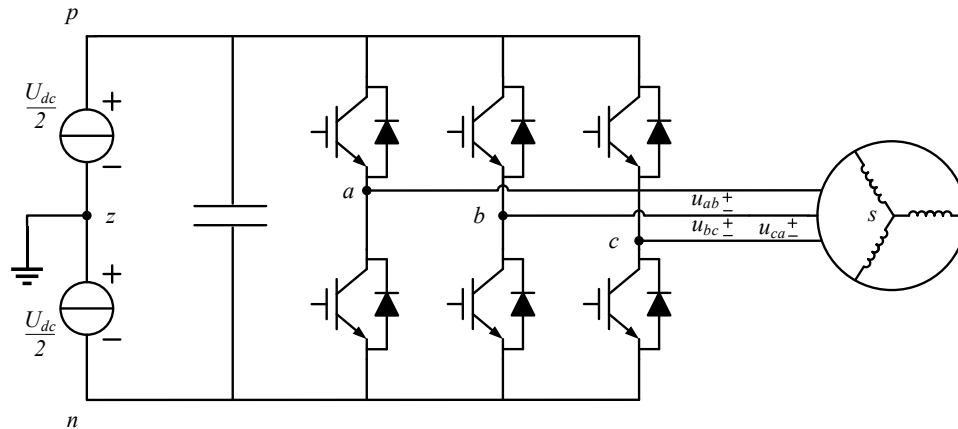


Figure 3.1. Three-phase voltage source converter schematic.

As it can be noticed from the analytical expression of the phase voltage, the presence of the terms  $\omega_o$  and  $\theta_o$  reveals that it is possible to derive from the harmonic content of the voltage, and consequently of the current, the speed

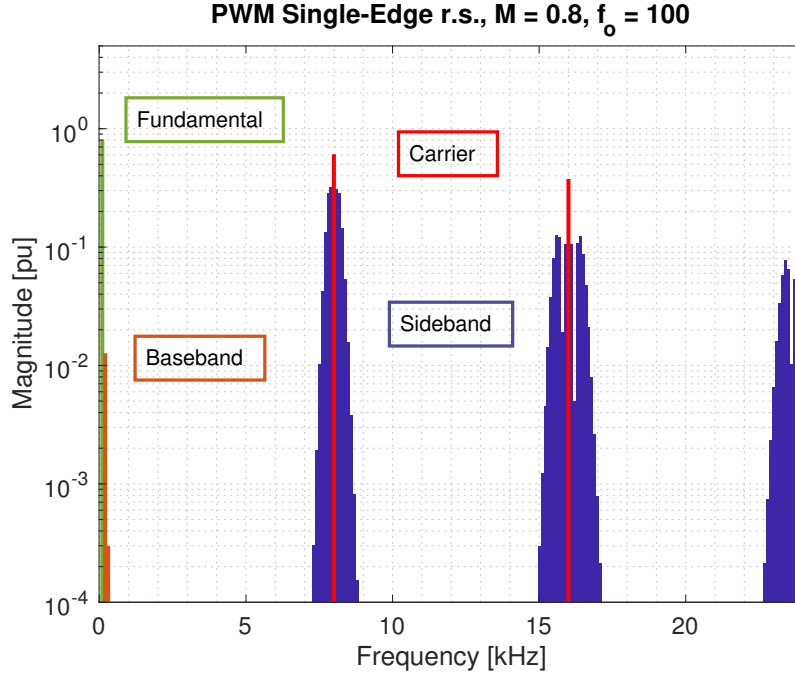


Figure 3.2. Analytical spectrum for PWM Single-Edge r.s. modulation and definition of the harmonic content, for  $M = 0.8$  and  $f_o = 100$  Hz

and the position information of a motor controlled by a converter making use of PWM. This information, as described in [1] and [2], can be extracted from the analysis of the only first sideband harmonics around the first carrier multiple. The dependency of the harmonic content from the motor operation, together with the motivations that bring to the choice of the harmonics to focus on, will be analysed in Subsection 3.2.5. The expression of these two harmonic components can be thus derived from the phase voltage expression (3.1), (3.2), (3.3) and (3.4), just for the indexes values  $m = 1$  and  $n = \pm 1$ :

$$u_{anc} = \underbrace{\frac{U_{dc}}{2}}_{\text{DC offset}} + \underbrace{\frac{U_{dc}}{\pi} [J_0(\pi M) + 1] \sin(\omega_c t + \theta_c)}_{\text{First carrier harmonic multiple}} \quad (3.5)$$

$$+ \underbrace{\frac{U_{dc}}{\pi} \frac{J_1([1 + 1/p] \pi M)}{1 + 1/p} \cos(\omega_c t + \theta_c + \omega_o t + \theta_o)}_{\text{First right sideband harmonic}} \quad (3.6)$$

$$+ \underbrace{\frac{U_{dc}}{\pi} \frac{J_{-1}([1 - 1/p] \pi M)}{1 - 1/p} \cos(\omega_c t + \theta_c - \omega_o t - \theta_o)}_{\text{First left sideband harmonic}} \quad (3.7)$$

where the subscript "c" in  $u_{anc}$  points out that it is referred to the harmonic

content around the first multiple of the carrier frequency. Introducing the following definitions:

$$\begin{cases} A^c = \frac{U_{dc}}{\pi} [J_0(\pi M) + 1] \\ A^+ = \frac{U_{dc}}{\pi} \frac{J_1([1 + 1/p]\pi M)}{1 + 1/p} \\ A^- = \frac{U_{dc}}{\pi} \frac{J_{-1}([1 - 1/p]\pi M)}{1 - 1/p} \end{cases} \quad (3.8)$$

it is possible to express the seeked harmonic content for all the three phases:

$$\begin{cases} u_{an_c} = \frac{U_{dc}}{2} + A^c \sin(\omega_c t + \theta_c) + A^+ \cos(\omega_c t + \theta_c + \omega_o t + \theta_o) + \\ \quad + A^- \cos(\omega_c t + \theta_c - \omega_o t - \theta_o) \\ u_{bn_c} = \frac{U_{dc}}{2} + A^c \sin(\omega_c t + \theta_c) + A^+ \cos(\omega_c t + \theta_c + \omega_o t + \theta_o - \frac{2\pi}{3}) + \\ \quad + A^- \cos(\omega_c t + \theta_c - \omega_o t - \theta_o + \frac{2\pi}{3}) \\ u_{cn_c} = \frac{U_{dc}}{2} + A^c \sin(\omega_c t + \theta_c) + A^+ \cos(\omega_c t + \theta_c + \omega_o t + \theta_o + \frac{2\pi}{3}) + \\ \quad + A^- \cos(\omega_c t + \theta_c - \omega_o t - \theta_o - \frac{2\pi}{3}) \end{cases} \quad (3.9)$$

The expressions for the phase to DC-link midpoint voltages  $u_{az_c}$ ,  $u_{bz_c}$  and  $u_{cz_c}$  would be the same as the ones in Equation (3.9), excepting the absence of the DC offset  $U_{dc}/2$ . Furthermore, as it can be noticed from Equation (3.9), the DC offset together with the sine wave at the carrier frequency have the same expressions for all the three phases and they will be consequently cancelled out in the  $\alpha\beta$  frame equations:

$$\begin{cases} u_{\alpha_c} = A^+ \cos(\omega_c t + \theta_c + \omega_o t + \theta_o) + A^- \cos(\omega_c t + \theta_c - \omega_o t - \theta_o) \\ u_{\beta_c} = A^+ \sin(\omega_c t + \theta_c + \omega_o t + \theta_o) - A^- \sin(\omega_c t + \theta_c - \omega_o t - \theta_o) \end{cases} \quad (3.10)$$

This cancellation implies that in the  $\alpha\beta$  voltage components spectra there are no harmonics at the carrier frequency, as it is the case for the line-to-line voltage spectra. As it will be mentioned in the following of the work, this cancellation plays a crucial role in the infeasibility of the zero speed operation of the intrinsic injection sensorless control.

In order to achieve a better distinction between the electrical and the mechanical variables in the electrical machine operations, in the pursuing of the

work, the electrical speed and the electrical position will be referred with  $\omega_{me}$  and  $\theta_{me}$ . The following substitutions can therefore be made:

$$\theta_c = \pi \quad (3.11)$$

$$\theta_o = \theta_{me}(0) + \theta_u^r(0) \quad (3.12)$$

$$\theta_{me}(t) = \omega_{me}t + \theta_{me}(0) \quad (3.13)$$

The substitution in Equation (3.11) involves a  $\pi$  radians phase shift of the carrier waveform, as proved by the simulations in [1]. The angle  $\theta_u^r$ , which appears in Equation (3.12), is the voltage vector angle in the  $dq$  reference frame and  $\theta_u^r(0)$  is its value at the initial instant. In the following,  $\theta_u^r(0)$  will be abbreviated as  $\theta_{u,0}^r$  just for sake of compactness sake. Equation (3.13) shows the impact of the initial position in the calculation of the position as integral of the angular speed. The equations in (3.10) can therefore be rewritten as:

$$\begin{cases} u_{\alpha_c} = A^+ \cos(\omega_c t + \pi + \theta_{me} + \theta_{u,0}^r) + A^- \cos(\omega_c t + \pi - \theta_{me} - \theta_{u,0}^r) \\ u_{\beta_c} = A^+ \sin(\omega_c t + \pi + \theta_{me} + \theta_{u,0}^r) - A^- \sin(\omega_c t + \pi - \theta_{me} - \theta_{u,0}^r) \end{cases} \quad (3.14)$$

Lastly, in a sensorless drive, there is no way to access to the actual speed and position  $\omega_{me}$  and  $\theta_{me}$ , since they are not available. Their estimates  $\hat{\omega}_{me}$  and  $\hat{\theta}_{me}$  are used instead. The harmonic content of the  $\alpha\beta$  voltage components relative to the indexes  $m = 1$  and  $n = \pm 1$  can finally be expressed as:

$$\begin{cases} u_{\alpha_c} = -A^+ \cos(\omega_c t + \hat{\theta}_{me} + \theta_{u,0}^r) - A^- \cos(\omega_c t - \hat{\theta}_{me} - \theta_{u,0}^r) \\ u_{\beta_c} = -A^+ \sin(\omega_c t + \hat{\theta}_{me} + \theta_{u,0}^r) + A^- \sin(\omega_c t - \hat{\theta}_{me} - \theta_{u,0}^r) \end{cases} \quad (3.15)$$

### 3.1.2 Searched current harmonic content calculation

By using the model of the machine at high frequencies, it is possible to express also the current harmonic content. The assumption behind this calculation, as pointed out in [17], is that, at frequencies much higher than the fundamental, the impedance of a synchronous machine can be simplified by the only self-inductance. In [18], the current harmonic content in the  $dq$  reference frame is computed for a voltage signal injection method sensorless. In [1] and [2] these calculations are repeated in the  $\alpha\beta$  frame and for two different frequencies voltage signals, which, as previously described, are relative

to the first sideband harmonics around the first carrier multiple. It is therefore possible to express the harmonic content of the  $\alpha\beta$  current components relative to the indexes  $m = 1$  and  $n = \pm 1$  as:

$$\begin{cases} i_{\alpha_c} = -I_0^+ \sin(\omega_c t + \hat{\theta}_{me} + \theta_{u,0}^r) - I_1^+ \sin(\omega_c t + \hat{\theta}_{me} + \theta_{u,0}^r - 2\theta_{me}) + \\ \quad - I_0^- \sin(\omega_c t - \hat{\theta}_{me} - \theta_{u,0}^r) - I_1^- \sin(\omega_c t - \hat{\theta}_{me} - \theta_{u,0}^r + 2\theta_{me}) \\ i_{\beta_c} = +I_0^+ \cos(\omega_c t + \hat{\theta}_{me} + \theta_{u,0}^r) - I_1^+ \cos(\omega_c t + \hat{\theta}_{me} + \theta_{u,0}^r - 2\theta_{me}) + \\ \quad - I_0^- \cos(\omega_c t - \hat{\theta}_{me} - \theta_{u,0}^r) + I_1^- \cos(\omega_c t - \hat{\theta}_{me} - \theta_{u,0}^r + 2\theta_{me}) \end{cases} \quad (3.16)$$

where the current harmonic coefficients are defined as:

$$\begin{cases} I_0^+ = \frac{L_\Sigma}{L_d L_q} \frac{A^+}{2(\omega_c + \hat{\omega}_{me})} \\ I_0^- = \frac{L_\Sigma}{L_d L_q} \frac{A^-}{2(\omega_c - \hat{\omega}_{me})} \\ I_1^+ = \frac{L_\Delta}{L_d L_q} \frac{A^+}{2(\omega_c + \hat{\omega}_{me})} \\ I_1^- = \frac{L_\Delta}{L_d L_q} \frac{A^-}{2(\omega_c - \hat{\omega}_{me})} \end{cases} \quad (3.17)$$

and the sum  $L_\Sigma$  and difference inductances  $L_\Delta$ , for a synchronous reluctance machine, are defined as:

$$\begin{cases} L_\Sigma = \frac{L_d + L_q}{2} \\ L_\Delta = \frac{L_d - L_q}{2} \end{cases} \quad (3.18)$$

Defining the  $d$ -axis as the axis where the higher flux component lays, for a machine provided with permanent magnets, instead,  $L_\Sigma$  and  $L_\Delta$  would be defined respectively as  $(L_q + L_d)/2$  and  $(L_q - L_d)/2$ .

### 3.1.3 Demodulation

The demodulation process described in [1] and [2] can be performed in a manner similar to the one advisable for traditional constant frequency signal injection algorithms. In [4] the demodulation is illustrated both for rotating and for pulsating signal injection for an interior permanent magnet synchronous machine (IPMSM). In [3] and [7], the demodulation is illustrated just for pulsating signal injection, in the first article for an IPMSM while in

the second for a PMSM. It is in fact important to highlight, as it will be done with further details in Subsection 3.2.2, that this sensorless algorithm, as well as the traditional constant frequency voltage injection methods, is effective for any kind of machine provided with reluctance.

The signal required for the demodulation is  $\omega_c t - \hat{\theta}_{me} - \theta_{u,0}^r$ . Its cosinus is multiplied with the  $\alpha$  current component of the seeked frequency  $i_{\alpha_c}$ , while its sinus is multiplied with the  $\beta$  component  $i_{\beta_c}$ . From the difference of this two signals, it is thus possible to calculate the following error signal:

$$\begin{aligned} \epsilon &= i_{\alpha_c} \cos(\omega_c t - \hat{\theta}_{me} - \theta_{u,0}^r) - i_{\beta_c} \sin(\omega_c t - \hat{\theta}_{me} - \theta_{u,0}^r) = \\ &= -I_0^+ \sin(2\omega_c t) - I_1^+ \sin(2(\hat{\theta}_{me} + \theta_{u,0}^r - \theta_{me})) + \\ &\quad - I_1^- \sin(2\omega_c t - 2(\hat{\theta}_{me} + \theta_{u,0}^r - \theta_{me})) \end{aligned} \quad (3.19)$$

If  $\epsilon$  is filtered with a low pass filter (LPF), it is possible to disregard the terms at the frequency  $2\omega_c$ :

$$\epsilon_{LP} = -I_1^+ \sin(2(\hat{\theta}_{me} + \theta_{u,0}^r - \theta_{me})) \quad (3.20)$$

Hence, introducing the following definitions:

$$\hat{\theta}'_{me} = \hat{\theta}_{me} + \theta_{u,0}^r \quad (3.21)$$

$$\Delta\theta'_{me} = \hat{\theta}'_{me} - \theta_{me} \quad (3.22)$$

$$\Delta\theta_{me} = \hat{\theta}_{me} - \theta_{me} \quad (3.23)$$

equation (3.20) can finally be rewritten as:

$$\epsilon_{LP} = -I_1^+ \sin(2\Delta\theta'_{me}) \quad (3.24)$$

If the estimated electrical angle  $\hat{\theta}'_{me}$  coincides with the actual electrical angle  $\theta_{me}$ , from Equation (3.22) the angle error  $\Delta\theta'_{me}$  turns to be zero. As a consequence, from Equation (3.24), also  $\sin(2\Delta\theta'_{me})$  and  $\epsilon_{LP}$  becomes equal to zero. On the other way around, if the signal  $\epsilon_{LP}$  is nullified at the hand of a PI regulator,  $\hat{\omega}_{me}$  estimates the actual electrical speed and its integral  $\hat{\theta}'_{me}$  estimates the actual electrical angle. Additional details and measures regarding this procedure are illustrated in Subsection 3.2.4.

The scheme of the estimator performing the demodulation and giving the estimates for the electrical position and the electrical speed is displayed in Figure 3.3 and will be further analysed in the following section.

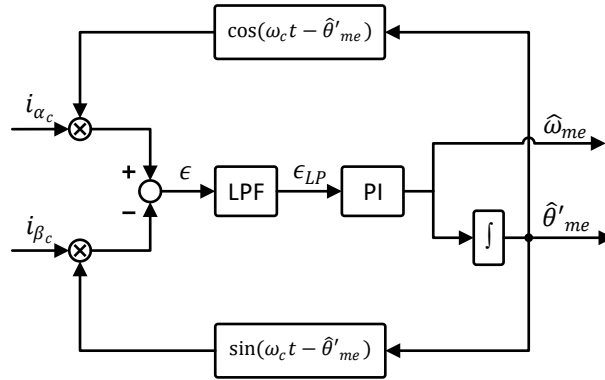


Figure 3.3. Intrinsic injection electrical position and speed estimator general schematic.

## 3.2 Considerations on the intrinsic injection sensorless estimator

In this Section, considerations on the intrinsic injection sensorless estimator are drawn from the analytical analysis carried out in Section 3.1. Firstly, the motor speed and load conditions influence on the voltage spectra is analysed in Subsection 3.2.1. Afterwards, the saliency influence is treated in Subsection 3.2.2. The filtering actions required and the consequences of their absence are then described in Subsection 3.2.3. The position error  $\hat{\theta}'_{me}$  and the demodulation process are then examined in Subsection 3.2.4. The motivations that push to investigate the aforementioned sought harmonic content are illustrated in Subsection 3.2.5. The reason why overmodulation has to be avoided is expressed in Subsection 3.2.6. Lastly, a summary of the limiting operation conditions is provided in Subsection 3.2.7.

### 3.2.1 Motor speed and load influence

In the previous section, the phase voltage harmonic content  $u_{an}$  has been analytically expressed for a PWM Single-Edge r.s. modulation in Equations (3.1), (3.2), (3.3) and (3.4). In particular, it is possible to notice from these equations the dependency of  $u_{an}$  in particular from the fundamental angular frequency  $\omega_o$  and from the modulation index  $M$ .

As already mentioned,  $\omega_o$  coincides with the motor electrical angular speed

$\omega_{me}$ . The way the speed affects the harmonic content can be effectively pointed out by expressing the frequency of the two  $n$  index sideband harmonics around the first carrier harmonic multiple ( $m = 1$ ):

$$f_{1,n} = f_c \pm n f_o \quad (3.25)$$

It is in fact possible to remark from Equation (3.25), that:

- the left and the right sideband harmonics with the same sideband index variable  $n$  are located symmetrically with respect to the carrier frequency  $f_c$ ;
- the higher is the  $n$  index for a given motor electrical frequency  $f_o$ , the farther are the two  $n$  index sideband harmonics from the carrier frequency  $f_c$ ;
- the higher is the motor electrical frequency  $f_o$  for a given  $n$  index, the farther are the two  $n$  index sideband harmonics from the carrier frequency  $f_c$ .

On the other hand, since the higher is the torque, the higher is the current and thus the fundamental voltage required by the machine,  $M$  can be correlated to the torque generated by the motor. However, as noticeable from  $u_{an}$  expression,  $M$  does not affect only the voltage fundamental magnitude, but the whole spectrum.

In Figure 3.4, the theoretical spectra around the carrier frequency are plotted for different fundamental frequency values. The modulation used is the PWM Single-Edge r.s., the modulation index is kept constant to the value of  $M = 0.8$  and the values for the fundamental frequency are  $f_o = 10$ ,  $f_o = 50$  and  $f_o = 100$ . For a two-poles machine, the operation at  $f_o = 100$  corresponds to its nominal speed operation. It is evident how the motor speed influences the spectrum according to the aforementioned behaviour, and it is possible to notice in particular:

- the higher is the fundamental frequency  $f_o$ , the more the sideband harmonic content is spread away from the carrier frequency;
- the influence of the fundamental frequency  $f_o$  on the harmonics magnitudes seems to be negligible.

With regard to the estimator performance, as it will be deepened in Subsection 3.2.3, a perfect filtering of just the components relative to the indexes  $m = 1$  and  $n = \pm 1$  is not practically possible. Therefore, the presence of other different harmonics is more troubling at low speed operation, when all the sideband harmonics are close one to another and close to the carrier frequency, than at high speed operation, when all the sideband harmonics are located in correspondence of more isolated frequencies. The worst condition would occur at zero speed operation, when all the sideband harmonics are shrunk at the frequency  $f_o$ .

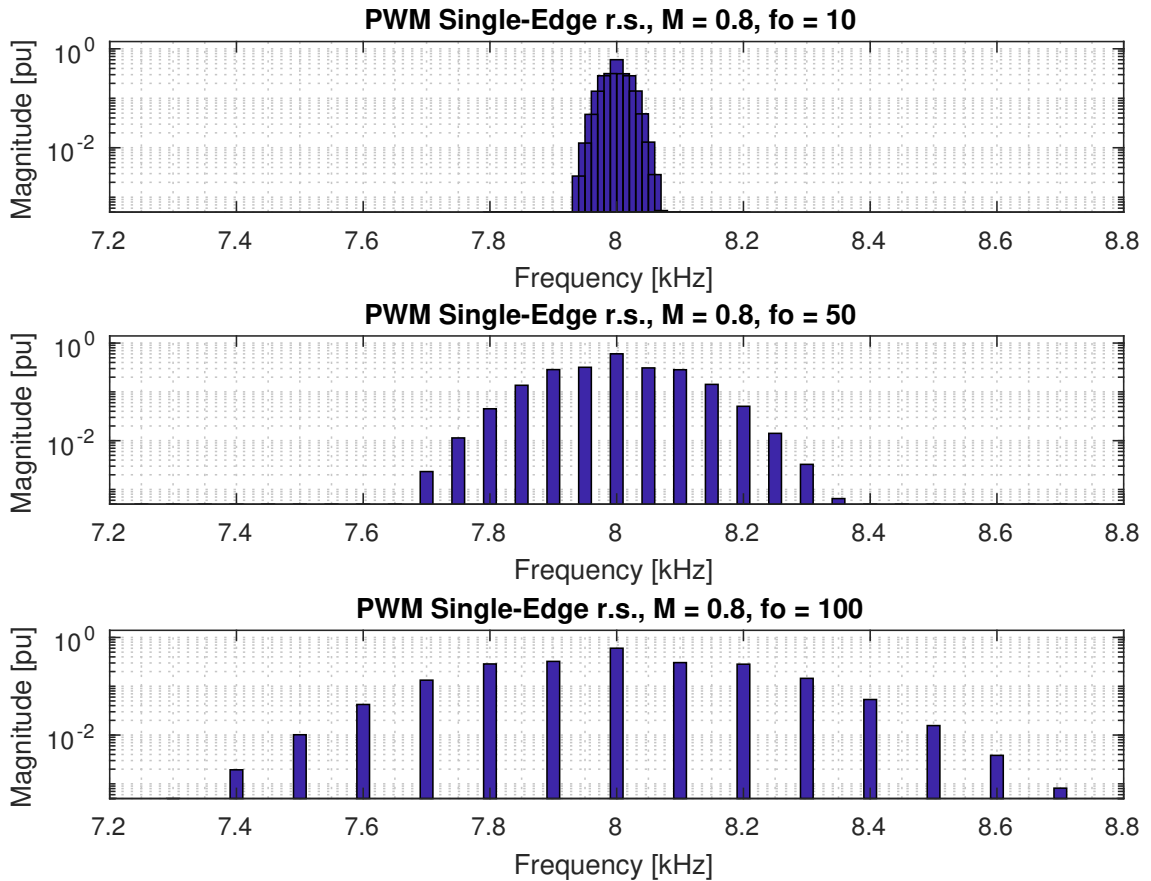


Figure 3.4. Electrical speed influence on the phase voltage spectrum for PWM Single-Edge r.s. modulation. Spectrum zoomed around the carrier frequency  $f_c = 8$  kHz. Operation for a constant modulation index  $M = 0.8$  and for the fundamental frequencies  $f_o = 10$ ,  $f_o = 50$  and  $f_o = 100$ .

In Figure 3.5 the theoretical spectra around the carrier frequency are plotted for different modulation index values, always using the PWM Single-Edge r.s. modulation. The fundamental frequency is kept constant to the value of  $f_o = 100$  and the values for the modulation index are  $M = 0.1$ ,  $M = 0.5$  and  $M = 1$ . The influence of the torque generated by the motor is noteworthy and in particular:

- the higher is the modulation index  $M$ , the more the harmonic content is shifted towards the higher  $n$  indexes sideband harmonics;
- the magnitude of the two sideband harmonics of interest ( $n = \pm 1$ ) is minimum for modulation indexes close to  $M = 0$  and to  $M = 1$  and is maximum for modulations indexes close to  $M = 0.5$ ;
- the modulation index  $M$  influence on the sideband harmonics frequencies is negligible.

With regard to the estimator performance, the variation of the voltage, and thus of the current, magnitudes of the two sideband harmonics of interest with different load conditions can result in a poor behaviour of the estimator. In fact, for  $M$  values around 0.5, the harmonics of interest have an high magnitude, which is also higher than the adjacent sideband harmonics magnitudes. The information needed by estimator from the current harmonic content would be consequently easier to be extracted, since the signal-to-noise ratio is high. This is not the case, instead, for lower or higher  $M$  values, for which the harmonics of interest have a lower magnitude, which, in the case of  $M$  close to the unity, is even lower than the adjacent sideband harmonics magnitudes.

Lastly, it has to be considered that in an electrical motor the voltage required at the stator terminal is roughly directly proportional to the rotational speed of the machine. Therefore, the influence of the motor speed and torque are highly interrelated each other with regard to the voltage harmonic content harmonic content.

### 3.2.2 Saliency influence

Assuming a rotor not provided with saliency, i.e.  $L_d = L_q$ , the difference inductance  $L_\Delta$ , according to its definition (3.18), is equal to zero. This

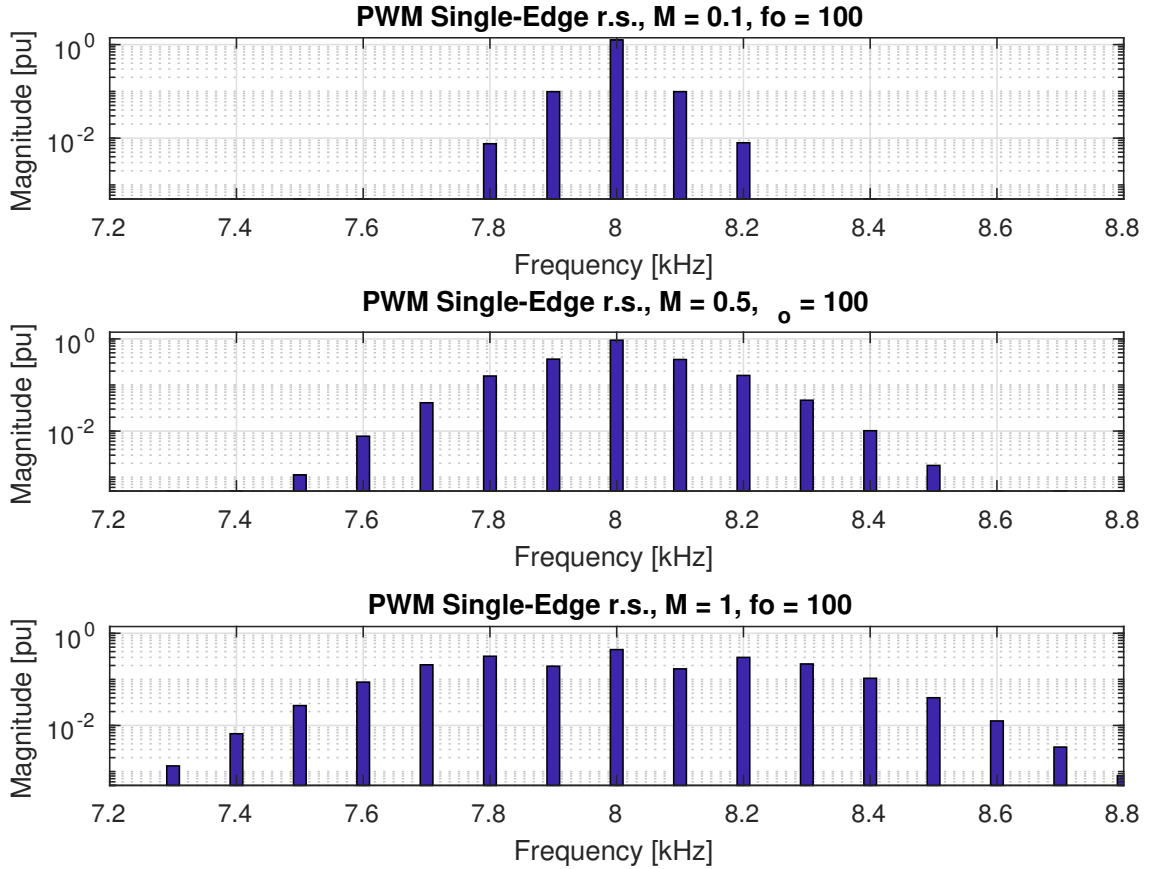


Figure 3.5. Torque influence on the phase voltage spectrum for PWM Single-Edge r.s. modulation. Spectrum zoomed around the carrier frequency  $f_c = 8 \text{ kHz}$ . Operation for a constant fundamental frequency  $f_o = 100$  and for the modulation indexes  $M = 0.1$ ,  $M = 0.5$  and  $M = 1$ .

involves, from the definitions in (3.17), that the current harmonic coefficients  $I_1^+$  and  $I_1^-$  are null as well. The  $\alpha\beta$  coordinates current harmonic components of interest expression (3.16) simplify therefore to:

$$\begin{cases} i_{\alpha_c} = -I_0^+ \sin(\omega_c t + \hat{\theta}_{me} + \theta_{u,0}^r) - I_0^- \sin(\omega_c t - \hat{\theta}_{me} - \theta_{u,0}^r) \\ i_{\beta_c} = +I_0^+ \cos(\omega_c t + \hat{\theta}_{me} + \theta_{u,0}^r) - I_0^- \cos(\omega_c t - \hat{\theta}_{me} - \theta_{u,0}^r) \end{cases} \quad (3.26)$$

It is evident that the actual electric position information  $\theta_{me}$  disappears from the expressions above, meaning that, similarly to all the other injection sensorless methods [4], the speed and the position estimation becomes impossible for an isotropic machine.

Furthermore, in a synchronous reluctance machine, while the presence of the magnetic bridges makes sure that the  $q$ -axis inductance saturates even for

small values of currents in the  $q$ -axis, the  $d$ -axis inductance saturates only for high currents in the  $d$ -axis [19]. This implies that the difference  $L_d - L_q$  remains approximately constant until a high module current is required by the motor, which involves the  $L_d$  drop. As a consequence, since the difference  $L_d - L_q$  is proportional to  $I_1^+$ , which, from Equation (3.24), is in turn proportional the error  $\epsilon_{LP}$ , in high load conditions the  $\epsilon_{LP}$  amplitude is decreased, which reduces the signal-to-noise ratio and makes more difficult the speed and the position estimation.

An infeasible solution to this problem would be the implementation of a variable PI, which would face the saliency change. A solution feasible for constant amplitude injection sensorless control is the implementation of a demodulation normalizing the injected signals and making the error signals being independent from the motor parameters [5]. Anyway, this solution is not viable for the intrinsic injection method, since the aforementioned normalization cannot be implemented for injected voltages whose amplitude and frequency are variable by nature.

### 3.2.3 Filtering actions

As displayed in Figure 3.3, the inputs of the estimator are the current components  $i_{\alpha\beta c}$ . These components can be profitably isolated from the measured currents  $i_{\alpha\beta}$  by means of suitable Band Pass Filters (BPF). In [1] and [2], a BPF operates on each  $\alpha\beta$  current component, and its centre frequency coincides with  $f_c$ . At the cost of affecting the magnitude of the  $n = \pm 1$  indexes sideband harmonics, it reduces considerably the higher  $n$  indexes sideband harmonics. Another possible approach, as probed in this work, can be the utilization, for each  $\alpha\beta$  component, of two variable centre frequency BPFs, respectively located on the frequencies of the  $n+ = 1$  and  $n = -1$  indexes sideband harmonics. The variation of these frequencies, as illustrated in 3.2.1, depends on the motor speed.

It is possible to carry out an examination on the consequences of a not perfect filtering, rather than of a complete lack of filtering actions. To carry out this analysis in an analytical way, the following assumptions have been made:

$$\theta_{u,0}^r = 0 \quad (3.27)$$

$$A^+ = A^- \quad (3.28)$$

$$L_q \gg L_d \Rightarrow L_\Sigma = L_\Delta \quad (3.29)$$

$$\omega_c \gg \hat{\omega}_{me} \quad (3.30)$$

The assumption (3.27) will be justified in Subsection 3.2.4. The assumption (3.28) is justified by the fact that, using PWM Single-Edge r.s. modulation, the magnitudes of the two first sideband harmonics, symmetric with respect to the carrier frequency, differ just a little. Assumption (3.29) is drastic, since the saliency ratio  $L_q/L_d$  in a synchronous machine is nearly equal to 10 and, when saturation occurs, it even decreases [19]. The last assumption (3.30) is more realistic, since the carrier frequency is approximately 100 times higher than the motor electrical frequency. With these hypothesis, the current harmonic coefficients defined in (3.17) are equal one another and they can be defined as:

$$I_0^+ = I_0^- = I_1^+ = I_1^- = \frac{I_1}{2} \quad (3.31)$$

If, in addition, if a perfect estimation of the angle  $\hat{\theta}'_{me} = \theta_{me}$  is assumed, the expression of the  $\alpha\beta$  coordinates currents relative to the sideband harmonics with indexes  $m = 1$  and  $n = \pm 1$  (3.16) can be approximated as:

$$\begin{cases} i_{\alpha_1} = -I_1 \sin(\omega_c t + \theta_{me}) - I_1 \sin(\omega_c t - \theta_{me}) \\ i_{\beta_1} = I_1 \cos(\omega_c t + \theta_{me}) - I_1 \cos(\omega_c t - \theta_{me}) \end{cases} \quad (3.32)$$

where the subscript "1" in  $i_{\alpha\beta_1}$  is referred to the fact that just the sideband harmonics of index  $n = \pm 1$  are taken into account. If the demodulation is now performed as well as in (3.19), the relative simplified error signal comes to be equal to:

$$\epsilon_1 = i_{\alpha_1} \cos(\omega_c t - \theta_{me}) - i_{\beta_1} \sin(\omega_c t - \theta_{me}) = -I_1 \sin(2\omega_c t) \quad (3.33)$$

and if  $\epsilon_1$  is low pass filtered, the resulting  $\epsilon_{1LP}$  is equal to zero, which implies that  $\hat{\theta}'_{me} = \theta_{me}$ , as previously assumed. This reasoning can be repeated also taking into account more sideband harmonics. If the sideband harmonics considered are the one up to  $n = \pm 3$ , the expression for the currents becomes:

$$\begin{cases} i_{\alpha_3} = -I_1 \sin(\omega_c t + \theta_{me}) - I_1 \sin(\omega_c t - \theta_{me}) - I_2 \sin(\omega_c t + 2\theta_{me}) \\ \quad - I_2 \sin(\omega_c t - 2\theta_{me}) - I_3 \sin(\omega_c t + 3\theta_{me}) - I_3 \sin(\omega_c t - 3\theta_{me}) \\ i_{\beta_3} = I_1 \cos(\omega_c t + \theta_{me}) - I_1 \cos(\omega_c t - \theta_{me}) + I_2 \cos(\omega_c t + 2\theta_{me}) \\ \quad - I_2 \cos(\omega_c t - 2\theta_{me}) + I_3 \cos(\omega_c t + 3\theta_{me}) - I_3 \cos(\omega_c t - 3\theta_{me}) \end{cases} \quad (3.34)$$

and, if the demodulation is performed, the resulting error is:

$$\begin{aligned} \epsilon_3 &= i_{\alpha_3} \cos(\omega_c t - \theta_{me}) - i_{\beta_3} \sin(\omega_c t - \theta_{me}) = \\ &= + I_3 \sin(2\theta_{me}) - I_3 \sin(2\omega_c t + 2\theta_{me}) \\ &\quad + I_2 \sin(\theta_{me}) - I_2 \sin(2\omega_c t + \theta_{me}) - I_1 \sin(2\omega_c t) \end{aligned} \quad (3.35)$$

which gives, if low pass filtered:

$$\epsilon_{3_{LP}} = I_3 \sin(2\theta_{me}) + I_2 \sin(\theta_{me}) \quad (3.36)$$

From this last equation, since both the estimated speed and the estimated position depend from  $\epsilon_{3_{LP}}$  through a PI, it is expected the presence of harmonics at frequencies multiple of the fundamental one. Furthermore, considered that the higher is the  $n$  index the lower is the voltage, and thus the current, sideband harmonics magnitude, it can be stated that  $I_1 > I_2 > I_3$ . This results in a less severe filtering action required from the LPF to get rid of the fundamental multiple harmonics in the estimated speed and position.

The reasoning previously carried out reveals that there is a trade-off between the choice to filter or not the  $\alpha\beta$  current components as inputs of the estimator.

If BPFs are adopted, the current harmonic content of interest for the estimator is better isolated, resulting in a lower harmonic content in the signals  $\epsilon$ ,  $\hat{\theta}_{me}$  and  $\hat{\omega}_{me}$  and allowing the pole of the LPF applied on  $\epsilon$  to be positioned on an higher frequency. Additionally, in accordance with the works in [1] and [2], it is possible to add further BPFs at the outputs of the  $\cos(\omega_c t + \hat{\theta}'_{me})$  and  $\sin(\omega_c t + \hat{\theta}'_{me})$  blocks, just before the multiplication with respectively  $i_{\alpha_c}$  and  $i_{\beta_c}$ . This choice is justified in [18], relatively to a traditional injection sensorless algorithm, with the compensation for the effects of the filters applied on the currents.

On the other hand, as explained in [3], the presence of filters increases the complexity of the calculation, introducing phase delay and, being the filtering not ideal, decreasing the magnitude of the required current harmonics.

As it is usual for traditional injection algorithms [18], also with the estimator analyzed in this work it is possible to reduce the harmonic content in the estimated speed  $\hat{\omega}_{me}$  by the insertion of a LPF, similarly to the solution of [1] and [2]. The drawback, again, would be a further impoverishment of the system dynamics in addition to the slowdown of the system that a sensorless control usually involves.

Another approach in order to reduce the noise in  $\hat{\omega}_{me}$  is the extraction of

this signal from the only integral part of the regulator, as suggested in [2]. Supposing that the position is estimated correctly,  $\epsilon_{LP} = 0$ , the output of the proportional part of the regulator is also zero and the estimation of the electrical speed depends on the only integral part of the regulator. Theoretically, also the position estimate would be possible from the only integral part, but that would impoverish the dynamics of the estimator.

This trade-off leads, in this work, to the implementation of three different estimator schemes, each of them adopting different filters or avoiding at all the use of filters and making use of different cut-off-frequencies in the LPF applied on  $\epsilon$ .

### 3.2.4 Position error considerations

As displayed in Figure 3.3, the outputs of the estimator are the estimated electrical speed  $\hat{\omega}_{me}$  and the estimated electrical position  $\hat{\theta}'_{me}$ .  $\hat{\omega}_{me}$  is required by the speed regulator, while the estimated electrical angle is used to perform the transformations  $\alpha\beta$  to  $dq$  and vice versa  $dq$  to  $\alpha\beta$ . As formulated in Equation (3.21), this angle is equal to the angle  $\hat{\theta}'_{me}$  decreased by the initial voltage vector angle in the  $dq$  reference frame at the initial instant  $\theta_{u,0}^r$ . However, unless the estimator operation is initiated while the machine is already in motion, at the starting of the drive  $\theta_{u,0}^r$  is equal to zero, since in the control the reference voltage vector  $u_{dq}^*$  is not calculated yet. That implies hence the following equalities:

$$\hat{\theta}_{me} = \hat{\theta}'_{me} \quad (3.37)$$

$$\Delta\theta_{me} = \Delta\theta'_{me} \quad (3.38)$$

That simplification involves that the outputs of the estimator displayed in Figure 3.3 are the estimated electrical speed  $\hat{\omega}_{me}$  and the estimated electrical position  $\hat{\theta}_{me}$ , which can both be used in the control.

Moreover, looking at Equation (3.24), bringing  $\epsilon_{LP}$  to zero with a PI regulator does not involve necessarily that  $\Delta\theta_{me}$  is equal to zero. Rewriting that equation, setting  $\epsilon_{LP} = 0$  and with the substitutions  $\theta'_{me} = \theta_{me}$ , described in the previous paragraph, and  $I_1^+ = I_1/2$ , described in Subsection 3.2.3, we obtain the equation:

$$0 = -\frac{I_1}{2} \sin(2\Delta\theta_{me}) \quad (3.39)$$

which, for small values of  $\Delta\theta_{me}$ , (3.39) can be simplified as:

$$0 = I_1 \sin(\Delta\theta_{me}) \quad (3.40)$$

The solutions of Equation (3.40) can be expressed as:

$$\Delta\theta_{me} = k\pi \quad k = 0, \pm 1, \pm 2... \quad (3.41)$$

With motors provided with permanent magnets, only the even values of  $k$  yield to stable solutions. The resulting error on the speed  $\Delta\theta_{me}$  would therefore be equal to  $0, \pm 2\pi, \pm 4\pi...$  This problem is faced and solved in [20] and [21], where the rotor position and magnetization polarity are identified before the starting of the motor thanks to an injected signal. On the contrary, with a synchronous reluctance motor, the absence of the magnets makes all the solutions of Equation (3.41) stable.

### 3.2.5 Searched harmonic content

The influence of the motor fundamental speed on the voltage, and thus on the current, harmonic content has been treated from an analytical point of view in Subsection 3.1.1 and from the analysis of the spectra in Subsection 3.2.1. Since all the sideband harmonics around all the carrier multiples revolve around  $\omega_o$ , it is licit to wonder why the searched harmonics correspond just to the indexes  $m = 1$  and  $n = \pm 1$ .

Foremost, the  $\alpha\beta$  current components, which the estimator makes use of, come from the phase current measurements. Since the frequency of the current components used as inputs by the estimator is in the same range of the switching frequency of the PWM converter ( $f_c \approx 10 \text{ kHz}$ ), a traditional sampling of the currents is not sufficient to properly measure such a high frequency harmonic content. For injection sensorless control, in [22] it is stated that traditional hall- or shunt based sensors with typical bandwidths around  $250 \text{ Hz}$  it is not enough, but anisotropic magnetoresistive (AMR) current sensors with higher bandwidths are desirable. In [23] and [24], in fact, a  $2 \text{ MHz}$  oversampling is applied in order to reduce measurements noise and quantization errors as much as possible.

Considering a fixed value for the oversampling frequency, if the sideband harmonics of interest were chosen around the  $m$ -th carrier multiple, the number of samples per period of the two sideband harmonics of interest would decrease approximately by a factor of  $1/m$ , resulting in a worse performance of

the estimator. On the other way around, aiming to maintain approximately the same number of samples per period of the two sideband harmonics of interest, choosing the  $m$ -th carrier multiple, the oversampling frequency would have to be increased by a  $m$  factor, resulting in a higher cost for the current measurement and, if  $m$  considerably high, even to the infeasibility to oversample at too high frequencies.

As regards the  $n$  index, the choice is dictated mainly by the implemented modulation harmonic magnitudes, but also by filtering reasons.

As described in the previous section, for the PWM Single-Edge r.s. modulation, with the exception of the cases when  $M$  is close to 1, the sideband harmonics with the highest magnitude are the ones relative to the  $n$  index. However, this is not the only modulation with that peculiarity. As illustrated in [16] and as presented in Section 5.2 with simulations results, this is the case also for the discontinuous modulations DPWMMAX and DPWMMIN regularly sampled. For these two modulations, it is possible to carry out an analysis absolutely analogous to the one in Subsection 3.1.1 and that would lead to the same expression (3.15) for the  $\alpha\beta$  voltage components relative to the indexes  $m = 1$  and  $n = \pm 1$ , but with a different definition for the voltage harmonic coefficients  $A^+$  and  $A^-$ . Moreover, as performed in [2] for the PWM Single-Edge n.s. modulation, the same analysis would bring to the same expression (3.15), but, since the two  $n = 1$  order sideband harmonics present the same magnitude, the coefficients  $A^+$  and  $A^-$  would be equal (Equation (A.5) in the Appendix).

Relatively to other s.r.s. (symmetrical regularly sampled) modulations, such as the PWM Double-Edge, the Space Vector Modulation (SVM) and the discontinuous DPWM0, DPWM1, DPWM2 and DPWM3, it occurs that the highest sideband harmonics are the ones related to  $n = 2$ . These modulations are therefore not recommended, no matter if filters are applied or not to the input currents. In fact, even in the case in which BPFs are used, both in the case with constant and variable center frequency, the presence of harmonics that are located in between the sought harmonics, of interest by virtue of their higher magnitude, makes the filtering process not effective. The result, as can be concluded from the calculations carried out in 3.2.3, would be a demodulation process from which the  $\epsilon$  harmonic content would be much higher and from which the speed information would be much more difficult to be extracted.

### 3.2.6 Overmodulation

A crucial aspect to be mentioned is the influence of the overmodulation operation. For a converter with a given DC-link voltage  $U_{dc}$ , overmodulation is usually embraced in order to achieve a higher voltage fundamental component without the need for an increase of  $U_{dc}$  [25]. On the other hand, from the voltage waveforms point of view, overmodulation implies that the phase voltage is clamped to the value of  $\pm U_{dc}/2$  for a certain time within the fundamental period. During that time, the phase voltage does not switch at carrier frequency and, consequently, no ripple is generated in the phase currents. The phase currents vary instead with a slope that is almost constant and that is positive, if the voltage is clamped to  $+U_{dc}/2$ , or negative, if the voltage is clamped to  $-U_{dc}/2$ . Therefore, since intrinsic injection sensorless control relies on that ripple, whose harmonic content has been previously described, if overmodulation occurs the extraction of the motor position and speed information is not possible.

### 3.2.7 Intrinsic injection sensorless summary

It is therefore possible to summarize in the following points the limiting conditions for the intrinsic injection sensorless estimator operation:

- Zero speed operation is not feasible, since all the sideband harmonics present the same frequency  $f_c$  and thus their information is lost during the voltage transformation from  $abc$  to  $\alpha\beta$  coordinates (Equation (3.14));
- Low-speed operation involves harmonics spectra where the sideband harmonics are shrunk around the carrier frequency, making the filtering and the demodulation processes more difficult (Subsection 3.2.1);
- Low- and high- load conditions involve a low magnitude of the harmonic of interest, implying a lower information from which the position and the speed can be estimated (Subsection 3.2.1);
- High-load condition may involve significant magnetic saturation and thus the loss of information from which the position and the speed can be estimated (Subsection 3.2.2);
- Overmodulation has to be avoided, since it involves the lack of current ripple and thus the impossibility to extract the position and speed information.

Furthermore, from the considerations about the filtering required (Subsection 3.2.3) and the angle error (Subsection 3.2.4), it is possible to draw the reference estimator scheme, displayed in Figure 3.6.

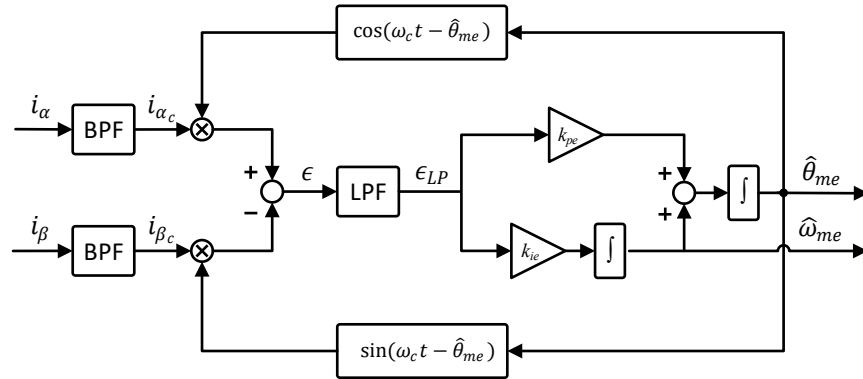


Figure 3.6. Intrinsic injection electrical position and speed estimator reference schematic.



# Chapter 4

## MODELLING OF THE SUBSYSTEMS

In this Chapter, the model of the sensorless drive simulated in a Matlab/Simulink environment is described. Firstly, in Section 4.1, the synchronous reluctance motor model is outlined. In Section 4.2, the converter model is depicted and the two implemented modulator topologies are illustrated, together with the eleven different modulation strategies that can be simulated from the drive model. Then, in Section 4.3, the current and speed regulators are described. In Section 4.4, finally, the sensorless control estimator (the object of this work) is modelled and three alternative schemes for its implementation are proposed. Lastly, in Section 4.5, all the model parameters are listed.

### 4.1 Motor model

In this Section, the Simulink model of the chosen synchronous reluctance motor is described. The set of equations modelling the motor is illustrated in Subsection 4.1.1 and the implementation of these equation in a Simulink environment is depicted in Subsection 4.1.2.

### 4.1.1 SynRM equations

Since, as illustrated in in Subsection 3.2.2, the intrinsic injection sensorless algorithm, as well as all the other injection methods, requires that the machine is provided with reluctance, for the present work a ABB's 11-kW Synchronous Reluctance machine prototype has been chosen. This is a point conflicting with the works where this algorithm is defined [1, 2], where an IPM motor was used.

As described in [26] and [27], the synchronous reluctance motor is a typology of motor that, compared to the permanent magnets synchronous machine, aims for lower costs and better field weakening capabilities. Compared to the induction machine, it presents higher efficiencies and comparable torque densities. Its main weak point is the difficult implementation of vectorial control, since the motor inductances vary consistently during the operation, due to iron saturation and cross saturation effects. Moreover, these phenomena have to be taken even more in consideration in sensorless control schemes.

For this reason, in the modelling of the motor, the  $dq$  frame magnetizing inductances have to be considered dependent from the  $dq$  reference frame currents [19]. Furthermore, the leakage inductance and the iron losses are disregarded, since not significant to the scope of this work. Considering the star point of the machine to be unavailable, it is possible to write down the well-known electric equation for the synchronous reluctance machine in the  $dq$  synchronous reference frame [28]:

$$u_{dq} = R_s i_{dq} + \frac{d\lambda_{dq}}{dt} + j\omega_{me}\lambda_{dq} \quad (4.1)$$

which, split in the  $d$ - and  $q$ -axis, becomes:

$$\begin{cases} u_d = R_s i_d + \frac{d\lambda_d}{dt} - \omega_{me}\lambda_q \\ u_q = R_s i_q + \frac{d\lambda_q}{dt} + \omega_{me}\lambda_d \end{cases} \quad (4.2)$$

For the complete electromechanical description, the torque expression (4.3) together with the mechanical dynamics equation (4.4) have to be taken into account:

$$\tau = \frac{3}{2}p(\lambda_d i_q - \lambda_q i_d) \quad (4.3)$$

$$J \frac{d\omega_m}{dt} = \tau - \tau_l - B\omega_m \quad (4.4)$$

where:

$$\omega_m = p \cdot \omega_{me} \quad (4.5)$$

The way in which the effect of saturation and cross-saturation can be taken into account can be understood from the following equations:

$$\begin{cases} \lambda_d = L_d(i_d, i_q) \cdot i_d \\ \lambda_q = L_q(i_d, i_q) \cdot i_q \end{cases} \quad (4.6)$$

where the dependency of  $L_d$  from  $i_d$  models the saturation and the one from  $i_q$  models the cross saturation. On the other way around, the dependency of  $L_q$  from  $i_q$  models the saturation and the one from  $i_d$  models the cross saturation.

The two equations (4.6) can be substituted in (4.2) and in (4.3), which, together with (4.4), provides the description of the SynRM modelling saturation and cross saturation:

$$\begin{cases} u_d = R_s i_{sd} + \frac{dL_d(i_d, i_q) \cdot i_d}{dt} - \omega_{me} \lambda_q \\ u_q = R_s i_{sq} + \frac{dL_d(i_d, i_q) \cdot i_q}{dt} + \omega_{me} \lambda_d \\ \tau = \frac{3}{2} p \left( L_d(i_d, i_q) - L_q(i_d, i_q) \right) i_q i_d \\ J \frac{d\omega_m}{dt} = \tau - \tau_l - B\omega_m \end{cases} \quad (4.7)$$

The 11-kW SynRM parameters relative to operations without flux weakening operation are listed in Table 4.1.

Parameter	Parameter value
$V_n$	400 V
$I_n$	18 A
$n_{mn}$	3000 rpm
$\tau_n$	17 Nm
$p$	2
$R_s$	0.72 $\Omega$
$J$	0.00351 kgm <sup>2</sup>

Table 4.1. 11-kW SynRM parameters.

Furthermore, experimental  $dq$ -axis flux measurements have been taken for variable  $dq$ -axis current values. In this way, it is possible implement the relationship between fluxes and currents in the motor model and, as illustrated in Subsection 4.3.2, also in the control.

From the plots of the relationship of the  $dq$ -axis fluxes and currents displayed in Figure 4.1, it is possible to notice how the cross-saturation emerges as an increase of one axis saturation in case of the increase of the opposite axis current. It is important to state that, considered the symmetry properties of the synchronous reluctance machine, the fluxes plots are symmetric with respect to the origin and the increase of negative currents on one axis causes the same saturation effects on the opposite axis as positive currents with the same magnitude.

From the aforementioned fluxes measurements, it is possible to calculate the incremental inductances as follows [29]:

$$\begin{cases} L_d = \frac{\Delta\lambda_d}{\Delta i_d} \Big|_{i_q=const} \\ L_q = \frac{\Delta\lambda_q}{\Delta i_q} \Big|_{i_d=const} \end{cases} \quad (4.8)$$

From their plots in Figure 4.2 it is possible to notice how the high-load conditions saturates the  $d$ -axis iron as much as the  $q$ -axis iron and how the cross saturation is more dominant for low current values. Thanks to symmetric properties of the machine, the  $dq$ -axis incremental inductances plots are symmetric with respect to zero-current axis.

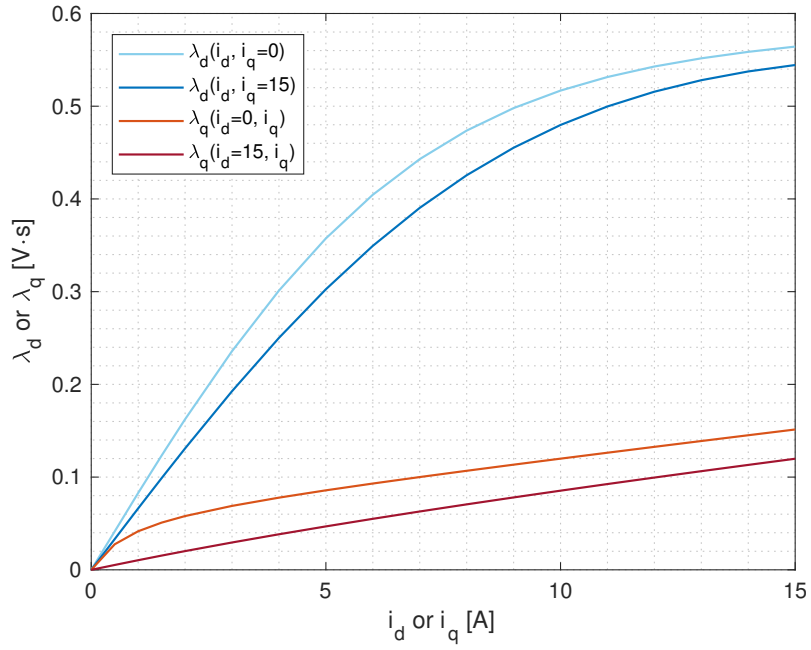


Figure 4.1.  $dq$ -axis fluxes dependence on  $dq$ -axis currents, with particular focus on the cross saturation effects.

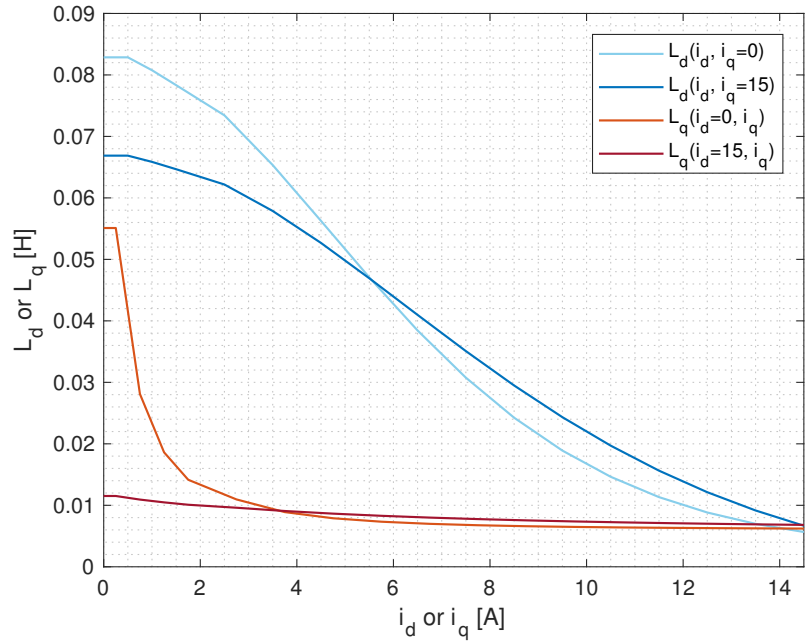


Figure 4.2.  $dq$ -axis incremental inductances dependence on  $dq$ -axis currents, with particular focus on the cross saturation effects.

### 4.1.2 SynRM model

The synchronous reluctance machine scheme in the  $dq$  reference frame is shown in Figure 4.3. It consists, basically, in the implementation of the vectorial equation (4.1).

The block  $\text{lambda\_dq} \Rightarrow \text{i\_dq}$  is expanded in Figure 4.4. The two LUTs Look-Up Table  $\text{lambda\_dq} \Rightarrow \text{i\_d}$  and Look-Up Table  $\text{lambda\_dq} \Rightarrow \text{i\_q}$  are implemented from the aforementioned fluxes and currents measurements. Considered the symmetric properties of the machine, only positive flux linkages are used and the signs are preserved by post-correcting the resulting currents based on the sign of the flux linkage, making use of the `sign()` block. The negative fluxes measurements are not used in order to avoid any asymmetrical behaviour in the model in case of measurements errors.

Figure 4.5 shows the implementation of the torque expression (4.3), while Figure 4.6 the implementation of the mechanical dynamics equation (4.4).

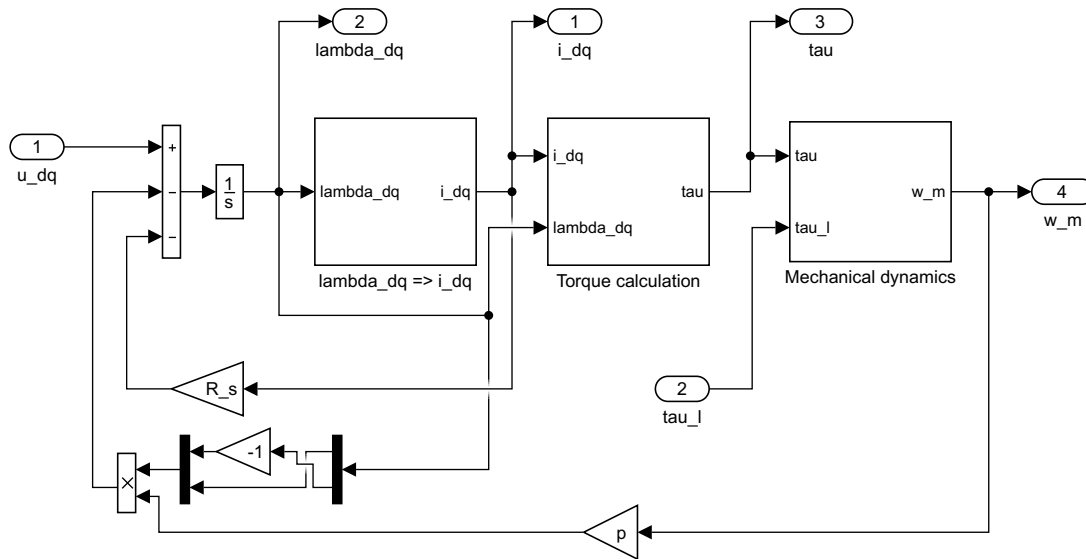


Figure 4.3. Simulink model of the SynRM in the  $dq$  coordinates.

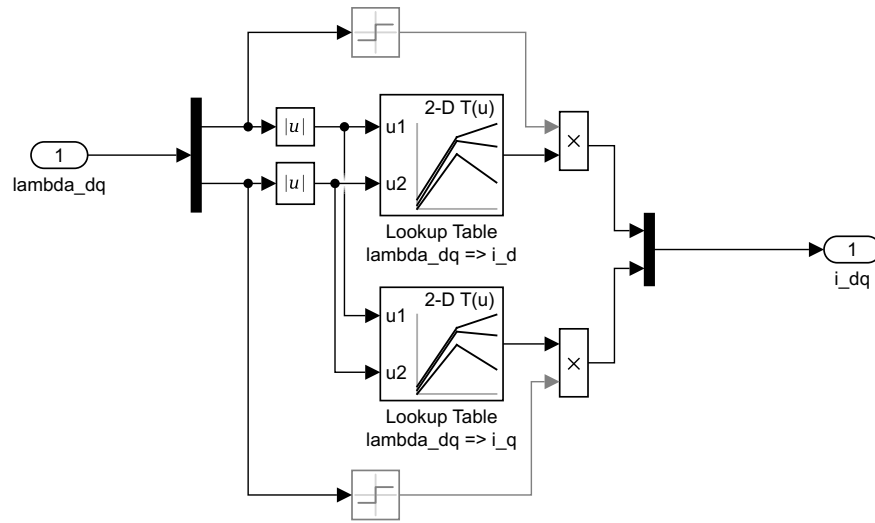


Figure 4.4. Simulink model of the fluxes to currents calculation, located inside the  $dq$  coordinates SynRM block of Figure 4.3.

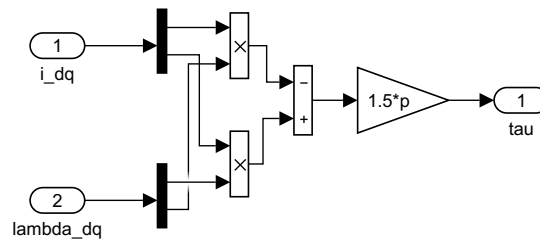


Figure 4.5. Simulink model of the torque calculation, located inside the  $dq$  coordinates SynRM block of Figure 4.3.

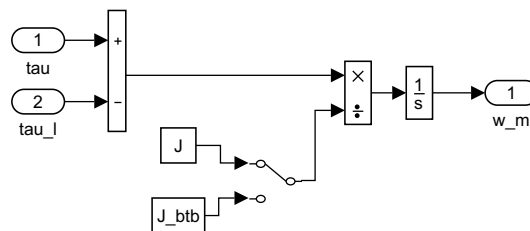


Figure 4.6. Simulink model of the mechanical dynamics equation, located inside the  $dq$  coordinates SynRM block of Figure 4.3.

## 4.2 PWM converter model

In this Section, the Simulink model of the PWM converter model is described. Firstly, the two main converter scheme subsystems are introduced in Subsection 4.2.1. Then the two implemented modulator topologies are depicted: the first topology using a carrier-reference comparison in Subsection 4.2.2, the second one based on the Unified Voltage Modulation Technique [30] in Subsection 4.2.3. The implementation of the different modulation strategies obtainable from the second modulator topology is further discussed in the last Subsection 4.2.4.

### 4.2.1 PWM converter model

The PWM converter has been modelled in Simulink without the use of any of the Simulink toolboxes, and its scheme can be seen in Figure 4.7. From the most simplistic point of view, the converter block can be considered to receive as input the phase voltage references, coming from the current controller, and to give as output the phase voltages applied to the terminals of the motor. The converter parameters are listed in Table 4.2.

Parameter	Parameter value
$U_{dc}$	560 V
$f_c$	8 kHz

Table 4.2. PWM converter parameters.

The PWM converter is composed by two main subsystems.

The first subsystem is the modulator, which gets as input the voltage references and computes the upper leg switches gate commands  $S_{abc}$ . It has been modelled following two different approaches.

According to the first one, the switching commands have been calculated through the comparison between a carrier and the three voltage references waveforms. It is discussed in Section 4.2.2.

The second approach makes use of a different technique named Unified Voltage Modulation Technique, and it is discussed in Section 4.2.3. A total of 11

different modulations have been implemented, of which 2 computed by the first modulator scheme and 9 by the second one.

The second subsystem is the converter itself, which gets as input the upper leg switches gate commands  $S_{abc}$  and gives as output the actual phase voltages. In particular, the switches are considered to be ideal and the phase voltage is considered to be equal to  $+U_{dc}/2$ , if the relative gate command is 1, and equal to  $-U_{dc}/2$ , if the relative gate command is 0:

$$\begin{cases} S_x = 1 : u_x = \frac{U_{dc}}{2} \\ S_x = 0 : u_x = -\frac{U_{dc}}{2} \end{cases} \quad \text{with } x = a,b,c \quad (4.9)$$

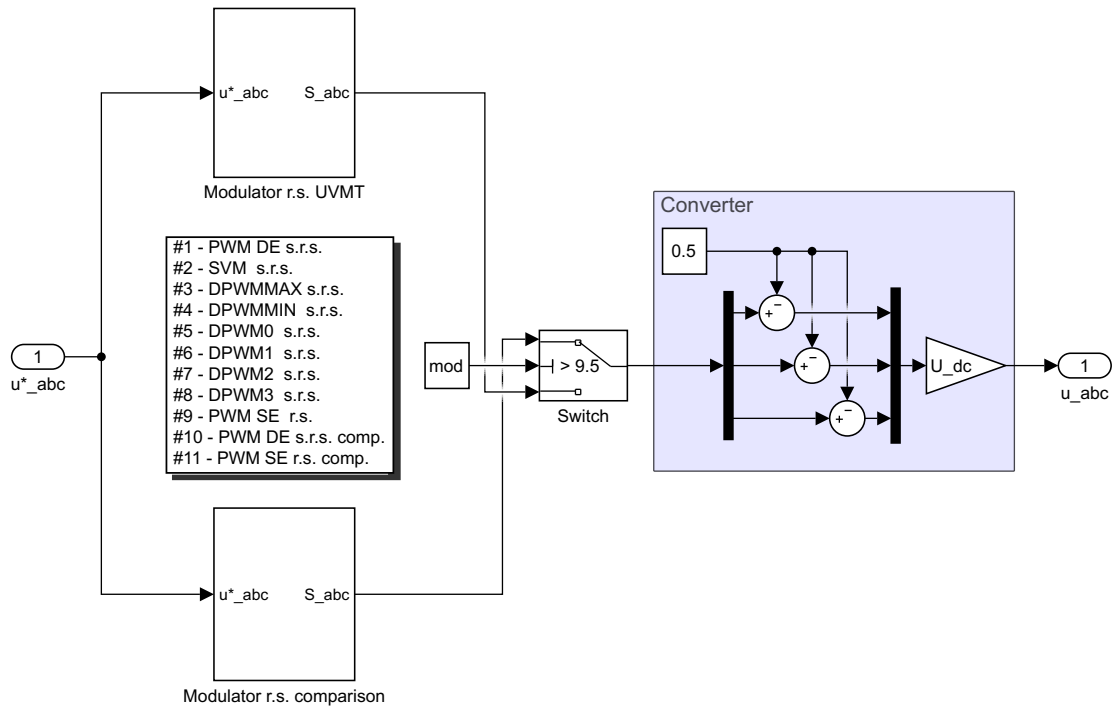


Figure 4.7. Simulink model of the PWM converter.

### 4.2.2 Modulator model using carrier-reference comparison

As illustrated in [16], the comparison between a fixed frequency carrier signal and the reference voltage waveform is the most common technique for the implementation of PWM based converters. According to the nature of the reference waveform, we can have naturally either regularly sampled modulation strategies.

However, a naturally sampled waveform is troublesome to implement in a digital modulation system, since the intersection between the reference and the carrier is defined by a transcendental equation difficult to calculate.

To overcome these difficulties, nowadays the regular sampling PWM strategy is the most adopted one. According to this strategy, the reference waveforms are sampled and kept constant during each carrier interval, as can be observed in Figure 4.8. Usually, the sampling instant is chosen to occur either at the positive or at the negative peak value of the carrier, in order to avoid instantaneous changes in the reference during the ramp, which may cause multiple switch transitions.

Making use of a sawtooth carrier, the sampling instant can be therefore chosen just at the end of the ramping period (Figure 4.8, top plot).

With a triangular carrier, instead, the sampling instant can be chosen at the positive peak (Figure 4.8, centre plot), at the negative peak or at both the positive and negative peaks (Figure 4.8, bottom plot).

In the first two cases the sampling is defined symmetrical, since symmetrical respect to the middle carrier period instant, and the reference is said to be "symmetrical regularly sampled" (s.r.s.). In the last case, instead, the sampling is defined asymmetrical and the reference is said to be "asymmetrical regularly sampled" (a.r.s.).

As it can be noticed from Figure 4.8, there is a phase delay between the reference and the sampled reference, which can be compensated by phase advancing the reference waveforms. This phase delay would consist of  $T_c/2$  for a sawtooth carrier and of  $T_c/4$  for a triangular carrier. Anyway, this "phase advanced sampled" (p.a.s.) reference is not taken into account in this work.

The Simulink scheme of the modulator making use of carrier-reference comparison (comp.) is shown in Figure 4.9. The sinusoidal voltage references, normalized by the factor  $U_{dc}/2$ , are compared to the carrier, which can be a triangular either a sawtooth continuous waveforms, both with a peak-to-peak amplitude equal to 1. In the former case the resulting modulation is

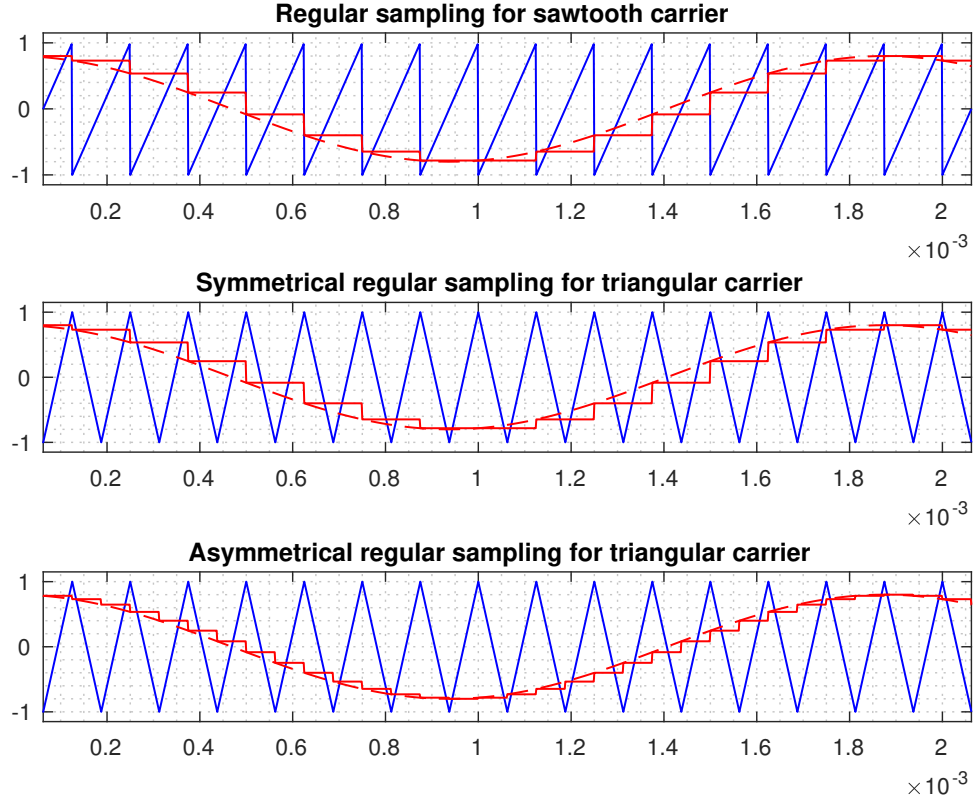


Figure 4.8. Regular sampling for sawtooth carrier (top), symmetrical (centre) and asymmetrical (bottom) regular sampling for triangular carrier.

the Double-Edge s.r.s. (#10), in the latter case the resulting modulation is the Single-Edge r.s. (#11).

The concept behind PWM modulation is that one of the upper legs switches is considered to be closed if the relative normalized reference voltage is greater than the carrier, which is the same for all the three phases references. On the other way around, it is considered to be open if the normalized reference voltage is lower than the carrier:

$$\begin{cases} \frac{u_x^*}{U_{dc}/2} \geq carrier : S_x = 1 \\ \frac{u_x^*}{U_{dc}/2} < carrier : S_x = 0 \end{cases} \quad \text{with } x = a, b, c \quad (4.10)$$

The block `D\A` models the way a digital control works. It is composed by a `Delay` block and by a `Zero-Order-Hold` block. The `Delay` block represents the time that is spent to complete all the computations during every calculation step of  $T_c$ . It has been assumed that this computation period lasts

$T_c/2$ . The Zero-Order-Hold models the fact that in a digital controller the gate commands are used by the converter in synchronisation with the PWM voltage generation.. A sampled time of  $T_c$  has then been used for this block.

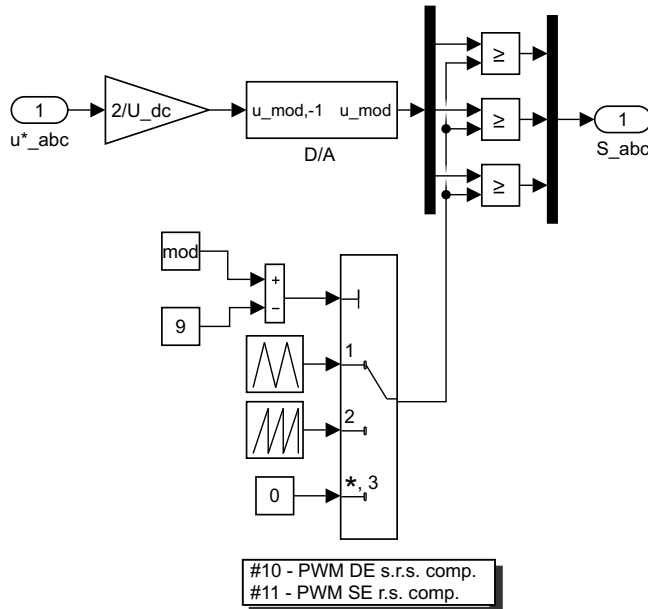


Figure 4.9. Simulink model of the modulator making use of the comparison carrier-reference, located in the PWM converter block of Figure 4.7.

### 4.2.3 Modulator model using UVMT

Since the different behaviour of the system, according to the implemented modulation, is of crucial interest for the scope of this work, a modulation technique, that facilitates the swap between different modulation strategies, has been implemented. This technique is named "Unified Voltage Modulation Technique" (UVMT), it is firstly introduced in [30] and applied also in [31].

Thanks to this modulation technique, a simple variation of an offset time makes it possible to switch the implemented modulation scheme, and this change can even occur real-time and seamlessly. Furthermore, as it will be illustrated below, this is achieved throughout a reduced computational burden, compared to the usual way these modulation schemes are implemented.

The UVMT calculation of the offset times is based on the concept of the imaginary switching times:

$$\begin{cases} T_{sa} = \frac{T_{sw}}{U_{dc}} \cdot u_a^* \\ T_{sb} = \frac{T_{sw}}{U_{dc}} \cdot u_b^* \\ T_{sc} = \frac{T_{sw}}{U_{dc}} \cdot u_c^* \end{cases} \quad (4.11)$$

The imaginary switching times are proportional to the reference voltages and are labelled imaginary because they can also assume negative values. They are needed for the computation of the effective time  $T_{eff}$ , which is the time within half a carrier period  $T_h = T_c/2$  during which an active voltage vector is applied:

$$T_{eff} = T_{max} - T_{min} \quad (4.12)$$

where:

$$\begin{cases} T_{max} = \max(T_{sa}, T_{sb}, T_{sc}) \\ T_{min} = \min(T_{sa}, T_{sb}, T_{sc}) \end{cases} \quad (4.13)$$

These relationships can be visualised in Figure 4.10(a). It is therefore straightforward to define the zero space vector time as:

$$T_0 = T_h - T_{eff} \quad (4.14)$$

As it can be noticed from Figure 4.10(b), the effective time can be relocated anywhere within the half carrier period  $T_h$ . This is equivalent to a different distribution of the zero voltage vectors (111) and (000) and to an implementation of a different modulation scheme, as it will be presented in subsection 4.2.4. This reallocation can be easily achieved by shifting the effective time interval by an appropriate offset time. In this way, it is possible to compute the actual gating time for each inverter arm:

$$\begin{cases} T_{ga} = T_{sa} + T_{offset} \\ T_{gb} = T_{sb} + T_{offset} \\ T_{gc} = T_{sc} + T_{offset} \end{cases} \quad (4.15)$$

As it can be seen from Figure 4.10(b), this is relative to the OFF sequence, i.e. the time interval during which the phase switches pass from the state 1 to the state 0. In order to have a symmetrical switching pulse pattern with

respect to the half carrier period instant, the gating times relative to the ON sequence have to be computed as follows:

$$\begin{cases} T_{ga} = T_h - T_{sa} \\ T_{gb} = T_h - T_{sb} \\ T_{gc} = T_h - T_{sc} \end{cases} \quad (4.16)$$

Furthermore, in order to guarantee that both the ON and the OFF sequences remain within the carrier period  $T_c$ , which is equivalent to the condition that the DC-link voltage is fully utilized, the conditions  $0 \leq T_{min} + T_{offset}$  and  $T_{max} + T_{offset} \leq T_s$  have to be respected. This lead to the definitions:

$$\begin{cases} T_{offset,min} = -T_{min} \\ T_{offset,max} = T_s - T_{max} \end{cases} \quad (4.17)$$

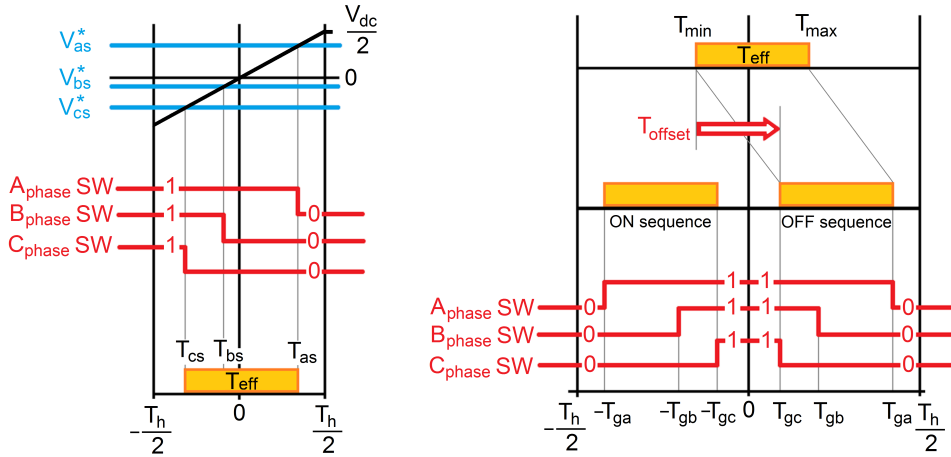


Figure 4.10. Unified Voltage Modulation Technique. On the left: relationship between voltage references, effective time and imaginary switching times. On the right: actual gating time generation.

The Simulink model for the modulator making use of r.s. references and of the UVMT is shown in Figure 4.11. Together with the gating times, that in the model are named **Instants**, for the switches command calculation it is also needed the information relative to the sector where the reference voltage is placed. The  $\alpha\beta$  frame is supposed to be split in the 6 sectors that are used for the DTC, i.e.  $(0, \pi/3)$ ,  $(\pi/3, 2/3\pi)$ ,  $(2/3\pi, \pi)$ ,  $(\pi, 4/3\pi)$ ,  $(4/3\pi, 5/3\pi)$  and

$(5/3\pi, 2\pi)$ . The sector is therefore obtained from a Look-Up Table, whose inputs are the signs and the ratios of the  $\alpha\beta$  voltage references components. From Figure 4.10(b), it is noticeable that a carrier period  $T_c$  can be divided in 7 different intervals, according to the change of the upper legs switching states. The switching pattern represented in Figure 4.10 is relative to the first sector, since the first switching state changing is the one of the phase a, then the one of the phase b and finally the one of the phase c. This is relative to the ON sequence, while, for the OFF sequence, the order is reversed, due to the symmetry reasons discussed above. This order changes according to the sector and is displayed in Table 4.3.

Sector	Phase switching sequence
I	a b c c b a
II	b a c c a b
III	b c a a c b
IV	c b a a b c
V	c a b b a c
VI	a c b b c a

Table 4.3. Upper switching states variation sequence for each of the 6 sectors of the  $\alpha\beta$  frame.

The gating times vector carries just the information relative to the switching instants and therefore it sets the limits for the 7 intervals within  $T_c$ . Thanks to a counter, it is thus straightforward the knowledge of the ongoing interval. The knowledge of the interval and of the sector are therefore enough to determine the state of the 3 upper switches.

These operations are performed in the `Upper switches command calculation` block. The block `D/A` is inserted to emulate the behaviour of the digital control and it is analogue to the block already described in the subsection 4.2.2. It is senseful to put this block after the end of the activation times calculation, which is carried out by the microprocessor, and the application of these signals, which is carried out by the FPGA.

The `Timing interval calculation` block is expanded in Figure 4.12 and consists of the implementation of the UVMT theory discussed above. The gating times for the s.r.s. modulations are implemented in the upper part of the scheme, while the r.s. PWM Single-Edge modulation is implemented separately in the lower part. In the `Imaginary switching times Tsx calculation` block, equations (4.11) are implemented. In the `Timing intervals calculation` block, Equations (4.15) and (4.16) are implemented and the

gating times are sorted from the smallest to the largest, both for the OFF than for the ON sequences.

The reason for which #9 modulation is set apart is that, since the sawtooth carrier is a trailing Single-Edge carrier, the instant at which all the 3 upper switches open is the same and it is at the end of the carrier period  $T_c$ . That implicates that for Single-Edge modulation the imaginary switching times are normalized respect to  $T_c$  and not to  $T_h$ , as for the modulations deriving from the Double-Edge scheme.

The `Offset time calculation` block is expanded in Figure 4.13. All the  $T_{offset}$  calculation blocks are illustrated in subsection 4.2.4.

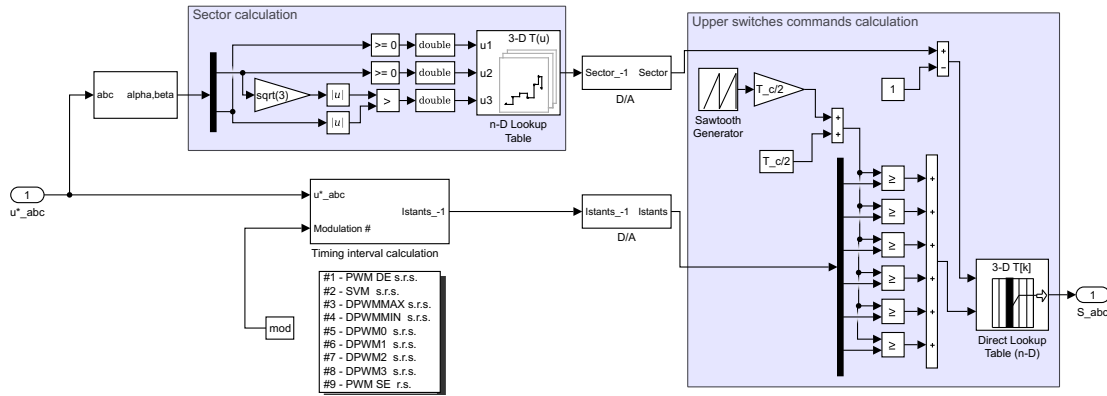


Figure 4.11. Simulink model of the modulator making use of the Unified Voltage Modulation Technique, located in the PWM converter block of Figure 4.7.

#### 4.2.4 Modulation schemes implementation for regularly sampled carrier

For this subsection, the books [16] and [25] are used as references for the modulation schemes theory and the articles [30] and [31] for their implementation using the UVMT theory.

The first implemented modulation is the PMW Double-Edge, labelled modulation #1. It relies on a simple sinusoidal reference and a triangular carrier, and thanks to its simplicity it is a classical and widely used method. Its main drawback is that the linear range of controllable voltage is limited to a

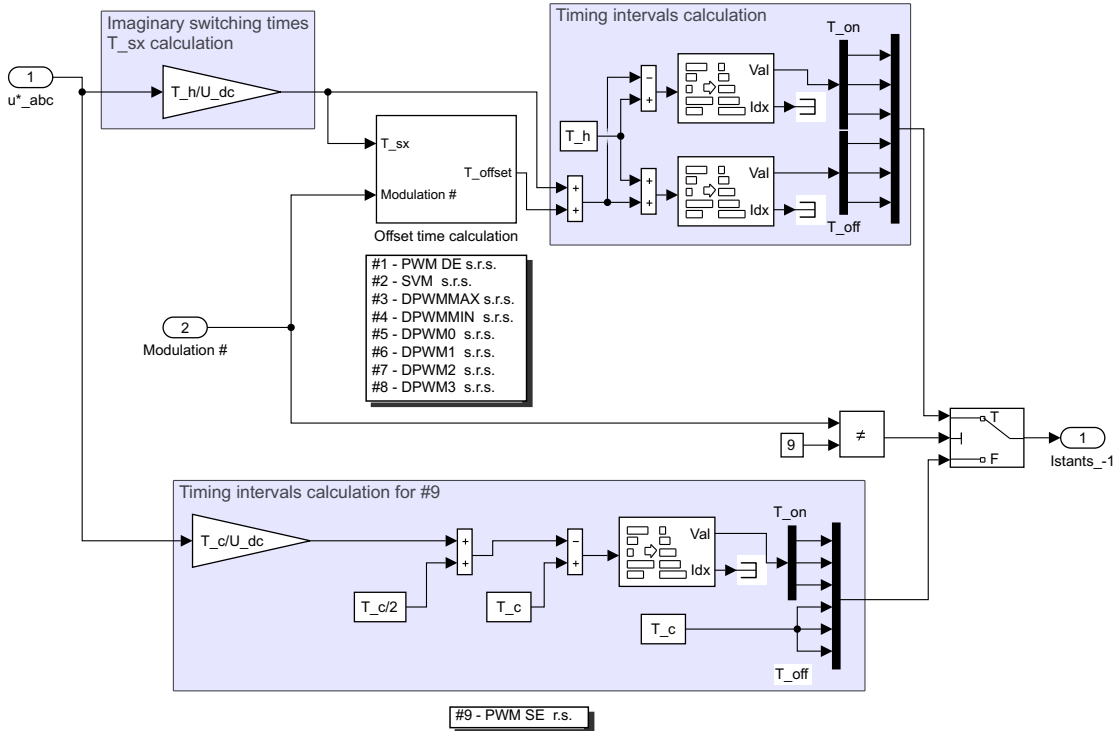


Figure 4.12. Simulink model for the calculation of the timing interval, located in the Modulator r.s. UVMT block of Figure 4.11.

modulation index  $M = 1$ , where, for carrier based modulations techniques,  $M$  is defined as:

$$M = \frac{u_{phase}^*}{U_{dc}} \quad (4.18)$$

This region is called so because the relationship between  $M$  and the output voltage fundamental frequency magnitude is linear. To increase further the amplitude of the output voltage,  $M$  is increased beyond 1. The overmodulation region is therefore reached and this relationship is not anymore linear. According to the UVMT theory, thanks to the equivalence between the phase voltage reference  $u_a^*$  and the pole voltage reference  $u_{an}^*$  referred to the midpoint of the DC-link  $n$ , a constant expression for the offset time can be derived:

$$T_{offset, \#1} = \frac{T_h}{2} \quad (4.19)$$

The modulation #2 is the Space Vector Modulation. The traditional way according to which the pulse pattern is generated relies on the creations of arbitrary vectors matching the sum of two active space vector volt-second

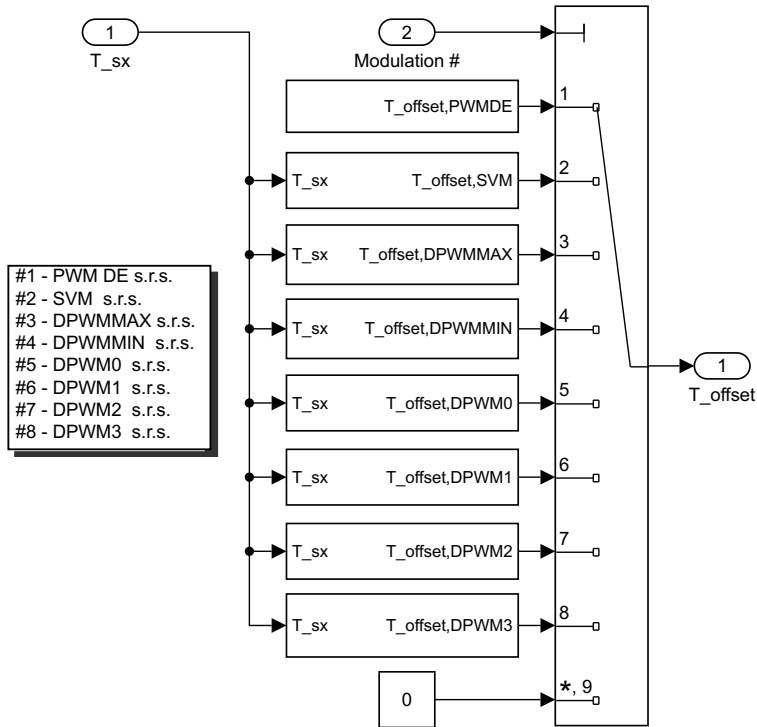


Figure 4.13. Simulink model for the calculation of the offset time, located in the Timing interval calculation block of Figure 4.12.

averages over an equivalent half carrier period, which makes that process intrinsically r.s.. The two active space vectors are the ones that border the sector where the reference vector is positioned, while during the remaining half carrier period the two zero space vectors are used.

Looking at the harmonic spectrum, SVM is characterized by a third harmonic component, which allows to extend the linear modulation range to  $M = 2/\sqrt{3} = 1.15$ , as it happens with the PWM Double-Edge s.r.s. with 1/6 third harmonic injection. Infact, that PWM method generates automatically the two nearest space vectors to create the output form. The only difference is that in the SVM implementation centers  $T_{eff}$  in each half carrier period and splits the remaining  $T_0$  equally between the zero vectors (111) and (000). That causes the harmonic spectrum for SVM s.r.s. really similar to the one of PWM Double-Edge s.r.s. with 1/6 third harmonic injection, but slightly preferable since the energy is transferred towards the outer sidebands harmonics.

With regards to the UVMT, the offset time has to be chosen in the middle

of  $T_{offset,min}$  and  $T_{offset,max}$ , i.e.:

$$T_{offset,\#2} = \frac{T_h}{2} - \frac{T_{max} + T_{min}}{2} \quad (4.20)$$

Together with the added complexity deriving from the needed sector information, one of the main possible drawbacks of SVM is the higher switching losses with respect to the other modulation techniques. They can in fact be reduced shifting the effective time within the half carrier period, taking into account the successive half carrier intervals, reducing thus the number of required switches. In this way, discontinuous modulation strategies can be achieved (DPWM).

The most straightforward way to achieve this is by eliminating one of the two zero vectors. In DPWMMAX modulation, the zero vector (000) is eliminated setting the offset time to the maximum achievable:

$$T_{offset,\#3} = T_{offset,max} = T_h - T_{max} \quad (4.21)$$

In DPWMMAX modulation, the zero vector (111) is eliminated setting the offset time to the minimum achievable:

$$T_{offset,\#4} = T_{offset,min} = -T_{min} \quad (4.22)$$

These two DPWM strategies are also known as 120° DPWM, since in each phase leg, while one device is always conducting, the other one is turned off during the 120° of its unmodulated region. That results in an unevenness in the share of the conduction losses across the two devices.

However, this inconvenient can be avoided switching between DPWMMAX and DPWMMIN every half cycle and achieving different other DPWM strategies. 60° DPWM can be achieved simply alternatively eliminating the zero space vectors (000) and (111) for successive 60° segments. Two different strategies can be achieved, named DPWM1 (#6) and DPWM3 (#8). They are the most suitable for resistive loads, since the nonswitching periods are symmetrically placed around the voltage positive and negative peaks, thus minimizing the switching losses. The following expressions for the offset time can be therefore be calculated:

$$T_{offset,\#6} = \begin{cases} T_h - T_{max} & \text{if } T_{min} + T_{max} \geq 0 \\ -T_{min} & \text{if } T_{min} + T_{max} < 0 \end{cases} \quad (4.23)$$

$$T_{offset,\#8} = \begin{cases} -T_{min} & \text{if } T_{min} + T_{max} \geq 0 \\ T_h - T_{max} & \text{if } T_{min} + T_{max} < 0 \end{cases} \quad (4.24)$$

The optimal reduction of the switching losses for not-unity power factor loads can be attained by shifting the switching instants by up to a maximum of  $30^\circ$ , realizing in this way  $30^\circ$  DPWM strategies. For a lagging power factor, DPWM2 (#7) is implemented by delaying the non-switching period of DPWM1 by  $30^\circ$ . For a leading power factor, DPWM0 (#5) is implemented by advancing the non-switching period of DPWM1 by  $30^\circ$ , which is equivalent to delaying the non-switching period of DPWM3 by  $30^\circ$ . This results in the following expressions:

$$T_{offset,\#7} = \begin{cases} T_h - T_{max} & \text{if } T_{min,x} + T_{max,x} \geq 0 \\ -T_{min} & \text{if } T_{min,x} + T_{max,x} < 0 \end{cases} \quad (4.25)$$

$$T_{offset,\#5} = \begin{cases} -T_{min} & \text{if } T_{min,x} + T_{max,x} \geq 0 \\ T_h - T_{max} & \text{if } T_{min,x} + T_{max,x} < 0 \end{cases} \quad (4.26)$$

where  $T_{min,x}$  and  $T_{max,x}$  are computed from the reference voltages retarded by  $30^\circ$ .

The last r.s. modulation implemented is the PWM Single-Edge. Its offset time expression derives from the PWM Double-Edge expression, for which  $T_{offset} = T_h/2$ . However, since with a sawtooth carrier the symmetry within the carrier period is lost and the OFF sequence can be thought to be shrunk at the  $T_c$  instant, it is not useful to think in terms of half carrier period. And, since the equivalence between the phase voltage reference  $u_a^*$  and the pole voltage reference  $u_{an}^*$  is required as in modulation #1, the offset time has to be chosen as:

$$T_{offset,\#9} = \frac{T_c}{2} \quad (4.27)$$

In table Table 4.4 the offset times for the 9 aforementioned modulations are reported, while in the appendix A.2 the Simulink calculation schemes are displayed.

Modulation #	Modulation	Offset time
#1	PWM Double-Edge s.r.s.	$T_h/2$
#2	SVM s.r.s.	$\frac{T_h}{2} - \frac{T_{max} + T_{min}}{2}$
#3	DPWMMAX s.r.s.	$T_h - T_{max}$
#4	DPWMMIN s.r.s.	$-T_{min}$
#5	DPWM0 s.r.s.	$\begin{cases} -T_{min} & \text{if } T_{min,x} + T_{max,x} \geq 0 \\ T_h - T_{max} & \text{if } T_{min,x} + T_{max,x} < 0 \end{cases}$
#6	DPWM1 s.r.s.	$\begin{cases} T_h - T_{max} & \text{if } T_{min} + T_{max} \geq 0 \\ -T_{min} & \text{if } T_{min} + T_{max} < 0 \end{cases}$
#7	DPWM2 s.r.s.	$\begin{cases} T_h - T_{max} & \text{if } T_{min,x} + T_{max,x} \geq 0 \\ -T_{min} & \text{if } T_{min,x} + T_{max,x} < 0 \end{cases}$
#8	DPWM3 s.r.s.	$\begin{cases} -T_{min} & \text{if } T_{min} + T_{max} \geq 0 \\ T_h - T_{max} & \text{if } T_{min} + T_{max} < 0 \end{cases}$
#9	PWM Single-Edge r.s.	$T_c/2$

Table 4.4. Offset times according to the UVMT for the implemented r.s. modulations.

## 4.3 Control model

In this Section, the Simulink model of the drive control is described. Firstly, the drive scheme without the presence of the signal injection estimator is depicted in Subsection 4.3.1. Subsequently, the current regulator is described in Subsection 4.3.2 and the speed regulator in Subsection 4.3.3.

### 4.3.1 Drive model without speed estimator

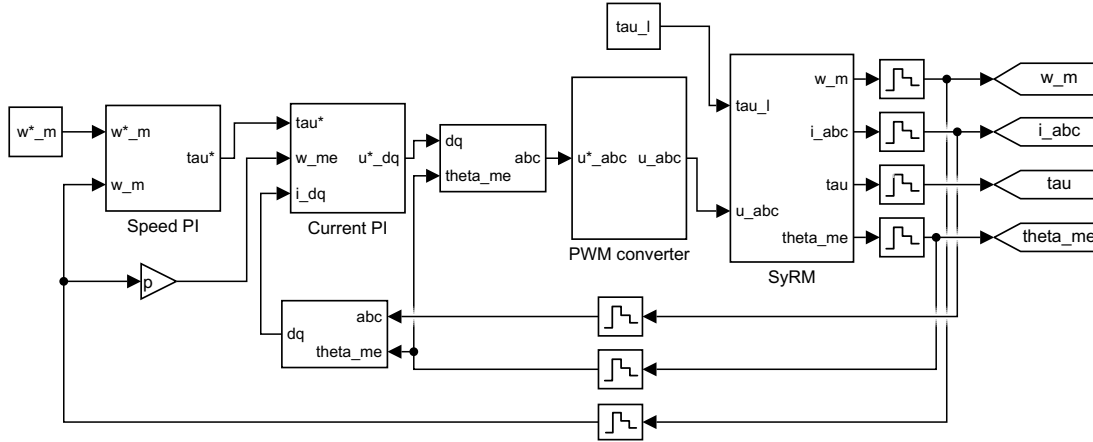


Figure 4.14. Simulink model of the drive without the implementation of the speed estimator.

The control scheme of the drive has been firstly realized without using of the signal injection estimator and it is presented in Figure 4.14. Its tuning has been firstly carried out with an ideal converter, where the voltage applied to the terminals of the motor overlaps the sinusoidal reference, making use of solely continuous quantities. Afterwards, the converter model discussed in the previous chapter has been included in the scheme and the whole control has been digitalized and made to work at the same frequency of the converter itself, i.e.  $f_c$ . Furthermore, all the measurements are modelled to be sampled at the sampling frequency  $T_s = 0.5 \text{ MHz}$ , which is the highest frequency that the hardware present in the laboratory of ABB Corporate Research Sweden in Västerås, where the present work has been carried out, is able to achieve.

In the  $abc$ - $dq$  transformation blocks, the triphase-biphase transformation  $abc$ - $\alpha\beta$  and the direct rotational transformation, shown respectively in (4.28) and

(4.30) are applied. On the other way around, in the  $dq$ - $abc$  transformation blocks, the inverse rotational transformation and the biphas-triphas transformation  $\alpha\beta$ - $abc$ , shown respectively in (4.31) and (4.29), are applied.

$$X_{\alpha\beta} = \begin{bmatrix} \frac{2}{3} & -\frac{1}{3} & -\frac{1}{3} \\ 0 & \frac{1}{\sqrt{3}} & -\frac{1}{\sqrt{3}} \end{bmatrix} X_{abc} \quad (4.28)$$

$$X_{abc} = \begin{bmatrix} 1 & 0 \\ -\frac{1}{2} & \frac{\sqrt{3}}{2} \\ \frac{1}{2} & -\frac{\sqrt{3}}{2} \end{bmatrix} X_{\alpha\beta} \quad (4.29)$$

$$X_{dq} = \begin{bmatrix} \cos\theta & \sin\theta \\ -\sin\theta & \cos\theta \end{bmatrix} X_{\alpha\beta} \quad (4.30)$$

$$X_{\alpha\beta} = \begin{bmatrix} \cos\theta & -\sin\theta \\ \sin\theta & \cos\theta \end{bmatrix} X_{dq} \quad (4.31)$$

where  $X$  is a general variable, of dimension 2 either 3 according to the case, and  $\theta$  is the rotation angle.

### 4.3.2 Current regulator

The guidelines for the current regulator implementation can be found in [32] and its scheme is shown in Figure 4.15.

The  $dq$ -axis current references are obtained from the corresponding LUTs describing the MTPA trajectory. This trajectory has been obtained in the  $dq$  reference frame from the intersection of the iso-current trajectories, i.e. circumferences with the radius equivalent to the amplitude of the current vector, and the iso-torque trajectories, computed with the Equation (4.3) and similar to hyperboles in that reference frame. The MTPA trajectory has been calculated from the flux and current measurements discussed in 4.1.1 and it is plotted in 4.16. It is noteworthy that, as for a typical reluctance machine, the slope of this trajectory tends to  $45^\circ$  for low torque values, while it is roughly  $70^\circ$  for higher torque values [19].

It is noteworthy that such a control scheme where both the  $d$ - and the  $q$ -axis

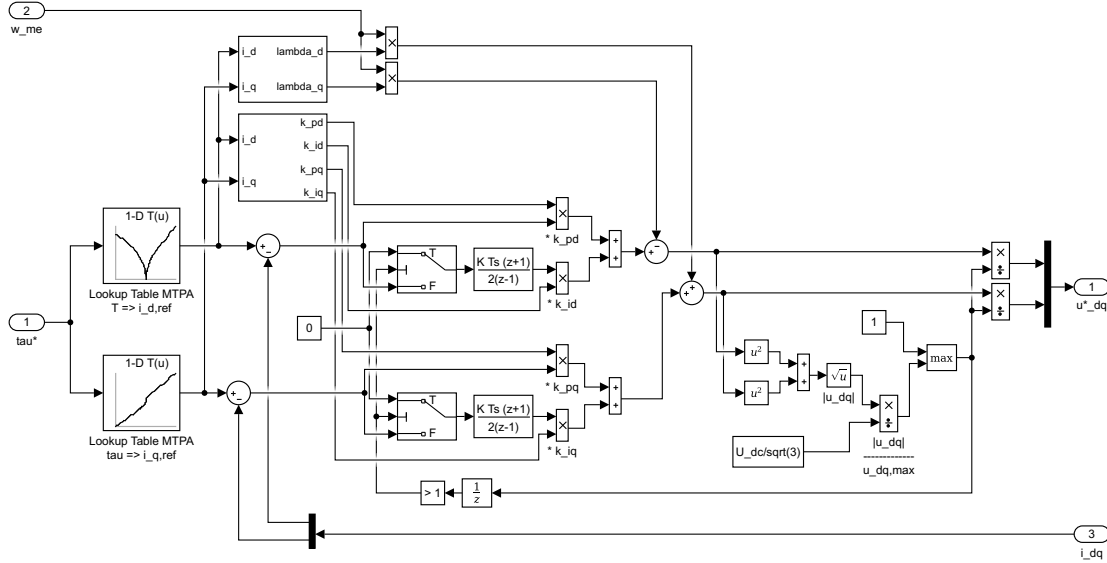


Figure 4.15. Simulink model of the current regulator, located inside the drive scheme of Figure 4.14.

current references are obtained from the MTPA trajectory can be successfully implemented since the iron losses are not of interest for the scope of this work [28].

The  $d$ - and  $q$ -axis can be decoupled by removing the influence of the back-electromotive force term  $j\omega_{me}\lambda_{dq}$ . As it can be perceived from the first two equations of (4.7), this can be achieved by adding the term  $-\omega_{me}\lambda_q$  at the output of the  $d$ -axis PI and the term  $\omega_{me}\lambda_d$  at the output of the  $q$ -axis PI. The values of  $\lambda_d$  and  $\lambda_q$  comes from the two LUTs shown in Figure 4.17, whose values originate from the same measurements previously mentioned. In this way, the voltage references at the output of the current regulators become:

$$\begin{cases} u_d^* = R_s i_d + \frac{d\lambda_d}{dt} \\ u_q^* = R_s i_q + \frac{d\lambda_q}{dt} \end{cases} \quad (4.32)$$

The regulators can be therefore tuned as if the system was linear and the axis decoupling results in the achieved equal bandwidth of the  $d$ - and  $q$ -axis current regulators, with a consequent considerable decrease in current ripple [28].

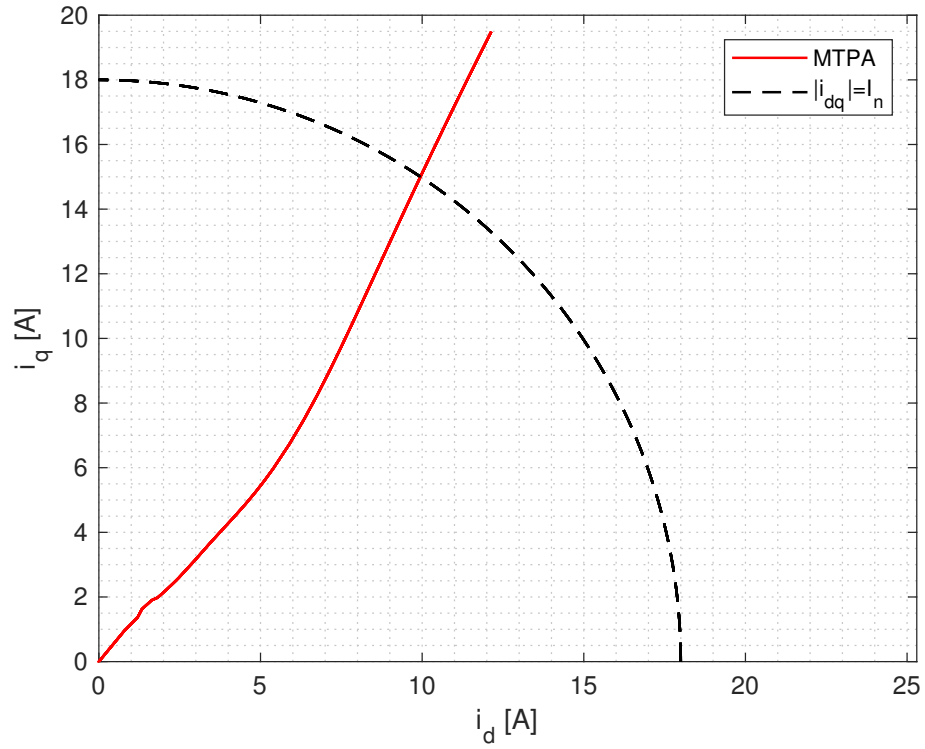


Figure 4.16. Calculated MTPA trajectory for the 11-kW SynRM.

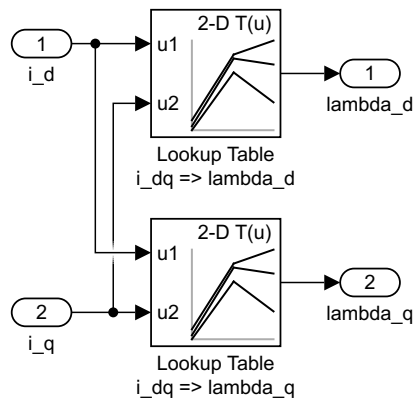


Figure 4.17. Flux linkages calculation block, located in the current regulator block of Figure 4.15.

The rise time of the current has been set to  $T_{ri} = 0.7 \text{ ms}$ , so that the current regulator bandwidth results in:

$$\alpha_c = \frac{\ln 9}{T_{ri}} \quad (4.33)$$

The current regulators gains can be thus firstly calculated as:

$$\begin{cases} k_{pd} = \alpha_c L_d \\ k_{pq} = \alpha_c L_q \\ k_{id} = \alpha_c^2 L_d \\ k_{iq} = \alpha_c^2 L_q \end{cases} \quad (4.34)$$

where, as noticeable from Figure 4.18, for the incremental inductances calculation the LUTs are again exploited. The corrective factors  $k_{kpd}$ ,  $k_{kid}$ ,  $k_{kpq}$  and  $k_{kiq}$  have then been tuned, aiming to achieve the fastest response in both the axis and allowing an overshoot lower than 10% of the reference for all the range of current reference.

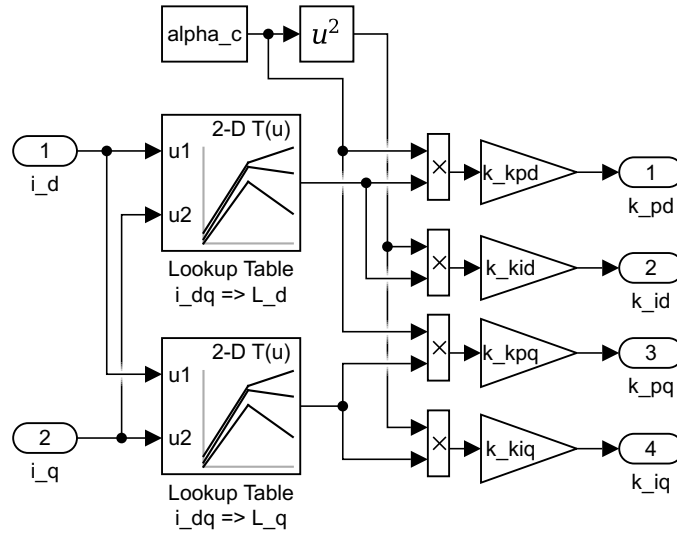


Figure 4.18. PI regulator gains calculation block, located in the current regulator block of Figure 4.15.

As described in [33], the use of LUTs in control algorithms to take into account the magnetic saturation is a much simpler solution compared to others

like the online parameter estimation or the use of explicit functions. On the other hand, it requires a large amount of measurements and memory, its operation range is limited by the measurements and its discontinuous nature may be troublesome with respect to the interpolation of the measured points. Furthermore, in the implemented control, the inputs of the LUTs are decided to be the current references instead of the measured or estimated currents, reducing thus the oscillations in the system behaviour.

The voltage saturation has been applied in the right side of the scheme in Figure 4.15. The concept behind is that, if the magnitude of the reference voltage vector  $u_{dq}^*$  is greater than the maximum voltage vector that can be provided by the converter, whose amplitude is  $U_{dc}/\sqrt{3}$ , then the reference voltage vector amplitude is reduced to  $U_{dc}/\sqrt{3}$ . In the other case, it is not changed and the vector references given to the converter are the same obtained from the two axis PI regulators. The benefit of this implementation is that the voltage reference vector phase in the  $dq$  frame is not altered in saturation conditions.

Since voltage saturation is taken into account, an antiwindup acting on the integral part of the regulators is needed. It consists in switching off the integral whenever voltage saturation occurs, so that the systems works like a simple proportional regulator and no error in the integrator is accumulated. The delay block is necessary in order to prevent an algebraic loop in the simulations and resembles a practical implementation in a microprocessor.

The method used for integration in the discrete domain has been decided to be the trapezoidal one, with a sample time equal to  $T_c$ .

Lastly, no flux weakening control has been implemented, because it was not of interest for the scope of this work.

All the current regulator parameters are reported in Table 4.5.

Parameter	Parameter value
$T_{ri}$	0.7 ms
$\alpha_c$	3 139 rad/s
$k_{kpd}$	1.2
$k_{kid}$	0.04
$k_{kpdq}$	1
$k_{kidiq}$	0.01

Table 4.5. Current regulator parameters.

### 4.3.3 Speed regulator

The speed regulator scheme is shown in Figure 4.19. Its bandwidth, as described in [32], has been set 10 times lower than the current regulator bandwidth:

$$\alpha_s = 0.1\alpha_c \quad (4.35)$$

The proportional and the integral gains have been firstly calculated as:

$$\begin{cases} k_{ps} = \frac{\alpha_s J}{0.9\lambda_{base}} \\ k_{is} = \frac{\alpha_s^2 J}{0.9\lambda_{base}} \end{cases} \quad (4.36)$$

where  $J$  is the motor inertia and the base flux  $\lambda_{base}$  is by definition:

$$\lambda_{base} = \frac{V_{base}}{\omega_{base}} = \frac{400 V}{3000 \frac{\pi}{30} \text{ rad/s}} \quad (4.37)$$

The torque reference has been saturated to the nominal torque value  $T_n$  and an antiwindup similar to the one described for the current controller has been implemented. The system has been eventually tuned and the speed regulator parameters are presented in Table 4.6.

Parameter	Parameter value
$\alpha_s$	313.9 rad/s
$k_{ps}$	0.958 Nm/rad/s
$k_{is}$	60.14 Nm/rad/s

Table 4.6. Speed regulator parameters.

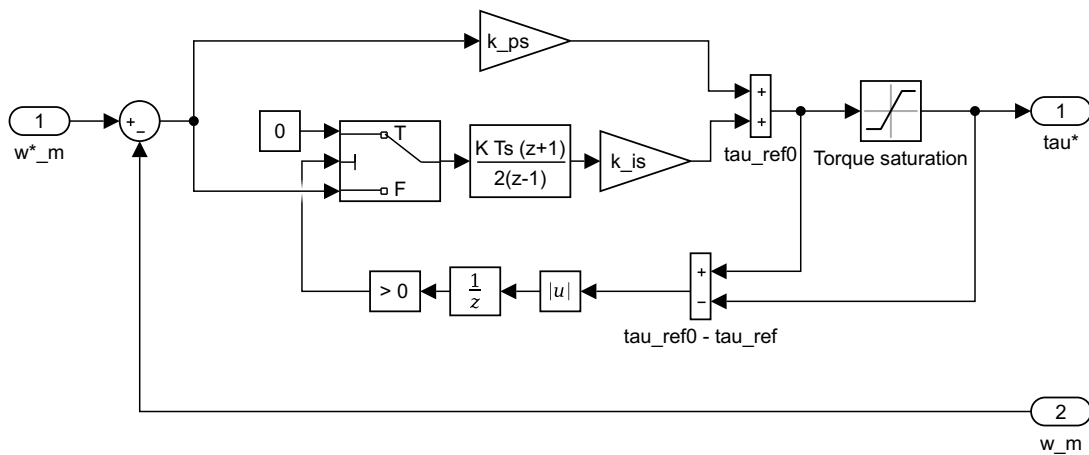


Figure 4.19. Simulink model of the speed regulator, located inside the drive scheme of Figure 4.14.

## 4.4 Intrinsic injection sensorless control model

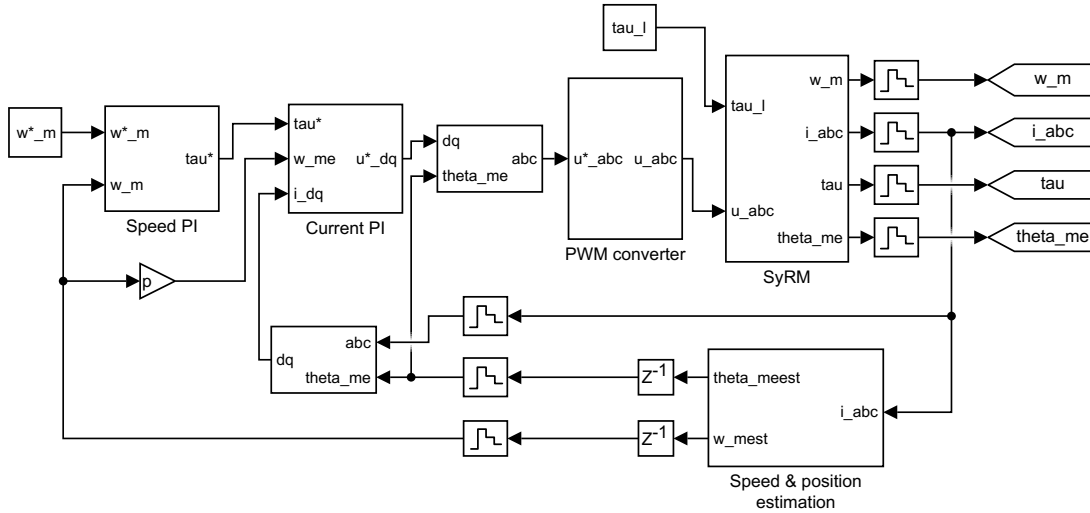


Figure 4.20. Simulink model of the drive with the implementation of the speed estimator.

In this Section, the Simulink model of the intrinsic injection sensorless control is illustrated. The proposed alternatives 1, 2 and 3 are described in Subsection 4.4.1, 4.4.3 and 4.4.4 respectively, while in Subsection 4.4.2 the current PLL and ripple calculator block is presented.

The Simulink model of the drive making use of the speed estimator is displayed in Figure 4.20.

### 4.4.1 Estimator alternative 1

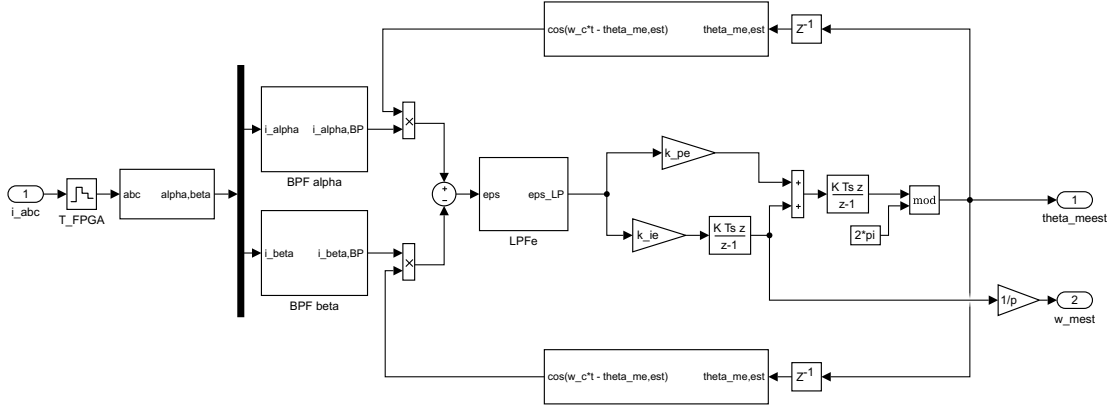


Figure 4.21. Simulink model of the alternative 1 proposed for the speed and position estimator, located inside the sensorless drive scheme of Figure 4.20.

Figure 4.21 displays the Simulink model of the first proposed alternative for the intrinsic injection based speed and position estimator. It is the most similar scheme to the one proposed in [1] and [2], with the only difference that no BPF has been inserted at the output of the demodulation terms  $\cos(\omega_{ct} + \hat{\theta}'_{me})$  and  $\sin(\omega_{ct} + \hat{\theta}'_{me})$ . As mentioned in Subsection 3.2.3, their presence is justified in [18] by a need for compensation for the effects of the filters applied on the currents. In this work, instead, it has been preferred to avoid the introduction of further delays, to avoid the increases in the complexity of the calculation and, being the frequency of this two terms variable, to avoid the trade-off between a decrease in the magnitude of the demodulation term with a fixed centre frequency BPFs and the choice of the implementation of more complicated variable centre frequency BPFs.

In this estimator alternative, as well as in [1] and [2], it has been decided to make use of BPFs centred around the first carrier frequency, in order to isolate the  $i_{\alpha\beta}$  harmonic components of interest, relative to the carrier index  $m = 1$  and the sideband indexes  $n = \pm 1$ . With this goal, the BPF Quality Factor  $Q$  has been chose in such a way that the filter band is reasonably large. As mentioned in 3.2.3 regarding the required filtering actions, the decrease in magnitude of the higher  $n$  indexes sideband harmonics is achieved at the cost of a slight reduction of the harmonic components needed for the estimation. Considered the symmetry of a BPF and the relationship  $f_{1,n} = f_c \pm n.f_{me}$  regarding the frequency of the harmonics of interest, moreover, the higher is

the motor speed, the higher is this reduction.

In 4.21, it is noteworthy how the input phase currents, measured at the the sampling frequency  $f_s = 0.5 \text{ MHz}$ , are further oversampled at at the higher frequency  $f_{FPGA} = 2 \text{ MHz}$ , which is the frequency at which the speed and position estimates are updated. The reason why the used subscript is "FPGA" is that this estimator has been supposed to be implemented on a Xilinx FPGA Virtex 6 platform, within a OPAL-RT OP5600 system [34]. The benefit of this process, which can be defined "fake oversampling", is the enhancement of the estimator performance without the demand for an higher sampling frequency of the current, which would result in higher costs or at the difficulty to find on the market devices able to measure currents with frequencies in the range  $1 \div 10 \text{ MHz}$ . The choice for the  $2 \text{ MHz}$  frequency has been suggested for a traditional sensorless control in [22]. As it comes out from simulation run in Section 5.6, this would be equivalent to increase the current sampling frequency to  $f_s = 2 \text{ MHz}$ .

For the implementation of both the BPF and the LPF, second order remapped Butterworth filters have been chosen [35].

The analog LPF transfer function is calculated from a second order normalized Butterworth LPF mapped into a LPF:

$$H_{LPF}(s) = \frac{\omega_{lc}^2}{s^2 + \sqrt{2}\omega_{lc} \cdot s + \omega_{lc}^2} \quad (4.38)$$

where  $\omega_{lc}$  is LPF cut-off frequency. The equivalent discrete transfer function is calculated through the bi-linear transformation:

$$s = c \cdot \left( \frac{z - 1}{z + 1} \right) \quad (4.39)$$

where  $c$  is the frequency warping coefficient, needed for the compensation for an inherent inaccuracy in the bi-linear transformation method, which is defined as:

$$c = \cot \left( \frac{K \cdot T_{FPGA}}{2} \right) \quad (4.40)$$

where coefficient  $K$  is set equal to  $-1$  in order to make the discrete filter cut-off frequency match with the analog filter one. The discrete LPF transfer function  $H_{LPF}(z)$  can finally be expressed as:

$$H_{LPF}(z) = \frac{n_0 + n_1 z^{-1} + n_2 z^{-2}}{d_0 + d_1 z^{-1} + d_2 z^{-2}} \quad (4.41)$$

where the LPF coefficients can be calculated as:

$$\begin{cases} n_0 = \omega_{lc}^2 \\ n_1 = 2 \cdot \omega_{lc}^2 \\ n_2 = \omega_{lc}^2 \\ d_0 = \omega_{lc}^2 - \sqrt{2} \cdot c \cdot \omega_{lc} + c^2 \\ d_1 = 2 \cdot \omega_{lc}^2 - 2 \cdot c^2 \\ d_2 = \omega_{lc}^2 + \sqrt{2} \cdot c \cdot \omega_{lc} + c^2 \end{cases} \quad (4.42)$$

With regard to the LPF applied on the error  $\epsilon$ , whose cut-off frequency is defined as  $\omega_{lce}$ , the subscript "e" is added to the coefficients expressions in (4.42). Its Simulink scheme is displayed in Figure 4.22.

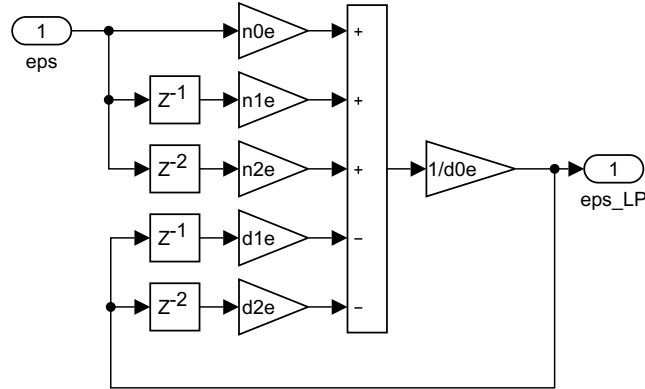


Figure 4.22. Simulink model of the variable cut-off frequency  $\omega_{lce}$  LPF applied on  $\epsilon$ , located inside the estimator alternative 1 of Figure 4.21, alternative 2 (Figure 4.27) and alternative 3 (Figure 4.28) schemes. Discrete transfer function displayed in (4.41) and coefficients defined in (4.42).

Regarding the choice of  $\omega_{lce}$ , as explained in Equation 3.20, the aim of LPF is to cut the components present in  $\epsilon$  at the frequency  $2\omega_c = 16\,000 \cdot 2\pi$ . Since the estimated position and speed depend from  $\epsilon$  through a PI regulator, their dynamics are strictly related to the error harmonic content. The choice of the LPF cut-off frequency is therefore dictated by a trade-off between that of a really fast system, in which the estimates are very noisy, or that of a slower system, in which the noise in the estimates is decreased. Hence, for the alternative 1 of the estimator,  $\omega_{lce}$  has been chosen equal to  $200 \cdot 2\pi \text{ rad/s}$ . The analog BPF transfer function is calculated from a first order normalized

Butterworth LPF mapped into a BPF:

$$H_{BPF}(s) = \frac{DF \cdot s}{s^2 + DF \cdot s + \omega_{cc}^2} \quad (4.43)$$

where  $\omega_{cc}$  is the BPF centre frequency and  $DF$  is the Depth Factor. The inverse value of  $DF$ :

$$Q = \frac{1}{DF} \quad (4.44)$$

is defined Quality Factor. The reason that makes that kind of filter expression appreciable is that, just by varying  $Q$ , it is possible to modify the bandwidth of the filter [7]. As shown in Figure 4.23, for low values of  $Q$  the BPF results wide and, on the other way around, for high values of  $Q$  the BPF results narrow. Furthermore, also the phase delay and the magnitude reduction ratios are dependent from  $Q$ .

The equivalent BPF discrete transfer function  $H_{BPF}(z)$  is derived with the same procedure valid for the LPF and can be expressed as:

$$H_{LPF}(z) = \frac{n_0 + n_1 z^{-1} + n_2 z^{-2}}{d_0 + d_1 z^{-1} + d_2 z^{-2}} \quad (4.45)$$

where the BPF coefficients can be calculated as:

$$\begin{cases} n_0 = -DF \cdot c \\ n_1 = 0 \\ n_2 = DF \cdot c \\ d_0 = \omega_{cc}^2 - DF \cdot c + c^2 \\ d_1 = 2 \cdot \omega_{cc}^2 - 2 \cdot c^2 \\ d_2 = \omega_{cc}^2 + DF \cdot c + c^2 \end{cases} \quad (4.46)$$

The BPF Simulink scheme is displayed in Figure 4.24.

With regards to the BPF parameters,  $\omega_{cc}$  has been chosen equal to  $2\pi \cdot f_c = 2\pi \cdot 8000 \text{ rad/s}$  and the Quality Factor  $Q$  equal to 0.05.

The last blocks to describe are the ones relative to the demodulation terms. With reference to the cosine signal, whose computation scheme is shown in Figure 4.25, the  $\omega_c t$  term has been modelled as a ramp wrapped to  $0 \div 2\pi$  at the frequency  $f_c$ .

The tuning of the PI regulator has led to the choice of the following gains:

$$\begin{cases} k_{pe} = 80000 \frac{\text{rad}}{\text{As}} \\ k_{ie} = 3000000 \frac{\text{rad}}{\text{As}^2} \end{cases} \quad (4.47)$$

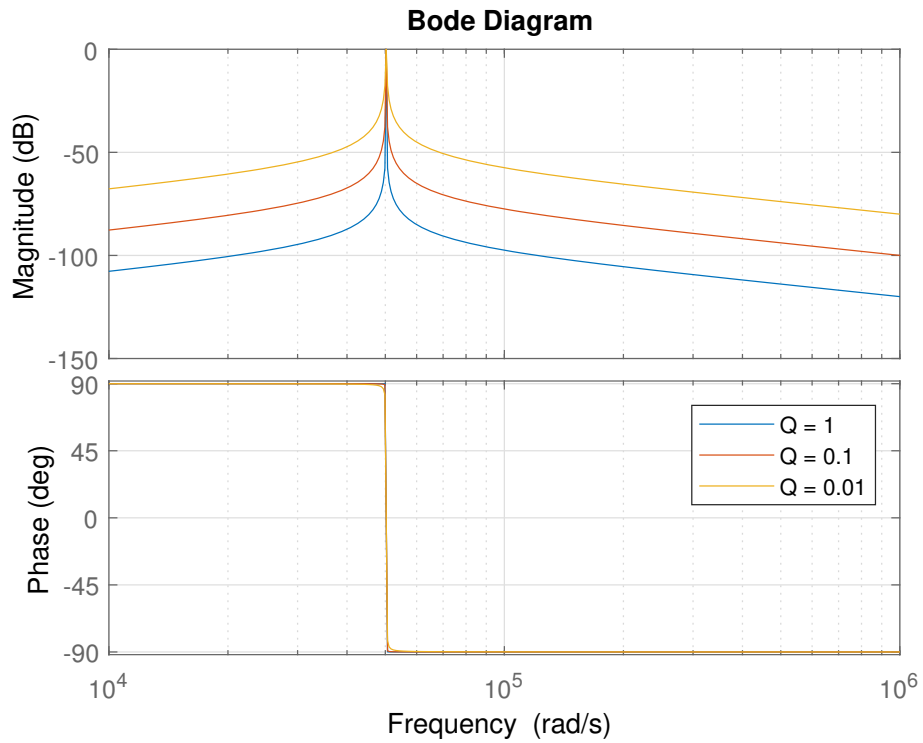


Figure 4.23. Influence of the Quality Factor  $Q$  on the Bode plots of the digital BPF, for a BPF centre frequency  $\omega_{cc} = 2\pi f_c$

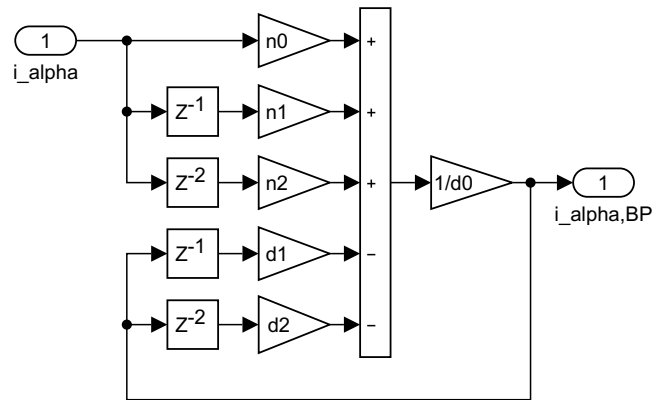


Figure 4.24. Simulink model of the BPF applied on  $i_{\alpha}$ , located inside the estimator alternative 1 scheme of Figure 4.21.



- it is possible to avoid the  $i_{\alpha\beta}$  filtering in order to decrease calculation complexity and delays and at the cost of an impoverishment of the signal-to-noise ratio and the presence of fundamental frequency harmonics in the estimates of the speed and position;
- it is possible to enhance the significance of the filtering actions with variable centre frequency BPFs, involving, on the other way around, an increase of the signal-to-noise ratio at the cost of larger calculation complexity and delays.

The first consideration brings to the estimator alternative 2, depicted in Subsection 4.4.3, while the second one brings to the estimator alternative 3, depicted in Subsection 4.4.4. Both of the two approaches are achieved thanks to the implementation of the block defined PLL and ripple calculator, which is displayed in Figure 4.26. It is composed by two main parts: the current PLL and the current ripple calculator.

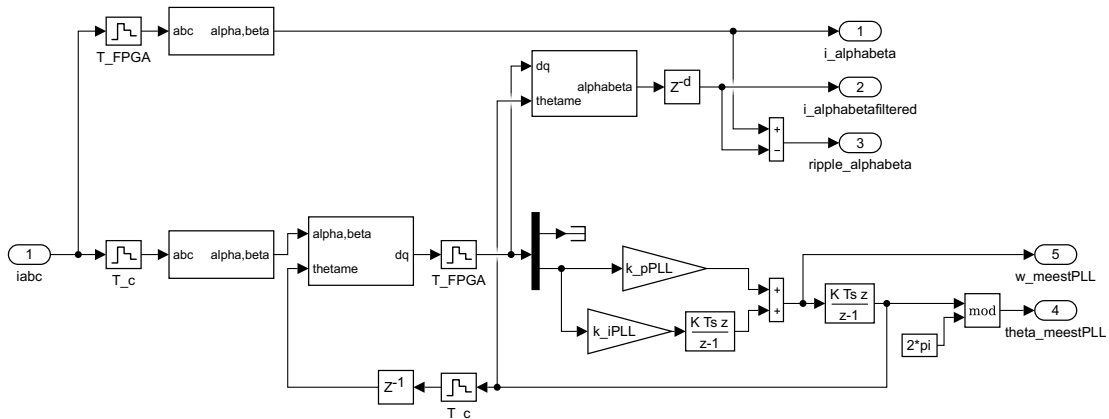


Figure 4.26. Simulink model of the current PLL (bottom) and ripple calculator (top), located inside the estimator alternative 2 of Figure 4.27 and alternative 3 of Figure 4.28 schemes.

The current PLL (Phase-Locked-Loop) is performed in the bottom part of the scheme of Figure 4.26. A PLL is a control system consisting of a closed-loop non-linear PI regulation that nullifies the phase difference between the input signal and estimated one, resulting in the estimation of the phase and of the rotational speed of the input signal [32]. In this case, the input signal is the current vector. The estimate of its phase coincides with an angle which is equivalent to the electrical position  $\theta_{me}$  added by the angle of the

estimated current vector in the estimated  $dq$  reference frame. From its information, however, it is not possible to estimate  $\theta_{me}$ . The estimate of its angular speed, instead, in steady state conditions, since current vector phase is constant, can directly provide the estimation of the electrical speed  $\omega_{me}$ . In Figure 4.26, first, the phase currents received as inputs by the PLL are undersampled at the frequency  $f_c = 8 \text{ kHz}$ , in order to remove the ripple caused by the PWM modulation and to take into account just the fundamental current harmonic, carrying the information needed by the PLL, but also some low frequency baseband harmonics. The PLL, however, has to work at the frequency  $f_{FPGA}$  at which the rest of the estimator is working. The information extractable from the PLL useful for the scope of this work is therefore the signal  $\hat{\omega}_{me}^{PLL}$ , from which the centre frequencies of the variable BPFs can be placed to:

$$\omega_{cc} = 2\pi \left( f_c \pm \hat{f}_{me}^{PLL} \right) \quad (4.48)$$

in order to follow the two sought current harmonics relative to the carrier index  $m = 1$  and the sideband indexes  $n = \pm 1$ . This solution will be implemented in the estimator alternative 3.

The current ripple calculation is performed in the top part of the scheme of Figure 4.26. The phase currents are oversampled, in parallel to the PLL, at the frequency  $f_{FPGA}$ , obtaining the same  $i_{\alpha\beta}$  used as input for the BPFs in the estimator alternative 1 of Figure 4.21. These currents are subtracted by their undersampled version, which carry just the fundamental current harmonic together with the baseband harmonics at the fundamental frequency. Hence, it is possible to extract the current ripple, which contains the carrier multiples with their sideband harmonics and from which it is possible to extract the speed and position information. Therefore, in the estimator alternative 3 this current ripple  $\Delta i_{\alpha\beta}$  is used in the estimator without the usage of any BPF.

The reason why it is desirable to get rid of the fundamental current component is that its magnitude is generally higher than any other current harmonic and, excluding further filtering actions on the  $\alpha\beta$  current signals, they cannot be successfully filtered neither by the LPF applied on  $\epsilon$ , neither by added LPF applied on  $\hat{\theta}_{me}$ .

Lastly, it is important to highlight that, since the currents sampled at the frequency  $f_c$  are subject to rotational transformations  $\alpha\beta$  to  $dq$  and on the other way around  $dq$  to  $\alpha\beta$  which make usage of the PLL estimated angle  $\hat{\theta}_{me}^{PLL}$ , the ripple calculation is consequently affected by the presence of the current PLL.

The PLL tuning has lead to the choice for the gains of the PLL regulator shown in Table 4.8.

Parameter	Parameter value
$k_p^{PLL}$	$8 \text{ rad/As}$
$k_i^{PLL}$	$1000 \text{ rad/As}^2$

Table 4.8. PLL regulator gains.

### 4.4.3 Estimator alternative 2

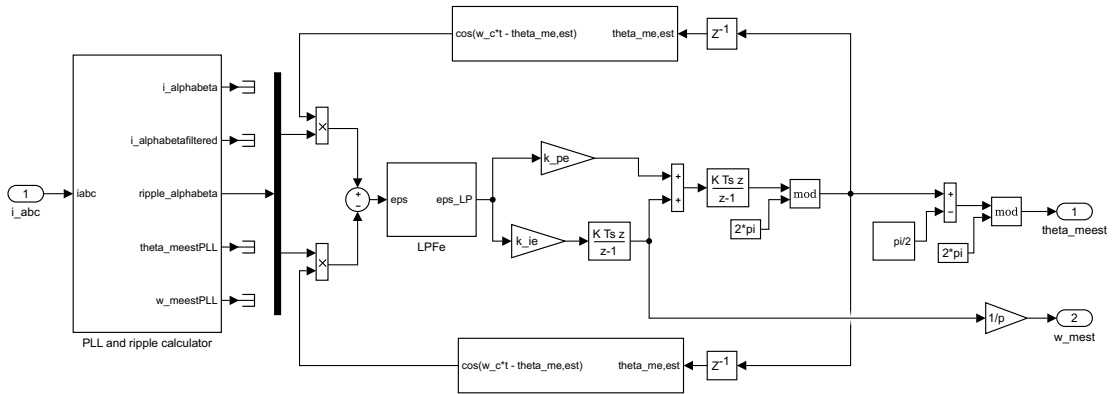


Figure 4.27. Simulink model of the alternative 2 proposed for the speed and position estimator, located inside the sensorless drive scheme of Figure 4.20.

In Figure 4.27 it is displayed the Simulink model of the second alternative proposed for the intrinsic injection based speed and position estimator. As mentioned in Subsection 4.4.2, this scheme does not entail any filtering actions on the  $\alpha\beta$  current signals and it receives as inputs the current ripple  $\Delta i_{\alpha\beta}$  calculated by the current PLL and ripple calculator.

All the blocks of the scheme are described in Subsection 4.4.1. The only adjustment is the  $\pi/2$  phase delay introduced in the angle estimate  $\hat{\theta}_{me}$ . This delay has turned out to be necessary when the current ripple  $\Delta i_{\alpha\beta}$  is used for the estimations. In the simulations, since both the true electrical angle  $\theta_{me}$

and its not-delayed estimate are initialized to zero, in order not to initiate the estimator with a  $\pi/2$  offset on the estimated electrical position (incorrect at the motor start in the simulations), the  $\pi/2$  phase delay is provided with a time ramp. The value for this time ramp has been chosen equal to 0.2 s for all the simulations.

The modelling choices and the tuned parameters values are summarized in 4.9.

Block	Presence and description
$i_{\alpha\beta}$ filtering	BPF not present
LPF on $\epsilon$ order	2nd order
$\hat{\omega}_{me}$ filtering	LPF not present
Current PLL signal	$\Delta i_{\alpha\beta}$
Parameter	Parameter value
$\omega_{lce}$	$50 \cdot 2\pi \text{ rad/s}$
$\omega_{cc}$	BPFs not present
$Q$	BPF not present
$k_{pe}$	$800 \text{ rad/As}$
$k_{ie}$	$60\,000 \text{ rad/As}^2$
$k_p^{PLL}$	$8 \text{ rad/As}$
$k_i^{PLL}$	$1000 \text{ rad/As}^2$
$\hat{\theta}_{me}$ delay	$\pi/2 \text{ rad}$

Table 4.9. Estimator alternative 2 modelling choices and parameters values.

#### 4.4.4 Estimator alternative 3

Figure 4.28 displays the Simulink model of the third and last alternative proposed for the intrinsic injection based speed and position estimator. As mentioned in Subsection 4.4.2, it makes usage of the electrical speed estimated by the PLL  $\hat{\omega}_{me}^{PLL}$  to vary the centre frequency of the BPF applied on the current components  $i_{\alpha\beta}$ , which are instead not affected by the PLL presence. With this goal, the BPF Quality Factor  $Q$  has been increased compared to the estimator alternative 1 in such a way that the filter band results narrower.

The variable centre frequency BPF Simulink model is displayed in Figure

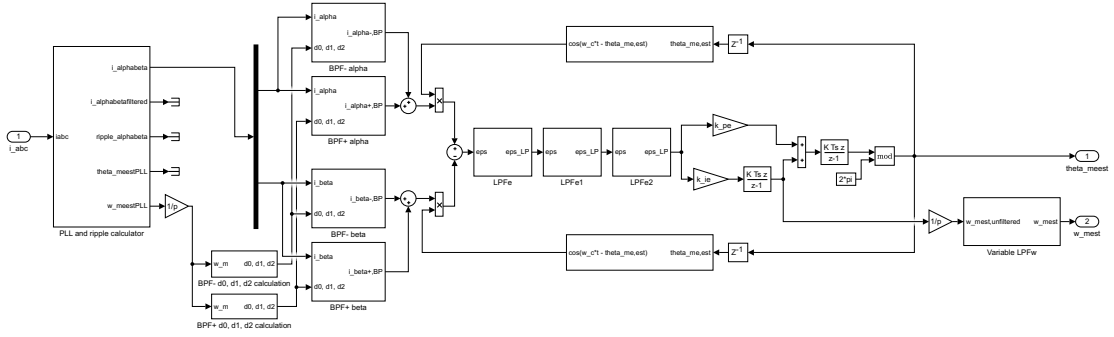


Figure 4.28. Simulink model of the alternative 3 proposed for the speed and position estimator, located inside the sensorless drive scheme of Figure 4.20.

4.29. On the left side, the denominator discrete parameters calculations are implemented, which are the only speed-varying parameters and whose definition is made explicit in (4.46). On the right side, instead, the discrete BPF transfer function of Equation 4.45 is implemented.

In the third alternative, a higher cut-off frequency for the LPF applied on  $\epsilon$  has been chosen. This has firstly implied the increase of the LPF order to the sixth order. In addition, considered the higher harmonic content in the estimated speed,  $\hat{\omega}_{me}$  has been low-pass filtered with a variable cut-off frequency  $\omega_{lcw}$  with the following expression:

$$\omega_{lcw} = 10 \cdot 2\pi + \hat{\omega}_{me} \quad (4.49)$$

This has turned out necessary because the aim of this filter is to eliminate the multiples of the fundamental harmonic, whose frequencies at the nominal speed of the two-poles machine are equal to 100, 200, 300...  $Hz$ . A 10  $Hz$  offset has been added in order not to have lowest bandwidths at low speed and ideally zero bandwidth at zero speed. The LPF Simulink model is displayed in Figure 4.30 and it is implemented from Equations (4.41), (4.42) and (4.49).

The modelling choices and the tuned parameters values are summarized in Table 4.10.

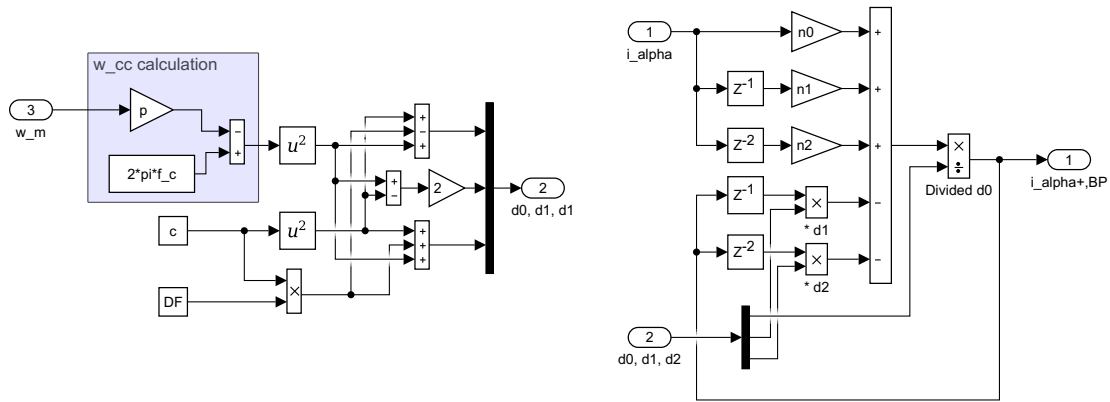


Figure 4.29. Simulink model of the variable centre frequency  $\omega_{cc}$  BPF applied on the  $m = 1$  and  $n = -1$  indexes  $i_\alpha$  current component, located inside the estimator alternative 3 scheme of Figure 4.28.

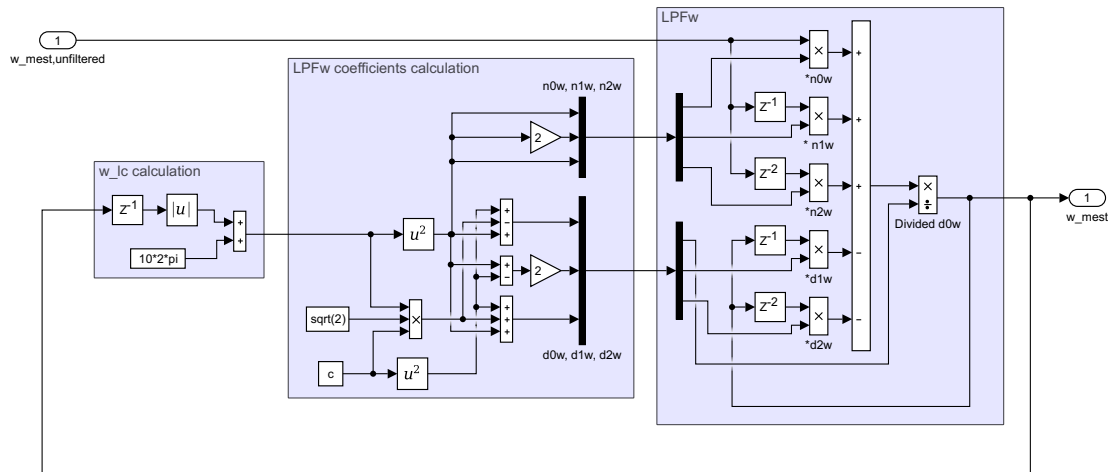


Figure 4.30. Simulink model of the variable cut-off frequency  $\omega_{lcw}$  LPF applied on  $\hat{w}_{me}$ , located inside the estimator alternative 3 scheme of Figure 4.28.

Block	Presence and description
$i_{\alpha\beta}$ filtering	Variable $\omega_{cc}$ BPF
LPF on $\epsilon$ order	6th order
$\hat{\omega}_{me}$ filtering	Variable $\omega_{lcv}$ LPF
Current PLL signal	$\hat{\omega}_{me}^{PLL}$
Parameter	Parameter value
$\omega_{lce}$	$500 \cdot 2\pi \text{ rad/s}$
$\omega_{cc}$	$2\pi (f_c \pm \hat{f}_{me}^{PLL})$
$Q$	$0.2 \text{ s}$
$k_{pe}$	$20\,000 \text{ rad/As}$
$k_{ie}$	$2\,500\,000 \text{ rad/As}^2$
$k_p^{PLL}$	$8 \text{ rad/As}$
$k_i^{PLL}$	$1000 \text{ rad/As}^2$
$\hat{\theta}_{me}$ delay	Not necessary

Table 4.10. Estimator alternative 3 modelling choices and parameters values.

## 4.5 Parameter values

Table 4.11 reports all the drive model parameters and in Table 4.12 the three estimator parameters together with the respective modelling choices are summarized. In Figure 4.31, the differences between the three proposed estimator alternatives are summarized.

It has to be remarked that the speed regulator bandwidth has to be decreased in order to reach a feasible estimator operation. The chose of this parameter, as it will be pointed out in Sections 5.4 and 5.5, has been chosen equal to 50  $rad/s$  for open-loop simulations and 30  $rad/s$  for closed-loop simulations.

Parameter	Parameter value
$V_n$	400 $V$
$I_n$	18 $A$
$n_{mn}$	3000 $rpm$
$\tau_n$	17 $Nm$
$p$	2
$R_s$	0.72 $\Omega$
$J$	0.00351 $kgm^2$
$L_d, L_q$	LUTs
$U_{dc}$	560 $V$
$f_c$	8 $kHz$
$T_{ri}$	0.7 $ms$
$\alpha_c$	3 139 $rad/s$
$k_{pd}, k_{id}, k_{pq}, k_{iq}$	LUTs
$\alpha_s$	50 or 30 $rad/s$
$k_{ps}$	0.153 or 0.0915 $Nm/rad/s$
$k_{is}$	1.50 or 0.549 $Nm/rad/s$

Table 4.11. Drive and control model parameters.

Block	Presence and description		
	Alternative 1	Alternative 2	Alternative 3
$i_{\alpha\beta}$ filtering LPF on $\epsilon$ order $\hat{\omega}_{me}$ filtering Current PLL signal	BPF centred in $f_c$ 2nd order LPF not present PLL not present	BPF not present 2nd order LPF not present $\Delta i_{\alpha\beta}$	Variable $\omega_{cc}$ BPF 6th order Variable $\omega_{lcw}$ LPF $\hat{\omega}_{me}^{PLL}$
Parameter	Parameter value		
	Alternative 1	Alternative 2	Alternative 3
$\omega_{lce}$	$200 \cdot 2\pi \text{ rad/s}$	$50 \cdot 2\pi \text{ rad/s}$	$500 \cdot 2\pi \text{ rad/s}$
$\omega_{cc}$	$2\pi \cdot 8000 \text{ rad/s}$	BPFs not present	$2\pi \cdot (f_c \pm \hat{f}_{me}^{PLL})$
$Q$	0.05 s	BPF not present	0.2 s
$k_{pe}$	80 000 rad/As	800 rad/As	20 000 rad/As
$k_{ie}$	3 000 000 rad/As <sup>2</sup>	60 000 rad/As <sup>2</sup>	2 500 000 rad/As <sup>2</sup>
$k_p^{PLL}$	PLL not present	8 rad/As	8 rad/As
$k_i^{PLL}$	PLL not present	1000 rad/As <sup>2</sup>	1000 rad/As <sup>2</sup>
$\hat{\theta}_{me}$ delay	Not necessary	$\pi/2 \text{ rad}$	Not necessary

Table 4.12. Modelling choices and parameters for the three estimator alternatives.

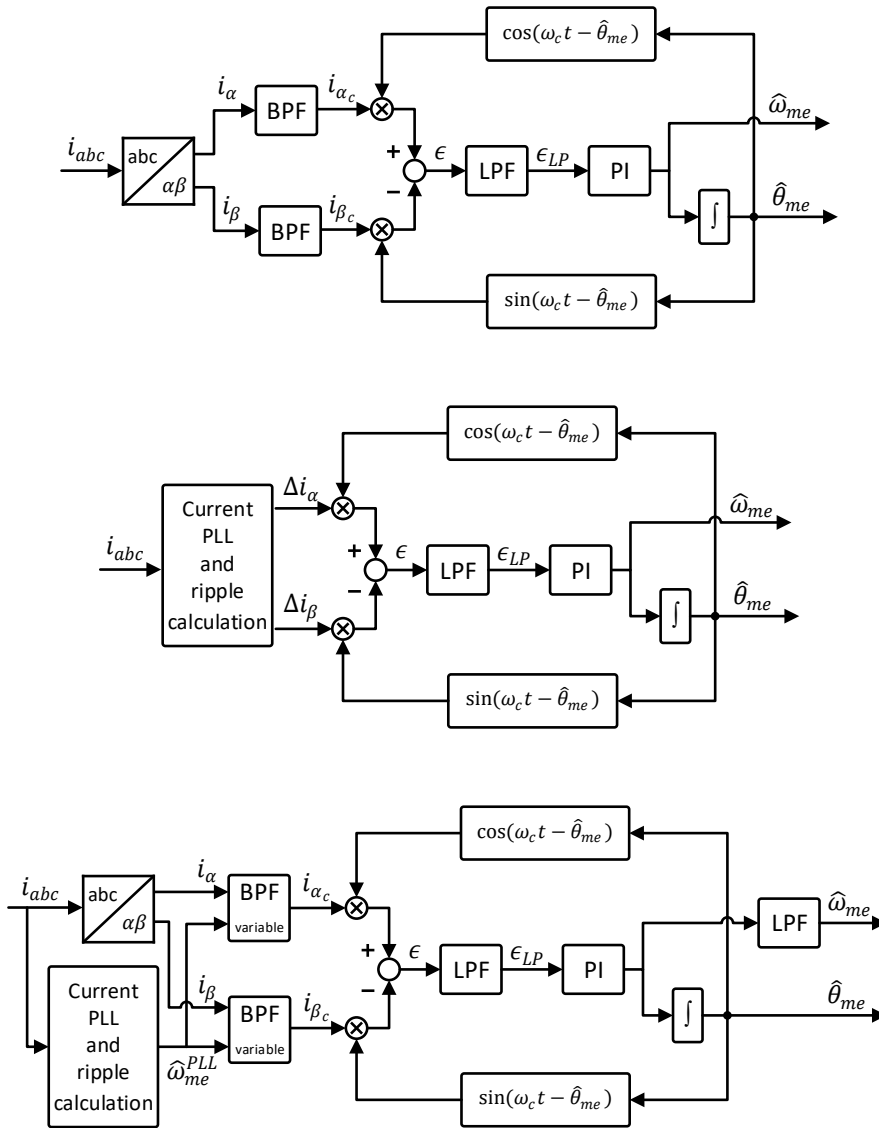


Figure 4.31. Schematic of the alternative 1 (top), alternative 2 (centre) and alternative 3 (bottom) proposed for the intrinsic injection based speed and position estimator.

# Chapter 5

## SIMULATIONS

### 5.1 Introduction

In this Chapter, the simulations run making use of the intrinsic injection sensorless control are presented.

Firstly, in Section 5.2, the PWM harmonic content is analysed and the most suitable modulation strategies for the implementation with the intrinsic injection sensorless control are chosen. In Section 5.3, the performance of the implemented current PLL and ripple calculator is illustrated. Therefore, in Section 5.4 and in Section 5.5, the simulations relative to the open-loop and the closed-loop operation respectively are described. In Section 5.6, then, the influence of the sampling frequency and of the introduced "fake" oversampling are investigated. In Section 5.7, the drive has been analysed with regards to a fan or pump application. Lastly, in Section 5.8, the DC-link voltage amplitude influence has been pointed out.

### 5.2 Harmonic analysis

In this Section, different simulations have been run in order to verify the modelled modulator operation. In particular, the UVMT modulator offset times and phase reference voltages are plotted in Subsection 5.2.1. Afterwards, for some modulation strategies, the spectra calculated from the simulations are compared with the ones expected from the theory in Subsection 5.2.2. Lastly, in Subsection 5.2.3, for all the eleven modulation strategies that can be implemented, the spectra are analysed in different conditions

and the most suitable harmonic components for the implementation with the intrinsic injection sensorless control are investigated.

### 5.2.1 UVMT modulation validation

Firstly, for the 8 s.r.s. modulation strategies computed thanks to the UVMT, the offset times plots together with the phase and the pole voltage references plots calculated in the model have been compared to the ones expected from the theory.

The simulations have been carried out with a switching frequency  $f_c = 8 \text{ kHz}$  and with a reference speed  $\omega_m^* = \omega_{mn}/2$  in no-load conditions.

The offset time plots are reported in Figure 5.1 and Figure 5.2, complying with what it is expected from the theory. Indeed, for the PWM Double-Edge modulation  $T_{offset}$  is constant and is equal to  $T_h/2$ , for the SVM modulation  $T_{offset}$  stands in the middle of  $T_{offset,max}$  and  $T_{offset,min}$ , which are the value respectively for DPWMMAX and DPWMMIN modulations  $T_{offset}$ , and the aforementioned  $30^\circ$  shifts between the other DPWM modulations  $T_{offset}$  can be appreciated.

The phase voltage references plots together with the phase to DC bus mid-point voltage references plots are reported in Figure 5.3 and Figure 5.4. The  $u_{an}^*$  has been calculated from the phase imaginary switching time  $T_{sa}$ , to which  $T_{offset}$  has been added and the sum has been resized to the DC bus voltage value. Here as well, the curves extracted from the simulations agree with what it is expected from the theory.

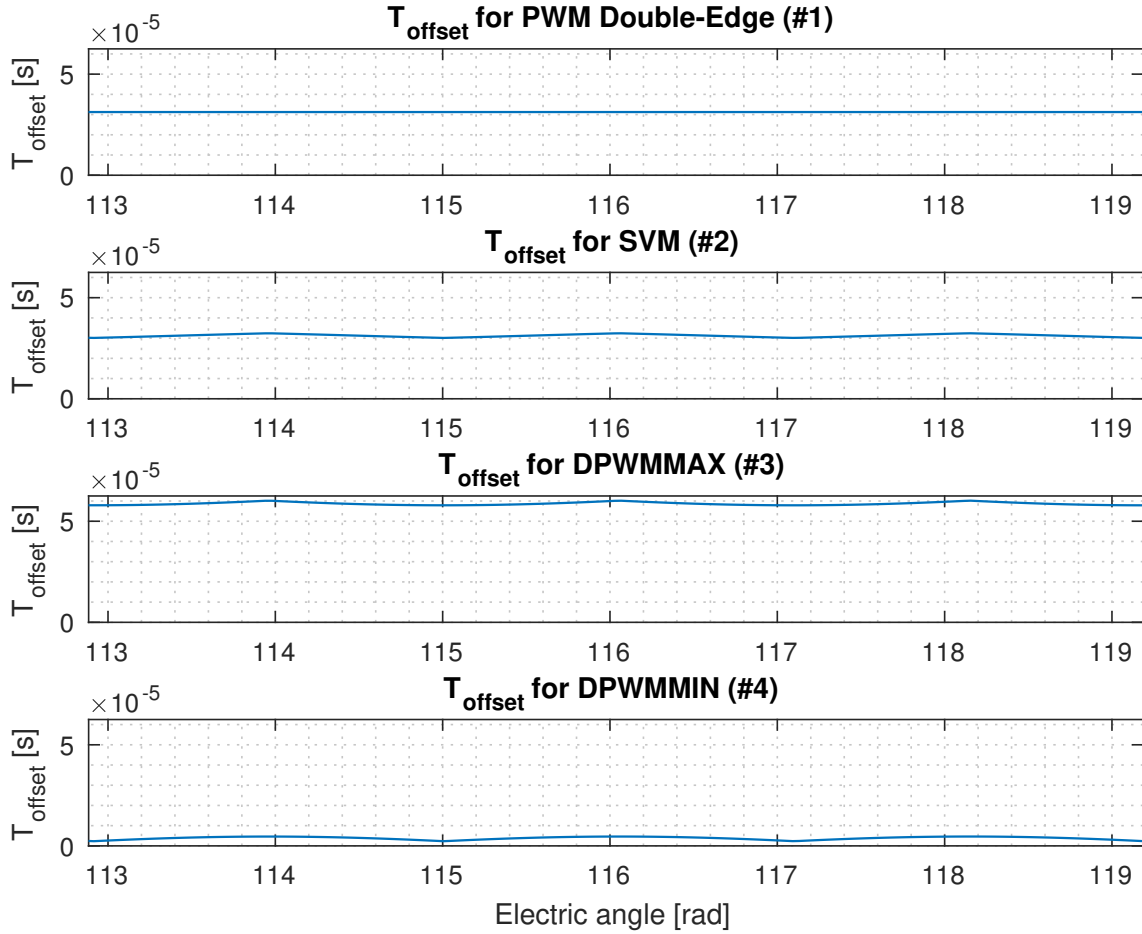


Figure 5.1. Simulated offset time plots for #1, #2, #3 and #4 modulation schemes. Horizontal axis: one electrical period in steady state conditions, for  $\omega_m^* = \omega_{mn}/2$ . Vertical axis: offset time scale from 0 to  $T_h = 62.5 \mu\text{s}$ , for  $f_c = 8 \text{ kHz}$

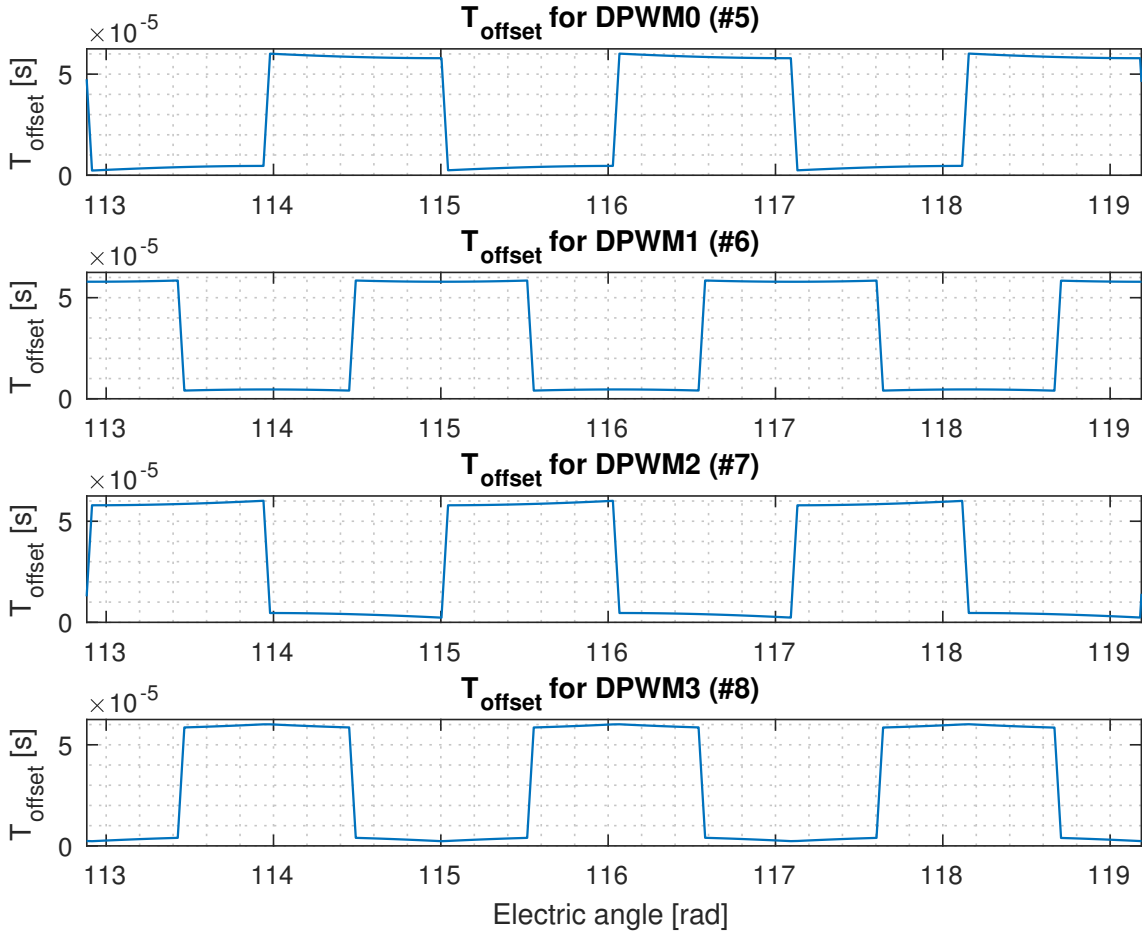


Figure 5.2. Simulated offset time plots for #5, #6, #7 and #8 modulation schemes. Horizontal axis: one electrical period in steady state conditions, for  $\omega_m^* = \omega_{mn}/2$ . Vertical axis: offset time scale from 0 to  $T_h = 62.5 \mu s$ , for  $f_c = 8 kHz$

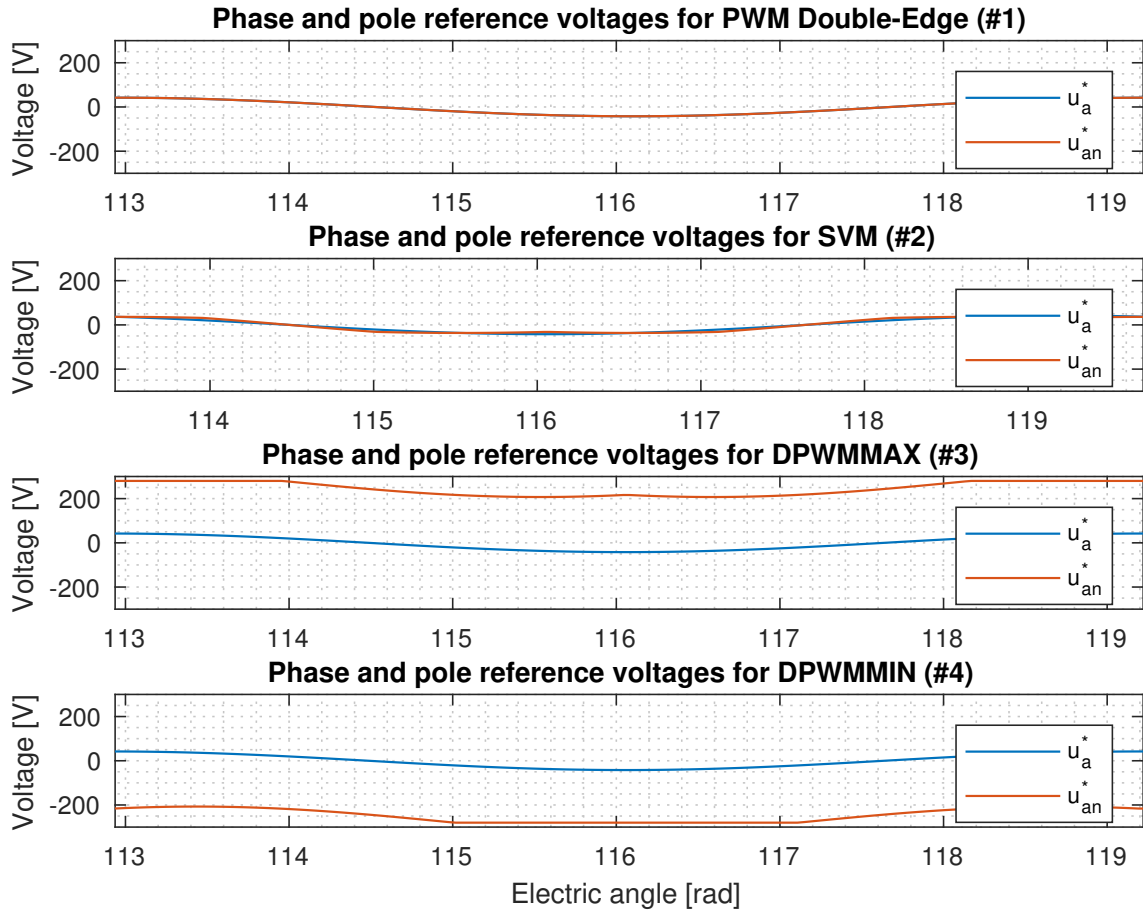


Figure 5.3. Simulated phase and pole voltage references plots for #1, #2, #3 and #4 modulation schemes. Horizontal axis: one electrical period in steady state conditions, for  $\omega_m^* = \omega_{mn}/2$ . Vertical axis: voltage scale from  $-U_{dc}/2 = -280$  V to  $U_{dc}/2 = 280$  V

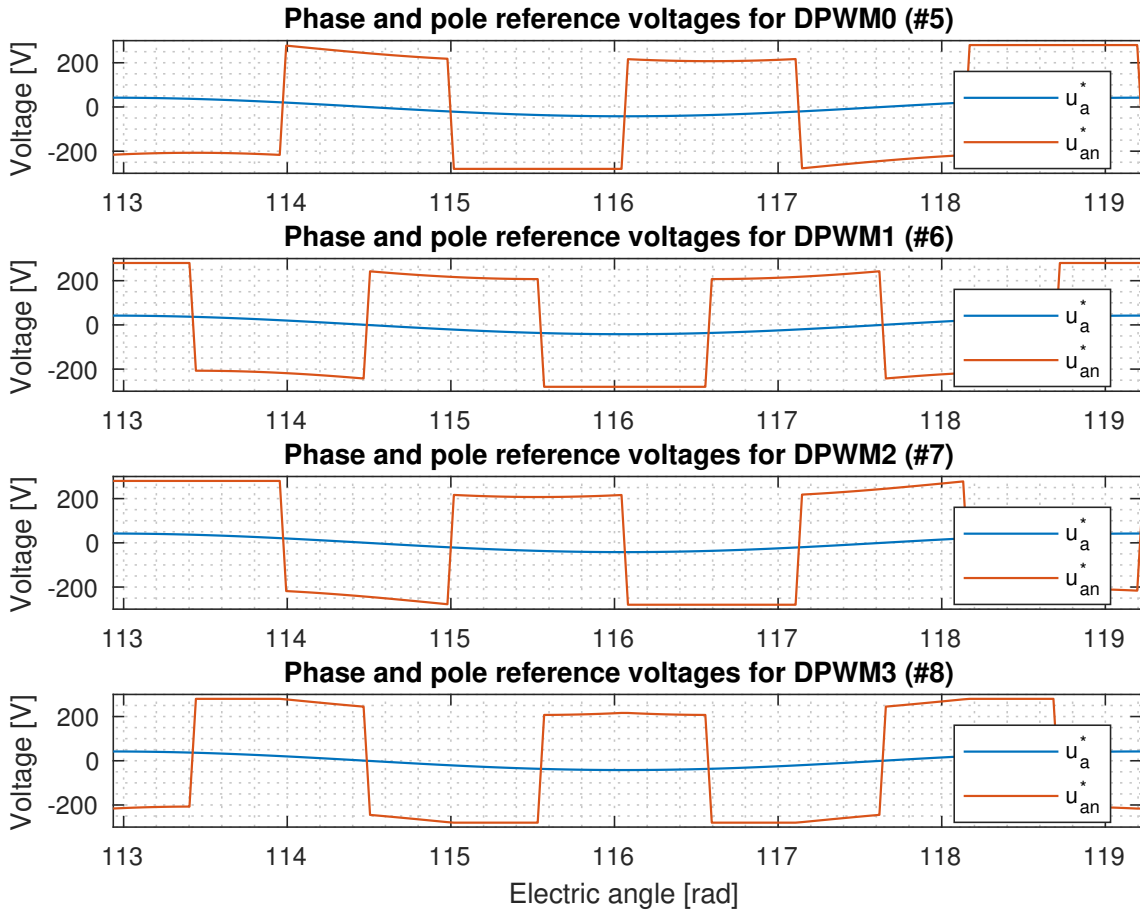


Figure 5.4. Simulated phase and pole voltage references plots for #5, #6, #7 and #8 modulation schemes. Horizontal axis: one electrical period in steady state conditions, for  $\omega_m^* = \omega_{mn}/2$ . Vertical axis: voltage scale from  $-U_{dc}/2 = -280$  V to  $U_{dc}/2 = 280$  V

### 5.2.2 Comparison of the simulation spectra with the theory

A second set of simulations has been run in order to check if the phase voltage spectra comply with what expected from the theory. These simulations concern modulations #1 and #10, #9 and #11, and #2. The analytical expressions of their complex Fourier coefficients can be found in the literature [16] and are listed in the Appendix A.1.

The results are shown from Figure 5.5 to Figure 5.9, where the comparisons between the simulated and the analytically-computed spectra are shown. For all the simulations, the reference speed for the motor has been set to its nominal value and a load torque equal to 0.4 times its nominal value has been applied.

The phase voltage spectra have been calculated with a 1-second time window, which results in a frequency resolution of 1 Hz. The signals have been windowed, in order to catch the exact harmonic content of the signals, and a flat-top window has been used, in order not to affect the signal amplitude. The complex Fourier coefficients have been calculated by setting, for each strategy, the modulation index  $M$  in order to impose the exactly same phase voltage fundamental magnitude of the respective simulation.

Looking at the graphs, the correspondence between the simulated and the theoretical spectra is satisfactory.

Regarding the PWM Double-Edge s.r.s. strategy, the modulation #10 achieved through the comparison between carrier and reference is definitely much more corresponding to the theoretical spectrum than the modulation achieved with UVMT #1, as it can be appreciated respectively from Figures 5.5 and 5.6. In particular, with the UVMT, the difference is higher for even (odd) sidebands multiple around odd (even) carrier multiples and the sideband harmonic content is much higher.

With regard to Single-Edge r.s. modulation, the spectra related to the UVMT #9 of Figure 5.8, despite the presence of an higher noise equally present throughout the all spectrum, is more fulfilling compared to the one achieved with carrier-reference #11 of Figure 5.7.

Lastly, SVM s.r.s. modulation implemented thanks to the UVMT gives a spectrum which complies really well with the one expected from the theory.

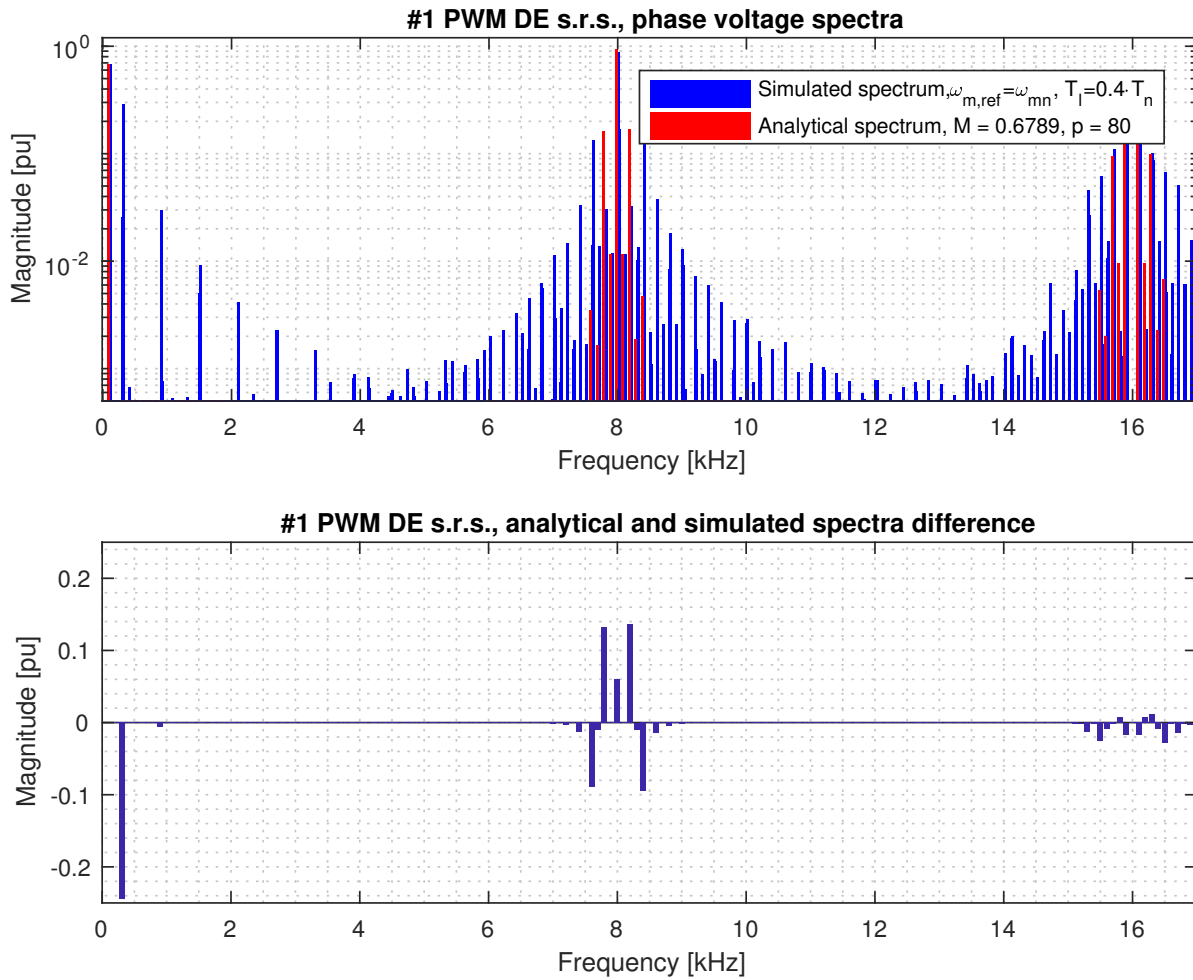


Figure 5.5. Comparison between the simulated and the analytically computed phase voltage spectra for #1 PWM Double-Edge s.r.s. modulation. Top: overlapped spectra. Bottom: magnitude difference.

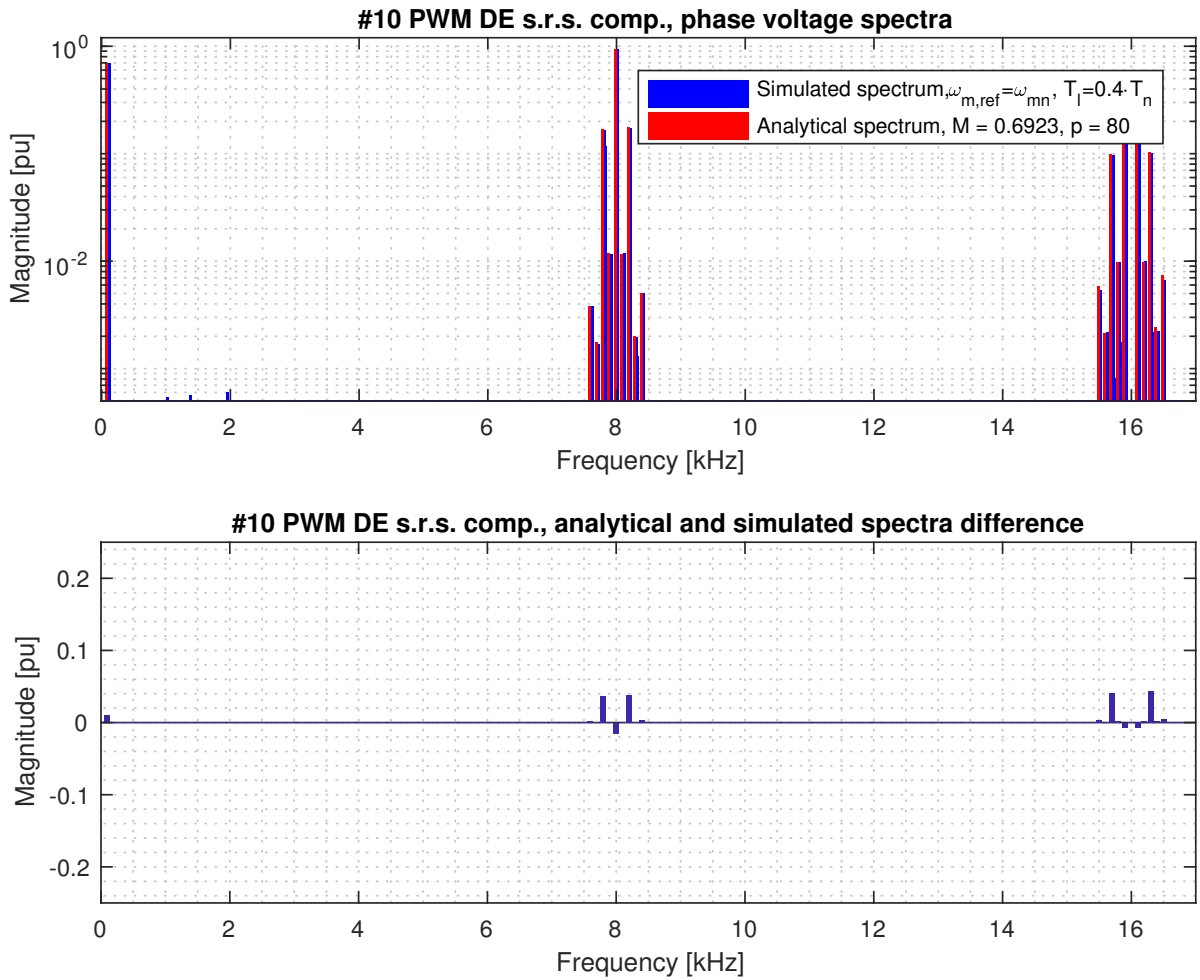


Figure 5.6. Comparison between the simulated and the analytically computed phase voltage spectra for #10 PWM Double-Edge s.r.s. comp. modulation. Top: overlapped spectra. Bottom: magnitude difference.

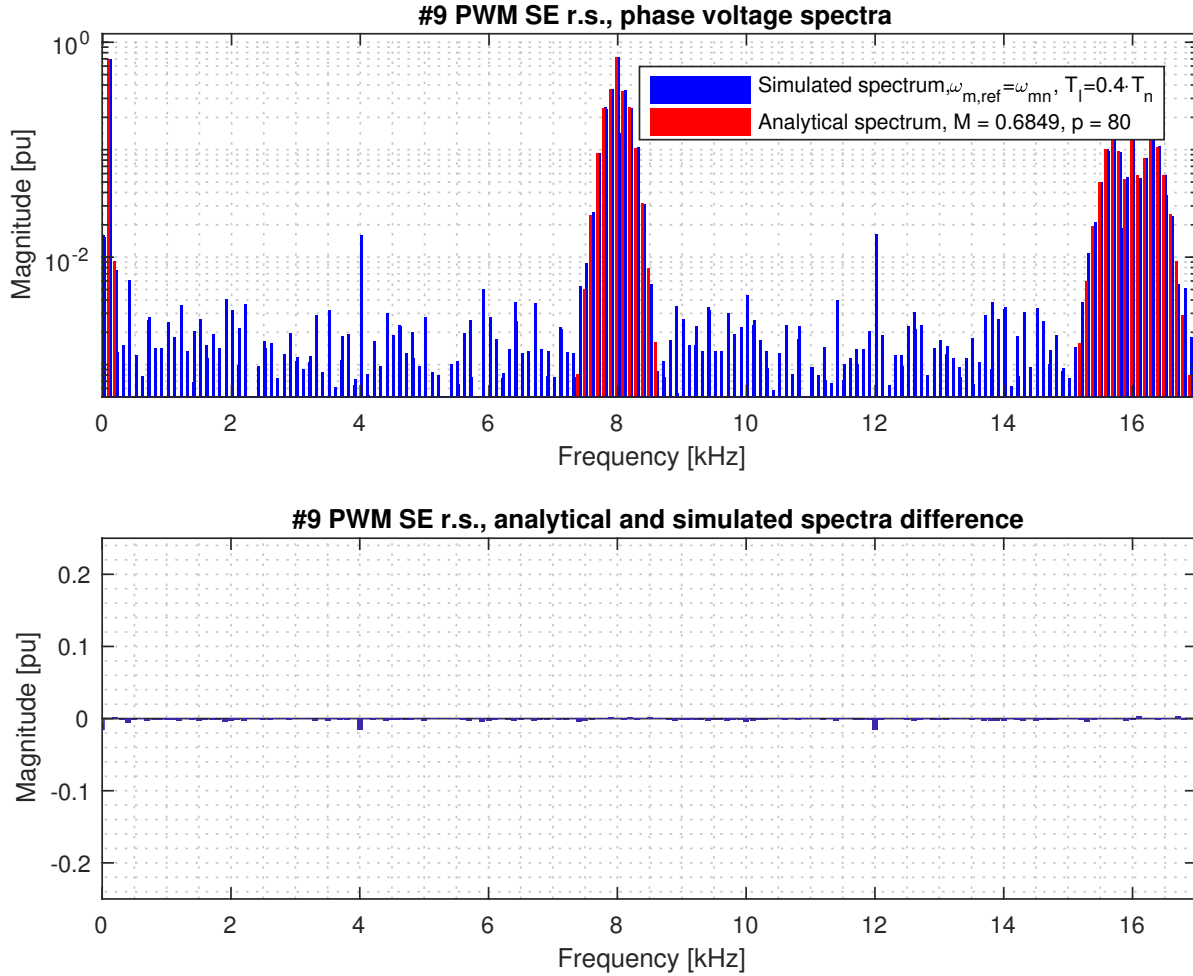


Figure 5.7. Comparison between the simulated and the analytically computed phase voltage spectra for #9 Single-Edge r.s. modulation. Top: overlapped spectra. Bottom: magnitude difference.

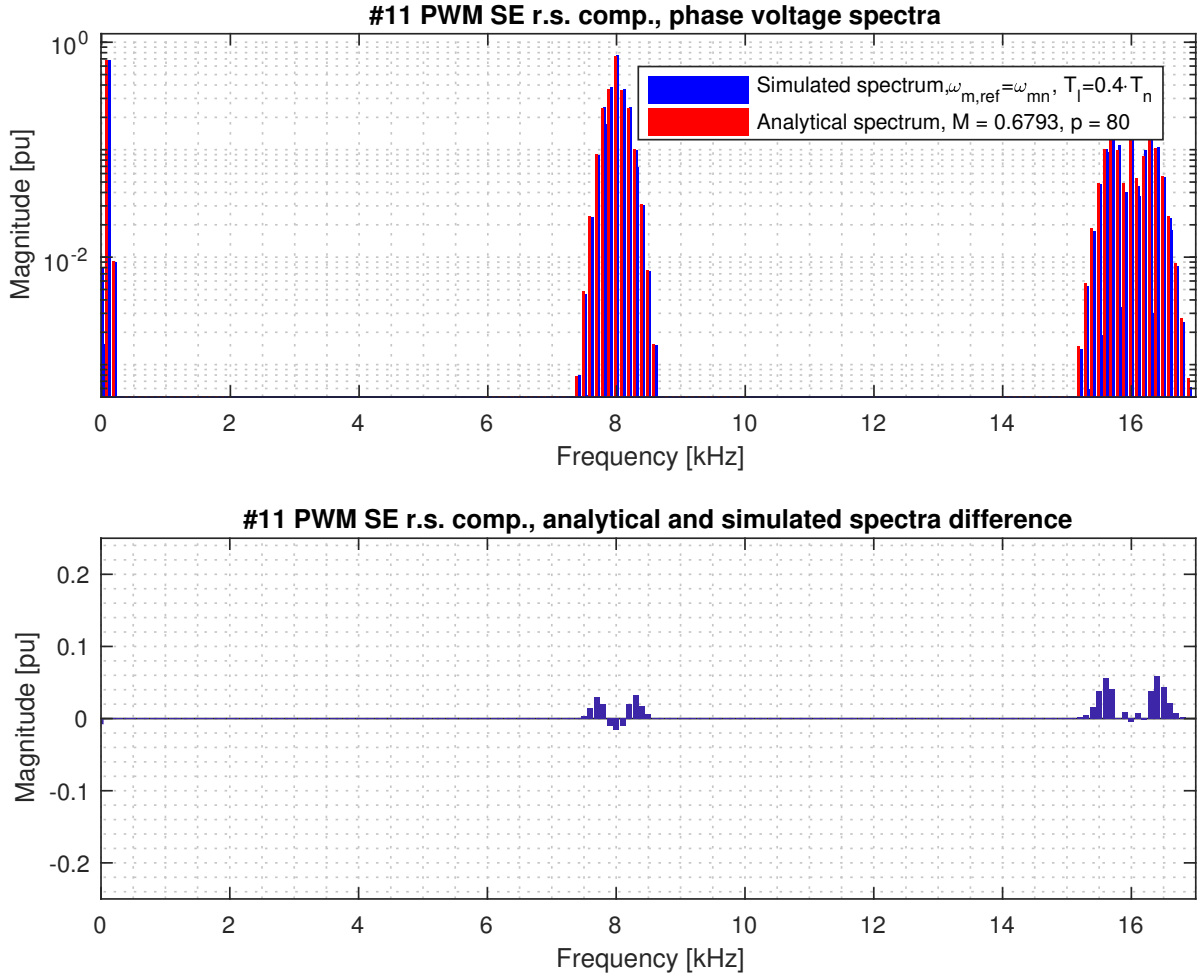


Figure 5.8. Comparison between the simulated and the analytically computed phase voltage spectra for #1 Single-Edge r.s. comp. modulation. Top: overlapped spectra. Bottom: magnitude difference.

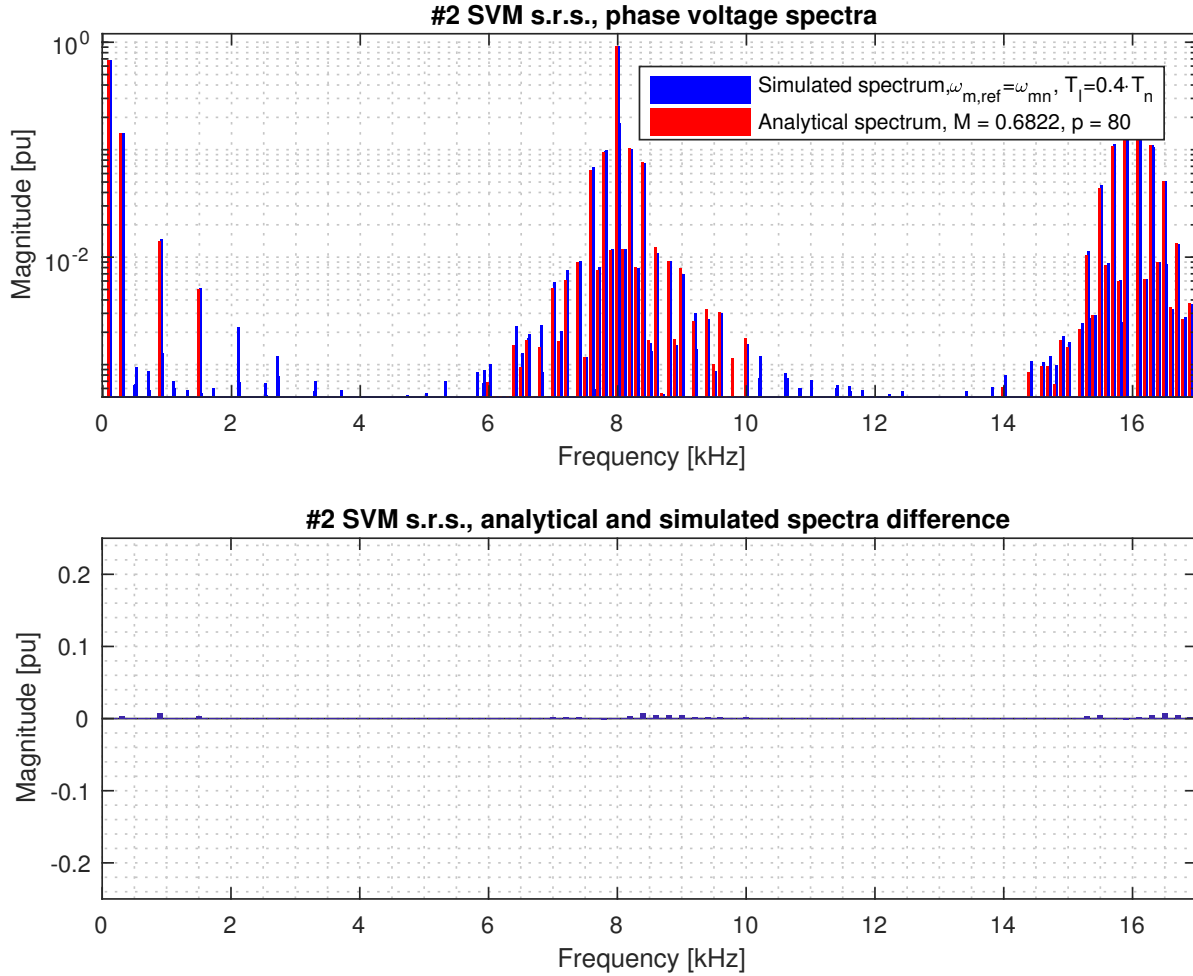


Figure 5.9. Comparison between the simulated and the analytically computed phase voltage spectra for #2 SVM s.r.s. modulation. Top: overlapped spectra. Bottom: magnitude difference.

### 5.2.3 Torque and speed influence

In this Subsection, simulations have been run in order to identify the harmonic content that each of the implemented modulations involves and to investigate the torque and the speed influences that are expected from the theoretical analysis carried out in Subsection 3.2. Afterwards, as regards to the harmonic content of interest for the intrinsic injection sensorless control examined in Subsection 3.2.5, the most significant sideband harmonic has been chosen for each modulation according to its highest signal-to-noise ratio in the different speed and torque conditions.

For each modulation strategy, the harmonic content of the  $\alpha$  voltage component has been calculated in steady state conditions for different motor speeds, respectively 0.02, 0.5 and 1 times  $\omega_{mn}$ , and different load torques, respectively 0, 0.5 and 1 times  $\tau_n$ .

It is important to highlight that the modelled drive is designed to work with a PWM Double-Edge modulation with third harmonic injection. Therefore, in order not to occur in overmodulation with the modulations strategies in which no third harmonic injection is present, particularly the Single- and Double-Edge modulations #1, #9, #10 and #11, the DC-link voltage  $U_{dc}$  has been risen to 750 V. The reason for this is that overmodulation would affect the spectra in such a way that the harmonic content is more shifted towards the external sideband harmonics.

Furthermore, the signals have been windowed with a 1-s flat-top window.

From Figure 5.10 to Figure 5.20 the results of these simulations are displayed. It is noteworthy to say that the voltages have been normalized with respect the half of the DC-link  $U_{dc}/2$ . The  $\alpha$  voltage component spectra display, furthermore, would be equivalent to the  $\beta$  component spectra and equivalent to the line-to-line voltages spectra, with the appropriate normalisation to  $U_{dc}/2\sqrt{3}$ . The reason for this is that both in the  $\alpha\beta$  and in the line-to-line voltages the carrier harmonic together with the triplen sideband harmonics are cancelled out.

As expected from Subsection 3.2, for all the modulations the two  $n$  index harmonics are symmetric with respect to the carrier frequency  $f_c$ , and the higher is  $n$  the farther are these two harmonics from  $f_c$ .

The speed, as envisioned, results to be decisive in the sideband harmonics frequency allocation. In addition, a prospect not expected from the theoretical spectra, in lowest speed conditions all the harmonic content around the carrier frequency has lowest magnitude, no matter which are the load

conditions and the implemented modulation. This operating conditions can therefore bring to poor intrinsic signal injection estimator performance at low speeds, due to the lowest signal-to-noise ratio.

The load torque influence complies with the theory in the way that the higher is the torque, the more the harmonic content is shifted towards the higher  $n$ -index sideband harmonics and that the torque influence on the harmonics frequencies is negligible. Anyway, the fact that the highest magnitudes of the two sideband harmonics of interest match with mid load torque values seems to be found not for all the modulation strategies. In particular, it is valid for #3 DPWMMAX, #4 DPWMMIN, #5 DPWM0, #6 DPWM1, #7 DPWM2 and #9 and #11 PWM Double-Edge.

After this first analysis, each modulation strategy has been evaluated in the perspective of an implementation for the intrinsic injection sensorless control. A couple of sideband harmonics has therefore been chosen for a given modulation strategy. The requirement for this harmonics is the highest signal-to-noise ratio in all the different speed and load conditions, in order to guarantee the best performance compared to any other harmonic for the given modulation strategy. For the sake of plotting, the harmonic on the left side of the carrier has been chosen, but its magnitude differs minimally from the one of its symmetric counterpart.

The chosen  $n$  index is equal to 1 for the modulations #3 DPWMMAX, #4 DPWMMIN and #9 and #11 PWM Double-Edge, while it is equal to 2 for the other modulations.

A map of the dependence of the chosen harmonic magnitude from the speed and the load conditions has been plotted for each modulation and the eleven graphs are displayed in Figure 5.21 and Figure 5.22. Moreover, their values are made explicit in Table 5.1.

From the comparison of these graphs, the modulation strategies, whose chosen harmonic has the highest signal-to-noise ratio in all the different speed and load conditions, have therefore been selected. The most suitable modulation strategies turn out to be the same ones where the chosen  $n$  index is equal to one, and in particular:

- #3 DPWMMAX s.r.s.;
- #4 DPWMMIN s.r.s.;
- #9 and #11 PWM Double-Edge s.r.s..

From the considerations drawn from these simulations, it is furthermore possible to update the considerations summarized in Subsection 3.2.7 regarding

the limiting conditions for the intrinsic injection sensorless estimator operation:

- Zero speed operation is not feasible with the proposed estimators working on the alpha-beta currents, since all the sideband harmonics present the same frequency  $f_c$  and thus their information is lost during the transformation from  $abc$  to  $\alpha\beta$  coordinates;
- Low speed operation involves the shrinking of the sideband harmonics around the carrier frequency, making the filtering and the demodulation processes more difficult;
- Low- and high-load conditions involve a low signal-to-noise ratio, making the extraction of the speed and position estimates more troublesome;
- High-load conditions may involve magnetic saturation and thus, because of the reduction of the saliency, a possible reduction of the information from which the position and the speed can be estimated;
- Overmodulation occurs in these simulations, but its influence cannot be noticed since the estimator performance is not taken into account.

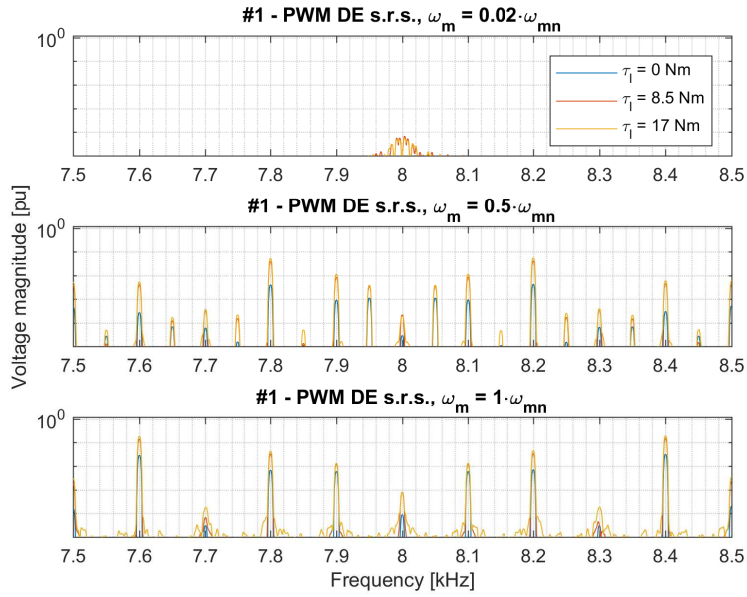


Figure 5.10.  $\alpha$  voltage spectra around  $f_c = 8 \text{ kHz}$  for different values of speed  $\omega_m$  and load torque  $\tau_l$  for modulation #1.

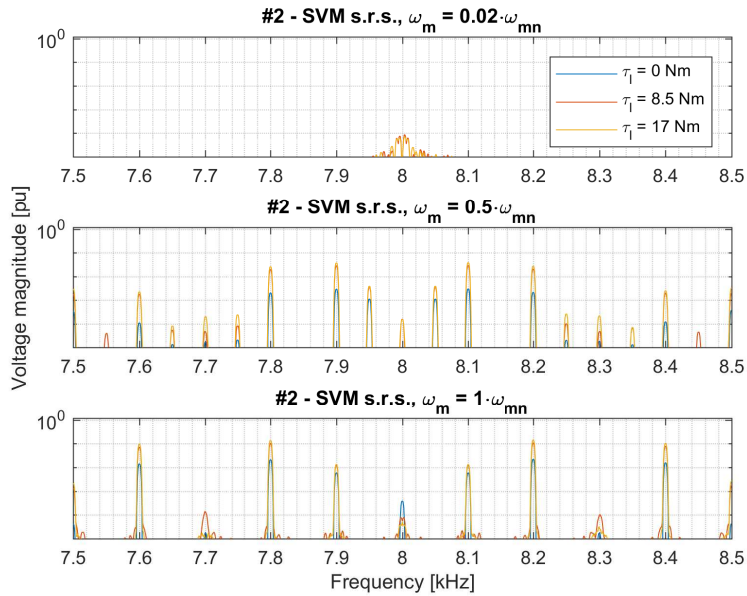


Figure 5.11.  $\alpha$  voltage spectra around  $f_c = 8 \text{ kHz}$  for different values of speed  $\omega_m$  and load torque  $\tau_l$  for modulation #2.

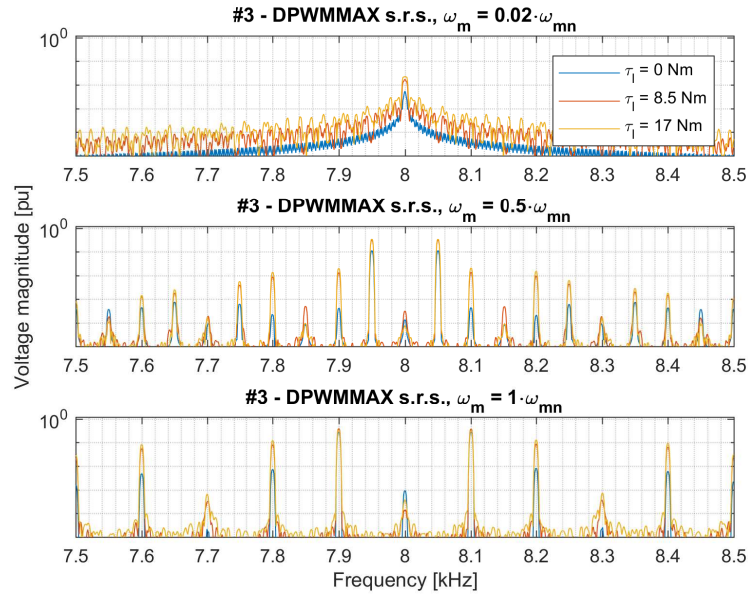


Figure 5.12.  $\alpha$  voltage spectra around  $f_c = 8 \text{ kHz}$  for different values of speed  $\omega_m$  and load torque  $\tau_l$  for modulation #3.

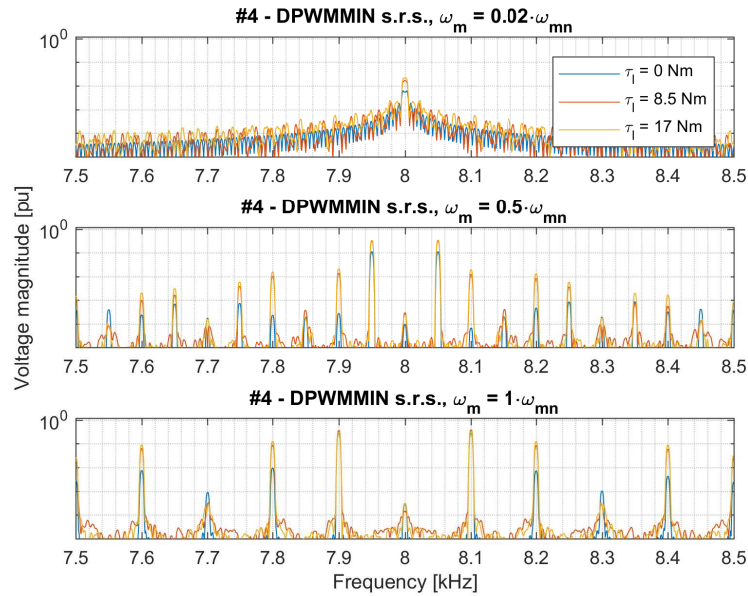


Figure 5.13.  $\alpha$  voltage spectra around  $f_c = 8 \text{ kHz}$  for different values of speed  $\omega_m$  and load torque  $\tau_l$  for modulation #4.

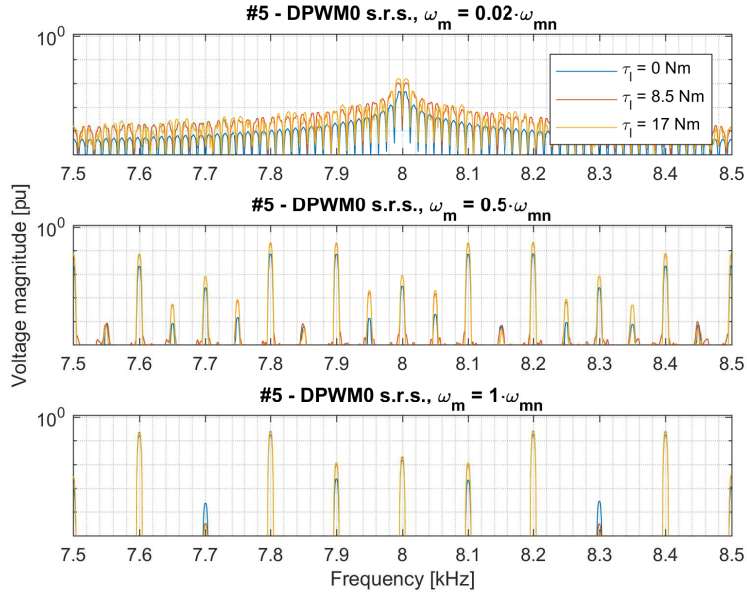


Figure 5.14.  $\alpha$  voltage spectra around  $f_c = 8 \text{ kHz}$  for different values of speed  $\omega_m$  and load torque  $\tau_l$  for modulation #5.

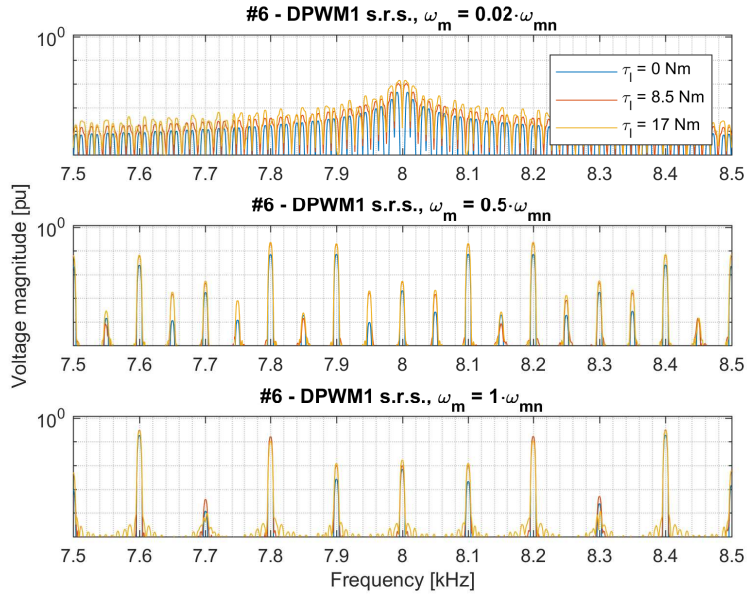


Figure 5.15.  $\alpha$  voltage spectra around  $f_c = 8 \text{ kHz}$  for different values of speed  $\omega_m$  and load torque  $\tau_l$  for modulation #6.

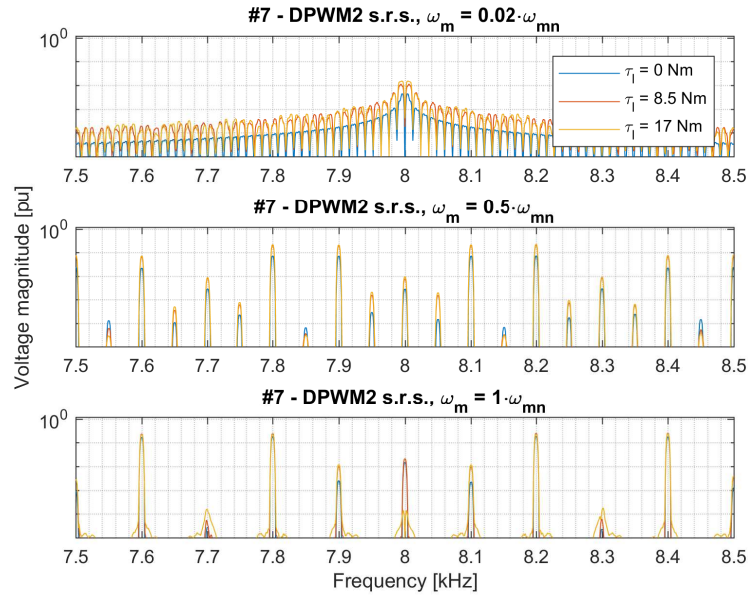


Figure 5.16.  $\alpha$  voltage spectra around  $f_c = 8 \text{ kHz}$  for different values of speed  $\omega_m$  and load torque  $\tau_l$  for modulation #7.

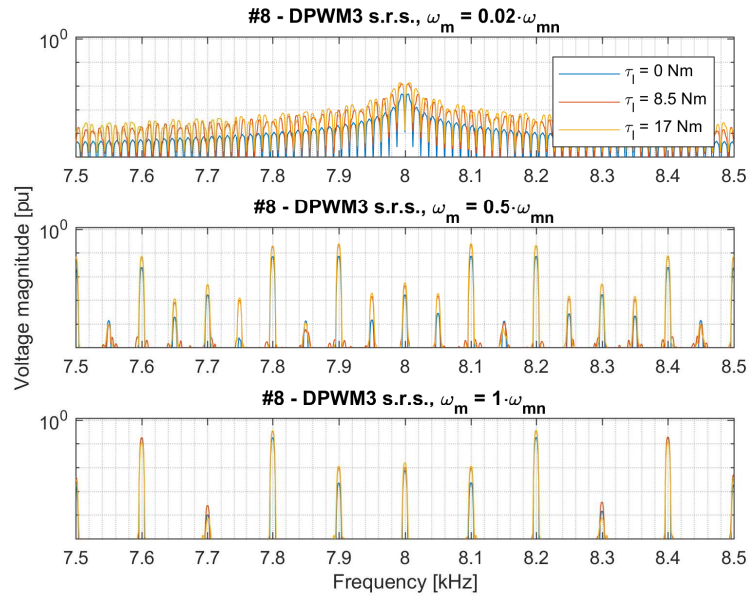


Figure 5.17.  $\alpha$  voltage spectra around  $f_c = 8 \text{ kHz}$  for different values of speed  $\omega_m$  and load torque  $\tau_l$  for modulation #8.

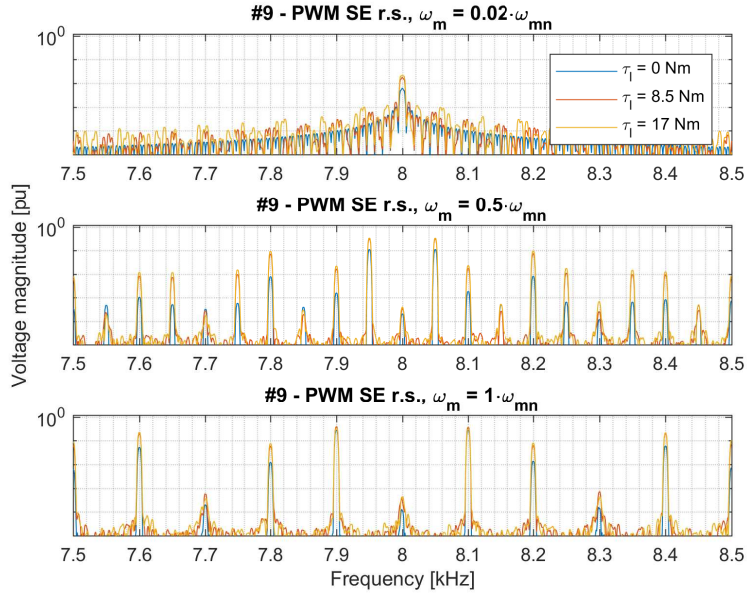


Figure 5.18.  $\alpha$  voltage spectra around  $f_c = 8 \text{ kHz}$  for different values of speed  $\omega_m$  and load torque  $\tau_l$  for modulation #9.

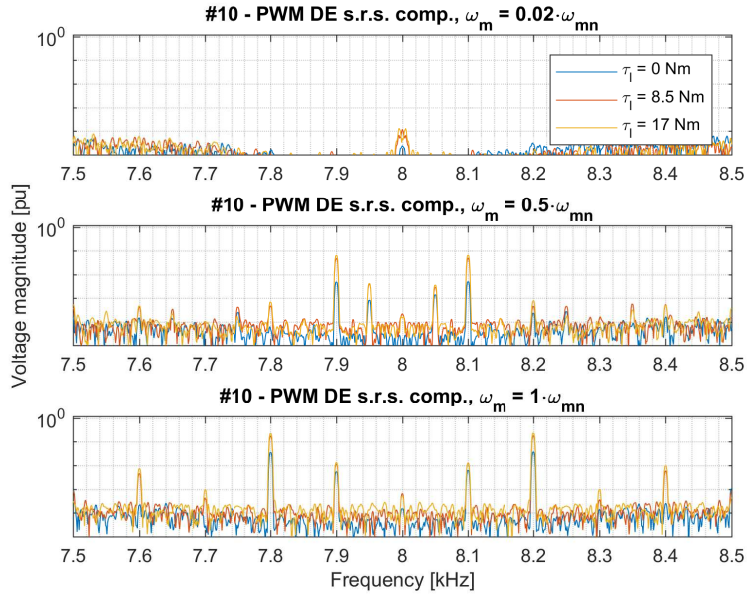


Figure 5.19.  $\alpha$  voltage spectra around  $f_c = 8 \text{ kHz}$  for different values of speed  $\omega_m$  and load torque  $\tau_l$  for modulation #10.

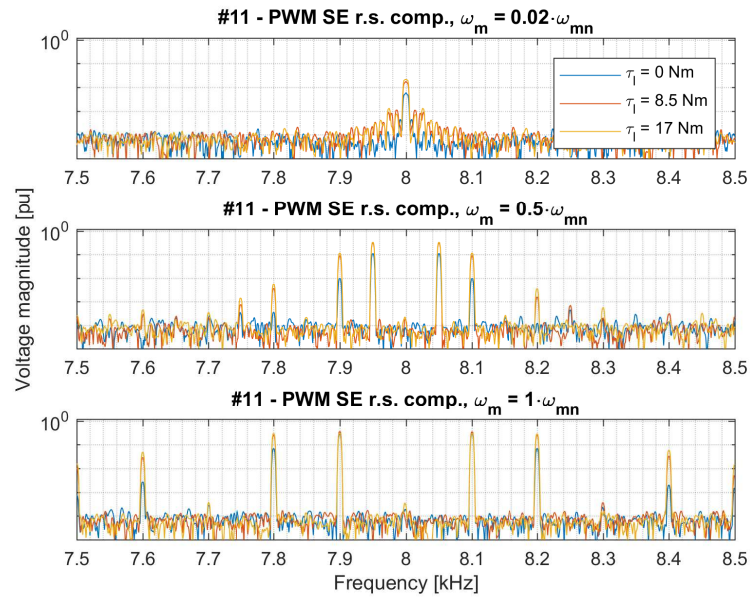


Figure 5.20.  $\alpha$  voltage spectra around  $f_c = 8$  kHz for different values of speed  $\omega_m$  and load torque  $\tau_l$  for modulation #11.

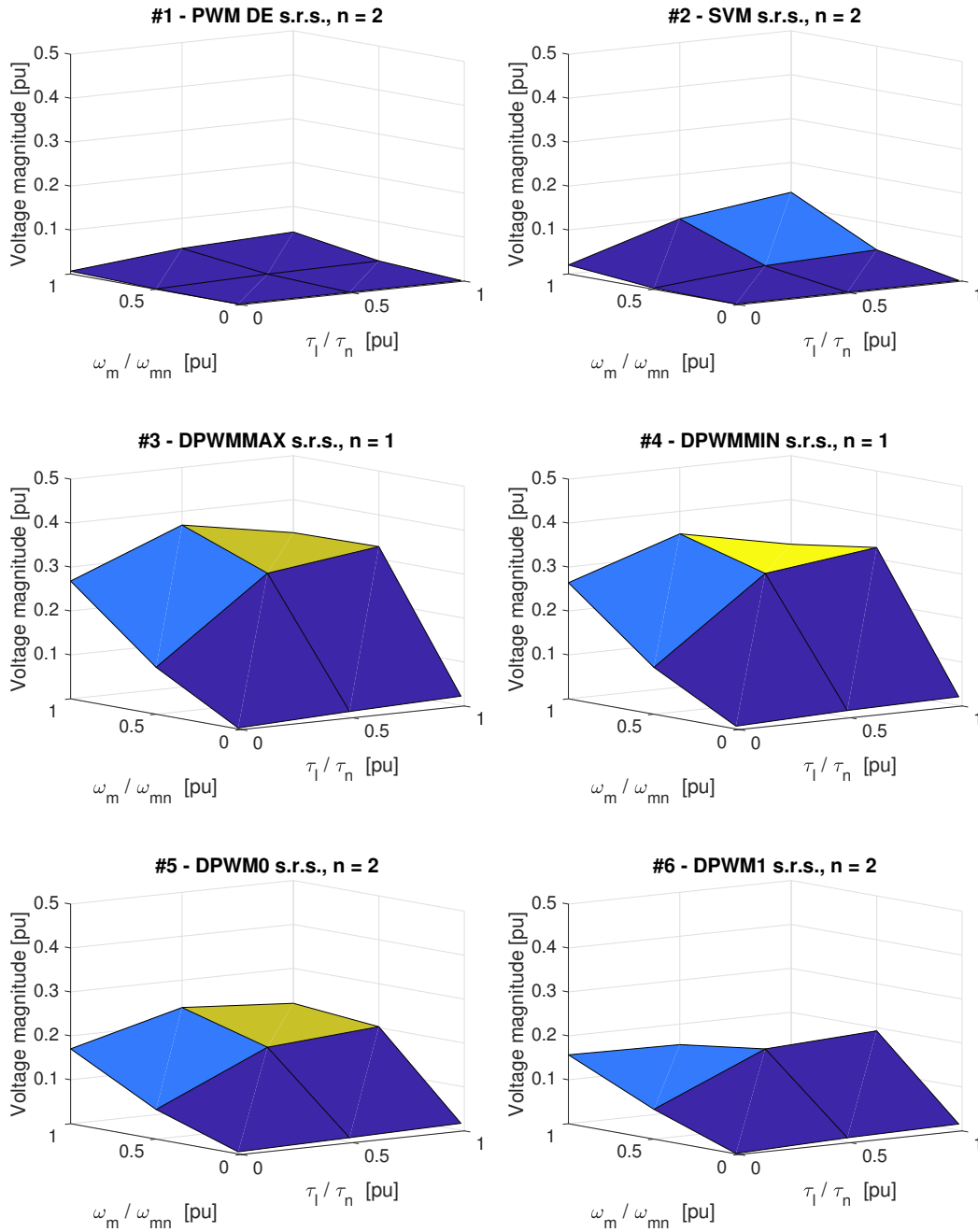


Figure 5.21. Chosen  $\alpha$  voltage harmonic magnitude, for different values of speed  $\omega_m$  and load torque  $\tau_l$ , for the modulation strategies #1, #2, #3, #4, #5 and #6.

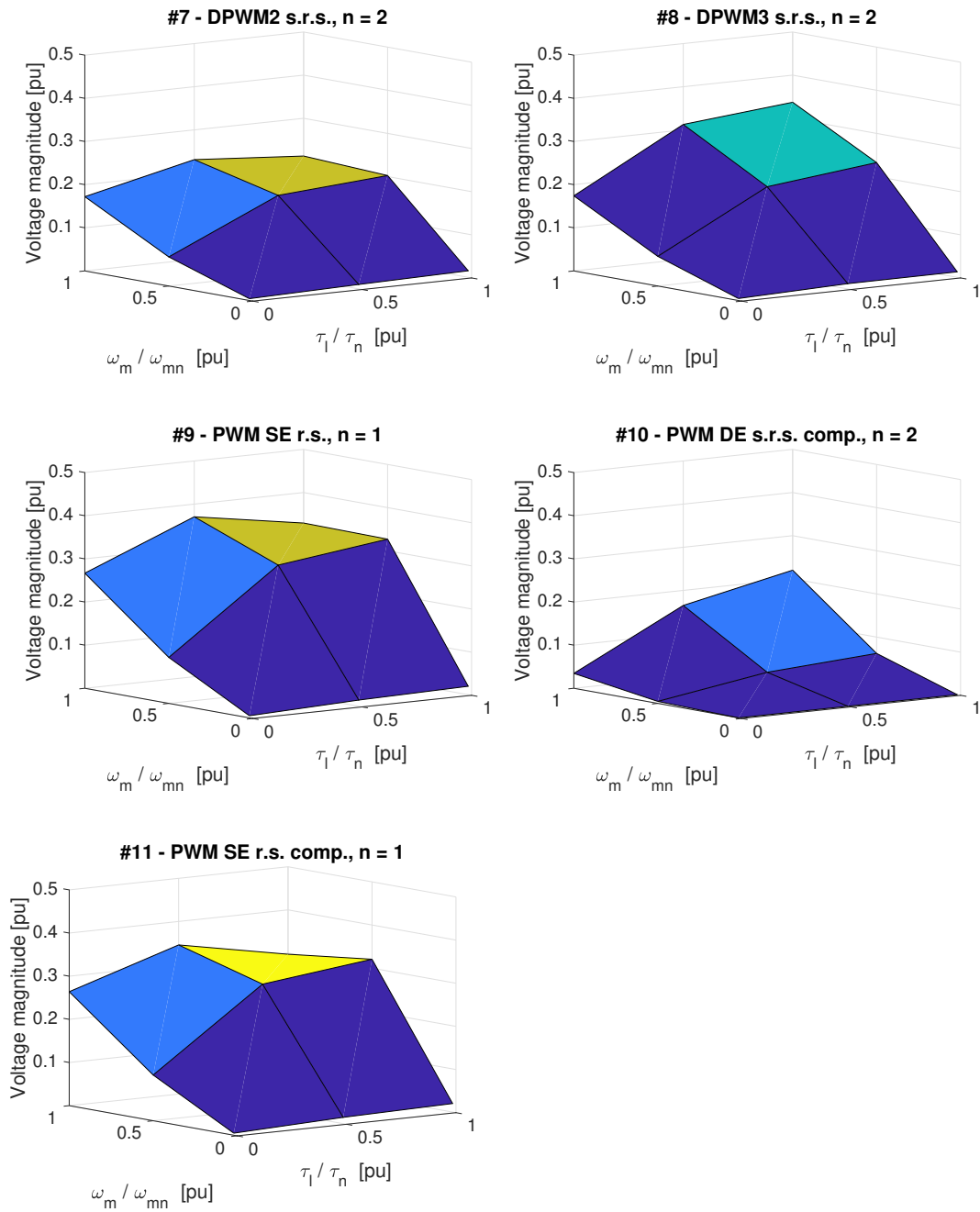


Figure 5.22. Chosen  $\alpha$  voltage harmonic magnitude, for different values of speed  $\omega_m$  and load torque  $\tau_l$ , for the modulation strategies #7, #8, #9, #10 and #11.

$\omega_m$ :		$0.02 \cdot \omega_{mn}$			$0.5 \cdot \omega_{mn}$			$\omega_{mn}$		
$\tau_l [Nm]$ :		0	8.5	17	0	8.5	17	0	8.5	17
<i>mod</i>	<i>n</i>									
#1	2	0	$5e - 5$	$5e - 5$	0.001	0.007	0.011	0.006	0.031	0.042
#2	2	0	$7e - 5$	$6e - 5$	0.003	0.027	0.036	0.020	0.099	0.132
#3	1	0.002	0.013	0.021	0.107	0.294	0.328	0.268	0.369	0.325
#4	1	0.006	0.015	0.020	0.107	0.294	0.326	0.264	0.349	0.298
#5	2	0.005	0.010	0.016	0.068	0.182	0.202	0.171	0.238	0.220
#6	2	$8e - 4$	0.001	0.014	0.068	0.178	0.193	0.157	0.153	0.100
#7	2	0.004	0.010	0.015	0.068	0.183	0.202	0.172	0.231	0.213
#8	2	0.005	0.012	0.013	0.069	0.203	0.232	0.174	0.313	0.337
#9	1	0.005	0.014	0.020	0.107	0.294	0.327	0.267	0.371	0.329
#10	2	$4e - 6$	$7e - 5$	$1e - 4$	0.005	0.045	0.062	0.035	0.165	0.220
#11	1	0.005	0.015	0.020	0.106	0.290	0.321	0.264	0.346	0.297

Table 5.1. Magnitude of the chosen  $n$ -index sideband harmonic for each one of the implemented modulation strategies, for different values of speed and load torque.

### 5.3 Current PLL and ripple calculator simulations

Before approaching the intrinsic injection based estimator simulations, it is important to analyse the performance and the dynamics of the implemented PLL. As described in 4.4.2, in fact its operation influences the  $\Delta i_{\alpha\beta}$  used by the estimator alternative 2 and it provides the estimated speed  $\hat{\omega}_{me}^{PLL}$  to the variable BPFs implemented in the estimator alternative 3.

In Figure 5.23, the estimated speed  $\hat{\omega}_{me}^{PLL}$  and the position error  $\Delta\theta^{PLL} = \hat{\theta}_{me}^{PLL} - \theta_{me}$  are plotted for a reference speed  $\omega_m^* = \omega_{mn}$  and load torque  $\tau_l = 16 \text{ Nm}$  at  $t = 1 \text{ s}$ . The chosen load torque value added by the viscous friction results to be close to the rated torque of the machine  $\tau_l = 17 \text{ Nm}$ . From the plots, it can be asserted that the speed is tracked in a really satisfactory manner, with low oscillations that dampen reasonably fast. The angle error, as mentioned in 4.4.2, stabilize around the value corresponding to the angle of the estimated current vector in the estimated  $dq$  reference frame, which is not useful for the position estimation scope.

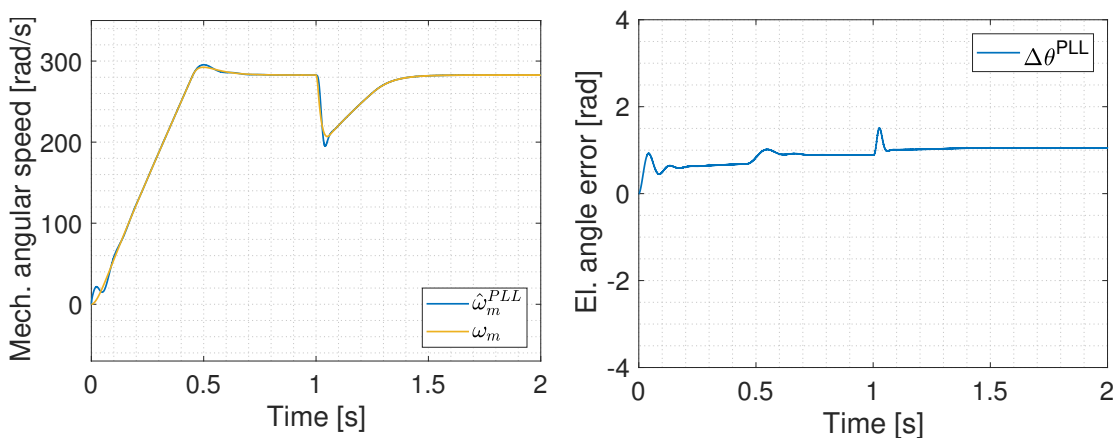


Figure 5.23. PLL estimated speed and angle error. Reference speed  $\omega_m^* = \omega_{mn}$  and load torque  $\tau_l = 16 \text{ Nm}$  at  $t = 1 \text{ s}$ .

## 5.4 Open-loop simulations

In this Section, the open-loop behaviour of the intrinsic injection estimator is analysed:

- for all the three proposed alternatives;
- for the four more desirable modulation strategies #3 DPWMMAX, #4 DPWMMIN and #9 and #11 PWM Double-Edge;
- for different values of speed.

With open-loop, it is intended that the drive is working with the measured speed and position used in the control, while the estimated speed and position are just examined in parallel, without using them in the control. In particular, the speed is used in the speed regulator for the calculation of the speed error and in the current regulator to perform the  $dq$ -axis decoupling, while the position is used for the rotational transformations. The schematic relative to the open-loop simulations is displayed in Figure 5.24.

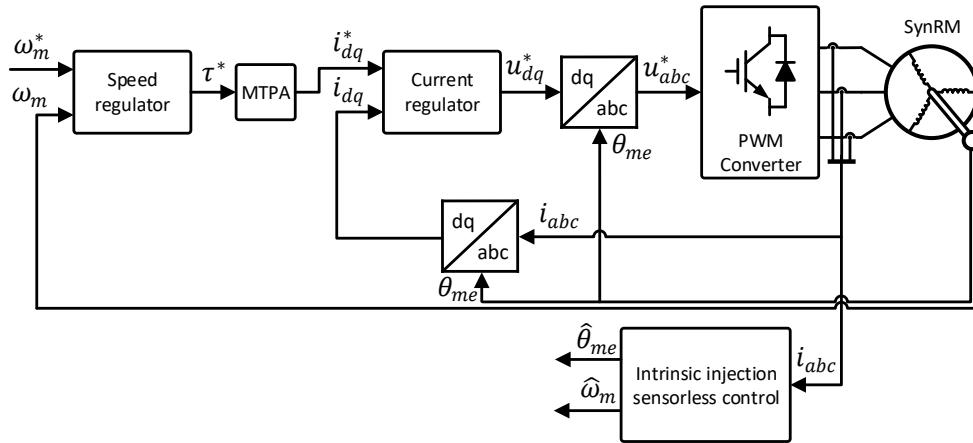


Figure 5.24. Drive schematic for the open-loop operation of the intrinsic injection estimator.

For the simulations, a reference speed  $\omega_m^*$  equal to  $0.9 \cdot \omega_{mn}$ ,  $0.5 \cdot \omega_{mn}$  and  $0.2 \cdot \omega_{mn}$  have been used. Reference speed ramps, lasting  $0.5 \text{ s}$  to reach the

nominal speed, have been adopted, in order to make the speed tracking possible from the starting of the motor. Furthermore, load torque  $\tau_l = 16 \text{ Nm}$  has been applied at  $t = 1 \text{ s}$ . Lastly, the speed regulator bandwidth has been decreased to  $50 \text{ rad/s}$ .

As the motor simulation transients depend on different speeds, the torque and inductance variations are plotted in Subsection 5.4.7 for each speed value. Furthermore, the only modulation for which it has been decided to analyse the speed influence is the #11 PWM Double-Edge r.s. coming from the carrier-reference comparison, since the simplest one to be implemented. For the spectra plots, a 0.4-s flat-top window has been applied.

A crucial aspect to be mentioned is that in this work the parameters of the modelled drive are relative to an existing converter present in the laboratory of ABB Corporate Research Sweden in Västerås, where the present work has been carried out. Relatively to that drive, the nominal speed of the motor can be easily achieved with the overmodulation operation of the converter. As illustrated in Subsection 3.2.6, overmodulation would imply the lack of the required ripple in the currents and thus the impossibility to extract the motor position and speed information. As a consequence, in order not to make use in the model of drive parameters different from the ones of the available hardware, and in particular of the converter DC-link voltage  $U_{dc}$ , whose influence is investigated in Section 5.8, it has been decided to limit the motor speed to values lower than the nominal.

### 5.4.1 Estimator 1 in open-loop

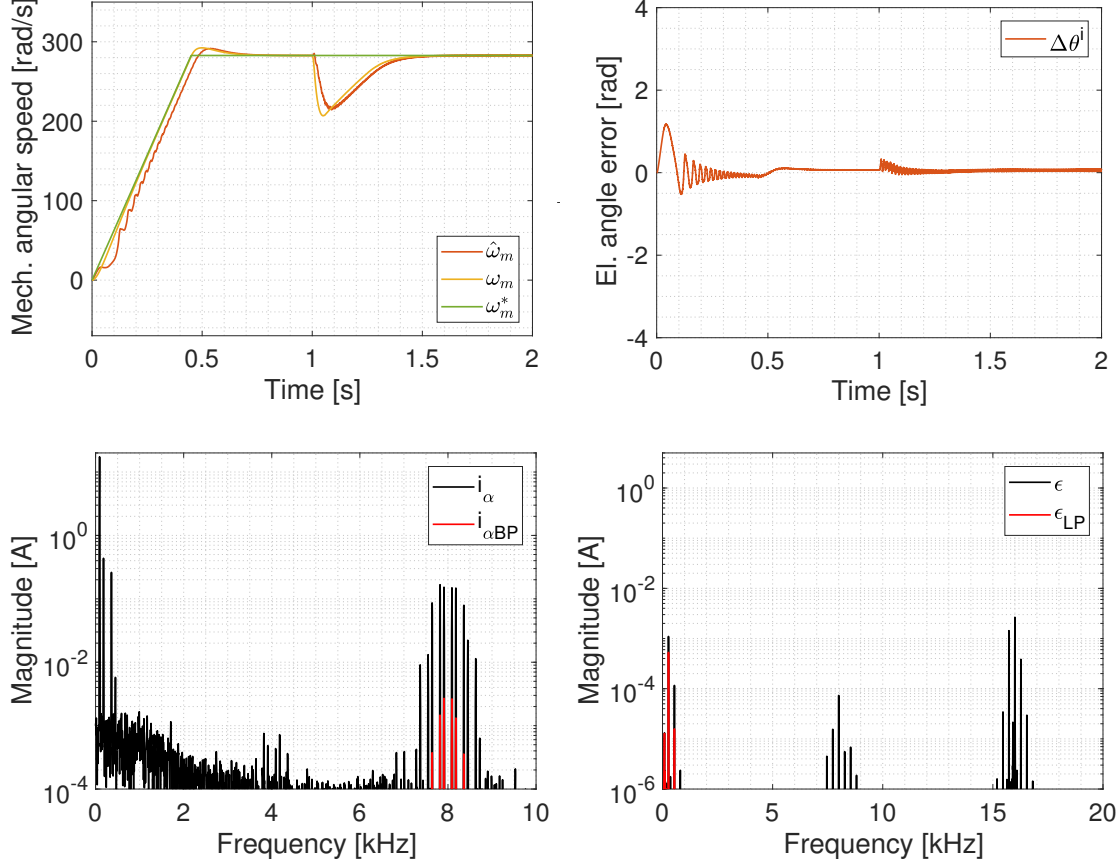


Figure 5.25. Estimator alternative 1 speed and angle error plots (top) and unfiltered and filtered harmonic spectra of  $i_\alpha$  and  $\epsilon$  (bottom). Open-Loop operation, reference speed  $\omega_m^* = 0.9 \cdot \omega_{mn}$  and load torque  $\tau_l = 16 \text{ Nm}$  at  $t = 1 \text{ s}$ . Modulation strategy employed #11 Single-Edge s.r.s. comp..

The open-loop simulation results for the estimator alternative 1 are summarized in Figure 5.25 relative to  $\omega_m^* = 0.9 \cdot \omega_{mn}$ , in Figure 5.26 relative to  $\omega_m^* = 0.5 \cdot \omega_{mn}$  and in Figure 5.27 relative to  $\omega_m^* = 0.2 \cdot \omega_{mn}$ .

The first aspect to underline is the expected bad performance of the estimator at low speeds. Considered that for reference speed values lower than  $0.2 \cdot \omega_{mn}$  the behaviour of the estimator has appeared to be poorest, no matter the implemented estimator alternative and the adopted modulation strategy, in the rest of the work this comment is not repeated any more.

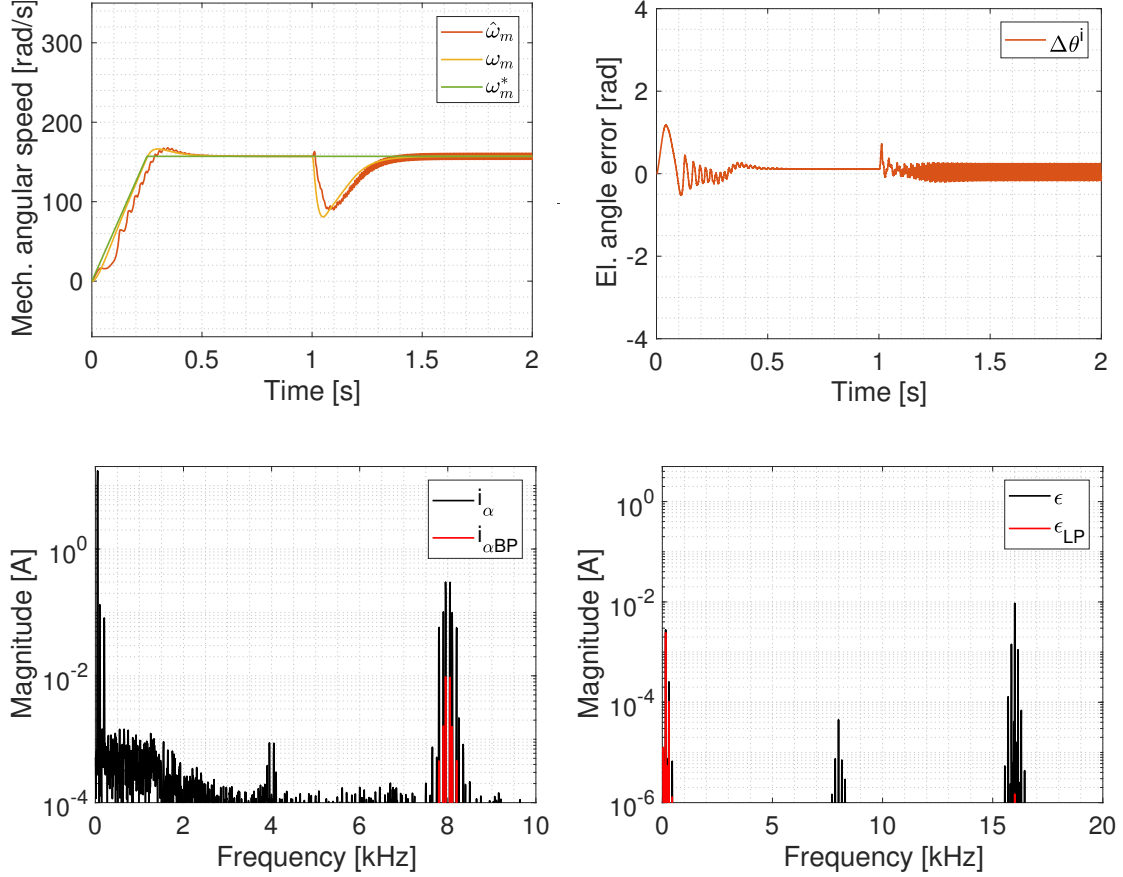


Figure 5.26. Estimator alternative 1 speed and angle error plots (top) and unfiltered and filtered harmonic spectra of  $i_\alpha$  and  $\epsilon$  (bottom). Open-Loop operation, reference speed  $\omega_m^* = 0.5 \cdot \omega_{mn}$  and load torque  $\tau_l = 16 \text{ Nm}$  at  $t = 1 \text{ s}$ . Modulation strategy employed #11 Single-Edge s.r.s. comp..

Nevertheless, the performance at higher speeds is satisfactory, and both the speed and the position are well tracked. A ripple is present both in the speed and in the position, and the lower is the speed the lower is this ripple magnitude and frequency. Its frequency, in fact, depends on the harmonic content present in  $\epsilon_{LP}$ , which consists, as depicted in Subsection 3.2.3, in the multiples of the fundamental frequency.

Furthermore, as noticeable from  $\epsilon$  and  $\epsilon_{LP}$  spectra, the LPF action, whose cut-off frequency  $\omega_{lce}$  is equal to  $200 \cdot 2\pi \text{ rad/s}$ , is evident.

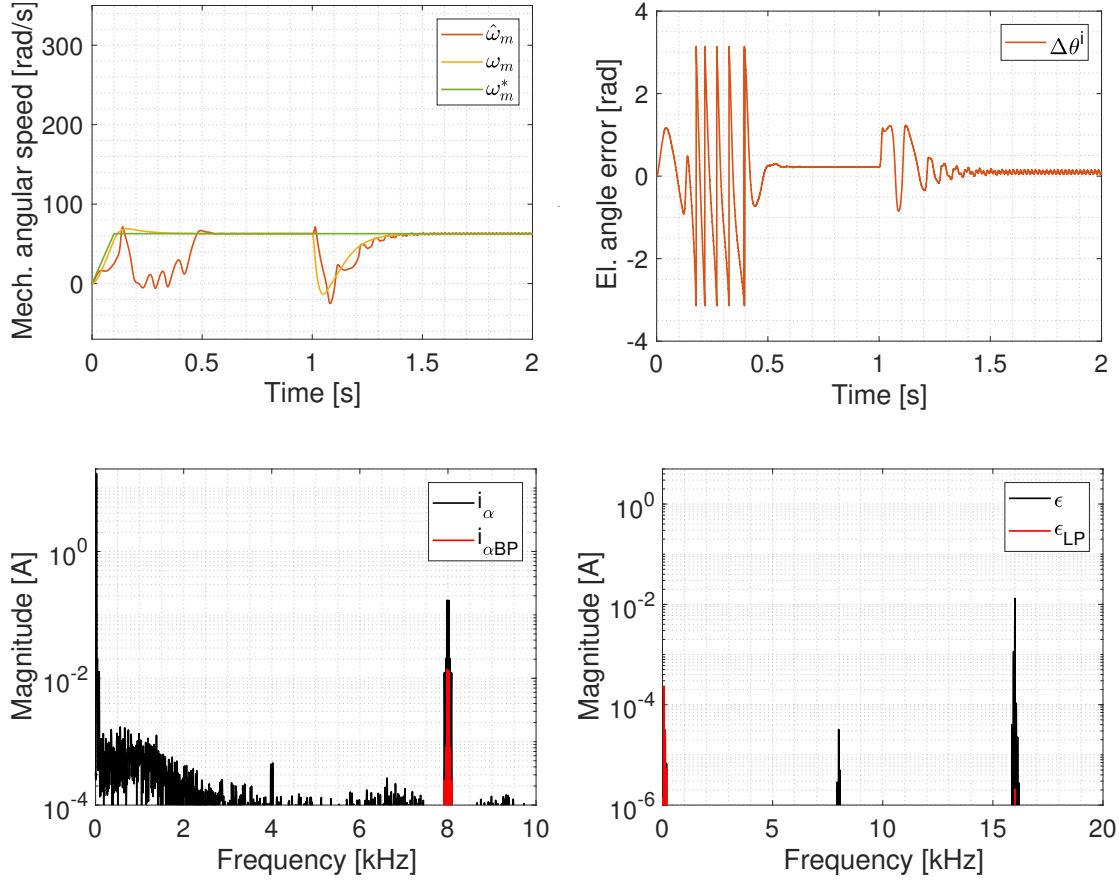


Figure 5.27. Estimator alternative 1 speed and angle error plots (top) and unfiltered and filtered harmonic spectra of  $i_\alpha$  and  $\epsilon$  (bottom). Open-Loop operation, reference speed  $\omega_m^* = 0.2 \cdot \omega_{mn}$  and load torque  $\tau_l = 16 \text{ Nm}$  at  $t = 1 \text{ s}$ . Modulation strategy employed #11 Single-Edge s.r.s. comp..

Looking at the currents harmonic contents, it is possible to notice the BPF action, which, being centred on  $f_c$ , decreases considerably the higher order sideband harmonics at the cost of affecting the useful ones. Moreover, the wideness of the currents sideband harmonics around  $f_c$  is reflected in the wideness of the  $\epsilon$  harmonics around  $2 \cdot f_c$ . In a similar way, the presence of lowest magnitude current harmonics around  $4 \text{ kHz}$  is reflected in  $\epsilon$  harmonics around  $8 \text{ kHz}$ , which are successfully eliminated by the LPF.

The influence of the iron saturation and of the collapse of the inductance when the high load occurs, displayed in Figure 5.43, seems not to play a rele-

vant role.

Lastly, it is important to remember that, since, as discussed in Subsection 3.2.4,  $\theta_{u,0}^r$  is equal to zero if the estimator and the motor are initiated simultaneously, referring to the angle error with  $\Delta\theta'$  or  $\Delta\theta$  is equivalent.

### 5.4.2 Estimator 1 in open-loop, other modulations

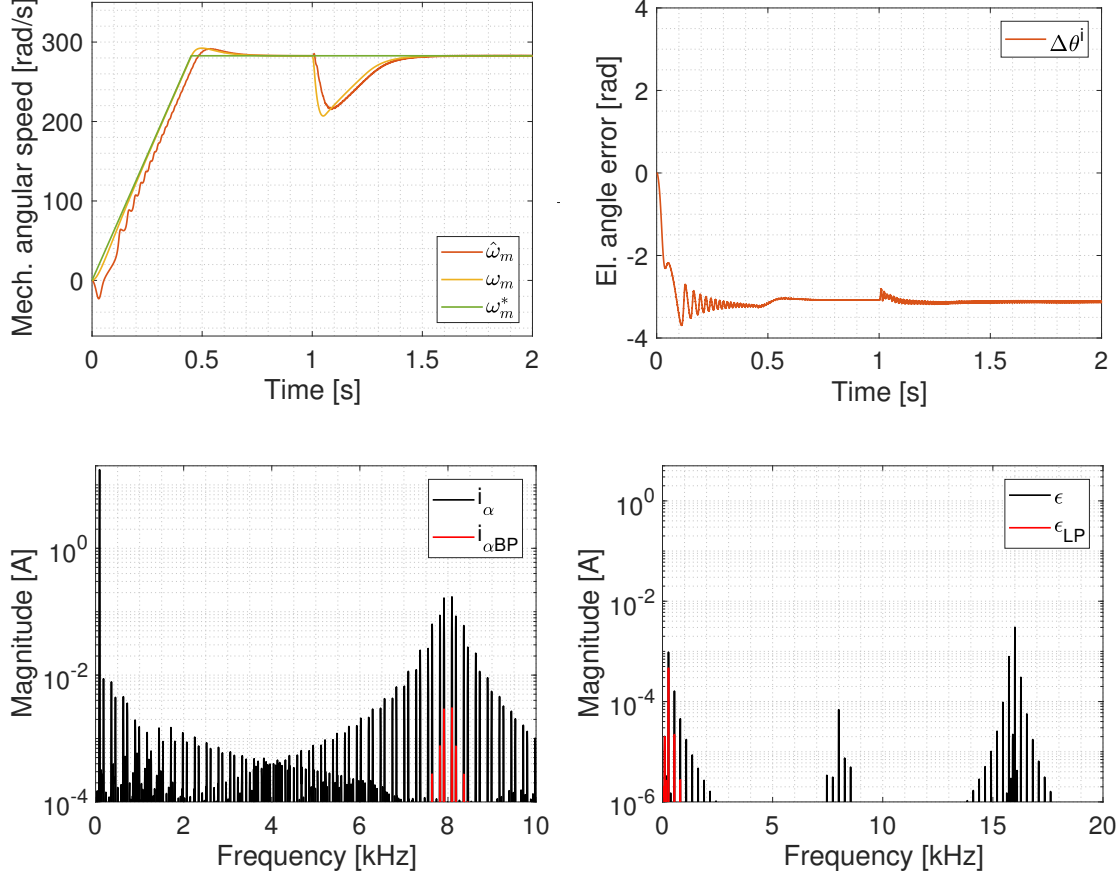


Figure 5.28. Estimator alternative 1 speed and angle error plots (top) and unfiltered and filtered harmonic spectra of  $i_\alpha$  and  $\epsilon$  (bottom). Open-Loop operation, reference speed  $\omega_m^* = 0.9 \cdot \omega_{mn}$  and load torque  $\tau_l = 16 \text{ Nm}$  at  $t = 1 \text{ s}$ . Modulation strategy employed #3 DPWMMAX s.r.s..

The open-loop simulations results for the estimator alternative 1 are summarized in Figure 5.28 relatively to DPWMMAX modulation, in Figure 5.29 relatively to DPWMMIN modulation and in Figure 5.30 relatively to Single-Edge UVMT computed modulation.

The estimator performance is in practice identical for all the four modulations regarding the way the speed and the position are tracked. This is mainly due to the current BPF action, which manages to isolate the same current harmonic components despite the different spectra, which differs remarkably

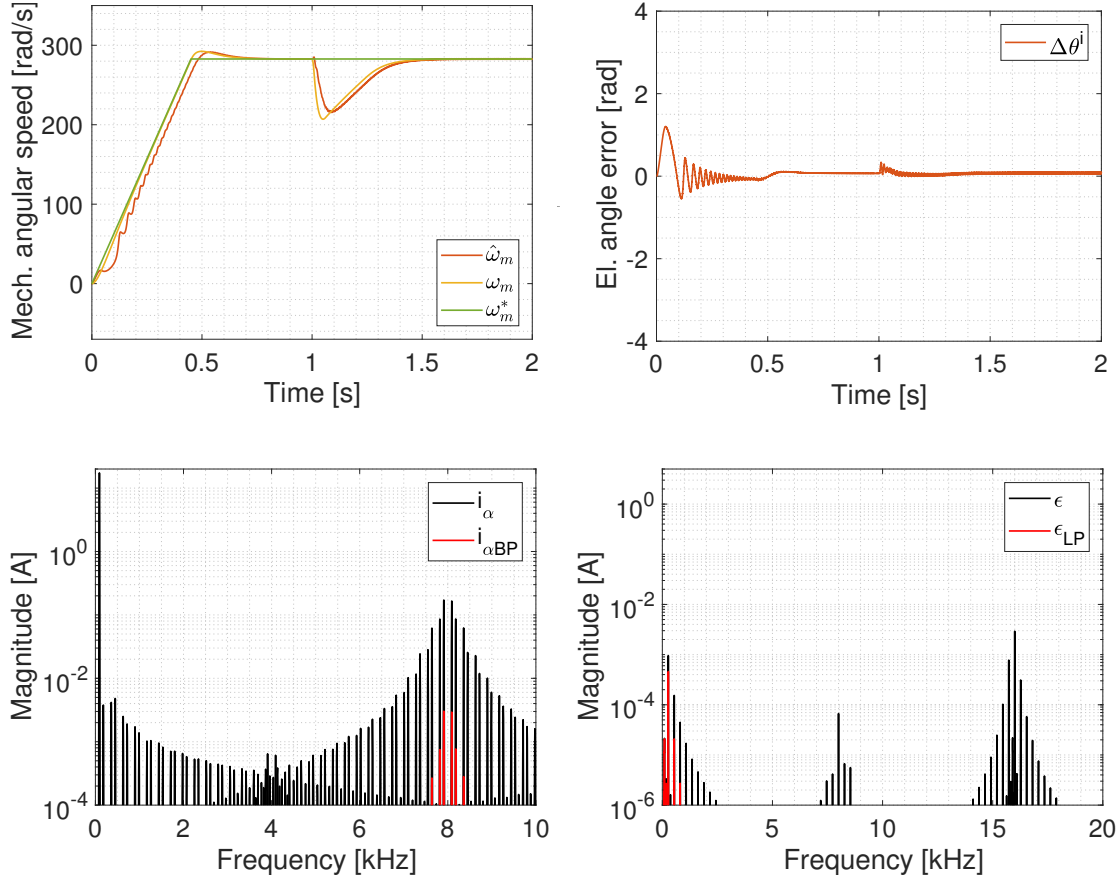


Figure 5.29. Estimator alternative 1 speed and angle error plots (top) and unfiltered and filtered harmonic spectra of  $i_\alpha$  and  $\epsilon$  (bottom). Open-Loop operation, reference speed  $\omega_m^* = 0.9 \cdot \omega_{mn}$  and load torque  $\tau_l = 16 \text{ Nm}$  at  $t = 1 \text{ s}$ . Modulation strategy employed #4 DPWMMIN s.r.s..

in DPWMMAX and DPWMMIN cases.

The most significant difference concerns DPWMMAX, for which the initial speed and position estimate is directed towards negative values. That implies that the the error angle  $\Delta\theta^i$  does not converge to 0, but to  $-\pi$ , which, as discussed in Subsection 3.2.4, represents an alternative solution to the nullification of  $\epsilon_{LP}$ .

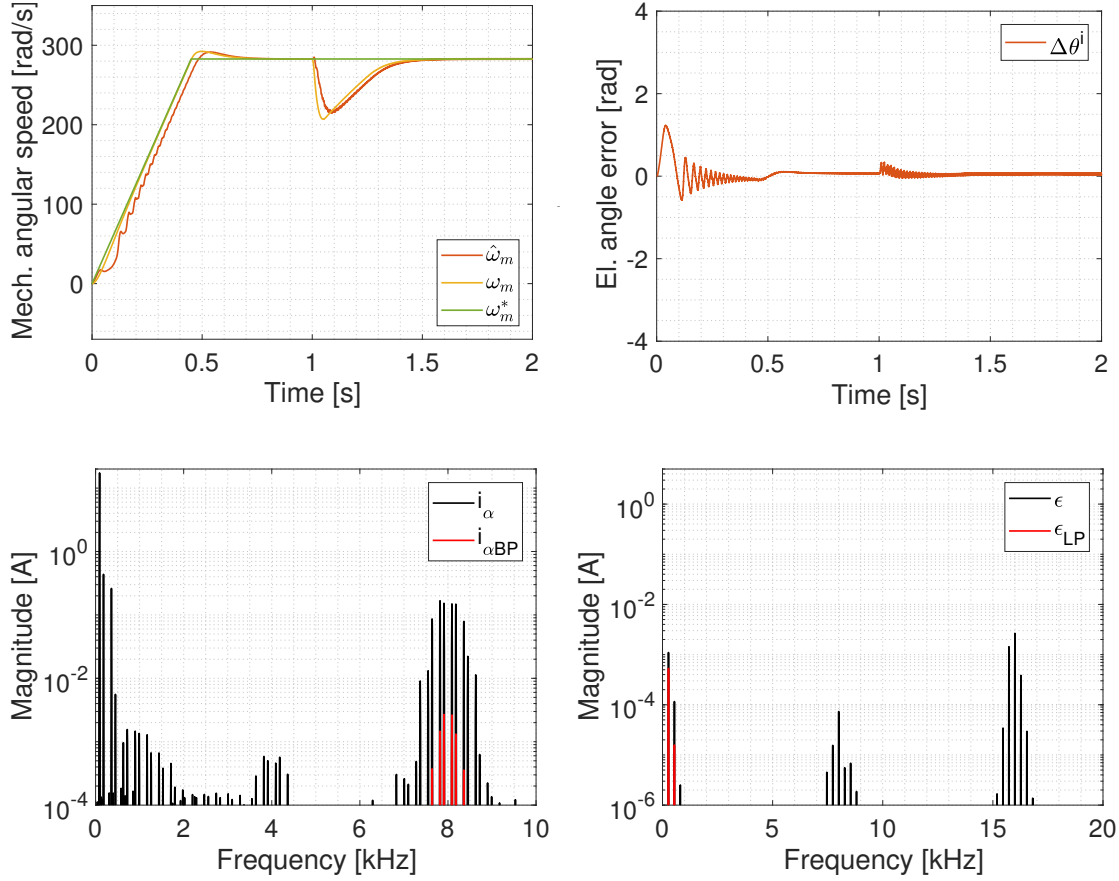


Figure 5.30. Estimator alternative 1 speed and angle error plots (top) and unfiltered and filtered harmonic spectra of  $i_\alpha$  and  $\epsilon$  (bottom). Open-Loop operation, reference speed  $\omega_m^* = 0.9 \cdot \omega_{mn}$  and load torque  $\tau_l = 16 \text{ Nm}$  at  $t = 1 \text{ s}$ . Modulation strategy employed #9 Single-Edge s.r.s. UVMT.

## 5.4.3 Estimator 2 in open-loop

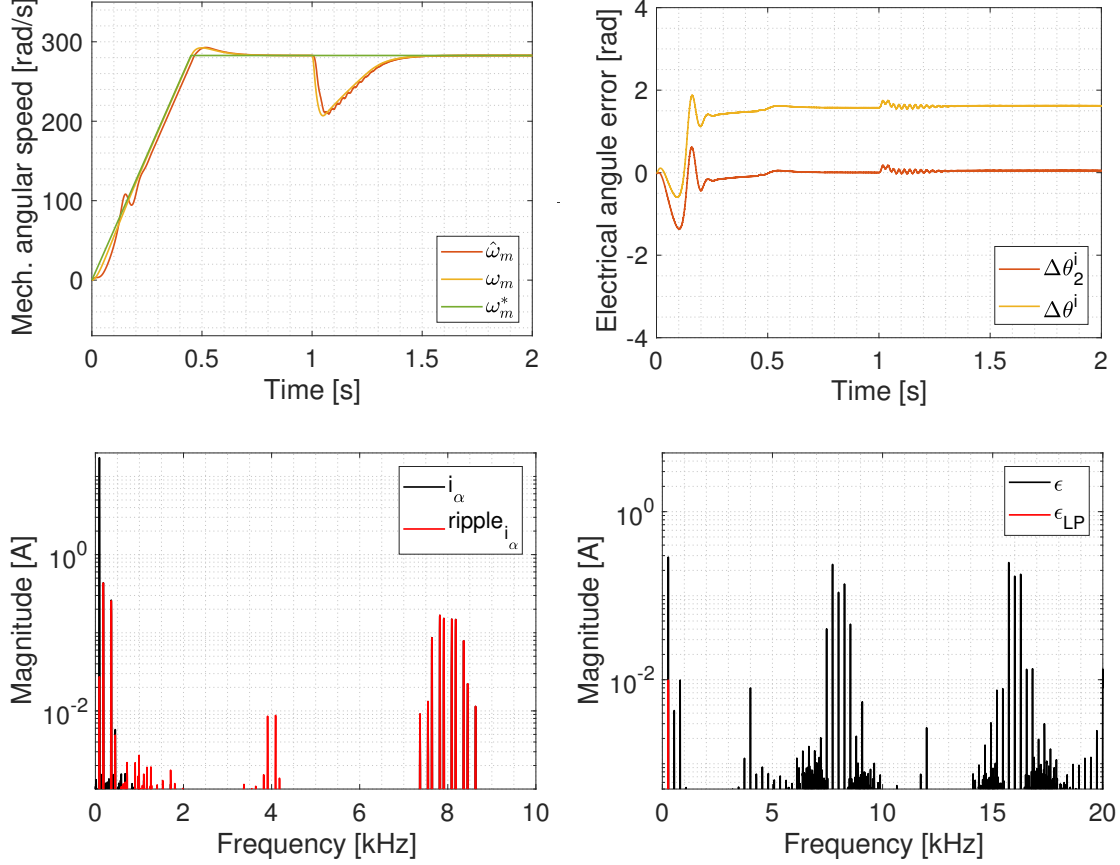


Figure 5.31. Estimator alternative 2 speed and angle error plots (top) and unfiltered and filtered harmonic spectra of  $i_\alpha$  and  $\epsilon$  (bottom). Open-Loop operation, reference speed  $\omega_m^* = 0.9 \cdot \omega_{mn}$  and load torque  $\tau_l = 16 \text{ Nm}$  at  $t = 1 \text{ s}$ . Modulation strategy employed #11 Single-Edge s.r.s. comp..

The open-loop simulations results for the estimator alternative 2 are summarized in Figure 5.31 relatively to  $\omega_m^* = 0.9 \cdot \omega_{mn}$ , in Figure 5.32 relatively to  $\omega_m^* = 0.5 \cdot \omega_{mn}$  and in Figure 5.33 relatively to  $\omega_m^* = 0.2 \cdot \omega_{mn}$ .

With the second alternative, again, the performance is really poor at low speeds, while it is satisfactory at high speeds.

As mentioned in Subsection 4.4.3, the estimated angle has been delayed by  $\pi/2$  during a  $0.2 \text{ s}$  ramp. The resulting angle error is therefore satisfactory nullified.

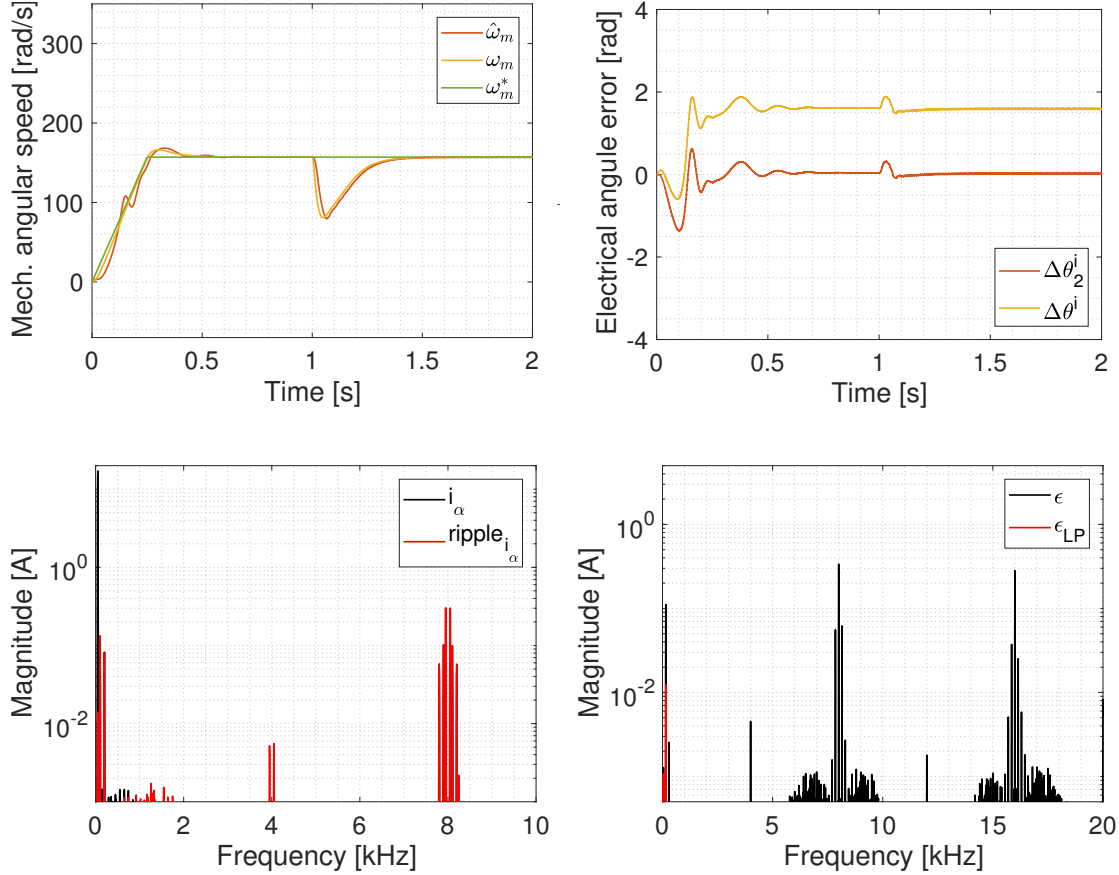


Figure 5.32. Estimator alternative 2 speed and angle error plots (top) and unfiltered and filtered harmonic spectra of  $i_\alpha$  and  $\epsilon$  (bottom). Open-Loop operation, reference speed  $\omega_m^* = 0.5 \cdot \omega_{mn}$  and load torque  $\tau_l = 16 \text{ Nm}$  at  $t = 1 \text{ s}$ . Modulation strategy employed #11 Single-Edge s.r.s. comp..

It is noteworthy to highlight that the torque presence at  $= 0.2 \cdot \omega_{mn}$  speed improves the estimation performance and the speed and position are consequently successfully tracked even at low speeds. Anyway, for higher speeds, the load introduction turns out to increase the ripple in the estimates. Again, the saturation seems not to play a relevant role.

Looking at the current spectra, it is possible to appreciate the effect of the current PLL and ripple calculator block, which makes available a current ripple cleaned of the fundamental component, which is, in heavy load condition,

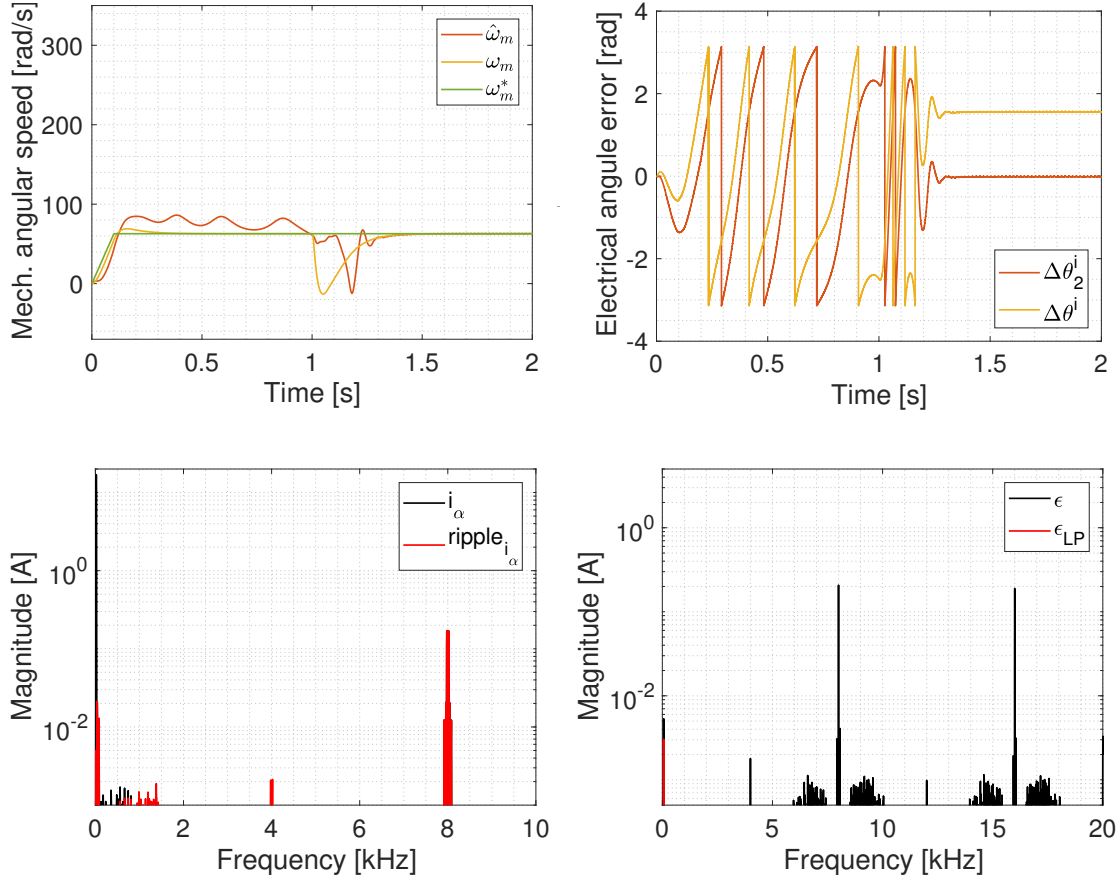


Figure 5.33. Estimator alternative 2 speed and angle error plots (top) and unfiltered and filtered harmonic spectra of  $i_\alpha$  and  $\epsilon$  (bottom). Open-Loop operation, reference speed  $\omega_m^* = 0.2 \cdot \omega_{mn}$  and load torque  $\tau_l = 16 \text{ Nm}$  at  $t = 1 \text{ s}$ . Modulation strategy employed #11 Single-Edge s.r.s. comp..

higher than any other harmonic.

Lastly, the harmonic content in  $\epsilon$  is remarkably higher compared to the one relatively to the estimator alternative 1, but the lower  $\omega_{lce} = 50 \cdot 2\pi \text{ rad/s}$  makes it possible to get rid of it.

### 5.4.4 Estimator 2 in open-loop, other modulations

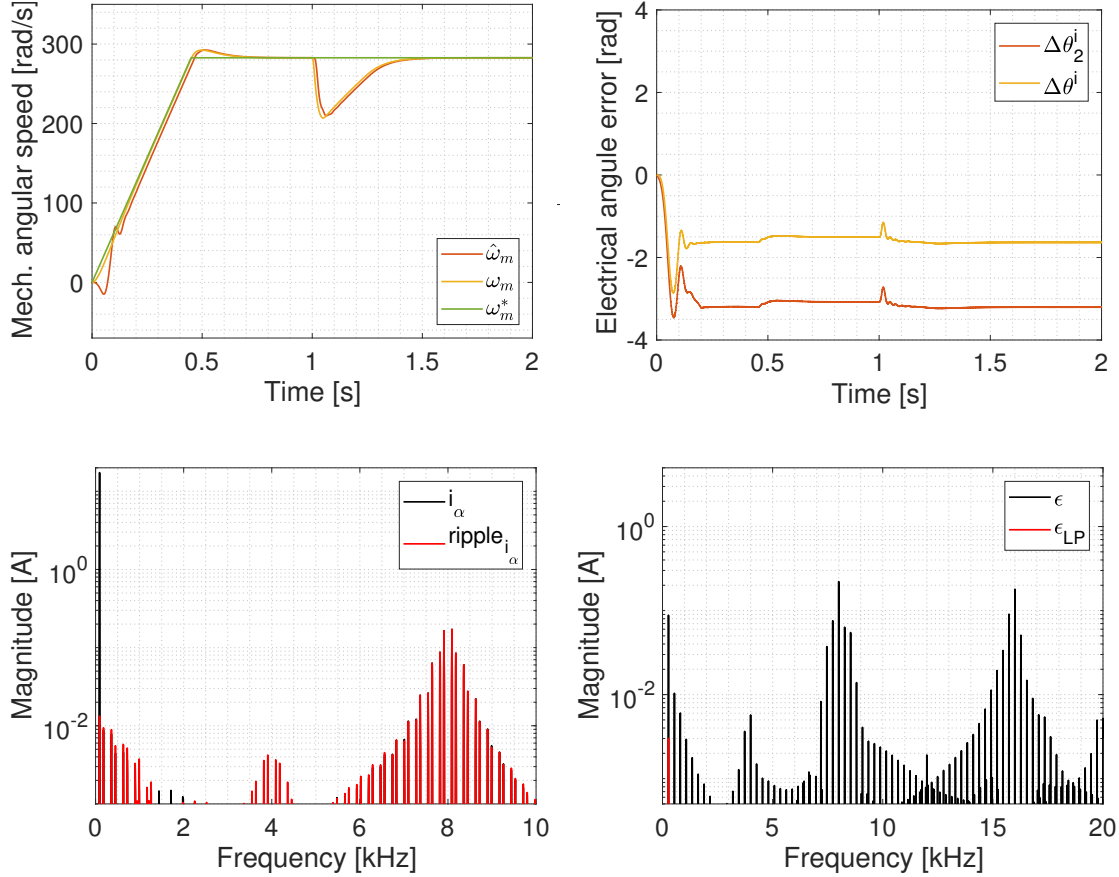


Figure 5.34. Estimator alternative 2 speed and angle error plots (top) and unfiltered and filtered harmonic spectra of  $i_\alpha$  and  $\epsilon$  (bottom). Open-Loop operation, reference speed  $\omega_m^* = 0.9 \cdot \omega_{mn}$  and load torque  $\tau_l = 16 \text{ Nm}$  at  $t = 1 \text{ s}$ . Modulation strategy employed #3 DPWMMAX s.r.s..

The open-loop simulations results for the estimator alternative 2 are summarized in Figure 5.34 relatively to DPWMMAX modulation, in Figure 5.35 relatively to DPWMMIN modulation and in Figure 5.36 relatively to Single-Edge UVMT computed modulation.

In this case, because of the lack of filtering actions around  $f_c$ , the performance with different modulations differs more significantly. While the modulation #9 is consistent with #11, the discontinue modulations are more peculiar. In particular, for DPWMMAX, the error angle  $\Delta\theta_2^i$ , and not  $\Delta\theta^i$  as with

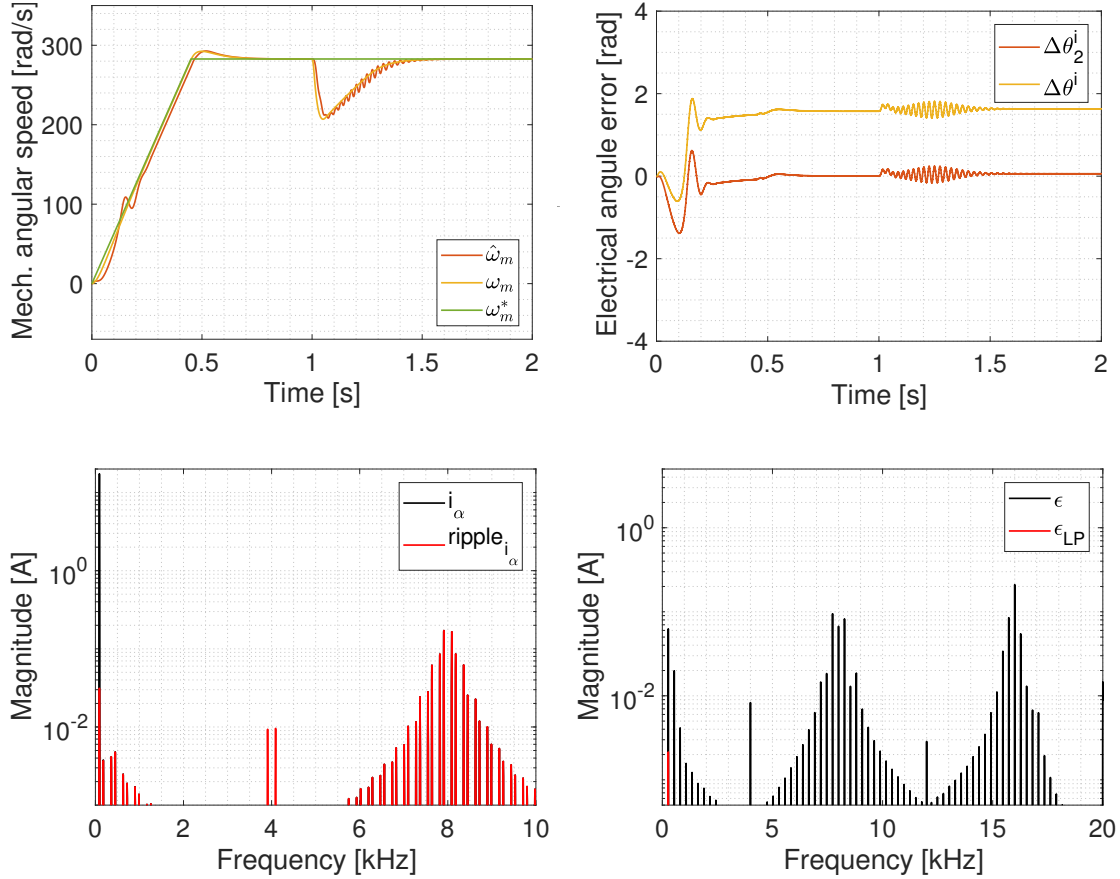


Figure 5.35. Estimator alternative 2 speed and angle error plots (top) and unfiltered and filtered harmonic spectra of  $i_\alpha$  and  $\epsilon$  (bottom). Open-Loop operation, reference speed  $\omega_m^* = 0.9 \cdot \omega_{mn}$  and load torque  $\tau_l = 16 \text{ Nm}$  at  $t = 1 \text{ s}$ . Modulation strategy employed #4 DPWMMIN s.r.s..

alternative 1, converges again to  $-\pi$ . With DPWMMAX, instead, the load insertion causes an important ripple in the estimates.

The difference in the currents and  $\epsilon$  spectra is due just to a different adopted axis scale.

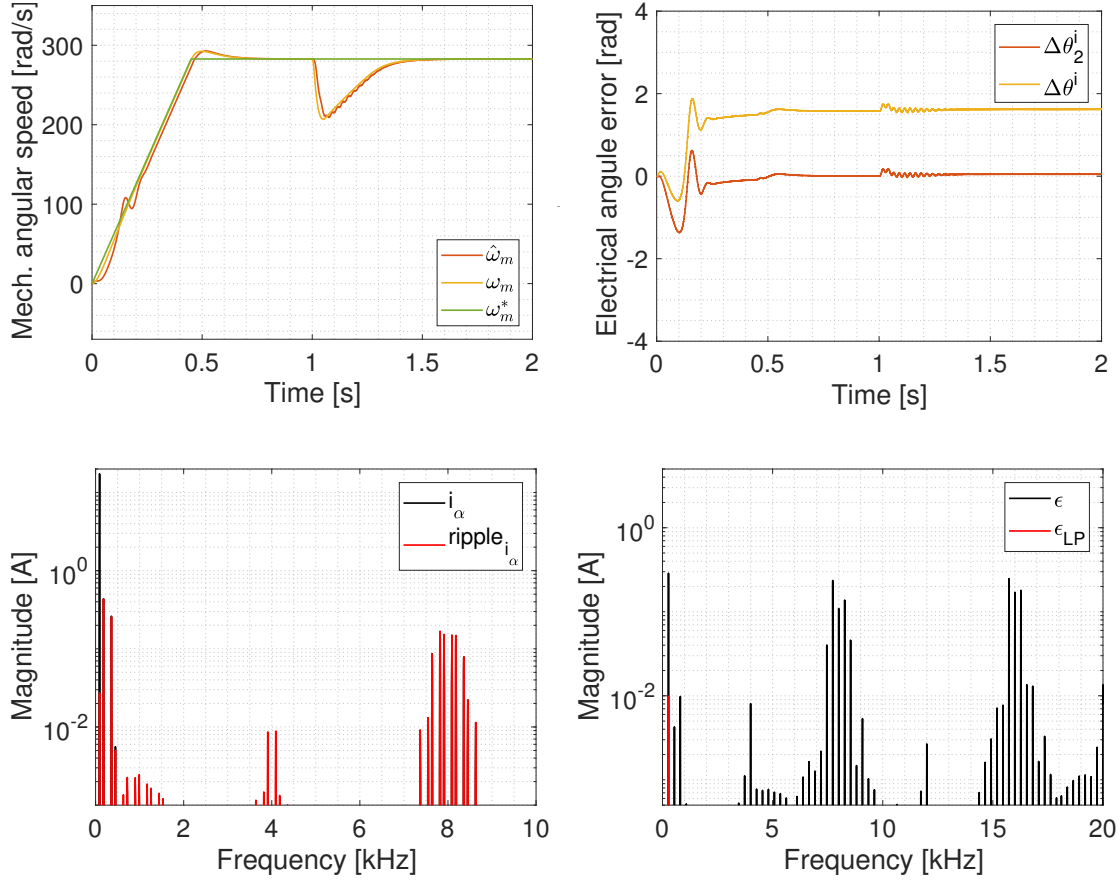


Figure 5.36. Estimator alternative 2 speed and angle error plots (top) and unfiltered and filtered harmonic spectra of  $i_\alpha$  and  $\epsilon$  (bottom). Open-Loop operation, reference speed  $\omega_m^* = 0.9 \cdot \omega_{mn}$  and load torque  $\tau_l = 16 \text{ Nm}$  at  $t = 1 \text{ s}$ . Modulation strategy employed #9 Single-Edge s.r.s. UVMT.

## 5.4.5 Estimator 3 in open-loop

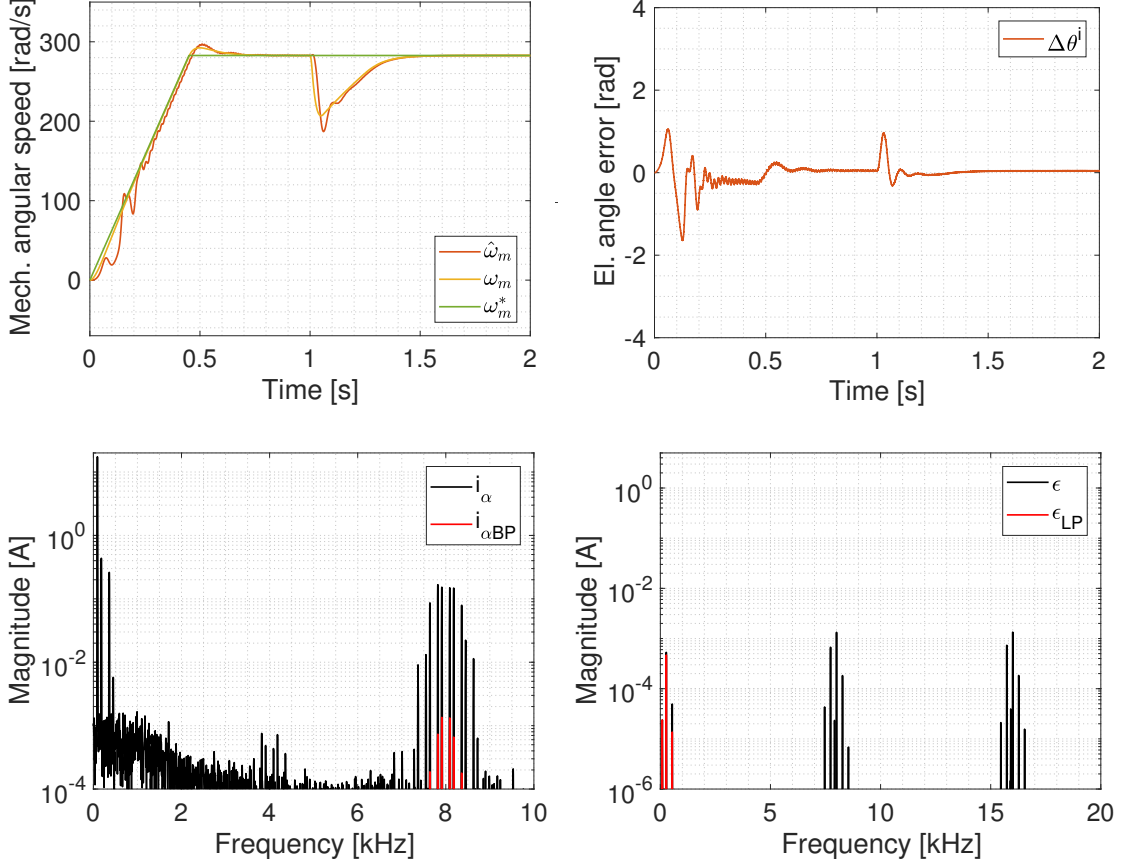


Figure 5.37. Estimator alternative 3 speed and angle error plots (top) and unfiltered and filtered harmonic spectra of  $i_\alpha$  and  $\epsilon$  (bottom). Open-Loop operation, reference speed  $\omega_m^* = 0.9 \cdot \omega_{mn}$  and load torque  $\tau_l = 16 \text{ Nm}$  at  $t = 1 \text{ s}$ . Modulation strategy employed #11 Single-Edge s.r.s. comp..

The open-loop simulations results for the estimator alternative 3 are summarized in Figure 5.37 relatively to  $\omega_m^* = 0.9 \cdot \omega_{mn}$ , in Figure 5.38 relatively to  $\omega_m^* = 0.5 \cdot \omega_{mn}$  and in Figure 5.39 relatively to  $\omega_m^* = 0.2 \cdot \omega_{mn}$ .

The performance of this third alternative is worse than the other solutions. The main reason for that is probably the dependence from the PLL estimated speed  $\hat{\omega}_{me}^{PLL}$ . In fact, relatively to the  $0.9 \cdot \omega_{mn}$  simulation, it can be noticed that in transient conditions, in particular at the starting, when the reference speed is reached and when the load is inserted, both the speed and

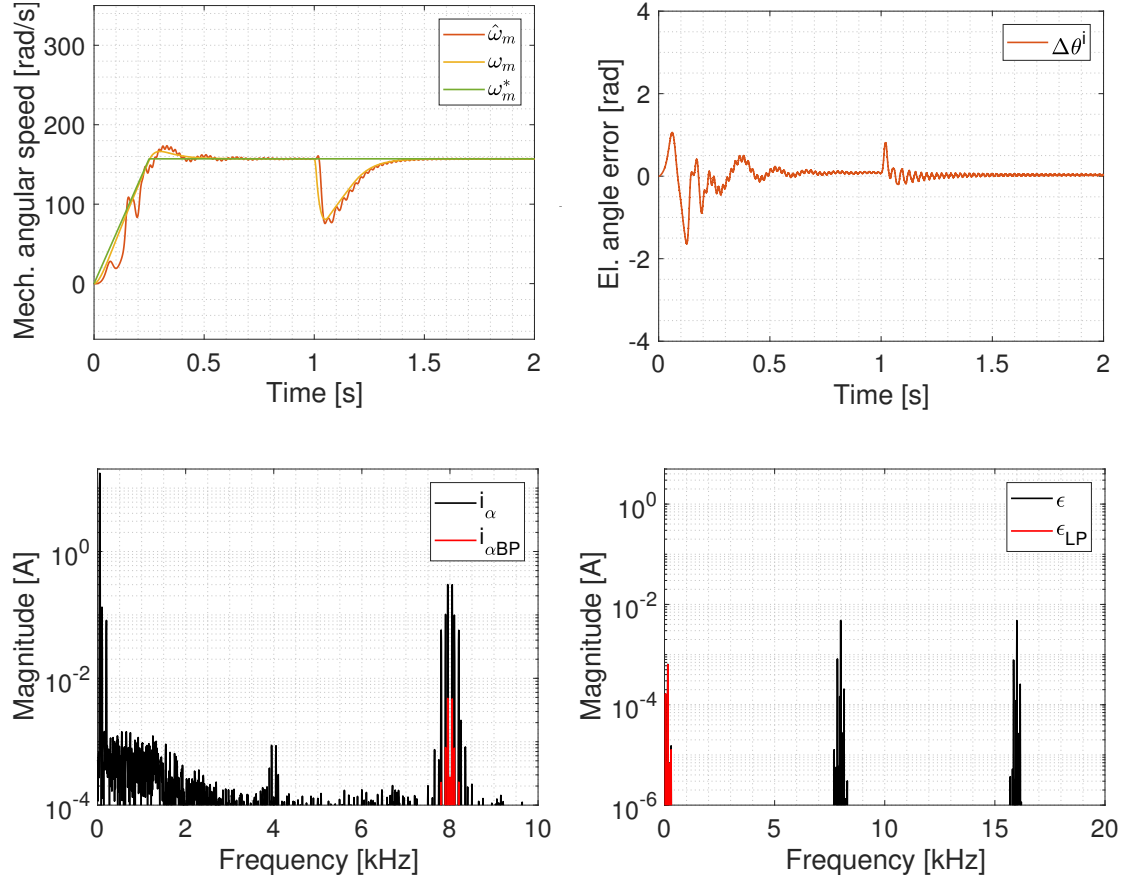


Figure 5.38. Estimator alternative 3 speed and angle error plots (top) and unfiltered and filtered harmonic spectra of  $i_\alpha$  and  $\epsilon$  (bottom). Open-Loop operation, reference speed  $\omega_m^* = 0.5 \cdot \omega_{mn}$  and load torque  $\tau_l = 16 \text{ Nm}$  at  $t = 1 \text{ s}$ . Modulation strategy employed #11 Single-Edge s.r.s. comp..

the position estimates presents the same overshoots of the PLL estimates displayed in Figure 5.23. In steady state, instead, the performance is more satisfactory and in heavy load conditions the estimates are even clean from any ripple.

At low speeds, the performance is poorest, but the load insertion turns again to be helpful.

Lastly, the variable BPF action is noticeable from the current spectra, but it is not as much effective as with the estimator alternative 1.

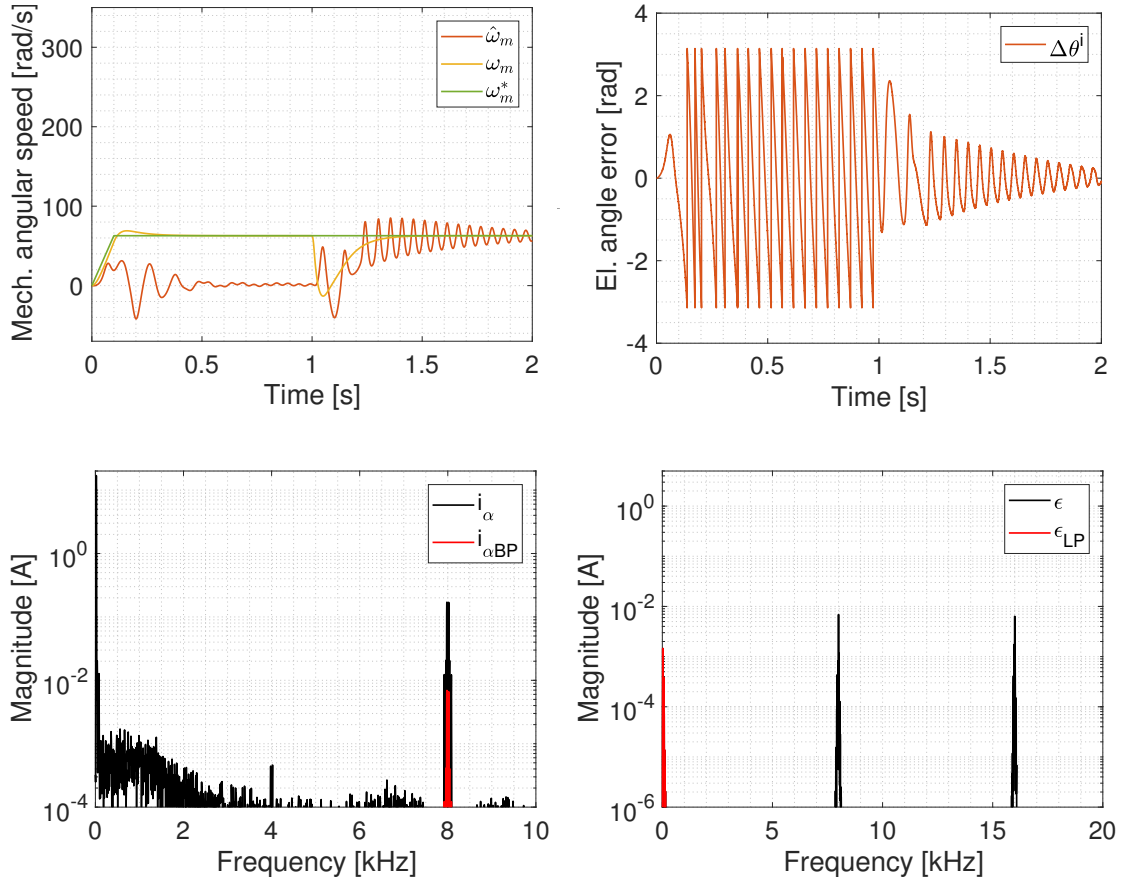


Figure 5.39. Estimator alternative 3 speed and angle error plots (top) and unfiltered and filtered harmonic spectra of  $i_\alpha$  and  $\epsilon$  (bottom). Open-Loop operation, reference speed  $\omega_m^* = 0.2 \cdot \omega_{mn}$  and load torque  $\tau_l = 16 \text{ Nm}$  at  $t = 1 \text{ s}$ . Modulation strategy employed #11 Single-Edge s.r.s. comp..

### 5.4.6 Estimator 3 in open-loop, other modulations

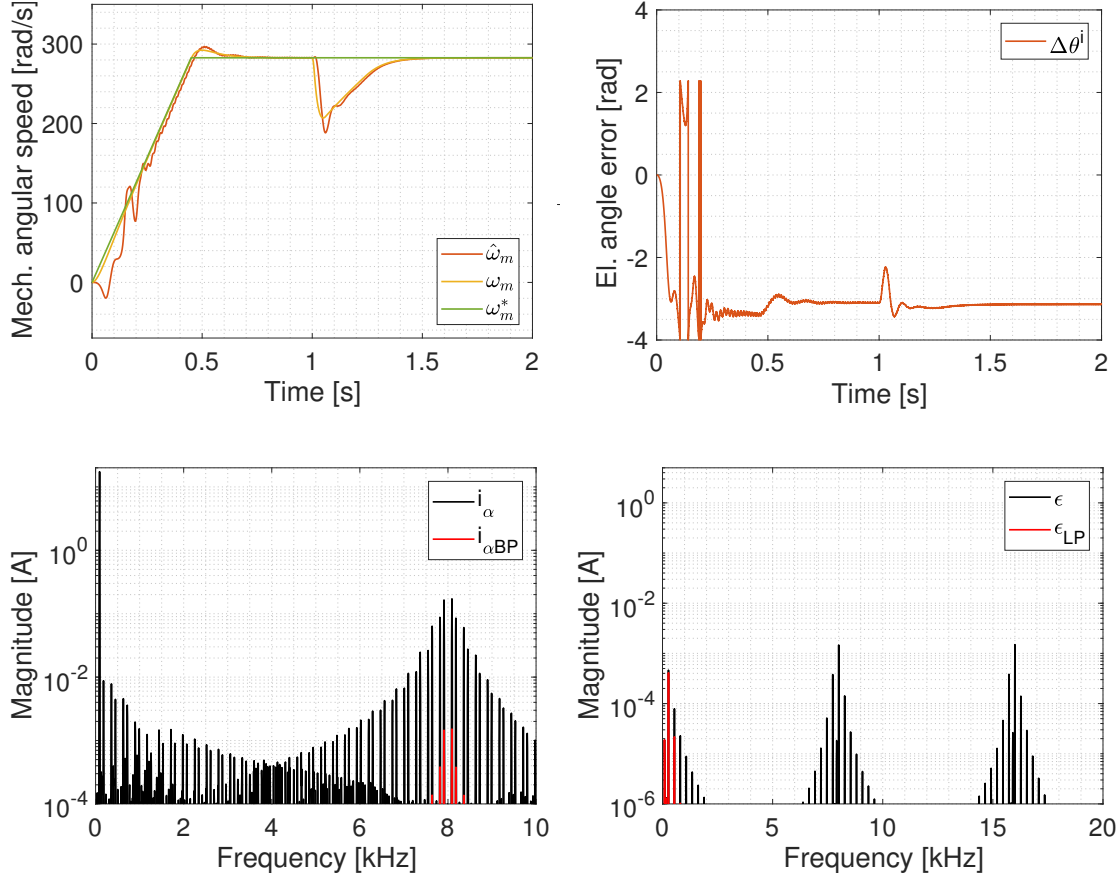


Figure 5.40. Estimator alternative 3 speed and angle error plots (top) and unfiltered and filtered harmonic spectra of  $i_\alpha$  and  $\epsilon$  (bottom). Open-Loop operation, reference speed  $\omega_m^* = 0.9 \cdot \omega_{mn}$  and load torque  $\tau_l = 16 \text{ Nm}$  at  $t = 1 \text{ s}$ . Modulation strategy employed #3 DPWMMAX s.r.s..

The open-loop simulations results for the estimator alternative 3 are summarized in Figure 5.40 relatively to DPWMMAX modulation, in Figure 5.41 relatively to DPWMMIN modulation and in Figure 5.42 relatively to Single-Edge UVMT computed modulation.

As with alternative 2, the BPF action makes the estimator performance independent from the employed modulation, and the PLL influence remains evident in the estimates. Moreover, as well as with both the other alternatives, moreover, with DPWMMAX the error  $\Delta\theta^i$  converges to  $-\pi$ .

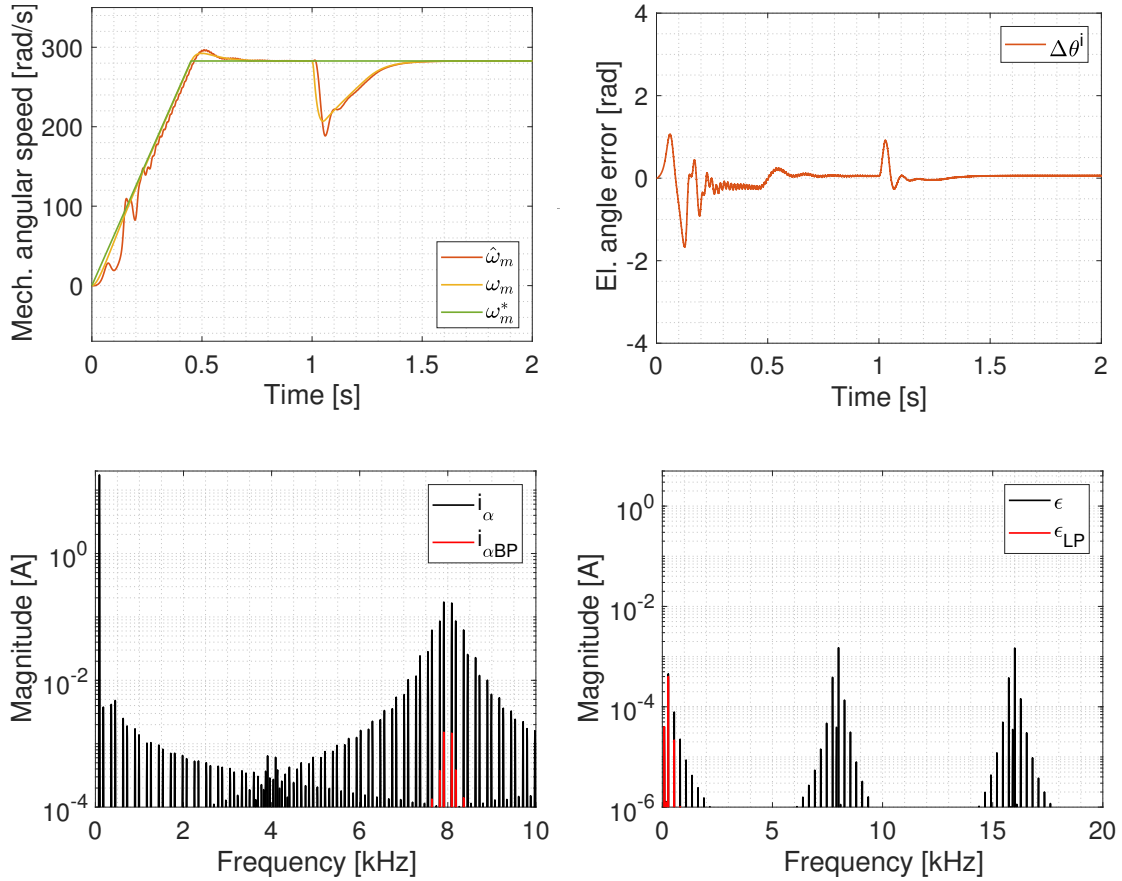


Figure 5.41. Estimator alternative 3 speed and angle error plots (top) and unfiltered and filtered harmonic spectra of  $i_\alpha$  and  $\epsilon$  (bottom). Open-Loop operation, reference speed  $\omega_m^* = 0.9 \cdot \omega_{mn}$  and load torque  $\tau_l = 16 \text{ Nm}$  at  $t = 1 \text{ s}$ . Modulation strategy employed #4 DPWMMIN s.r.s..

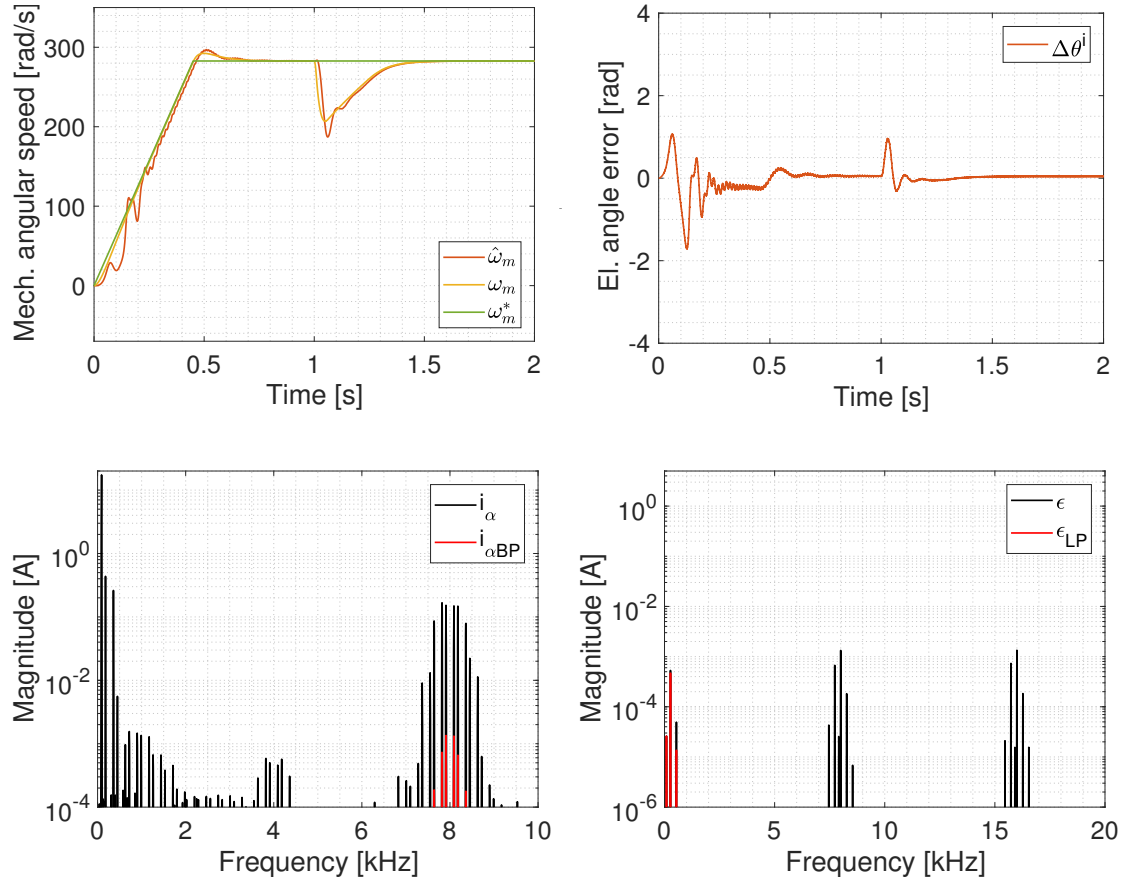


Figure 5.42. Estimator alternative 3 speed and angle error plots (top) and unfiltered and filtered harmonic spectra of  $i_\alpha$  and  $\epsilon$  (bottom). Open-Loop operation, reference speed  $\omega_m^* = 0.9 \cdot \omega_{mn}$  and load torque  $\tau_l = 16 \text{ Nm}$  at  $t = 1 \text{ s}$ . Modulation strategy employed #9 Single-Edge s.r.s. UVMT.

### 5.4.7 Open-Loop torque and inductances

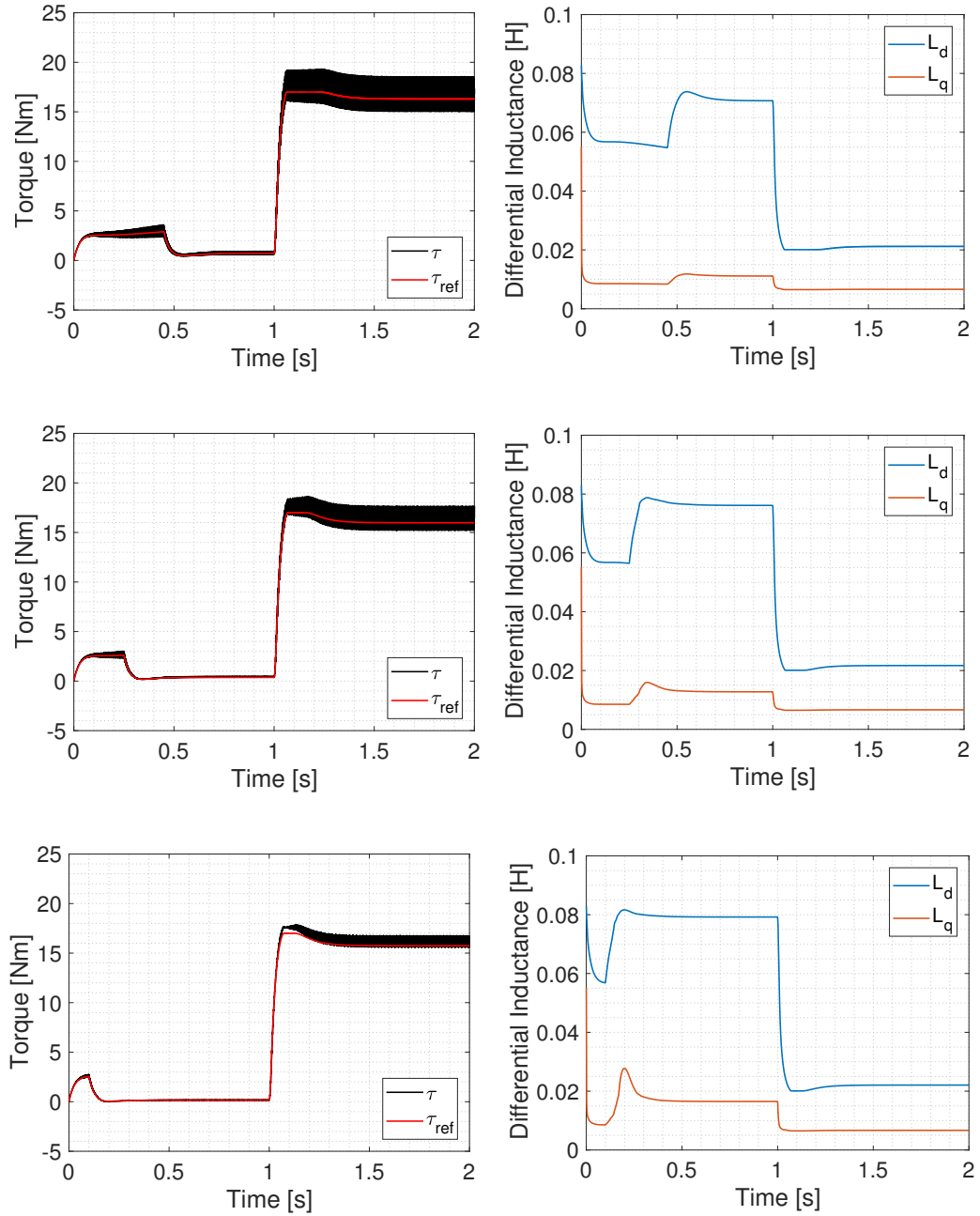


Figure 5.43. Reference and actual torques and inductances variation for the Open-Loop simulations. Reference speed  $\omega_m^*$  equal to  $0.9 \cdot \omega_{mn}$  (top),  $0.5 \cdot \omega_{mn}$  (centre) and  $0.2 \cdot \omega_{mn}$  (bottom) and load torque  $\tau_l = 16 \text{ Nm}$  at  $t = 1 \text{ s}$ .

## 5.5 Closed-loop simulations

In this Section, the closed-loop behaviour of the intrinsic injection estimator is analysed:

- for just the first two proposed alternatives;
- for the four more desirable modulation strategies #3 DPWMMAX, #4 DPWMMIN and #9 and #11 PWM Double-Edge;
- for different values of speed.

With Closed-Loop, it is intended that the drive is working with the estimated speed and position used in the control. In particular, the estimated speed is used in the speed regulator for the calculation of the estimated speed error and in the current regulator to perform the  $dq$ -axis decoupling, while the estimated position is used for the rotational transformations. The schematic relative to the closed-loop simulations is displayed in Figure 5.44.

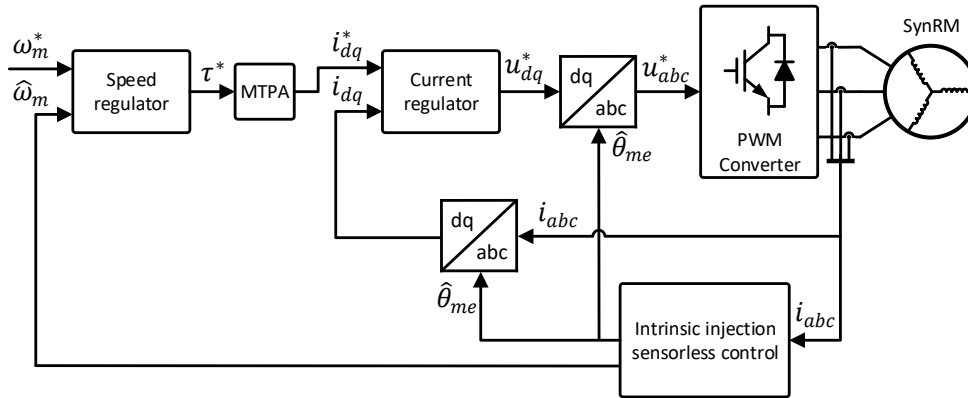


Figure 5.44. Drive schematic for the closed-loop operation of the intrinsic injection estimator.

The reason why the estimator alternative 3 has been pulled out from the current analysis is that the effects that in open-loop only impoverish its performance, and in particular the strong dependence of the estimated speed and

position from the PLL dynamics, in closed-loop make its operation infeasible.

Low speed operations confirms to be a limit also in the closed-loop operation, and, as it is shown in Subsections 5.5.1 and 5.5.3, even in a more severe way.

Reference speed ramps have been adopted again, but they have been set slower than the ones adopted for the open-loop simulations, lasting in particular 1 s to reach ideally the nominal speed. A further limiting factor has turned out to be the load torque. With the motor running in no-load condition, a sudden load insertion higher than 3 Nm makes the estimator lose the tracking. Considering a motor nominal torque equal to 17 Nm, it represents a severe limitation. Therefore, in the simulations this load torque is provided with a ramp, because a sudden insertions may cause the instability of the system. Lastly, the speed regulator bandwidth has been decreased to 30 rad/s.

For each simulation, it has been preferred not to plot the  $i_\alpha$  and the  $\epsilon$  spectra, since they are really noisy and not helpful for the understanding of the phenomena.

### 5.5.1 Estimator 1 in closed-loop

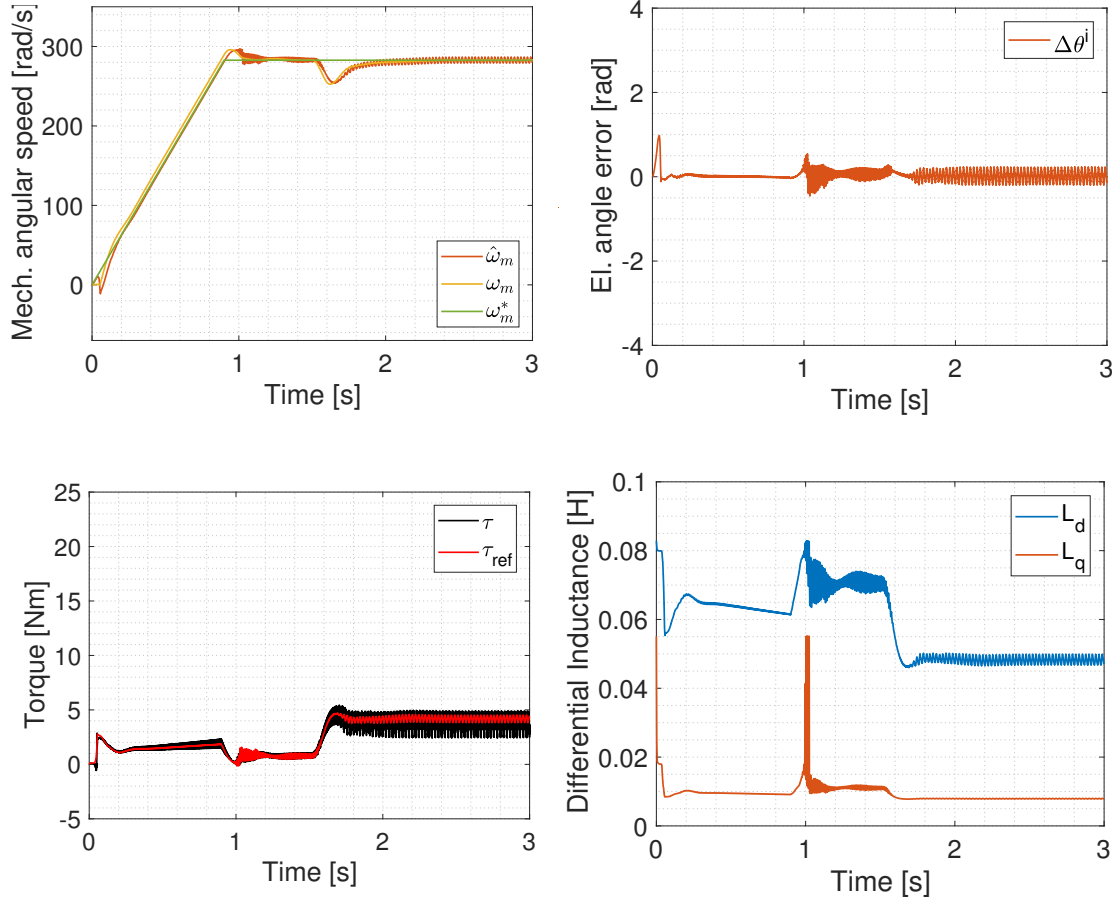


Figure 5.45. Estimator alternative 1 speed and angle error plots (top), reference and actual torques and inductances variation (bottom). Closed-Loop operation, reference speed  $\omega_m^* = 0.9 \cdot \omega_{mn}$  and load torque  $\tau_l = 3 \text{ Nm}$  at  $t = 1.5 \text{ s}$ . Modulation strategy employed #11 Single-Edge s.r.s. comp..

The closed-loop simulation results for the estimator alternative 1 are summarized in Figure 5.45 relatively to  $\omega_m^* = 0.9 \cdot \omega_{mn}$  and in Figure 5.46 relatively to  $\omega_m^* = 0.5 \cdot \omega_{mn}$ .

With the reduced value of load torque, the system behaviour is satisfactory at high speeds. The reference speed ramp is tracked with low deviations and in steady state, both in load and in no-load conditions, the angle error  $\Delta\theta'$  oscillates around zero with bearable oscillation amplitudes. However, if the

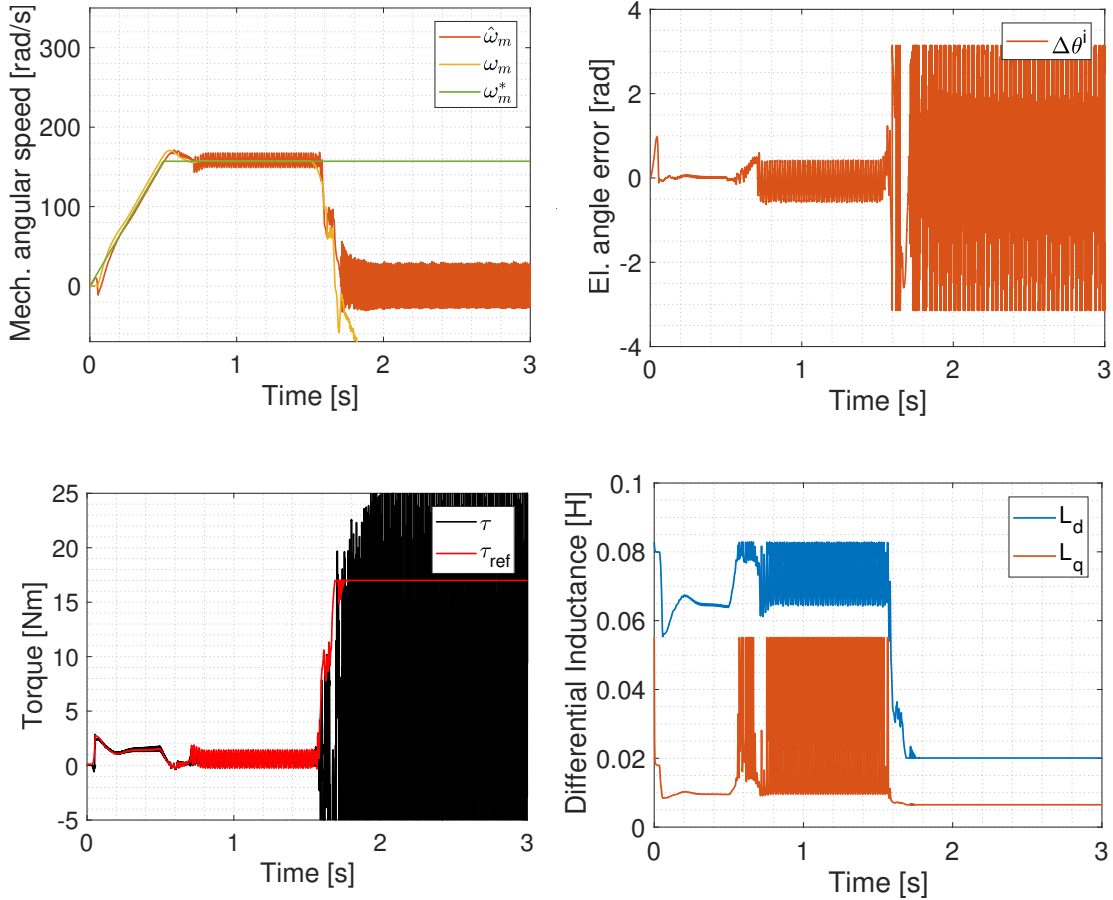


Figure 5.46. Estimator alternative 1 speed and angle error plots (top), reference and actual torques and inductances variation (bottom). Closed-Loop operation, reference speed  $\omega_m^* = 0.5 \cdot \omega_{mn}$  and load torque  $\tau_l = 3 \text{ Nm}$  at  $t = 1.5 \text{ s}$ . Modulation strategy employed #11 Single-Edge s.r.s. comp..

load is increased, the amplitude of these oscillations grows more and more until the point in which the estimator loses the tracking. The saturation and the consequent decrease of the difference  $L_d - L_q$  can be one of its causes, as depicted in Subsection 3.2.2.

For lower values of speed, instead, the magnitude of these oscillations is greater also in no-load conditions and the  $3 \text{ Nm}$  load torque is enough to involve the loss of the tracking.

### 5.5.2 Estimator 1 in closed-loop, other modulations

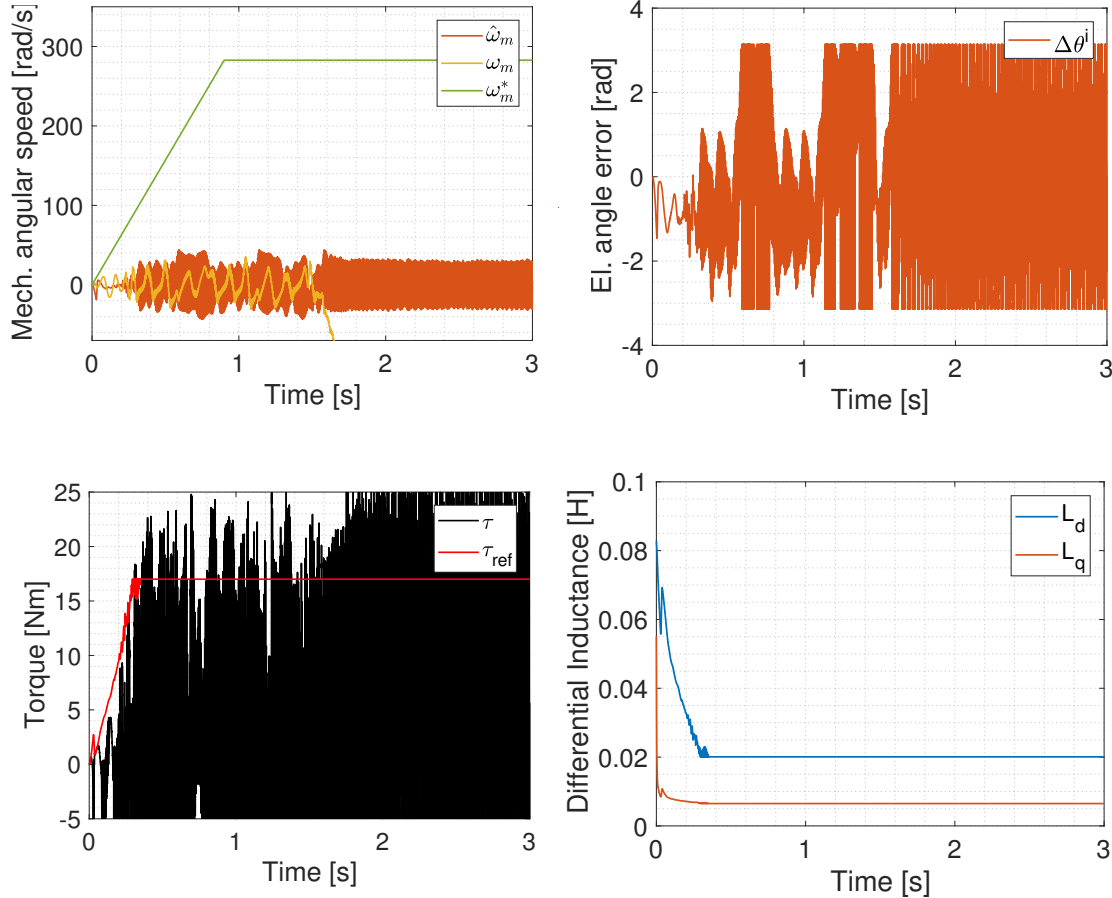


Figure 5.47. Estimator alternative 1 speed and angle error plots (top), reference and actual torques and inductances variation (bottom). Closed-Loop operation, reference speed  $\omega_m^* = 0.9 \cdot \omega_{mn}$  and load torque  $\tau_l = 3 \text{ Nm}$  at  $t = 1.5 \text{ s}$ . Modulation strategy employed #3 DPWMMAX s.r.s..

The closed-loop simulations results for the estimator alternative 1 are summarized in Figure 5.47 relatively to DPWMMAX modulation, in Figure 5.48 relatively to DPWMMIN modulation and in Figure 5.49 relatively to Single-Edge UVMT computed modulation.

Both with DPWMMIN than with the PWM Single-Edge UVMT modulations, the system behaviour does not vary considerably from the comparison PWM Single-Edge, with the former presenting a general higher ripple on

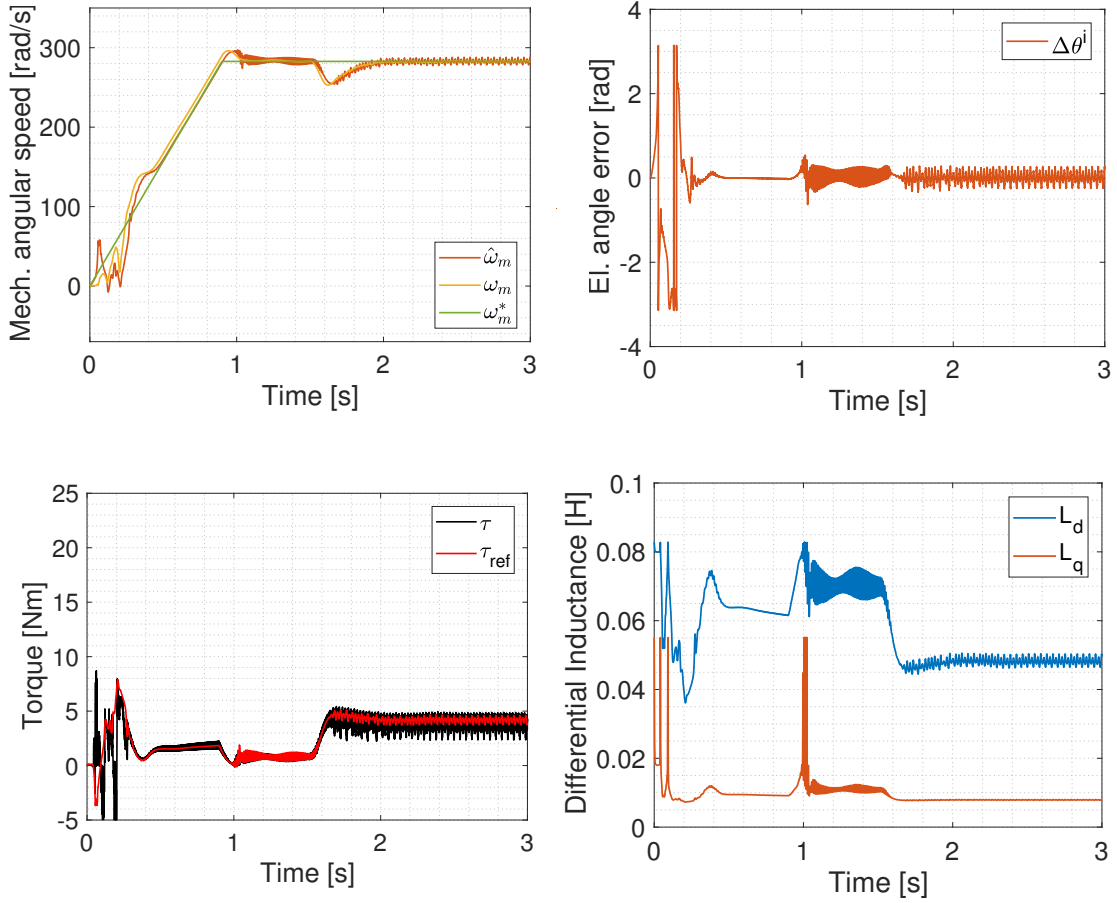


Figure 5.48. Estimator alternative 1 speed and angle error plots (top), reference and actual torques and inductances variation (bottom). Closed-Loop operation, reference speed  $\omega_m^* = 0.9 \cdot \omega_{mn}$  and load torque  $\tau_l = 3 \text{ Nm}$  at  $t = 1.5 \text{ s}$ . Modulation strategy employed #4 DPWMMIN s.r.s..

the estimates. Regarding the DPWMMAX, instead, the fact that the initial speed and position estimate is directed towards negative values, while in open-loop implies just that the error angle  $\Delta\theta'$  converges to the other stable solution  $-\pi$ , in closed-loop it involves the loss of the track, with the drive that is not able to start.

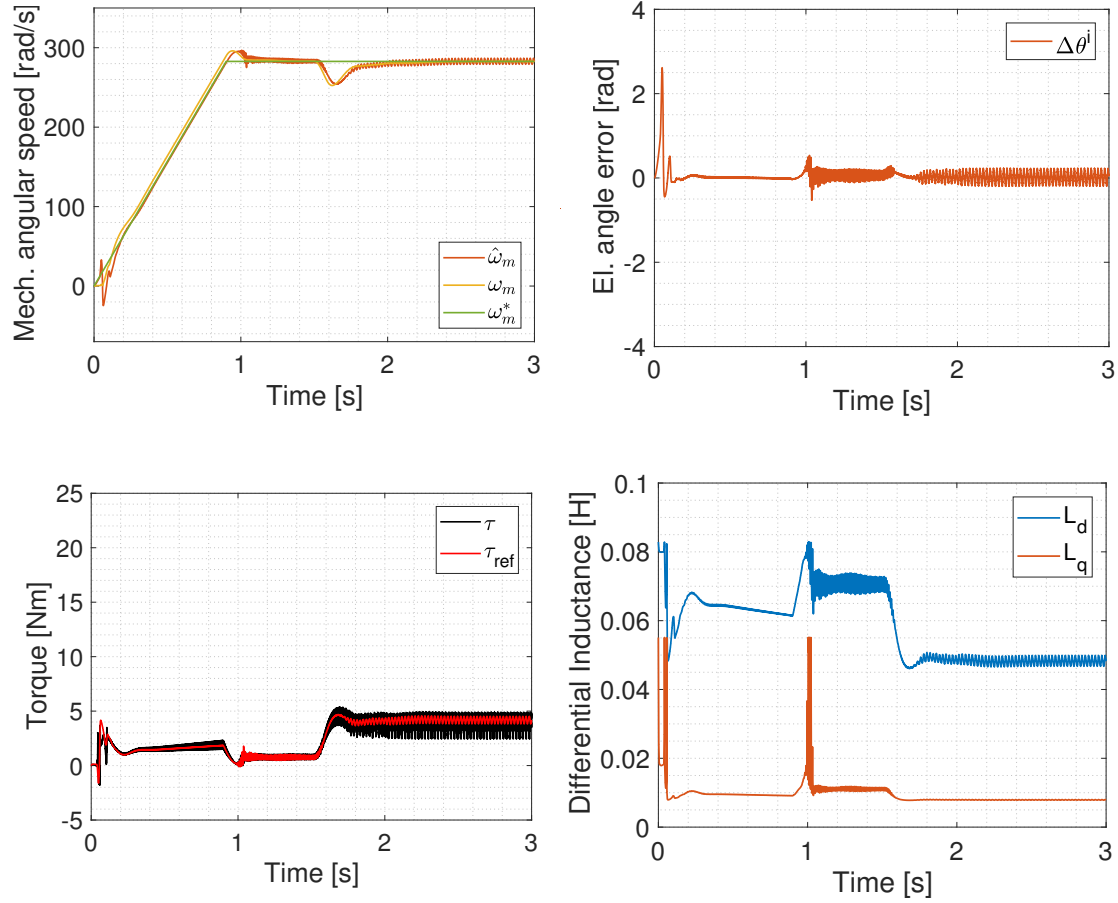


Figure 5.49. Estimator alternative 1 speed and angle error plots (top), reference and actual torques and inductances variation (bottom). Closed-Loop operation, reference speed  $\omega_m^* = 0.9 \cdot \omega_{mn}$  and load torque  $\tau_l = 3 \text{ Nm}$  at  $t = 1.5 \text{ s}$ . Modulation strategy employed #9 Single-Edge s.r.s. UVMT.

## 5.5.3 Estimator 2 in closed-loop

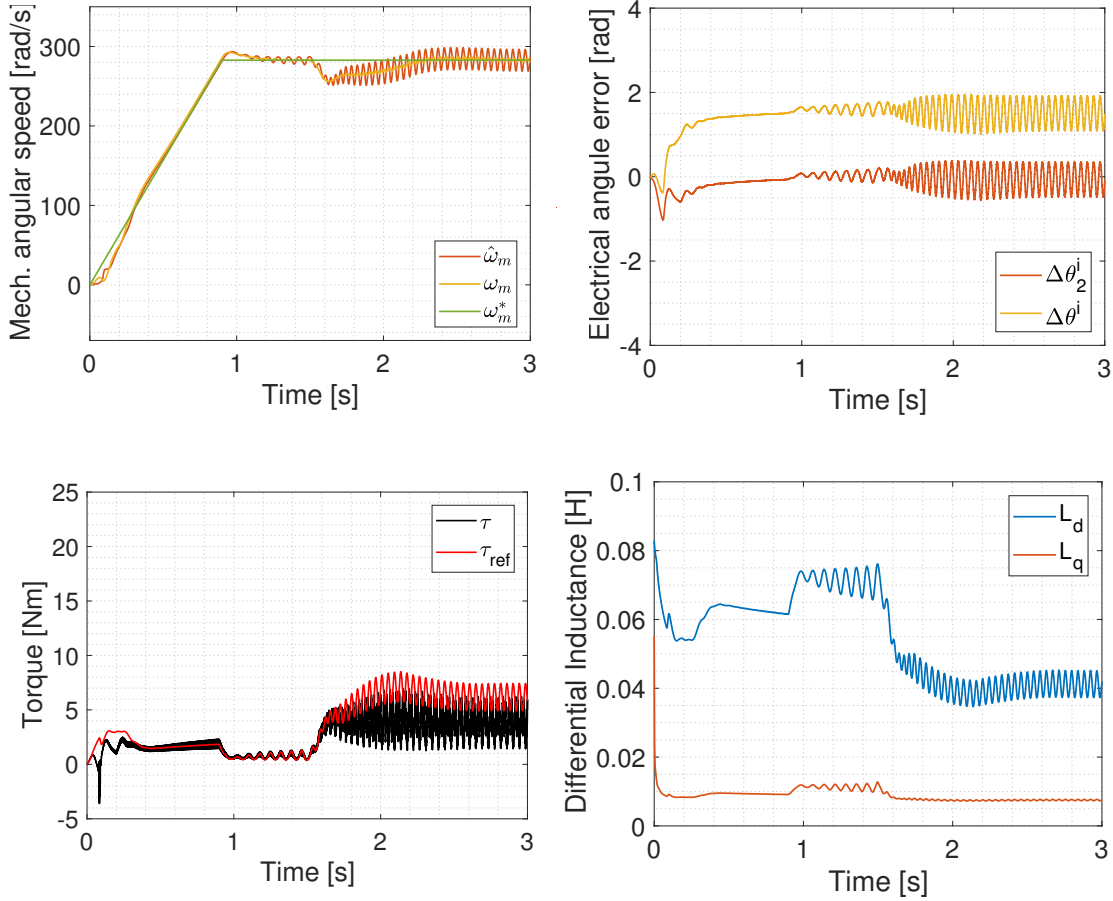


Figure 5.50. Estimator alternative 2 speed and angle error plots (top), reference and actual torques and inductances variation (bottom). Closed-Loop operation, reference speed  $\omega_m^* = 0.9 \cdot \omega_{mn}$  and load torque  $\tau_l = 3 \text{ Nm}$  at  $t = 1.5 \text{ s}$ . Modulation strategy employed #11 Single-Edge s.r.s. comp..

The closed-loop simulations results for the estimator alternative 2 are summarized in Figure 5.50 relatively to  $\omega_m^* = 0.9 \cdot \omega_{mn}$  and in Figure 5.51 relatively to  $\omega_m^* = 0.5 \cdot \omega_{mn}$ .

At high speeds, the performance of the estimator is worse than the alternative 1. The reason for that is the presence in the speed and position estimates of low frequency harmonics. In the case relative to the reference speed of  $0.9 \cdot \omega_{mn}$ , the value of these frequencies is roughly  $15 \text{ Hz}$  in no-load conditions

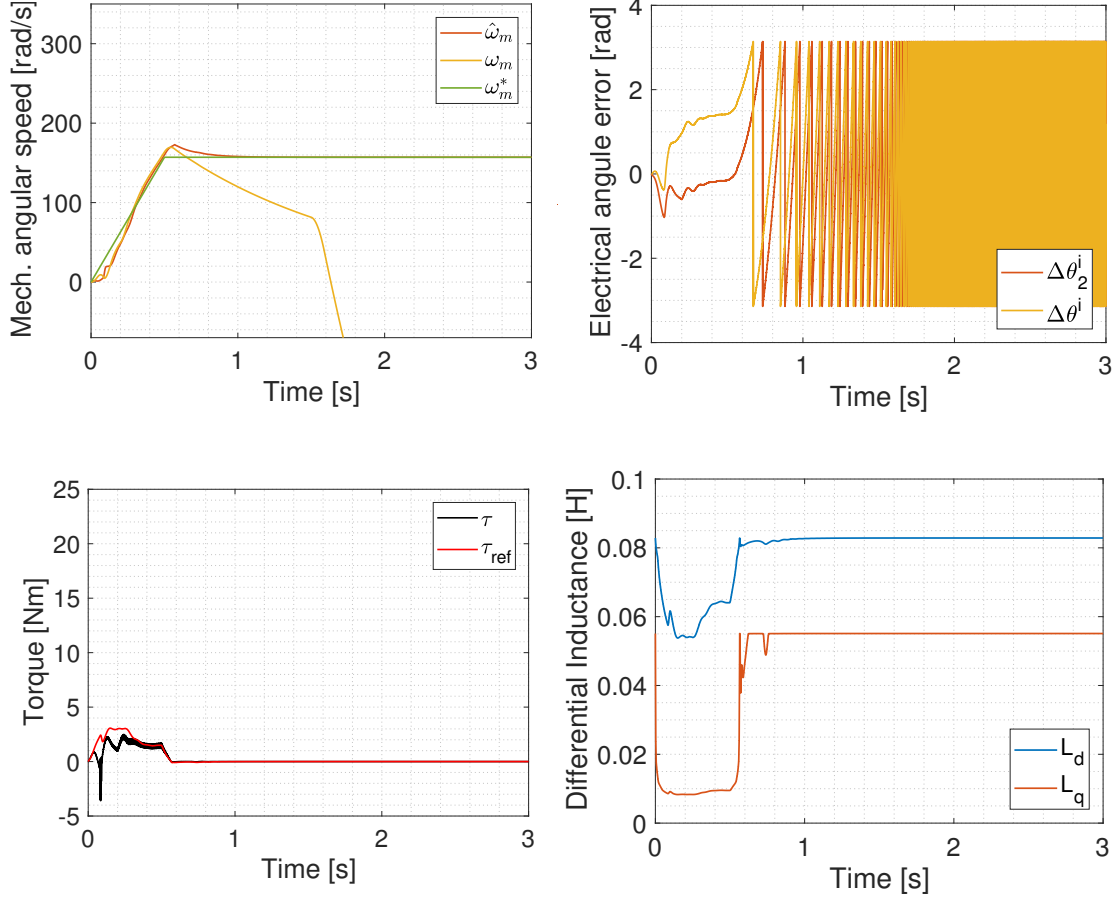


Figure 5.51. Estimator alternative 2 speed and angle error plots (top), reference and actual torques and inductances variation (bottom). Closed-Loop operation, reference speed  $\omega_m^* = 0.5 \cdot \omega_{mn}$  and load torque  $\tau_l = 3 \text{ Nm}$  at  $t = 1.5 \text{ s}$ . Modulation strategy employed #11 Single-Edge s.r.s. comp..

and 25 Hz when the load is inserted. The LPF operating on  $\epsilon$  is not able to affect them since its cut-off frequency cannot be reduced further. Their origin has likely to be related to the PI regulator.

Again, the angle error going close to zero for the alternative 2 is  $\Delta\theta'_2$ .

For lower values of speed, the system is not able to reach the reference neither in no-load conditions. It happens, instead, that the estimated speed is controlled equal to the reference, while the actual speed collapses.

## 5.5.4 Estimator 2 in closed-loop, other modulations

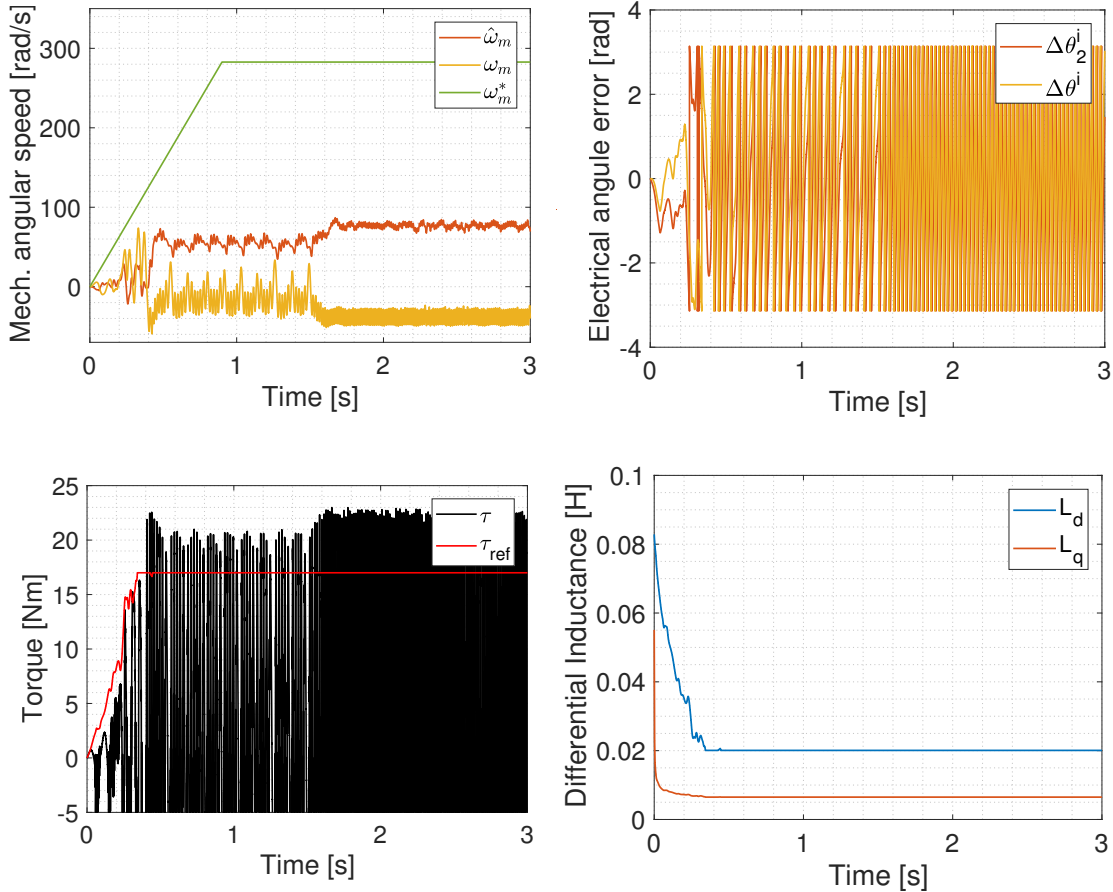


Figure 5.52. Estimator alternative 2 speed and angle error plots (top), reference and actual torques and inductances variation (bottom). Closed-Loop operation, reference speed  $\omega_m^* = 0.9 \cdot \omega_{mn}$  and load torque  $\tau_l = 3 \text{ Nm}$  at  $t = 1.5 \text{ s}$ . Modulation strategy employed #3 DPWMMAX s.r.s..

The closed-loop simulations results for the estimator alternative 2 are summarized in Figure 5.52 relatively to DPWMMAX modulation, in Figure 5.53 relatively to DPWMMIN modulation and in Figure 5.54 relatively to Single-Edge UVMT computed modulation.

In this case, just UVMT PWM Single-Edge presents behaviours similar to the comparison PWM Single-Edge ones, with oscillations slightly higher. With DPWMMAX, in fact, the loss of the track occurs again like with alternative 1,

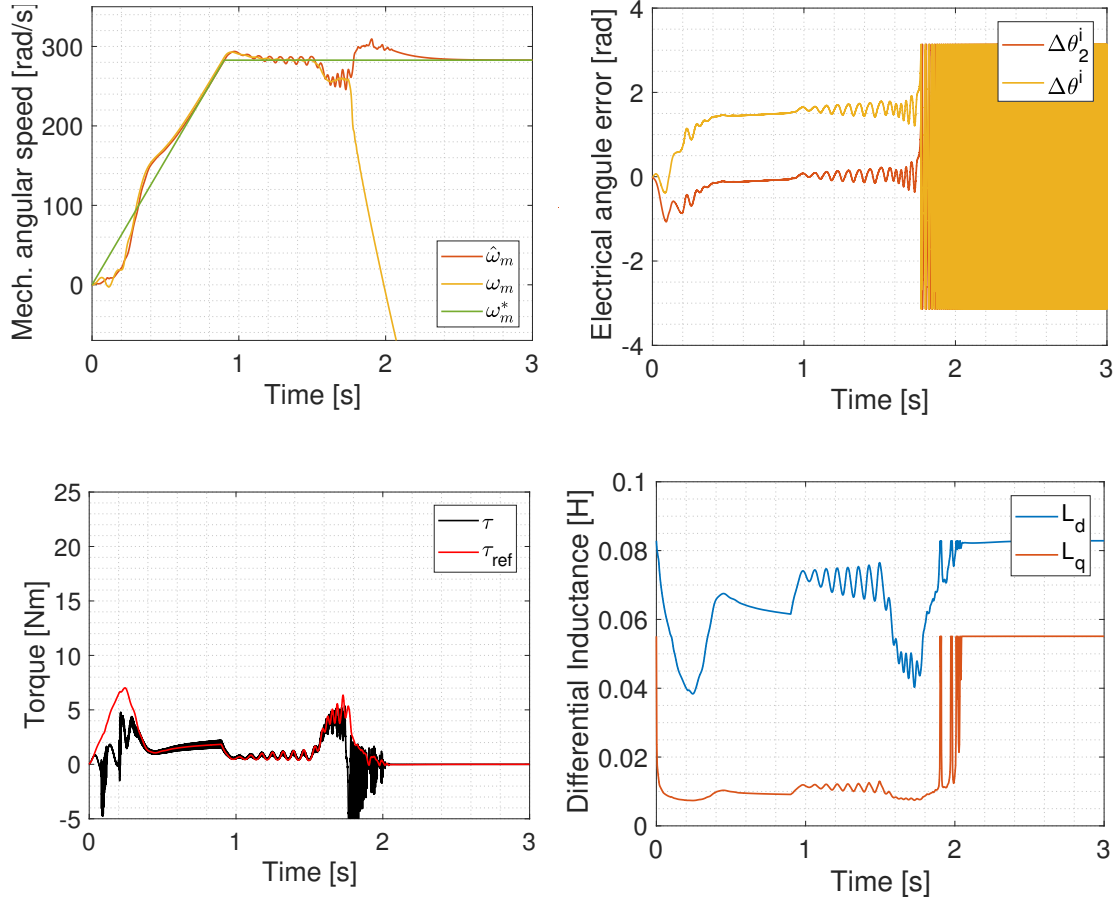


Figure 5.53. Estimator alternative 2 speed and angle error plots (top), reference and actual torques and inductances variation (bottom). Closed-Loop operation, reference speed  $\omega_m^* = 0.9 \cdot \omega_{mn}$  and load torque  $\tau_l = 3 \text{ Nm}$  at  $t = 1.5 \text{ s}$ . Modulation strategy employed #4 DPWMMIN s.r.s..

implying the impossibility for the drive to start. With DPWMMIN, instead, when the load is inserted, it happens again, as well as for low speeds, that the estimated speed is controlled equal to the reference, while the actual speed collapses.

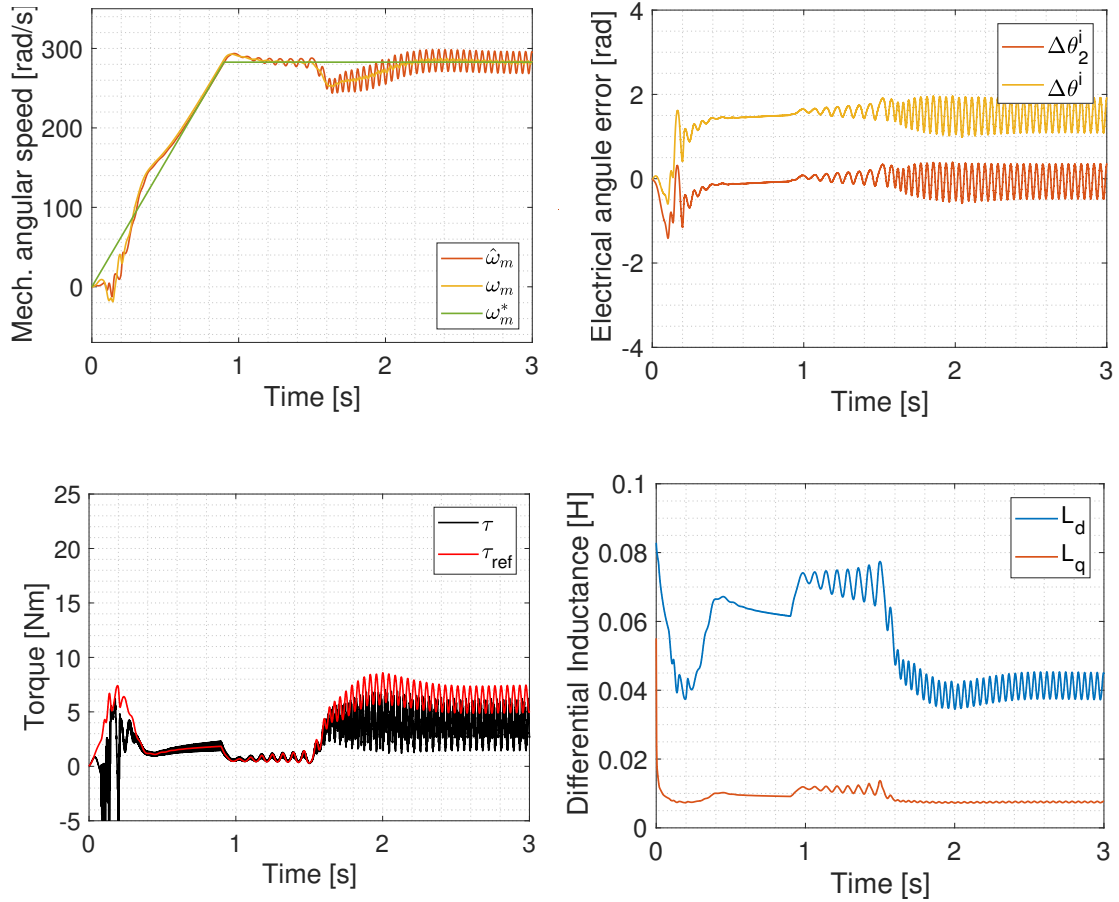


Figure 5.54. Estimator alternative 2 speed and angle error plots (top), reference and actual torques and inductances variation (bottom). Closed-Loop operation, reference speed  $\omega_m^* = 0.9 \cdot \omega_{mn}$  and load torque  $\tau_l = 3 \text{ Nm}$  at  $t = 1.5 \text{ s}$ . Modulation strategy employed #9 Single-Edge s.r.s. UVMT.

## 5.6 Sampling and oversampling

In this Section, the influence of the sampling frequency  $T_s$  and of the "fake" oversampling introduced are analysed for the three different proposed estimator alternatives.

The reference simulation is the same as the one relative to the open-loop, with a reference speed  $\omega_m^* = 0.9 \cdot \omega_{mn}$  and load torque  $\tau_l = 16 \text{ Nm}$  at  $t = 1 \text{ s}$  and the modulation strategy #11 Single-Edge s.r.s. comp. employed.

It is noteworthy to say that the sampling frequency chosen is in the range of  $2 \text{ MHz}$ , as proposed in [23] and [24] for an injection sensorless control. The use of such an high frequency in that application is aimed to the reduction of measurements noise and quantization errors. Moreover, as illustrated in this Section, also the increase of the "fake" oversampling frequency can play a relevant role in the behaviour of the digital control system.

## 5.6.1 Estimator 1

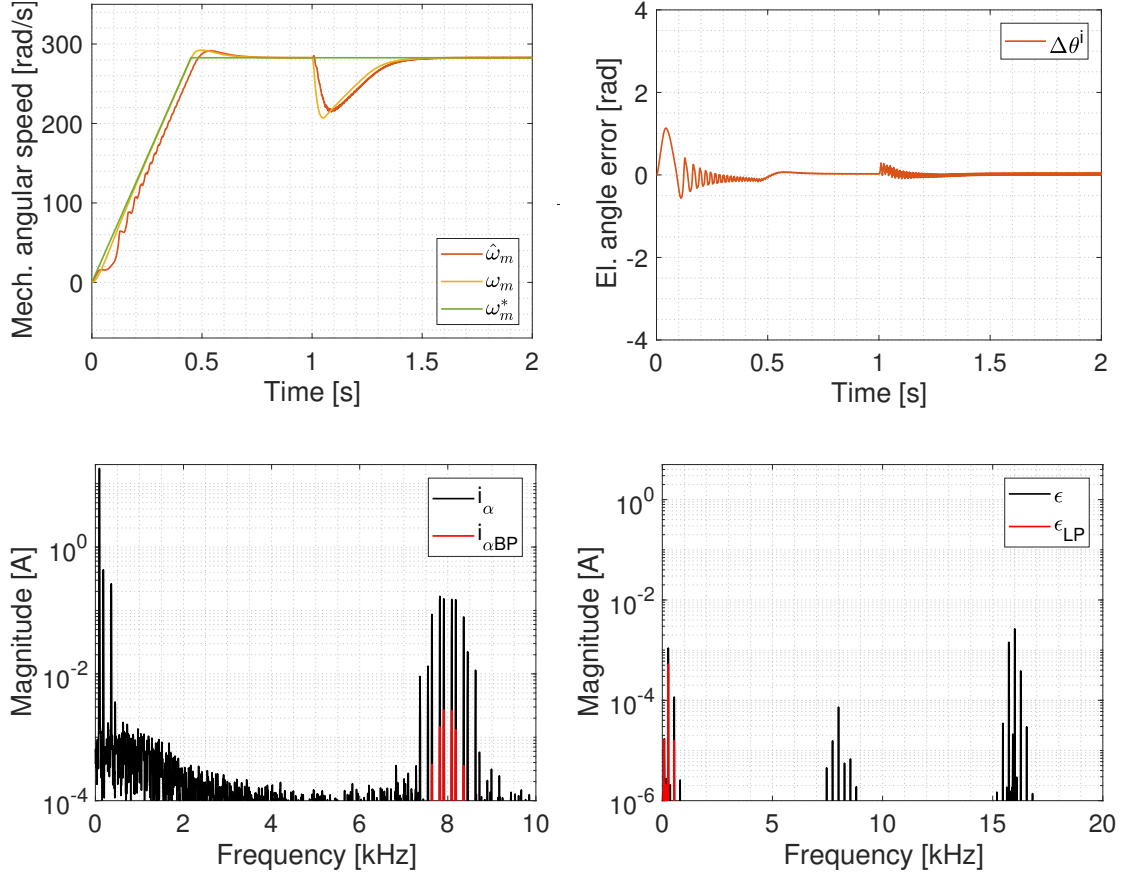


Figure 5.55. Estimator alternative 1 open-loop simulation. Current sampling frequency  $f_s = 2 \text{ MHz}$  and equal FPGA fake oversampling at  $f_{FPGA} = 2 \text{ MHz}$ .

The simulation results showing the sampling influence for the estimator alternative 1 are summarized in Figure 5.55 relatively to  $f_s = 2 \text{ MHz}$ , in Figure 5.56 and Figure 5.57 relatively to  $f_s = 0.5 \text{ MHz}$  and in Figure 5.58 relatively to  $f_s = 0.25 \text{ MHz}$ . The oversampling at a higher frequency is applied only relative to the simulation of Figure 5.56, otherwise  $T_{FPGA} = T_s$ .

Relatively to this estimator alternative, it can be noticed that the lower is  $T_s$ , the higher is the noise in the current spectra and consequently in the  $\epsilon$  spectra, resulting thus in a lower signal-to-noise ratio. This involves, therefore, a worse estimator performance, with higher amplitude ripple in the estimates for lower sampling frequencies.

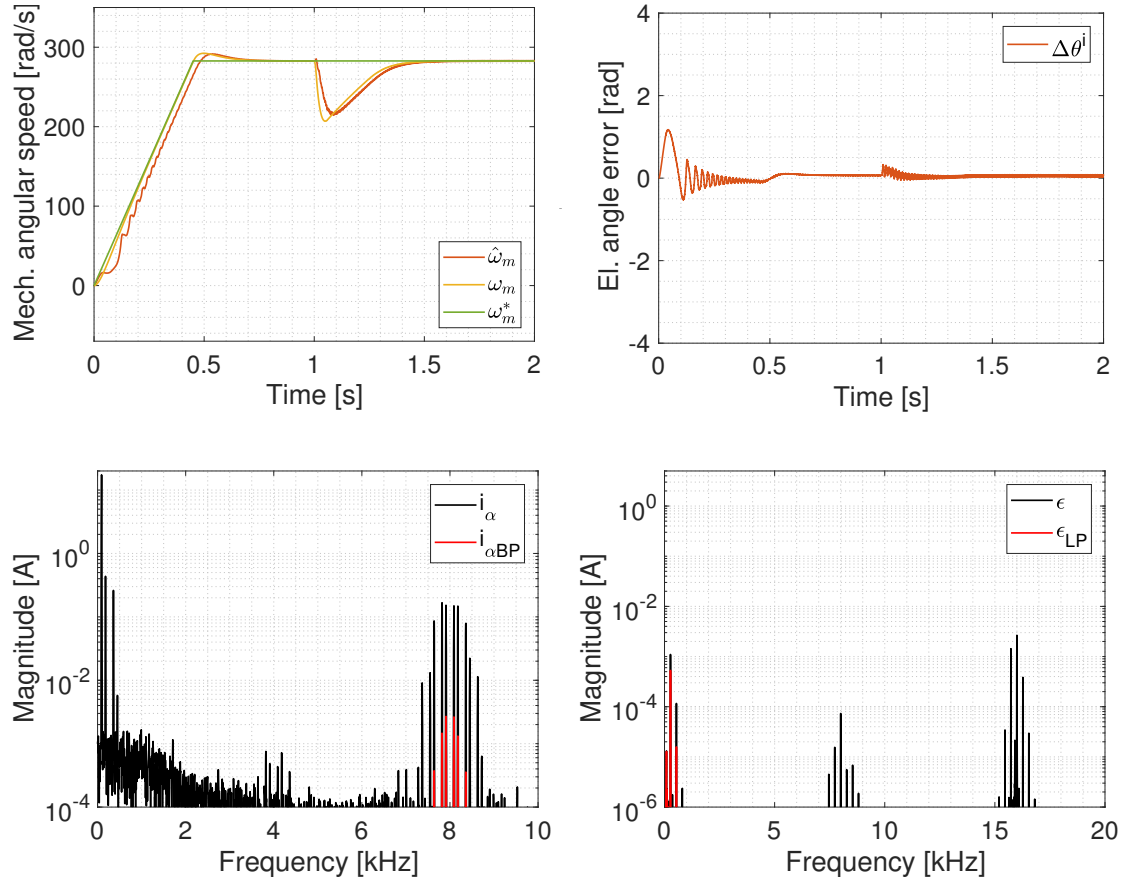


Figure 5.56. Estimator alternative 1 open-loop simulation. Current sampling frequency  $f_s = 0.5 \text{ MHz}$  and FPGA fake oversampling at  $f_{FPGA} = 2 \text{ MHz}$ , i.e. the choice adopted in the rest of the work.

Moreover, from the comparison between Figures 5.56 and 5.57, a remarkable aspect is that the increase of the "fake" oversampling frequency  $T_{FPGA}$  involves an improvement of the signal-to-noise ratio as if the currents were sampled at an higher  $T_s$  equal to  $T_{FPGA}$ .

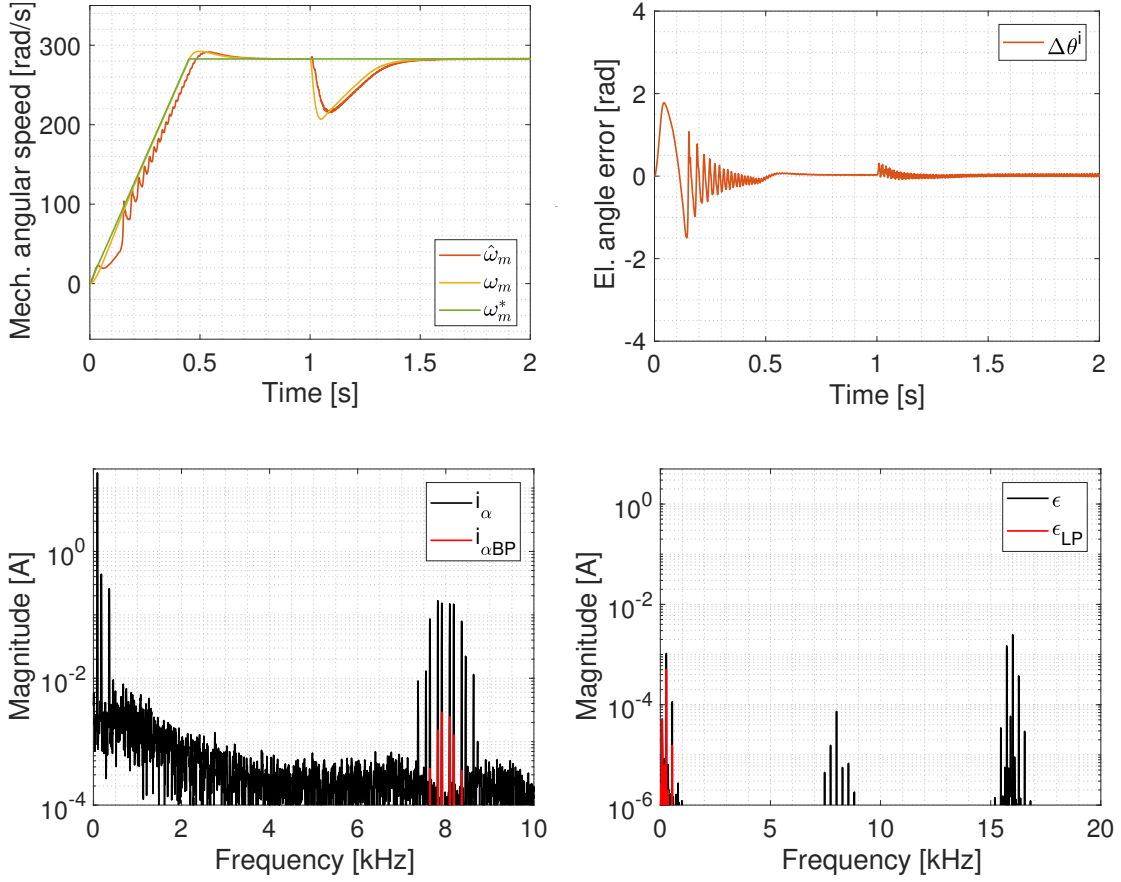


Figure 5.57. Estimator alternative 1 open-loop simulation. Current sampling frequency  $f_s = 0.5 \text{ MHz}$  and equal FPGA fake oversampling at  $f_{FPGA} = 0.5 \text{ MHz}$ .

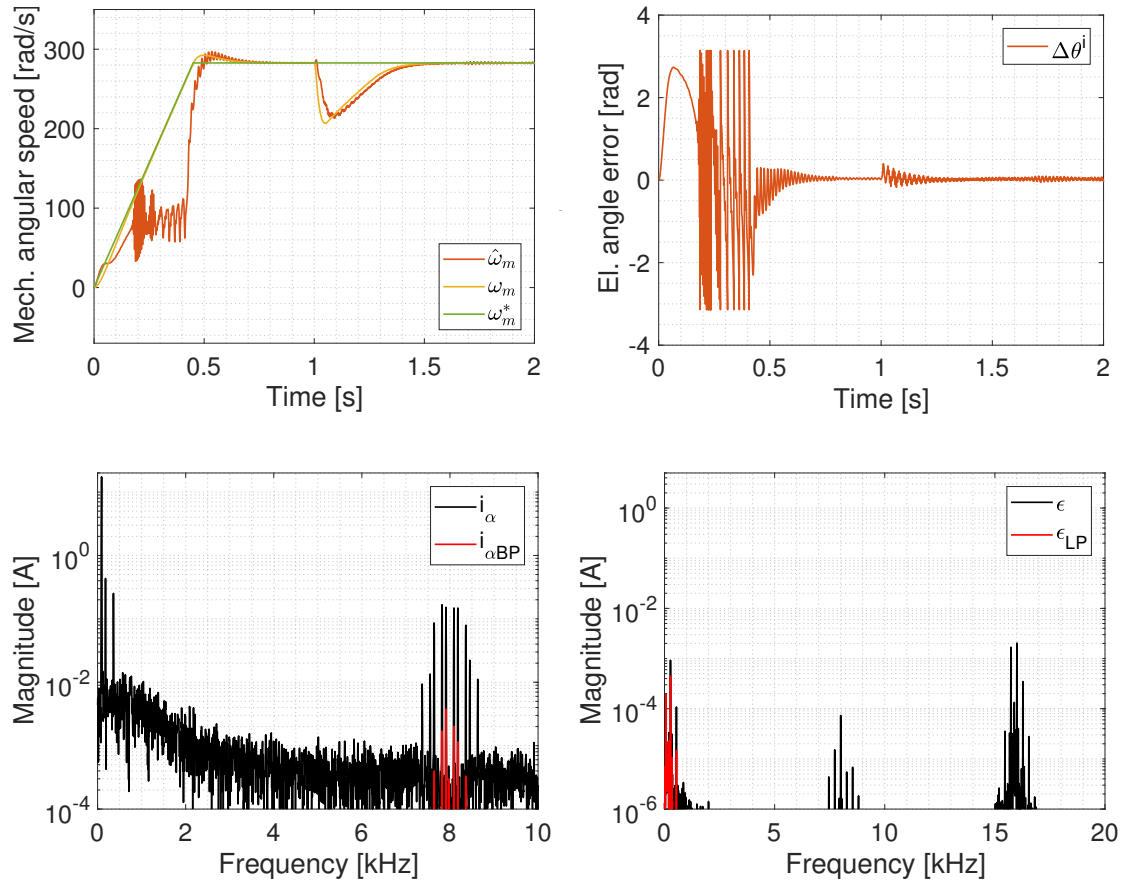


Figure 5.58. Estimator alternative 1 open-loop simulation. Current sampling frequency  $f_s = 0.25 \text{ MHz}$  and equal FPGA fake oversampling at  $f_{FPGA} = 0.25 \text{ MHz}$ .

## 5.6.2 Estimator 2

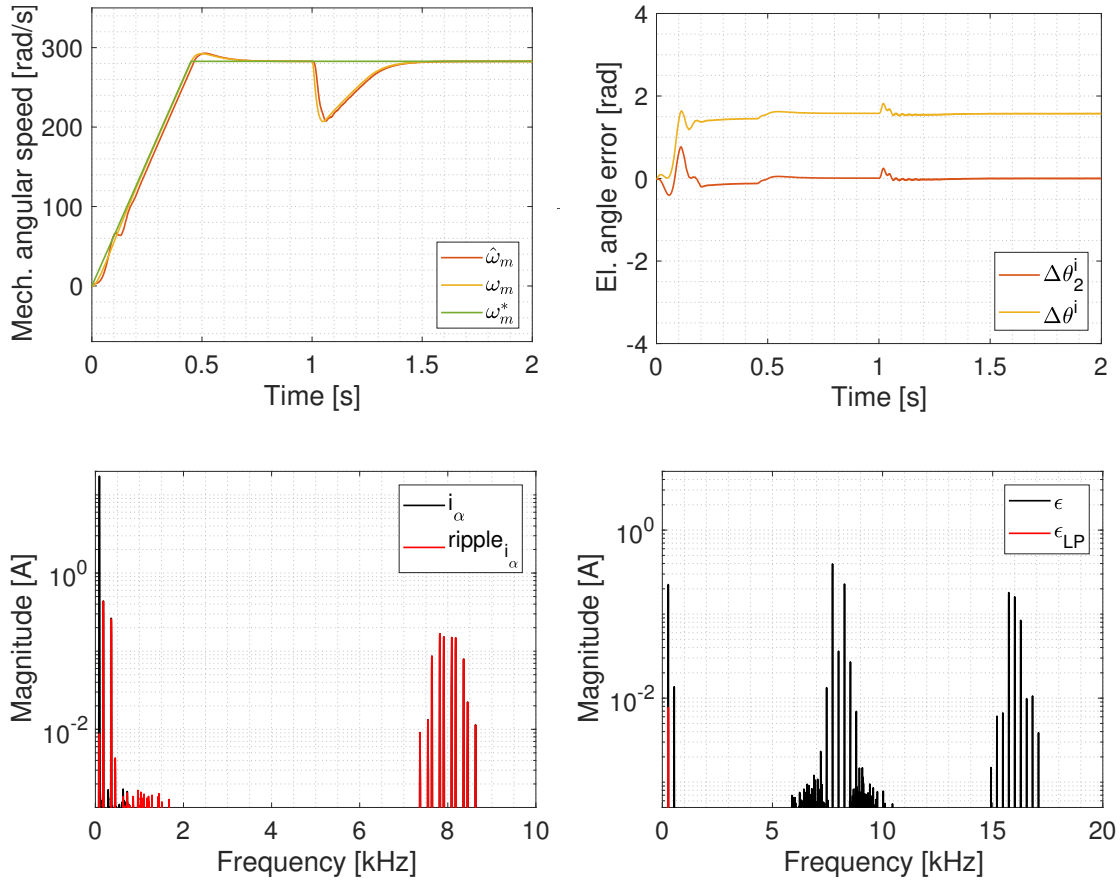


Figure 5.59. Estimator alternative 2 open-loop simulation. Current sampling frequency  $f_s = 2 \text{ MHz}$  and equal FPGA fake oversampling at  $f_{FPGA} = 2 \text{ MHz}$ .

The simulation results showing the sampling influence for the estimator alternative 2 are summarized in Figure 5.59 relatively to  $f_s = 2 \text{ MHz}$ , in Figure 5.60 and Figure 5.61 relatively to  $f_s = 0.5 \text{ MHz}$  and in Figure 5.62 relatively to  $f_s = 0.25 \text{ MHz}$ . The oversampling at a higher frequency is applied only relative to the simulation of Figure 5.60, otherwise  $T_{FPGA} = T_s$ .

Relatively to this estimator alternative, differently from the first alternative, the lower noise in the current spectra for higher sample frequencies does not affect the estimator performance.

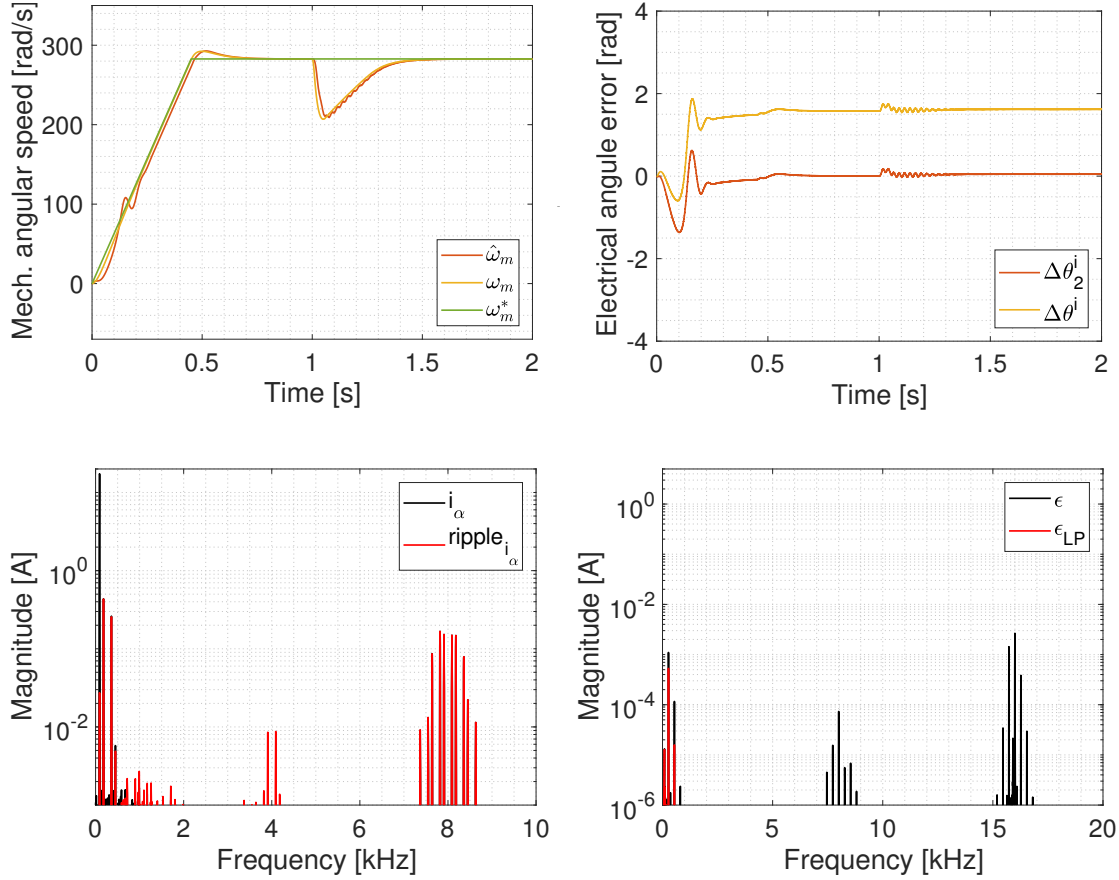


Figure 5.60. Estimator alternative 2 open-loop simulation. Current sampling frequency  $f_s = 0.5 \text{ MHz}$  and FPGA fake oversampling at  $f_{FPGA} = 2 \text{ MHz}$ , i.e. the choice adopted in the rest of the work.

Furthermore, it can be noticed that, while the higher "fake" oversampling frequency at  $T_{FPGA} = 2 \text{ MHz}$  when  $T_s = 0.5 \text{ MHz}$  involves higher signal-to-noise ratio in steady state operation compared to the case where  $T_{FPGA} = T_s = 0.5 \text{ MHz}$ , in the transient it results less effective and the estimates appeared less damped.

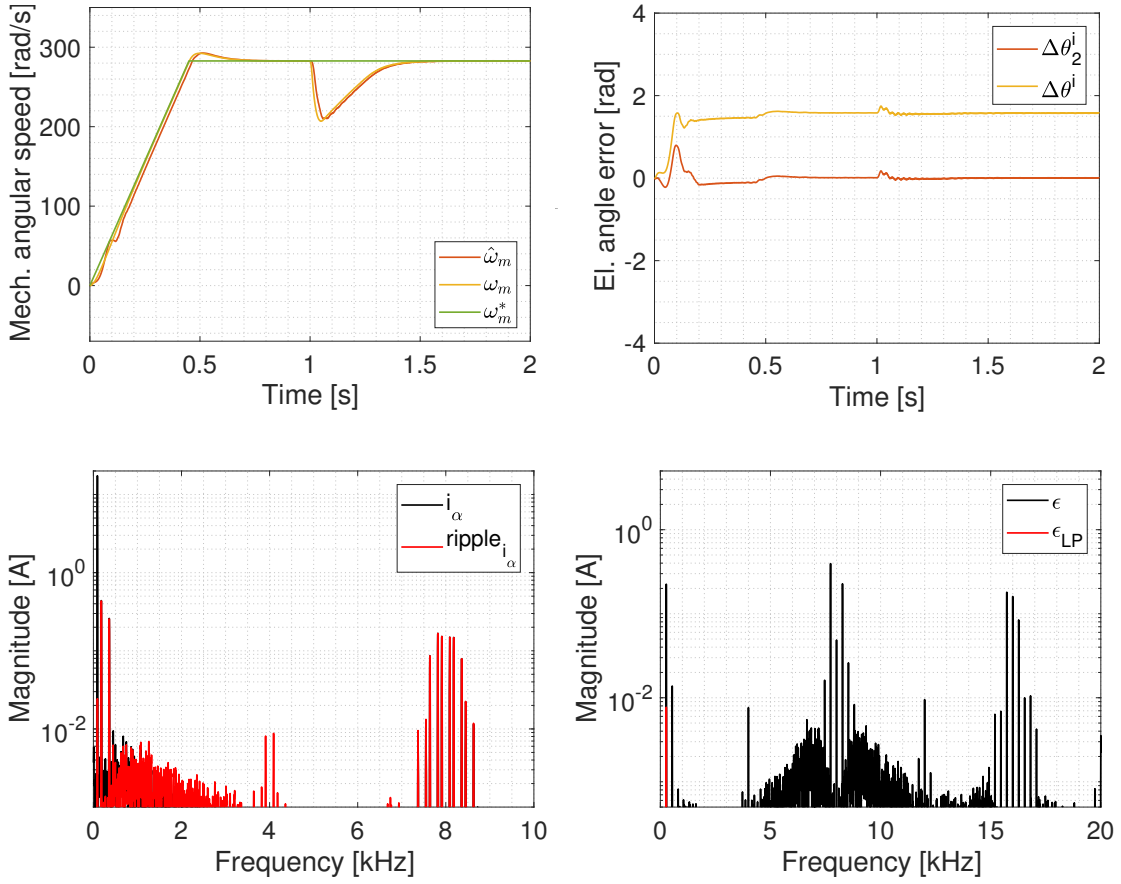


Figure 5.61. Estimator alternative 2 open-loop simulation. Current sampling frequency  $f_s = 0.5 \text{ MHz}$  and equal FPGA fake oversampling at  $f_{FPGA} = 0.5 \text{ MHz}$ .

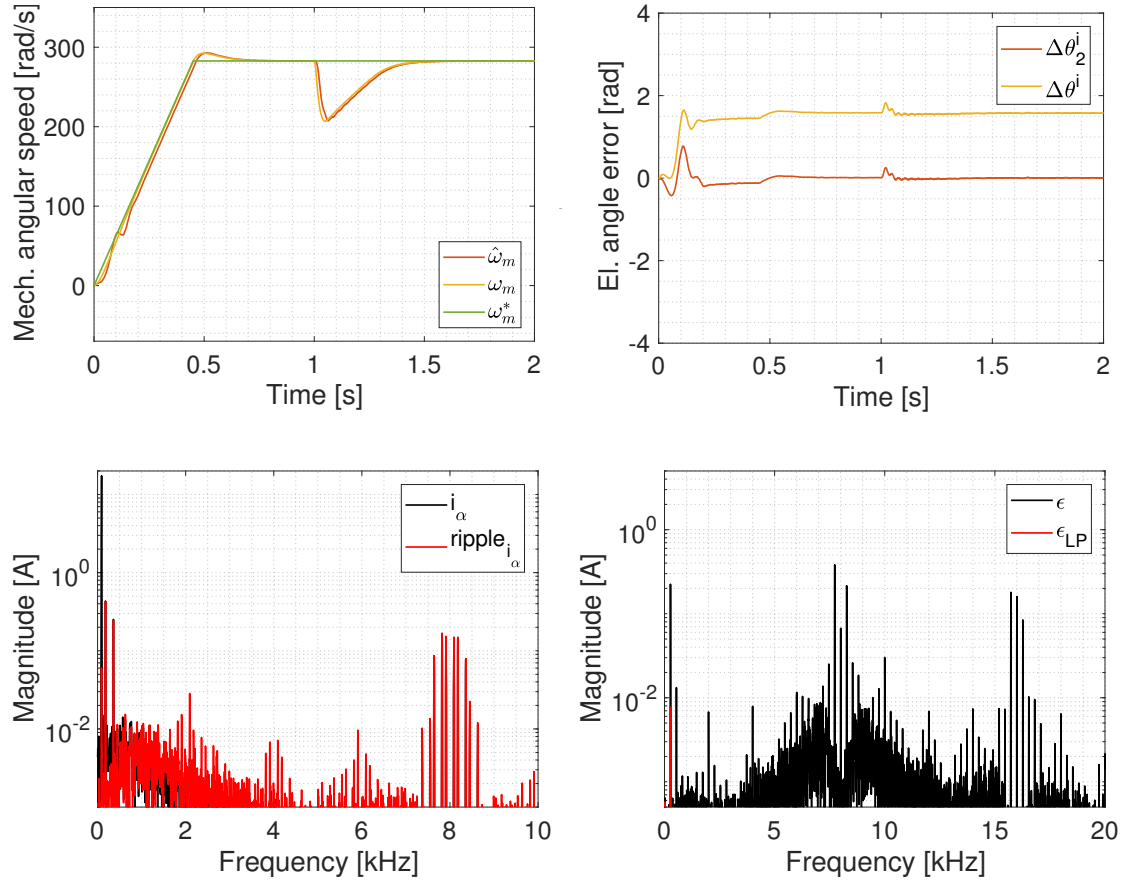


Figure 5.62. Estimator alternative 2 open-loop simulation. Current sampling frequency  $f_s = 0.25 \text{ MHz}$  and equal FPGA fake oversampling at  $f_{FPGA} = 0.25 \text{ MHz}$ .

## 5.6.3 Estimator 3

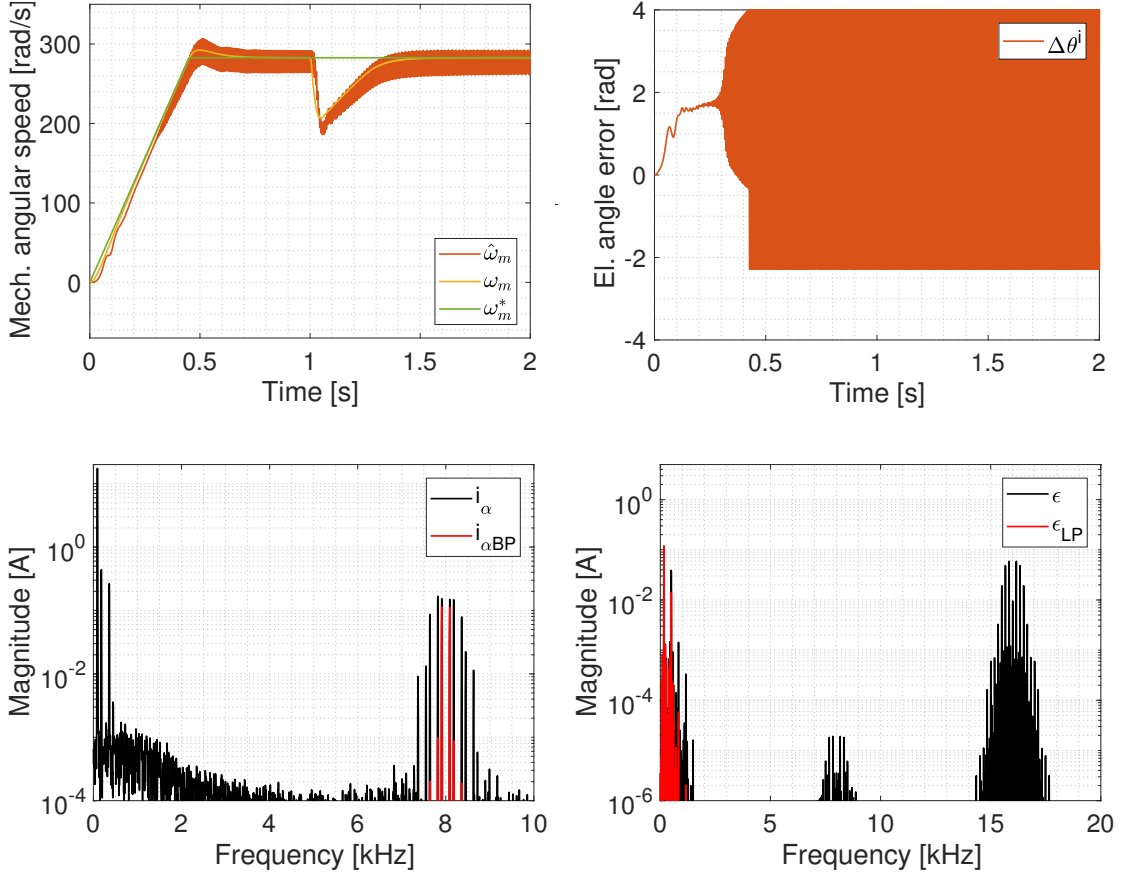


Figure 5.63. Estimator alternative 3 open-loop simulation. Current sampling frequency  $f_s = 2 \text{ MHz}$  and equal FPGA fake oversampling at  $f_{FPGA} = 2 \text{ MHz}$ .

The simulation results showing the sampling influence for the estimator alternative 3 are summarized in Figure 5.63 relatively to  $f_s = 2 \text{ MHz}$ , in Figure 5.64 and Figure 5.65 relatively to  $f_s = 0.5 \text{ MHz}$  and in Figure 5.66 relatively to  $f_s = 0.25 \text{ MHz}$ . The oversampling at a higher frequency is applied only relative to the simulation of Figure 5.64, otherwise  $T_{FPGA} = T_s$ .

In this last alternative, where a massive use of filtering actions has been made, the effect of the higher sampling frequency is crucial. In fact, not only for lower  $T_s$  the estimator performance is impoverished, but it even happens that the estimator loses the tracking. A low-frequency ripple, in fact, appears in the estimates, which, in the case with a  $f_s = 0.25 \text{ MHz}$ , cannot track the real position and speed. This is mainly due to the fact

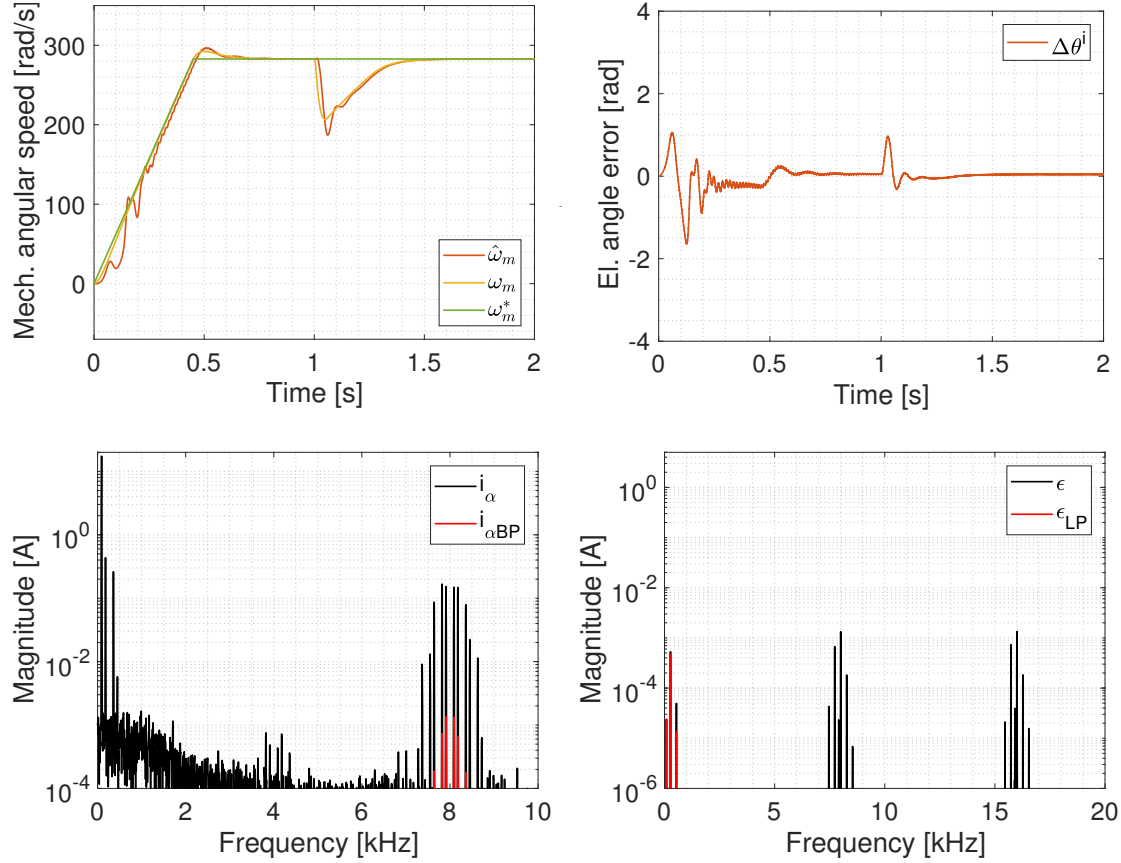


Figure 5.64. Estimator alternative 3 open-loop simulation. Current sampling frequency  $f_s = 0.5 \text{ MHz}$  and FPGA fake oversampling at  $f_{FPGA} = 2 \text{ MHz}$ , i.e. the choice adopted in the rest of the work.

that, as noticeable from the comparison between Figures 5.63, 5.65 and 5.66, the magnitude of the two first sideband harmonics of interest is lower as the sampling frequency is decreased.

With regard to the "fake" oversampling adoption  $f_{FPGA} = 2 \text{ MHz}$ , in this case the signal-to-noise ratio is improved respect to the case where  $f_s = f_{FPGA} = 0.5 \text{ MHz}$ , while the magnitude of the needed current component is reduced. This result, however, is an improvement to the performance. In this case, furthermore, the performance is even better compared to the case  $f_s = f_{FPGA} = 2 \text{ MHz}$ , which presents the highest ripple in  $\epsilon$  and consequently in both the position and the speed estimates. Regarding the speed, in fact, the adopted LPF is not enough to reduce its ripple.

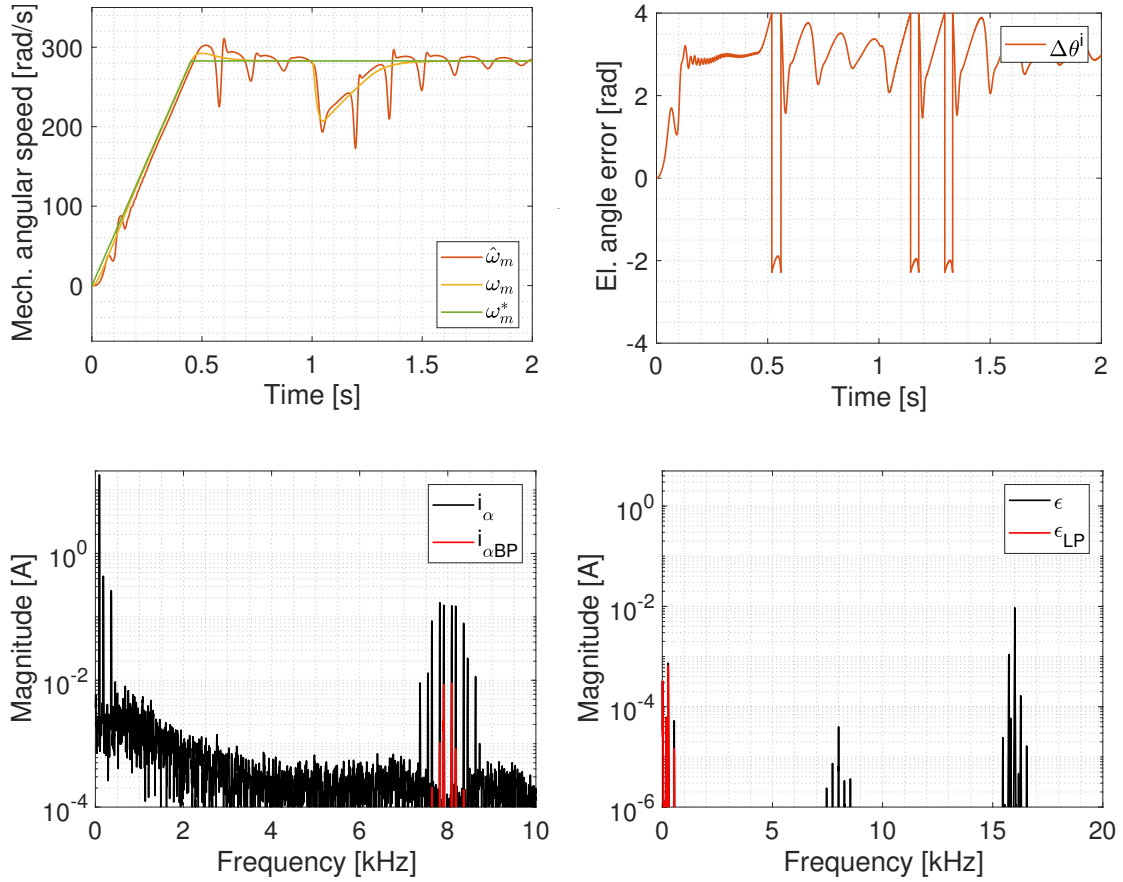


Figure 5.65. Estimator alternative 3 open-loop simulation. Current sampling frequency  $f_s = 0.5 \text{ MHz}$  and equal FPGA fake oversampling at  $f_{FPGA} = 0.5 \text{ MHz}$ .

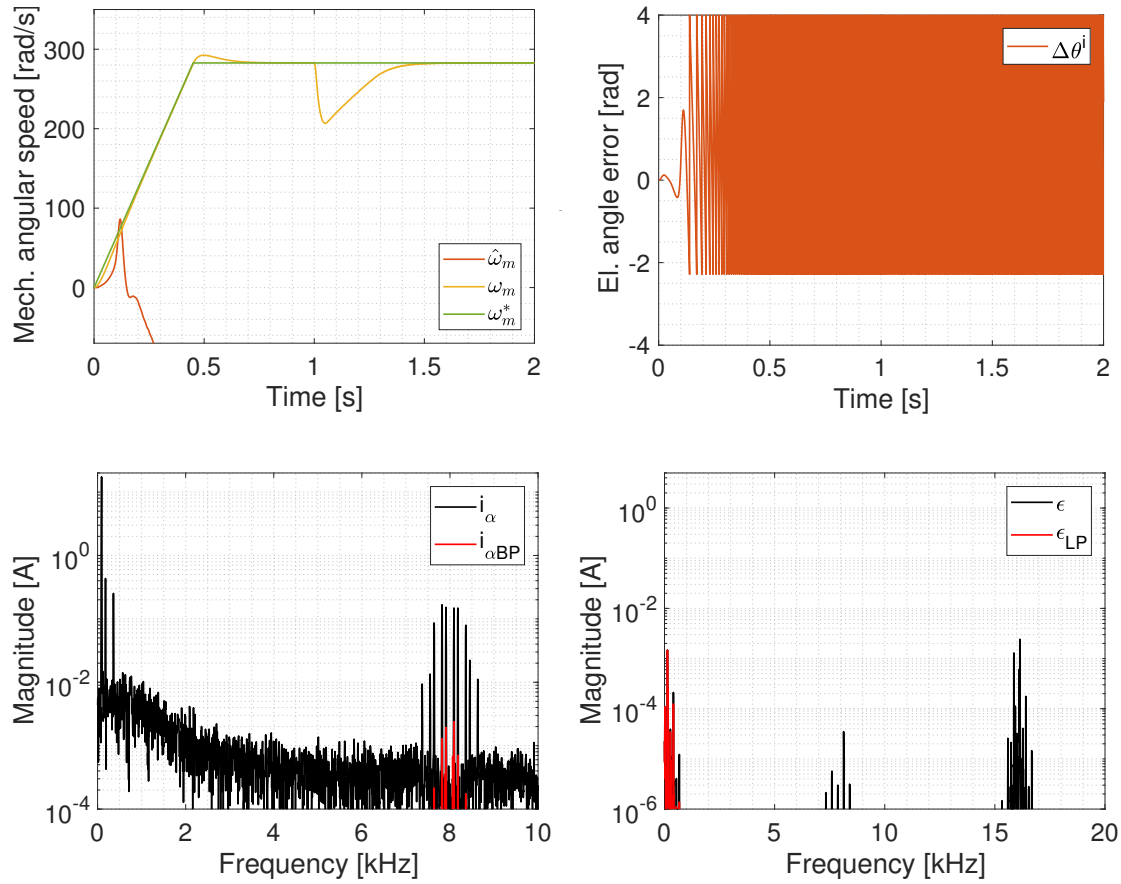


Figure 5.66. Estimator alternative 3 open-loop simulation. Current sampling frequency  $f_s = 0.25 \text{ MHz}$  and equal FPGA fake oversampling at  $f_{FPGA} = 0.25 \text{ MHz}$ .

## 5.7 Fan or pump application

As remarked from the simulations presented in Section 5.5, the closed-loop operation is troublesome. Not only, in fact, low speed operation is not possible, but even small values of load torque make the estimator easily lose the tracking. Furthermore, the dynamics of the drive are poor: the speed regulator bandwidth has to be decreased and both speed references step and sudden load insertion can not be afforded by the drive.

Considered all these limitations, in this Section, the drive has been tested with regards to a fan or pump application. For this application, in fact, much lower dynamics are required and the estimator turns also out to be able to face load torque values close to the nominal.

The load torque for a centrifugal pump can be modelled proportional to the square of the mechanical speed:

$$\tau_{load} = C \cdot \omega_m^2 \quad (5.1)$$

where the constant  $C$  has been chosen in order that at nominal speed of the motor 3000 *rpm* the load torque is equal to the motor nominal torque  $\tau_{nm} = 17 \text{ Nm}$ .

In the simulations, the reference value for the speed has been further limited compared to the previous simulations, since the overmodulation appears at lower speed when higher torques are applied.

### 5.7.1 Estimator 1 and 2

The simulations results for the fan/pump operation with the estimator alternative 1 are summarized in Figure 5.67 for  $\omega_m^* = 0.75 \cdot \omega_{mn}$  and in Figure 5.68 for  $\omega_m^* = 0.3 \cdot \omega_{mn}$  relatively to Single-Edge s.r.s. modulation, while in Figure 5.69 relatively to  $\omega_m^* = 0.75 \cdot \omega_{mn}$  and DPWMMIN s.r.s.. With estimator alternative 1, they are summarized in Figure 5.70 relatively to  $\omega_m^* = 0.75 \cdot \omega_{mn}$  and to Single-Edge s.r.s. modulation.

Relatively to the estimator 1, the performance of the drive is satisfactory and also high loads can be faced, almost close to the nominal value. Speed

and position estimates are affected by a low frequency ripple, roughly around 25 Hz, but it is not critical and the tracking is not lost. The actual speed, instead, is cleared from this ripple. From the current spectra, the action of the BPFs can be appreciated.

The performance making use of DPWMMIN modulation is slightly worse, being the amplitude of these oscillations is lower. Furthermore, it is remarkable that the error angle  $\Delta\theta'_2$  is stabilized around  $\pi$  instead of 0. DPWMMAX, on the contrary, as in the case of the closed-loop simulations, turns again undesirable, since it involves the loss of tracking.

For lower values of speed, instead, the magnitude of these oscillations is smaller, differently from the close-loop case, and the performance is satisfactory. This might be caused by the less severe magnetic saturation and the consequent higher saliency ratio. Anyway, the operation at very low speeds remains impossible.

Relatively to the estimator 2, instead, as it is the case for the closed-loop simulations, the performance is worse than the alternative 1. The reason for that is the higher magnitude of the low-frequency harmonics present in the estimates, which remains roughly around 25 Hz. This makes the operation at lower speeds not possible for the drive making use of the estimator alternative 2.

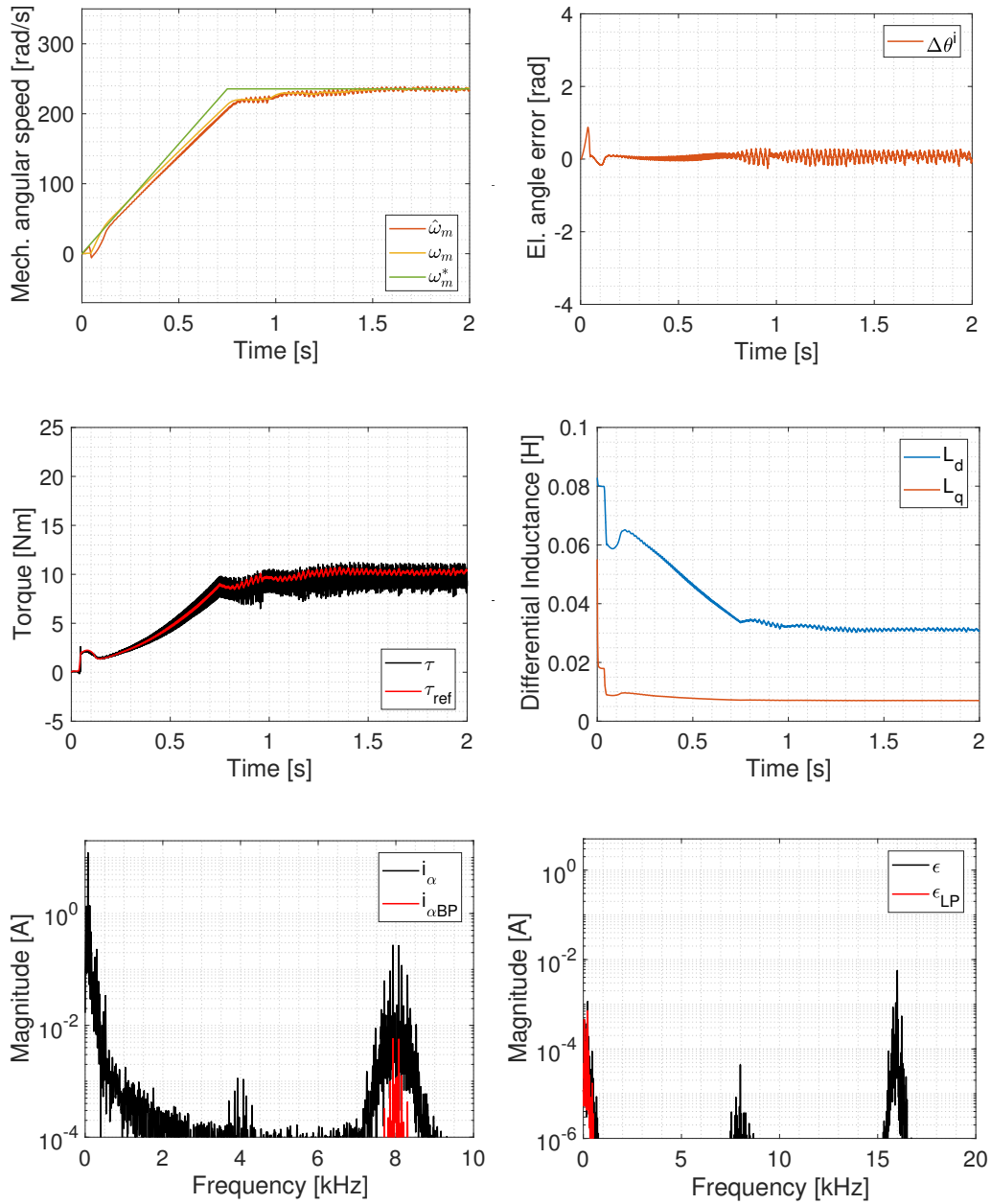


Figure 5.67. Fan/pump operation for estimator alternative 1, with reference speed  $\omega_m^* = 0.75 \cdot \omega_{mn}$  and modulation employed #11 Single-Edge s.r.s. comp..

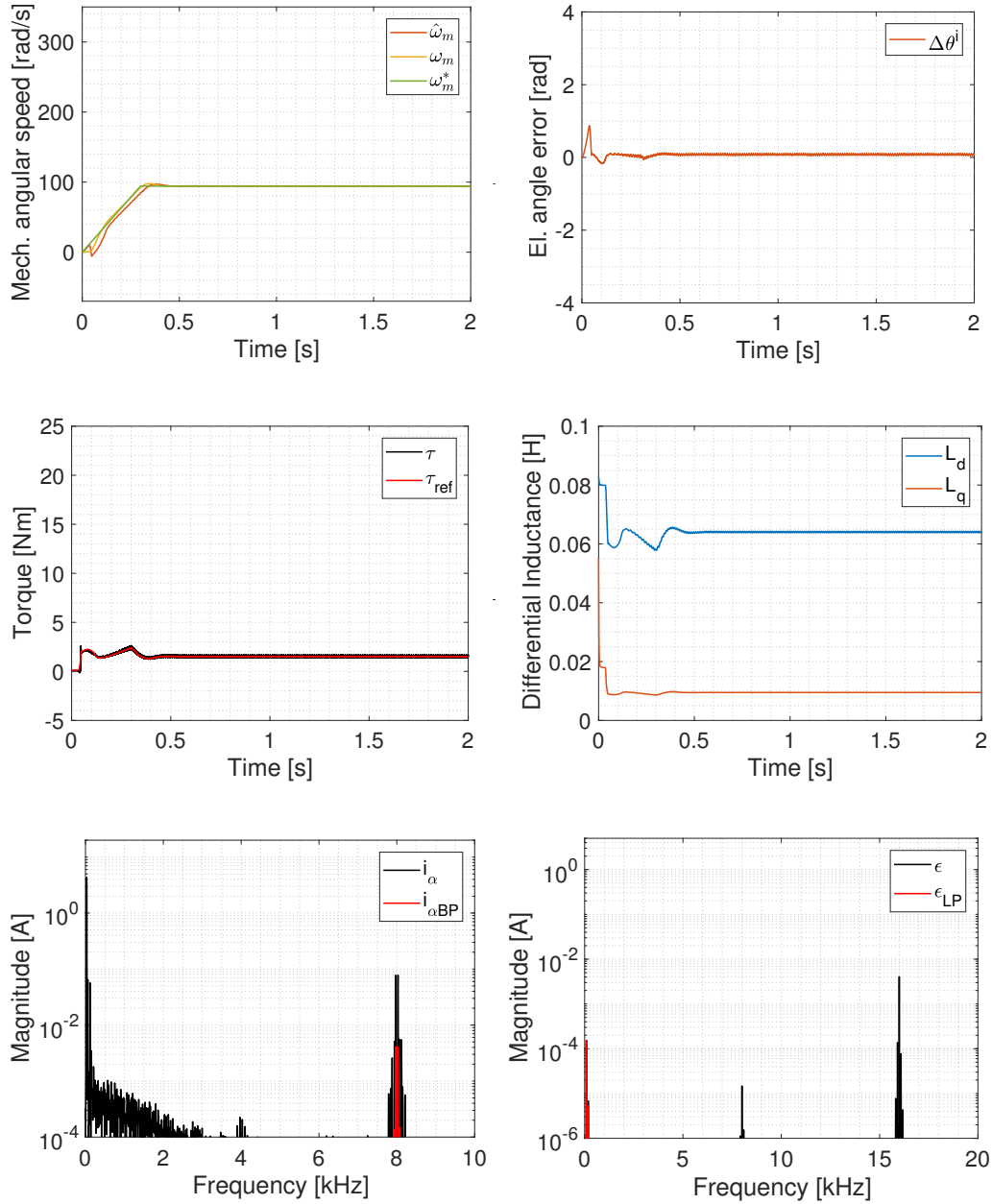


Figure 5.68. Fan/pump operation for estimator alternative 1, with reference speed  $\omega_m^* = 0.3 \cdot \omega_{mn}$  and modulation employed #11 Single-Edge s.r.s. comp..

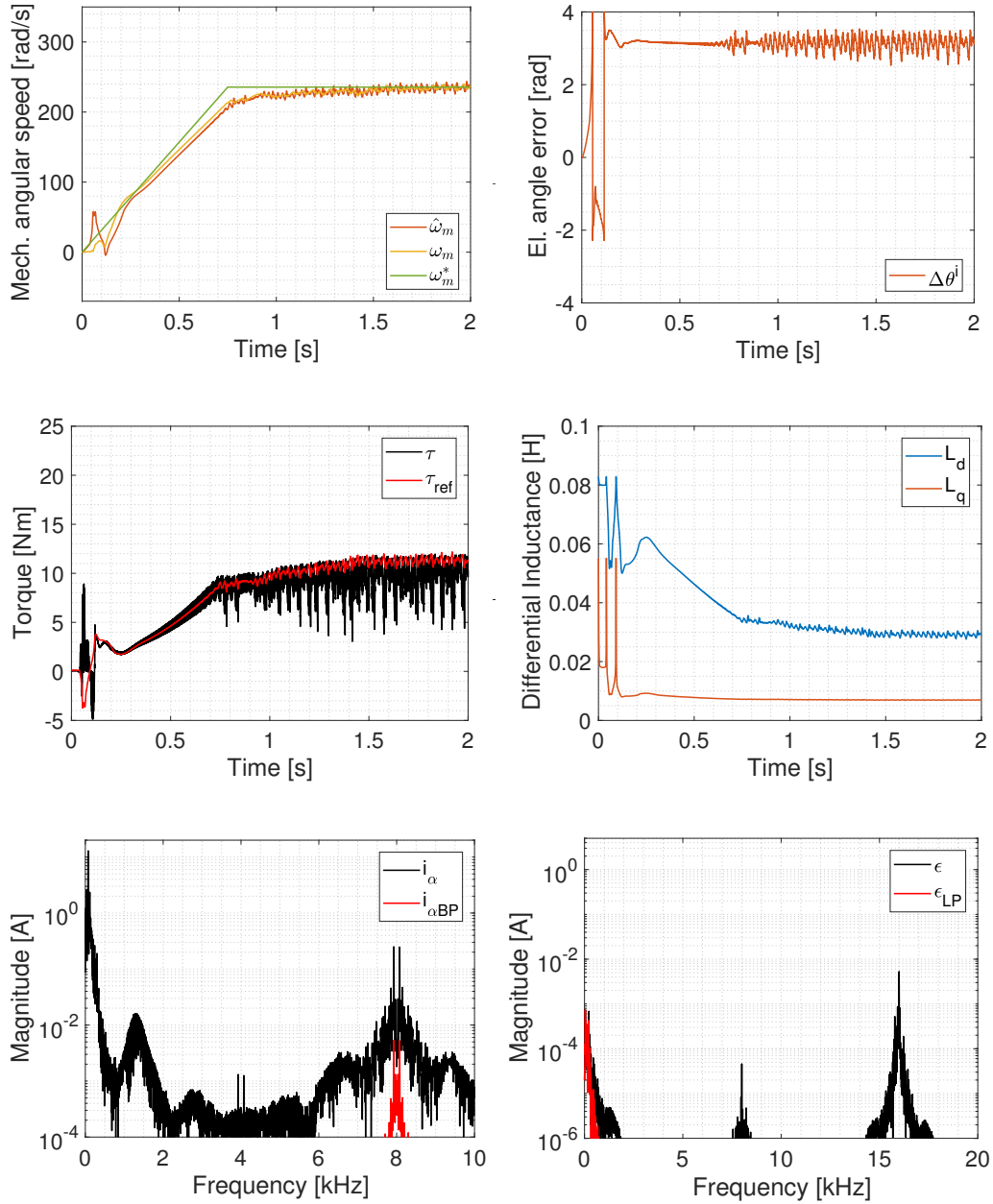


Figure 5.69. Fan/pump operation for estimator alternative 1 for , with reference speed  $\omega_m^* = 0.75 \cdot \omega_{mn}$  and modulation employed #4 DPWMMIN s.r.s..

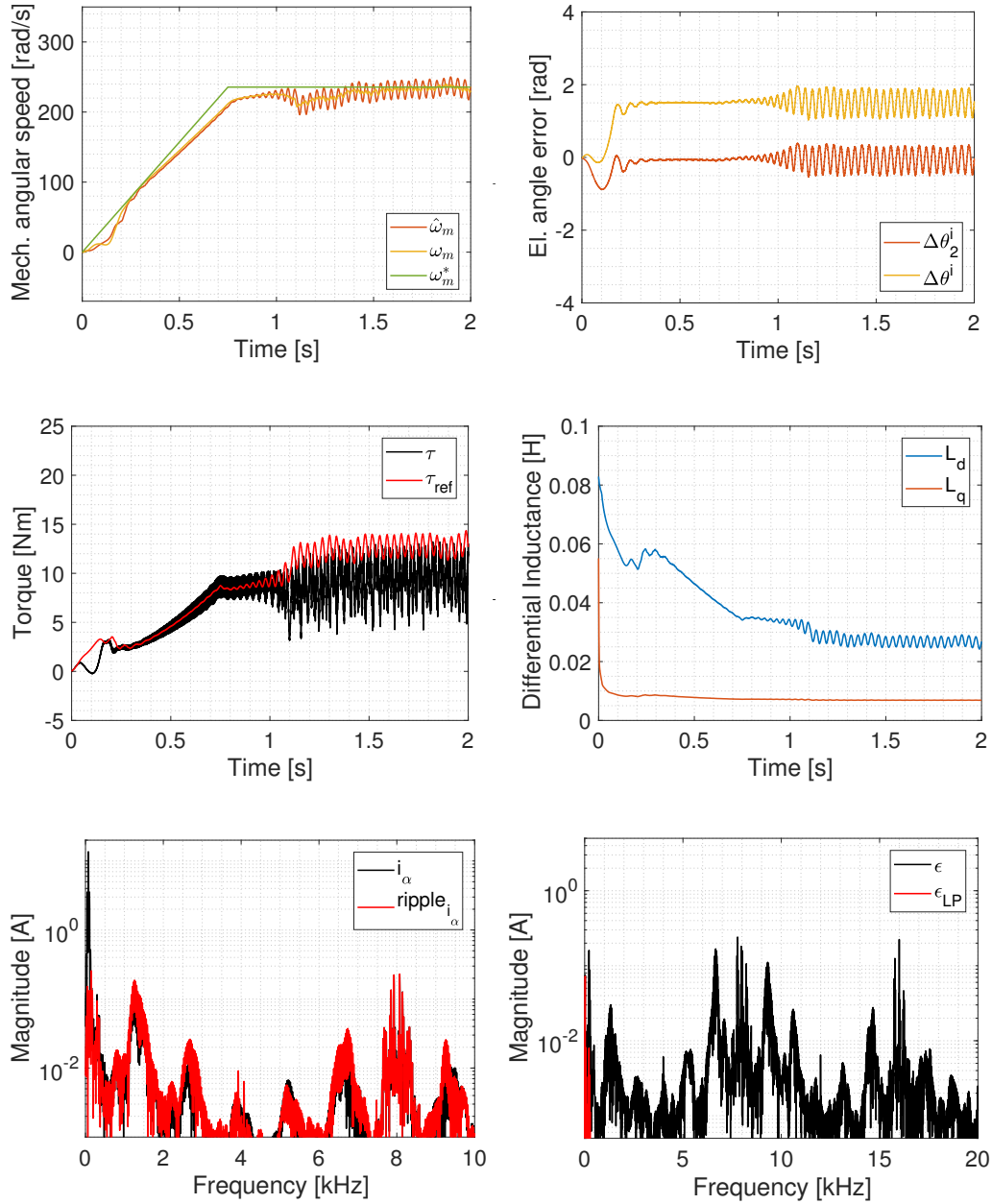


Figure 5.70. Fan/pump operation for estimator alternative 2, with reference speed  $\omega_m^* = 0.75 \cdot \omega_{mn}$  and modulation employed #11 Single-Edge s.r.s. comp..

## 5.8 DC link voltage amplitude influence

In this Section, the effects of the variation of the DC link voltage amplitude on the estimator performance have been investigated.

From the analytical calculation carried out in Section 3.1, it is important to notice that the magnitude of the current harmonic components of interest, whose expression depends on the coefficients  $I_0^+$ ,  $I_0^-$ ,  $I_1^+$ ,  $I_1^-$  defined in (3.17), is directly proportional, through the coefficients  $A^c$ ,  $A^+$ ,  $A^-$  defined in (3.8), to the DC-link voltage  $U_{dc}$ . Therefore, the increase of  $U_{dc}$  is expected to involve benefits to the estimation process in the sense of a more important information available in the currents.

Furthermore, as mentioned in the previous Sections, the simulations reference speed has been limited in order not to incur in overmodulation. The reason for this is that overmodulation implies that the phase voltage is clamped to the value of  $\pm U_{dc}/2$  for a certain time within the fundamental period, which involves the lack of current ripple, which is needed by the intrinsic injection sensorless control. Therefore, an increase of  $U_{dc}$  can allow the drive to reach the nominal speed and to face high torques without incurring overmodulation.

Regarding the simulations, the DC link voltage amplitude has been risen from 560 V to 800 V. Their results are summarized in Figure 5.71 relatively to  $\omega_m^* = 1 \cdot \omega_{mn}$ , in Figure 5.72 relatively to  $\omega_m^* = 0.75 \cdot \omega_{mn}$  and in Figure 5.73 relatively to  $\omega_m^* = 0.3 \cdot \omega_{mn}$ .

Furthermore, just the influence on the motor operation as a fan/pump has been investigated and only #11 Single-Edge s.r.s. modulation has been employed. The speed regulator bandwidth is the same as in the closed-loop simulations, i.e.  $\alpha_s = 30 \text{ rad/s}$

Only the estimator alternative 1 has been taken into account. The impoverishment of the performance faced at low speeds makes in fact the starting of the motor impossible if the estimator alternative 2 is adopted.

Looking at the plots, the first aspect to be mentioned is the expected possibility for the drive to reach the nominal speed. It even happens with the presence of really low ripple in the speed and position estimates at steady state.

Furthermore looking at the simulation at  $0.75 \cdot \omega_{mn}$  and comparing it with the one where  $U_{dc}$  is not increased in Figure 5.67, it can be noticed that this ripple is not present in the case with  $U_{dc} = 800 \text{ V}$ . This can be related to the

aforementioned benefits brought by the higher DC-link voltage in the sense of an higher signal-to-noise ratio. In fact, looking at the current spectra, it can be notice that the first two sideband harmonics magnitude is roughly 0.15 A if  $U_{dc} = 560$  V, while it increase to roughly 0.3 A if  $U_{dc} = 800$  V. Also the filtered current amplitudes take advantage from the DC-link voltage increase.

Regarding the inductance effects, it can be noticed that despite the big variations of the inductances in heavy-load conditions, the performance of the estimator is not affected in the simulation run at the nominal speed.

On the other hand, the  $U_{dc}$  increase impoverish the performance during transients at low speeds, with the presence of huge estimated angle oscillations and with the actual speed that presents an overshoot around 100 rad/s. The behaviour, anyway, can be improved by further tuning the estimator parameters or by varying the speed regulator bandwidth  $\alpha_s$  and the speed reference ramp times.

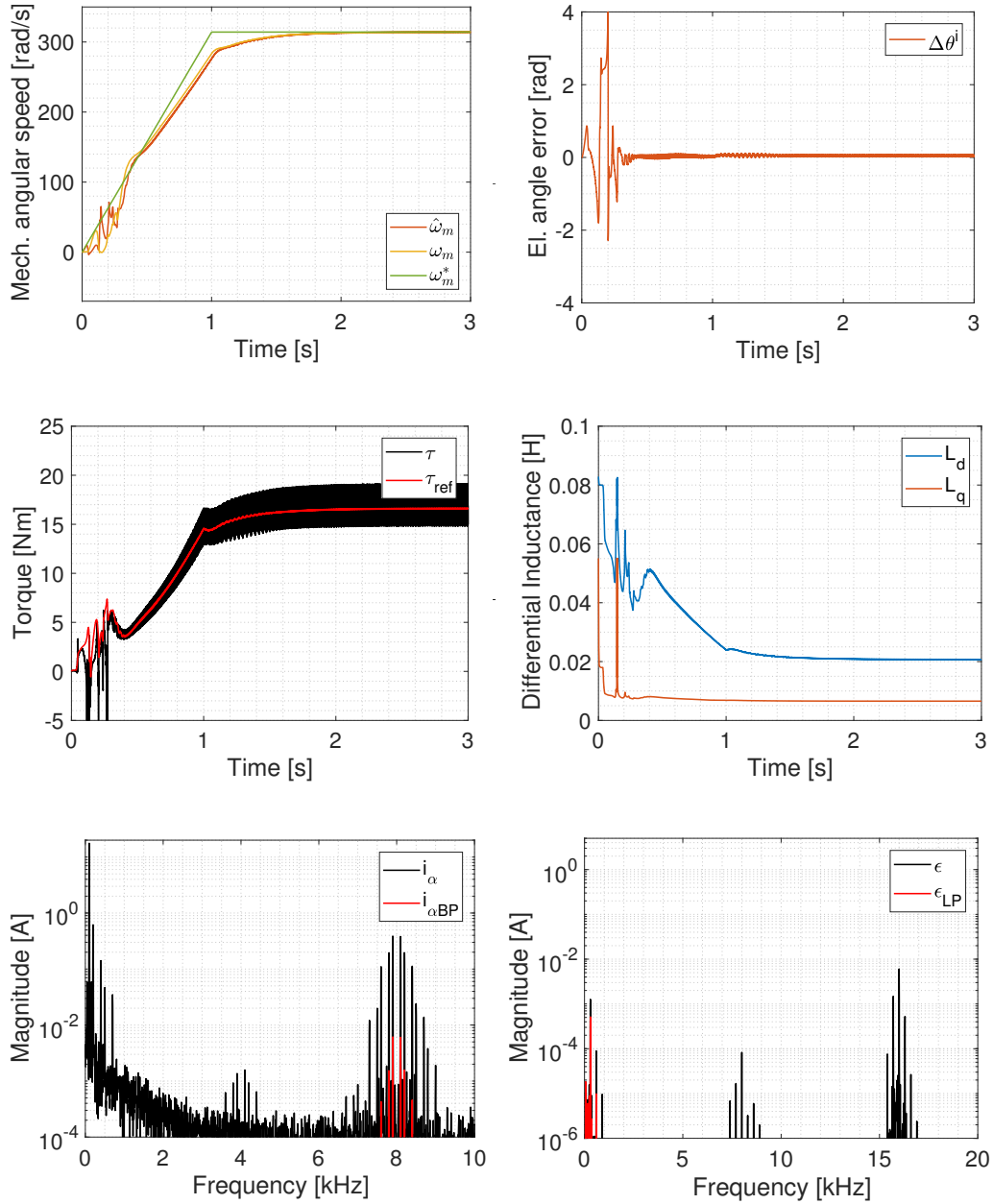


Figure 5.71. Fan/pump operation for estimator alternative 1, with DC-link voltage raised to  $U_{dc} = 800 \text{ V}$  and reference speed  $\omega_m^* = 1 \cdot \omega_{mn}$

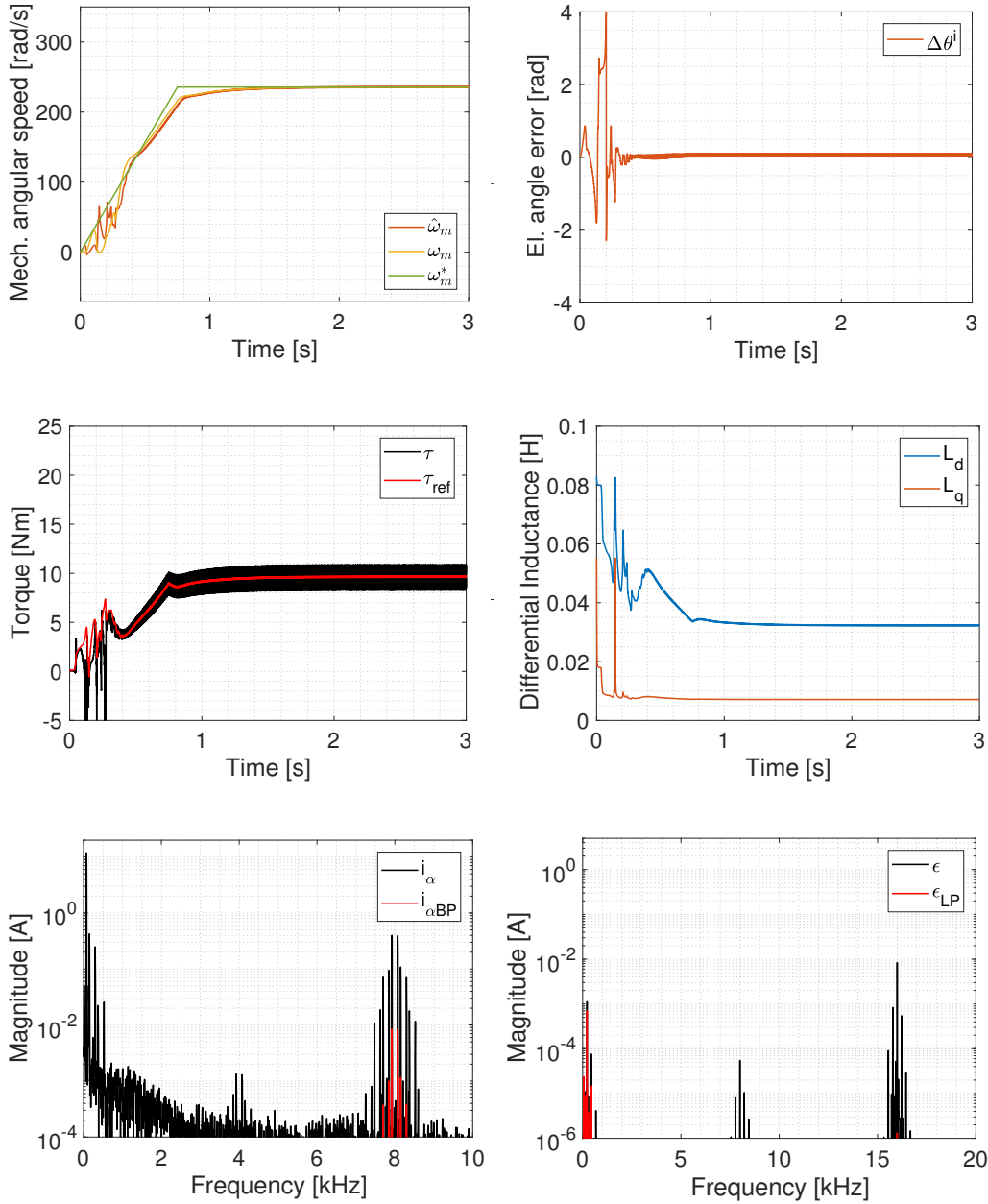


Figure 5.72. Fan/pump operation for estimator alternative 1, with DC-link voltage raised to  $U_{dc} = 800 \text{ V}$  and reference speed  $\omega_m^* = 0.75 \cdot \omega_{mn}$

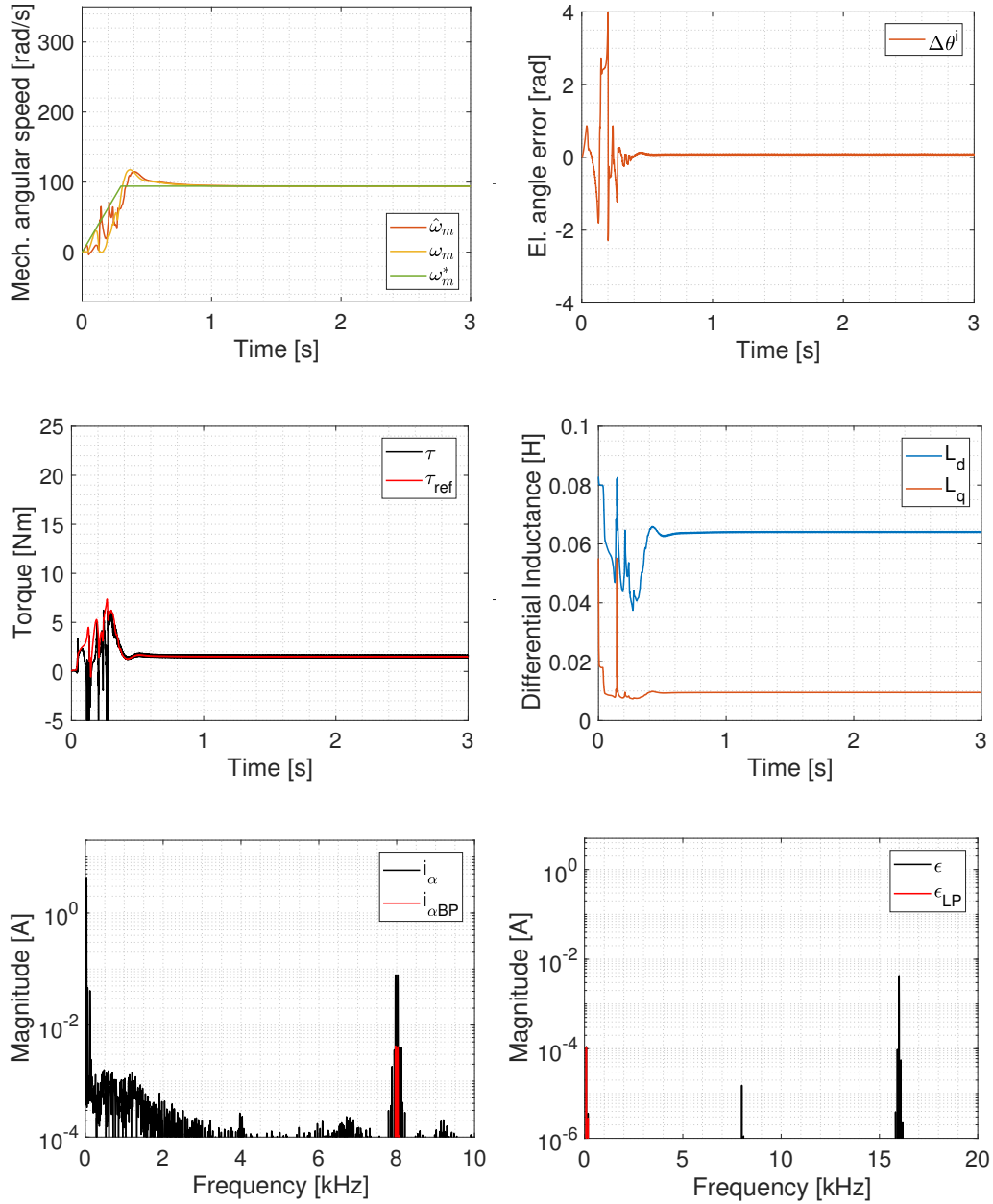


Figure 5.73. Fan/pump operation for estimator alternative 1, with DC-link voltage raised to  $U_{dc} = 800 \text{ V}$  and reference speed  $\omega_m^* = 0.3 \cdot \omega_{mn}$



# Chapter 6

## CONCLUSIONS

In this work, the modelling in Matlab/Simulink environment of an intrinsic injection sensorless control has been analysed.

In order to investigate the trade-off between a system making use of an important filtering action or a system which does not make use of filters in order to avoid delays, three different schemes have been proposed:

- in the first alternative, BPFs are used for the current filtering;
- in the second alternative, the input currents are not filtered and just their fundamental magnitude is removed thanks to a current PLL and ripple calculator;
- in the third alternative, variable centre frequency BPFs are used for the current filtering, and their variation relies on the speed estimated by a current PLL and ripple calculator.

From the simulations results, the first alternative presents the best performance in open-loop and in closed-loop, resulting in the most suitable for the hardware implementation.

However, the limitations expected from the theory find a match in the simulations results. In particular:

- Zero speed operation is not feasible, since all the sideband harmonics present the same frequency  $f_c$  and thus their information is lost during the transformation from  $abc$  to  $\alpha\beta$  coordinates;

- Low-speed operation involves the shrinking of the sideband harmonics around the carrier frequency, making the filtering and the demodulation processes more difficult;
- Low- and high-load conditions involve a low signal-to-noise ratio, making troublesome the extraction of the speed and position estimates;
- High-load condition may involve significant magnetic saturation and thus the loss of information from which the position and the speed can be estimated;
- Overmodulation has to be avoided, since it involves the lack of current ripple and thus the impossibility to extract the position and speed information.

Furthermore, the system results to have poorest dynamics compared to the drive making use of measured speed and position and high load condition involve easily the loss of the track.

For this reason, the drive has been tested relatively to a pump or a fan application, for which high dynamics are not required. The sensorless drive performance is thus satisfying for this application, and higher torque loads can be successfully faced. Moreover, the DC-link voltage turns out to be relevant for the estimator performance and in particular at high speeds, avoiding the overmodulation insurgence.

However, it might be possible to modify the estimator in order to partially reduce its limitations. In particular, a variable PI regulator might be implemented, whose gains vary according to the load torque. In this way, the different signal-to-noise ratio caused by the different harmonic contents at different torque levels can be taken in account.

Moreover, the magnetic saturation influence, even if playing a minor role, can be further reduced. Anyway, the implementation of variable gains would increase the complexity of the sensorless parameters tuning, which is already remarkably difficult.

Lastly, the employment of the intrinsic injection control can be thought to take place beside a traditional sensorless control in an alternative hybrid scheme. Given the operation of the intrinsic injection estimator at high speeds, a traditional injection estimator can be used for the starting and for low speeds. A similar solution is applied nowadays in hybrid sensorless control schemes, where an injection estimator is used until a certain speed

---

and the control switches seamlessly into a model-based estimator. This approach would comply with the impossibility of operation at low speeds for the intrinsic injection control and with the limitation of the traditional injection estimator at high speeds in relation to the reduced DC-voltage margin. Moreover, given the similarities between traditional and the intrinsic injection methods relative to the demodulation process and of the nullification of the resulting error, from the point of view of the implementation, this alternative hybrid scheme would result to be less complex compared to the traditional hybrid sensorless control scheme.



# Chapter 7

## FUTURE WORK

The estimator alternative one is ready for the implementation on a Xilinx FPGA Virtex 6 board, within a OPAL-RT OP5600 system, in the laboratory of ABB Corporate Research Sweden in Västerås.



# Appendix A

## APPENDIX

In this Appendix, in Section A.1 the analytical expressions of the complex Fourier coefficients are made explicit for some modulation strategies, while in Section A.2 the Simulink schemes for the UMVT offset times calculation are displayed.

### A.1 Theoretical complex Fourier coefficients

The expressions of the theoretical complex Fourier coefficients relative to the modulations labelled in this work as #1, #2, #9, #10 and #11 can be found in [16]. Furthermore, the expressions relative to the modulation strategies PWM Double-Edge n.s. and PWM Single-Edge n.s. are reported for the sake of comparison.

PWM Double-Edge s.r.s. (modulations #1 and #10):

$$C_{mn} = \frac{2U_{dc}}{\pi} \frac{J_n \left( \left[ m + \frac{n}{p} \right] \frac{\pi}{2} M \right)}{m + \frac{n}{p}} \sin \left( \left[ m + \frac{n}{p} + n \right] \frac{\pi}{2} \right) \quad (\text{A.1})$$

SVM s.r.s. (modulation #2):

$$\begin{cases} C_{01} = \frac{U_{dc}}{2}M \\ C_{n=3,9,15,\dots} = \frac{3\sqrt{3}MU_{dc}}{2\pi(n^2-1)} \sin\left(n\frac{\pi}{6}\right) \sin\left(n\frac{\pi}{2}\right) \\ C_{mn} = \frac{4U_{dc}}{m\pi^2} [C_1 + C_2 + C_3 + C_4] \end{cases} \quad (\text{A.2})$$

where:

$$\begin{cases} C_1 = \frac{\pi}{6} \sin\left([q+n]\frac{\pi}{2}\right) \left\{ J_n\left(q\frac{3\pi}{4}M\right) + 2\cos\left(n\frac{\pi}{6}\right) J_n\left(q\frac{\sqrt{3}\pi}{4}M\right) \right\} \\ C_2 = \frac{1}{n} \sin\left(q\frac{\pi}{2}\right) \cos\left(n\frac{\pi}{2}\right) \sin\left(q\frac{\pi}{6}\right) \left\{ J_0\left(q\frac{3\pi}{4}M\right) - J_0\left(q\frac{\sqrt{3}\pi}{4}M\right) \right\} \Big|_{n \neq 0} \\ C_3 = \sum_{\substack{k=1 \\ k \neq -n}}^{\infty} \left[ \frac{1}{[n+k]} \sin\left([q+k]\frac{\pi}{2}\right) \cos\left([n+k]\frac{\pi}{2}\right) \sin\left([n+k]\frac{\pi}{6}\right) \right. \\ \left. \times \left\{ J_k\left(q\frac{3\pi}{4}M\right) + 2\cos\left([2n+3k]\frac{\pi}{6}\right) J_k\left(q\frac{\sqrt{3}\pi}{4}M\right) \right\} \right] \\ C_4 = \sum_{\substack{k=1 \\ k \neq n}}^{\infty} \left[ \frac{1}{[n-k]} \sin\left([q+k]\frac{\pi}{2}\right) \cos\left([n-k]\frac{\pi}{2}\right) \sin\left([n-k]\frac{\pi}{6}\right) \right. \\ \left. \times \left\{ J_k\left(q\frac{3\pi}{4}M\right) + 2\cos\left([2n-3k]\frac{\pi}{6}\right) J_k\left(q\frac{\sqrt{3}\pi}{4}M\right) \right\} \right] \\ q = m + n \frac{\omega_o}{\omega_c} \end{cases}$$

PWM Single-Edge r.s. (modulations #9 and #11):

$$\begin{cases} C_{0n} = \frac{U_{dc}}{\pi \frac{p}{n}} J_n\left(\frac{n}{p}\pi M\right) \left[ \sin\left(n\frac{\pi}{2}\right) + j \cdot \cos\left(n\frac{\pi}{2}\right) \right] \\ C_{m0} = j \cdot \frac{U_{dc}}{m\pi} [J_0(m\pi M) - \cos(m\pi)] \\ C_{mn} = \frac{U_{dc}}{\pi} \frac{J_n\left(\left[m + \frac{n}{p}\right]\pi M\right)}{m + \frac{n}{p}} \left[ \sin\left(n\frac{\pi}{2}\right) + j \cdot \cos\left(n\frac{\pi}{2}\right) \right] \end{cases} \quad (\text{A.3})$$

PWM Double-Edge n.s.:

$$\begin{cases} C_{0n} = \frac{U_{dc}}{2} M \\ C_{mn} = \frac{2U_{dc}}{m\pi} J_n \left( m \frac{\pi}{2} M \right) \sin \left( [m+n] \frac{\pi}{2} \right) \end{cases} \quad (\text{A.4})$$

PWM Single-Edge n.s.:

$$\begin{cases} C_{0n} = \frac{U_{dc}}{2} M \\ C_{m0} = j \cdot \frac{U_{dc}}{m\pi} [J_0(m\pi M) - \cos(m\pi)] \\ C_{mn} = \frac{U_{dc}}{m\pi} J_n(m\pi M) \left[ \sin \left( n \frac{\pi}{2} \right) + j \cdot \cos \left( n \frac{\pi}{2} \right) \right] \end{cases} \quad (\text{A.5})$$

## A.2 UVMT offset time calculation blocks

The Simulink schemes for the UMVT offset times calculation described in 4.2.4 are displayed from Figure A.1 to Figure A.8.

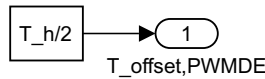


Figure A.1. Offset time calculation Simulink scheme for modulation #1: PWM Double-Edge s.r.s..

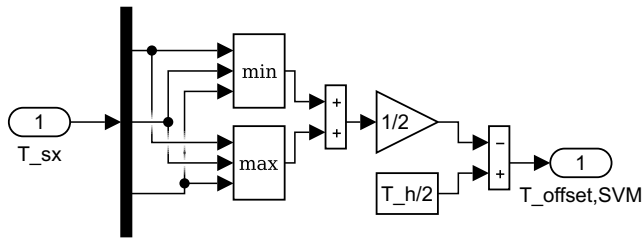


Figure A.2. Offset time calculation Simulink scheme for modulation #2: SVM s.r.s..

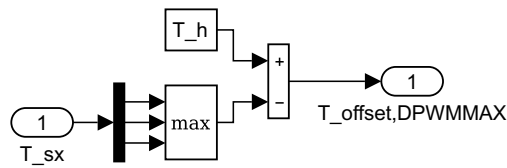


Figure A.3. Offset time calculation Simulink scheme for modulation #3: DPWMMAX s.r.s..

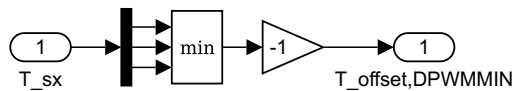


Figure A.4. Offset time calculation Simulink scheme for modulation #4: DPWMMIN s.r.s..

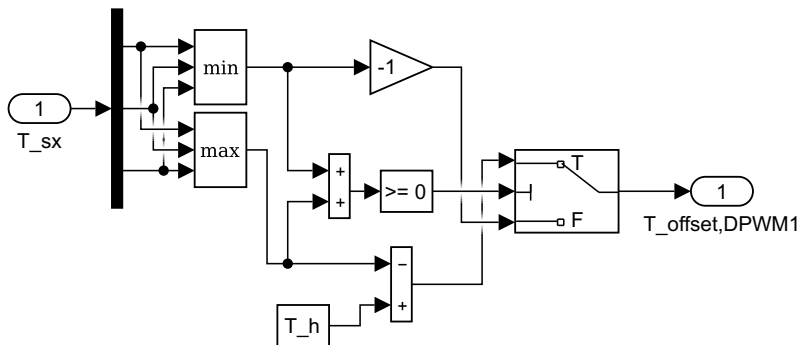


Figure A.5. Offset time calculation Simulink scheme for modulation #6: DPWM1 s.r.s..

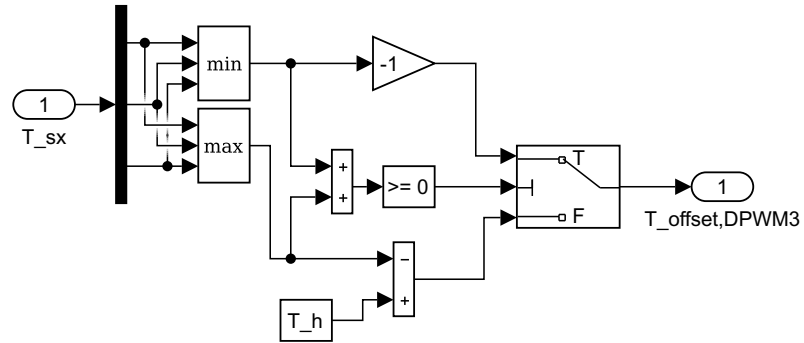


Figure A.6. Offset time calculation Simulink scheme for modulation #8: DPWM3 s.r.s..

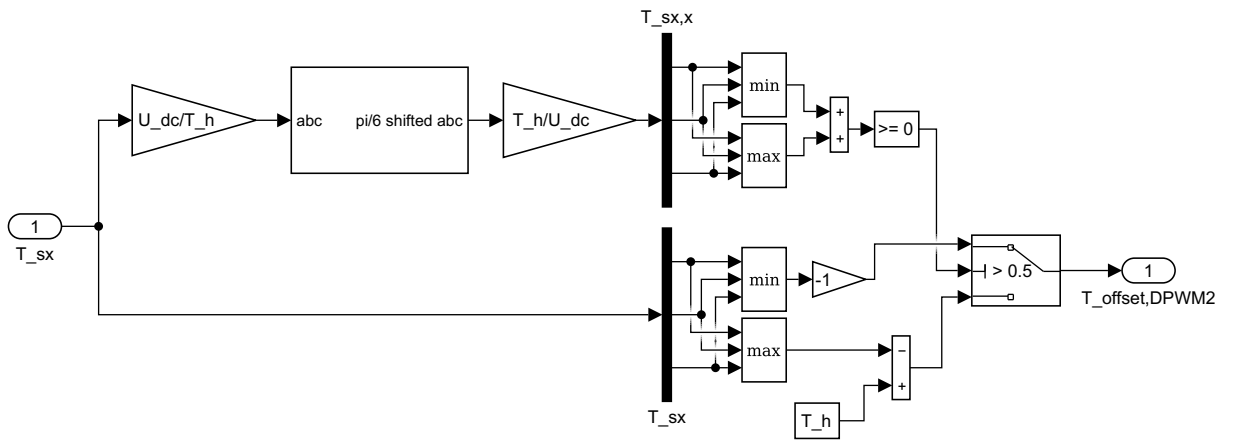


Figure A.7. Offset time calculation Simulink scheme for modulation #5: DPWM0 s.r.s..

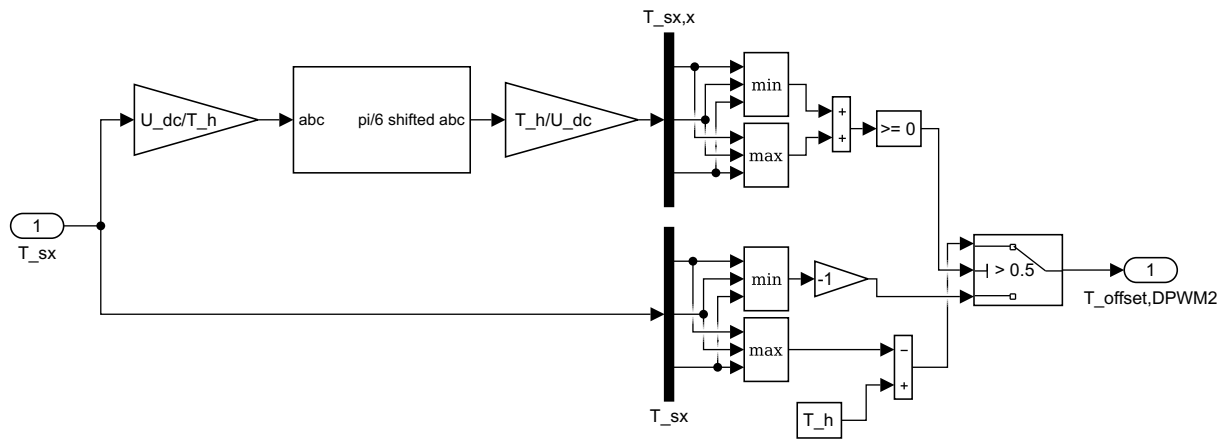


Figure A.8. Offset time calculation Simulink scheme for modulation #7: DPWM2 s.r.s..

# REFERENCES

- [1] A. Faggion and S. Bolognani, "A new proposal of rotor position estimation in IPM motor drives based on PWM current harmonics," *2010 First Symposium on Sensorless Control for Electrical Drives*, pp. 86–92, 9-10 July 2010, Padova, Italy.
- [2] S. Bolognani, A. Faggion, and L. Sgarbossa, "Rotor position estimation in IPM motor drives based on PWM current harmonics," *2011 IEEE International Electric Machines and Drives Conference (IEMDC)*, pp. 430–435, 15-18 May 2011, Niagara Falls, ON, Canada.
- [3] H. Zhu, X. Xiao, and Y. Li, "A Simplified High Frequency Injection Method For PMSM Sensorless Control," *2009 IEEE 6th International Power Electronics and Motion Control Conference*, pp. 401–405, 17-20 May 2009, Wuhan, China.
- [4] S. Sul, Y. Kwon, and Y. Lee, "Sensorless Control of IPMSM] for Last 10 Years and Next 5 Years," *CES Transactions on Electrical Machines and Systems*, vol. 1, pp. 91–99, 2017.
- [5] G. el Murr, D. Giaouris, and J. W. Finch, "Universal PLL Strategy for Sensorless Speed and Position Estimation of PMSM," *2008 IEEE Region 10 and the Third international Conference on Industrial and Information Systems*, pp. 1–6, 8-10 December 2008, Kharagpur, India.
- [6] G. Zhang, G. Wang, and D. Xu, "Saliency-Based Position Sensorless Control Methods for PMSM Drives - a Review," *Chinese Journal of Electrical Engineering*, vol. 3, no. 2, pp. 14–23, September 2017.
- [7] S. Jung and J. Ha, "Design and Analysis of Analog Filtering Method for Signal Injection Based Sensorless Control," *2014 Twenty-Ninth Annual IEEE Applied Power Electronics Conference and Exposition (APEC)*, pp. 1573–1578, 16-20 March 2014, Fort Worth, TX, USA.

- [8] M. Cirrincione and M. Pucci, "An MRAS-based sensorless high-performance induction motor drive with a predictive adaptive model," *IEEE Transactions on Industrial Electronics*, vol. 52, pp. 532–551, 2005.
- [9] M. Barut, S. Bogosyan, and M. Gokasan, "Speed-Sensorless Estimation for Induction Motors Using Extended Kalman Filters," *IEEE Transactions on Industrial Electronics*, vol. 54, pp. 272–280, 2007.
- [10] Y. D. Yoon, S. K. Sul, S. Morimoto, and K. Ide, "High-bandwidth sensorless algorithm for AC machines based on square wave-type voltage injection," *IEEE Transactions on Industrial Application*, vol. 47, pp. 1361–1370, May/June 2011.
- [11] S. Shinnaka, "A New Speed-Varying Ellipse Voltage Injection Method for Sensorless Drive of Permanent-Magnet Synchronous Motors With Pole Saliency - New PLL Method Using High-Frequency Current Component Multiplied Signal," *IEEE Transactions on industry applications*, vol. 44, no. 3, pp. 777–788, May-June 2008.
- [12] E. Robeischl and M. Schroedl, "Optimized inform measurement sequence for sensorless PM synchronous motor drives with respect to minimum current distortion," *IEEE Transactions on Industrial Application*, vol. 40, no. 2, pp. 591–598, 2004.
- [13] C. Caruana, G. M. Asher, and M. Sumner, "Performance of HF signal injection techniques for zero-low-frequency vector control of induction machines under sensorless conditions," *IEEE Transactions on Industrial Electronics*, vol. 53, no. 1, pp. 225–238, 2006.
- [14] R. D. Lorenz, "Key technologies for future motor drives," *ICEMS 2005: Proceedings of the Eighth International Conference on Electrical Machines and systems*, vol. 1, pp. 1–6, 27-29 September 2005, Nanjing, China.
- [15] P. Nussbaumer, T. M. Wolbank, and M. A. Vogelsberger, "Sensitivity analysis of insulation state indicator in dependence of sampling rate and bit resolution to define hardware requirements," *IEEE International Conference on Industrial Technology (ICIT)*, pp. 392–397, 25-28 February 2013, Cape Town, South Africa.
- [16] D. G. Holmes and T. A. Lipo, *Pulse Width Modulation for power converters: Principles and Practice*, 1st ed., J. W. . Sons, Ed. Wiley-IEEE PRESS, 2003.
- [17] L. Wang and R. D. Lorenz, "Rotor Position Estimation for Permanent Magnet Synchronous Motor Using Saliency-Tracking Self-Sensing Method," *2000*

- 
- Industry Applications Conference. Conference Record of the 2000 IEEE*, pp. 445–450, 8-12 October 2000, Rome, Italy.
- [18] N. Bianchi, S. Bolognani, and A. Faggion, “Predicted and measured errors in estimating rotor position by signal injection for salient-pole PM synchronous motors,” *IEEE International Electric Machines and Drives Conference 2009. IEMDC '09*, pp. 1565–1572, 3-6 May 2009, Miami, FL, USA.
- [19] A. Vagati, M. Pastorelli, F. Scapino, and G. Franceschini, “Impact of Cross Saturation in Synchronous Reluctance Motors of the Transverse-Laminated Type,” *IEEE Transactions on Industrial Application*, vol. 36, no. 4, pp. 1039–1046, July/August 2000.
- [20] T. Aihara, A. Toba, T. Yanase, A. Mashimo, and K. Endo, “Sensorless torque control of salient-pole synchronous motor at zero-speed operation,” *IEEE Transactions on Power Electronics*, vol. 14, no. 1, pp. 202–208, January 1999.
- [21] J. Holtz, “Initial Rotor Polarity Detection and Sensorless Control of PM Synchronous Machines,” *Industry Applications Conference, 2006. 41st IAS Annual Meeting. Conference Record of the 2006 IEEE*, vol. 4, pp. 2040–2047, 8-12 October 2006, Tampa, FL, USA.
- [22] R. Slatter, M. Brusius, and H. Knoll, “Development of high bandwidth current sensors based on the magnetoresistive effect,” *2016 18th European Conference on Power Electronics and Applications (EPE 16 ECCE Europe)*, pp. 1–10, 5-9 September 2016, Karlsruhe, Germany.
- [23] P. Landsmann, D. Paulus, A. Dötlinger, and R. Kennel, “Silent Injection for Saliency based Sensorless Control by means of Current Oversampling,” *2013 IEEE International Conference on Industrial Technology (ICIT)*, pp. 398–403, 25-28 February 2013, Cape Town, South Africa.
- [24] P. Landsmann and R. Kennel, “Rotor Position Estimation based on Current Oversampling,” *Proc. of 13th MRSymposium*, 2015.
- [25] N. Mohan, T. M. Undeland, and W. P. Robbins, *Power Electronics. Converter, Applications, and Design*, 3rd ed., J. W. . Sons, Ed. John Wiley and Sons, Inc, 2003.
- [26] A. Kiltbau and J. M. Pacas, “Parameter-measurement and control of the synchronous reluctance machine including cross saturation,” *Conference Record of the 2001 IEEE Industry Applications Conference, 2001. Thirty-Sixth IAS Annual Meeting.*, vol. 4, pp. 2302–2309, 30 September - 4 October 2001, Chicago, IL, USA.

- [27] —, “Appropriate models for the control of the synchronous reluctance machine,” *Conference Record of the Industry Applications Conference, 2002. 37th IAS Annual Meeting.*, vol. 4, pp. 2289–2295, 13-18 October 2002, Pittsburgh, PA, USA.
- [28] A. Vagati, M. Pastorelli, and G. Franceschini, “High-Performance Control of Synchronous Reluctance Motors,” *IEEE Transactions on Industrial Application*, vol. 33, no. 4, pp. 983–991, July/August 1997.
- [29] D. Mingardi, M. Morandin, S. Bolognani, and N. Bianchi, “On the Proprieties of the Differential Cross-Saturation Inductance in Synchronous Machines,” *IEEE Transactions on Industrial Application*, vol. 53, no. 3, pp. 991–1000, October 2016.
- [30] D. Chung, J. Kim, and S. Sul, “Unified Voltage Modulation Technique for Real-Time Three-Phase Power Conversion,” *IEEE Transactions on Industry Applications*, vol. 34, no. 2, pp. 374–380, March/April 1998.
- [31] P. R. Mohan, T. B. Reddy, and M. V. Kumar, “Simple and efficient high-performance PWM algorithm for induction motor drives,” *Journal of Electrical Engineering*, vol. 11, pp. 353–360, 2011.
- [32] L. Harnefors, M. Hinkkanen, and O. Wallmark, *Control of Voltage-Source Converters and Variable-Speed Drives*, 2017.
- [33] Z. Qu, T. Tuovinen, and M. Hinkkanen, “Inclusion of magnetic saturation in dynamic models of synchronous reluctance motors,” *2012 XXth International Conference on Electrical Machines (ICEM)*, pp. 994–1000, 2-5 September 2012, Marseilles, France.
- [34] Y. Bouzid, “OP5600 & OP7000 High performance Real-Time simulators,” *6th International Conference on Real-Time Simulation Technologies*, June 2013.
- [35] B. T. Boulter, “Digital Filter Design. Writing Difference Equations For Digital Filters,” *ApICS LLC. APPLIED INDUSTRIAL CONTROL SOLUTIONS*.